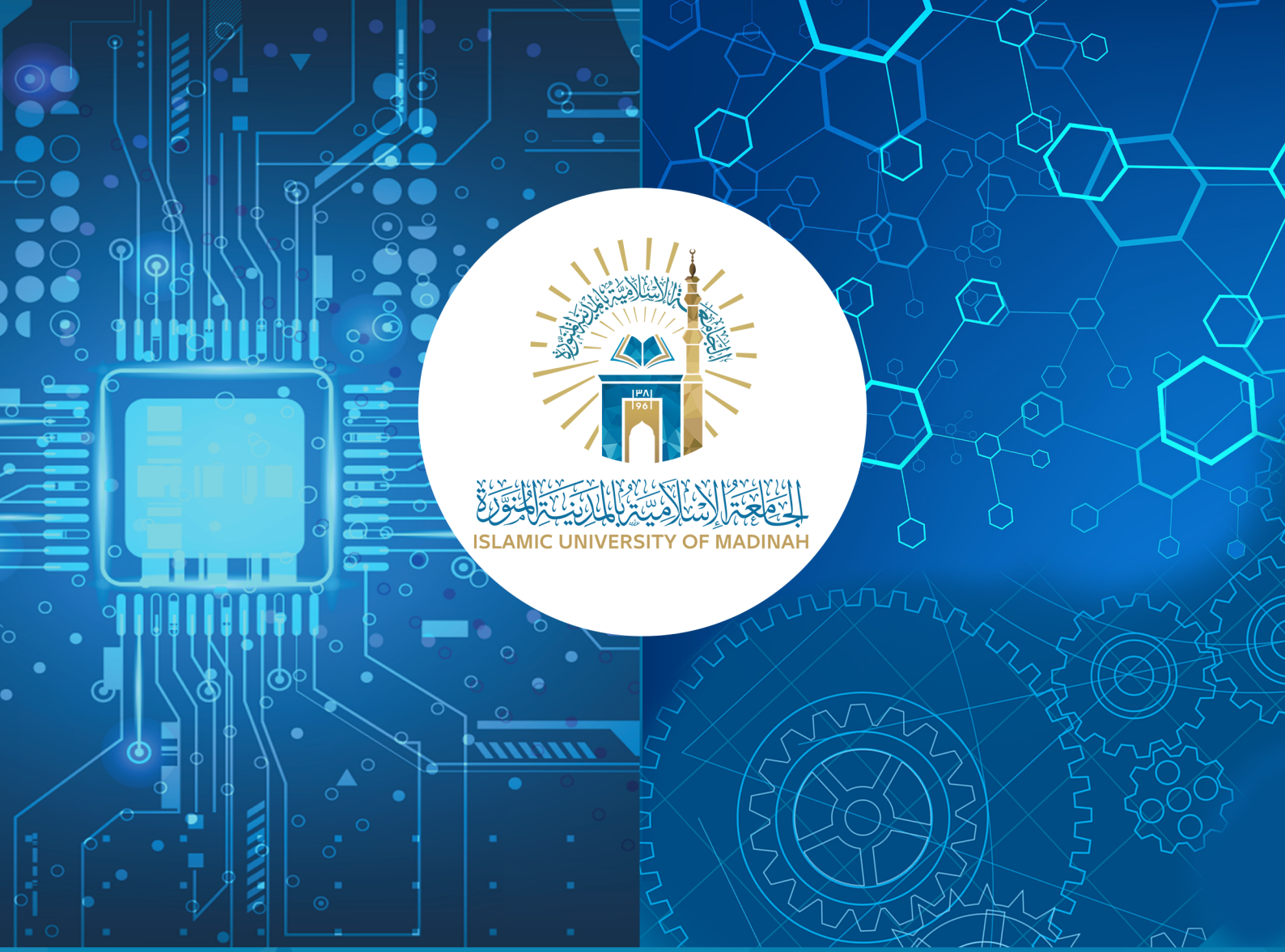


# Journal of
## Engineering Science & Computing

Vol : 1 Issue : 1 Year : 2019


بسم الله الرحمن الرحيم

**Paper version**

Filed at the King Fahd National Library No. 8742/1439 and the date of 17/09/1439 AH

International serial number of periodicals (ISSN) 1658-7936

**Online version**

Filed at the King Fahd National Library No. 8742/1439 and the date of 17/09/1439 AH

International Serial Number of Periodicals (e-ISSN) 1658-7944

**the journal's website**

https://journals.iu.edu.sa/JESC/index.html

The papers are sent in the name of the Editor-in –Chief of the Journal to this E-mail address

jesc@iu.edu.sa

# Publication Rules at the Journal (*)

❖ **General rules:**

- Report original scientific research (the main results and conclusions must not have been published or submitted elsewhere).
- Fit with the topics of the journal.
- Report novel results, innovative work and show a new scientific contribution.
- Not to bear similarity of more than 25% of a previously published work of the same author(s).
- Follow the rules, regulation and authentic research methodologies.
- Fulfill the required items and the format of the journal provided in appendix below related to the guide for author.
- Opinions expressed in published articles commit the authors themselves only and not necessarily the opinion of the journal.

❖ **For all articles:**

- The exclusive right to publish and distribute and article, and to grant rights to others, including commercial purposes.
- For open access articles, IU will apply the relevant third-party user license where IU publishes the article on its online platforms.
- The right to provide the article in all forms and media so the article can be used on the latest technology even after publication.
- The authority to enforce the rights in the article, on behalf of an author, against third parties, for example in the case of plagiarism or copyright infringement.

---

(*) These general rules are explained in details along with other rules for Author's guide in the journal's website: https://journals.iu.edu.sa/JESC/index.html

# (JESC)

# *The Journal of Engineering, Science and Computing*

**Issued By**

**The Islamic University of Almadinah-Almunawarah**

**Almadinah-Almunawarah, Saudi Arabia**

Dear friends and colleagues,

With great please, I am delighted to present you the inaugural issue of the Journal of Engineering, Science, and Computing (JESC) managed by the Islamic University of Madinah, Saudi Arabia.

The mission of the JESC is to discriminate the state-of-the-art contemporary research work from researchers across the globe in the areas of Engineering, Science and Computing.

The first issue of the journal attracted quite substantial numbers of submissions, which brought great pleasure to us. The editorial board including the Editor-in-Chief and the editorial advisory board would like to thank all of those who contributed to this issue and would like to welcome potential authors to contribute in future issues.

It is a privilege to share with you the inaugural issue of the journal and wish you happy reading.

Mohammad Abdeen, Ph.D., P.Eng.

Editor-in-Chief

The Journal of Engineering, Science and Computing (JESC)

# Table of Content

# Investigation of the Influence of Formulation Method on Dispersion Stability and Thermal Properties of $Al_2O_3$-CC-DW Nanofluids

**Noor Afifah Ahmad  Syahrullail Samion  Aminuddin Saat**

School of Mechanical Engineering, Faculty of Engineering, Universiti Teknologi Malaysia, 81310 Skudai, Johor, Malaysia.

noorafifahahmad90@gmail.com, syahruls@mail.fkm.utm.my, aminudin@utm.my

**Nor Azwadi Che Sidik**

Malaysia – Japan International Institute of Technology (MJIIT), University Teknologi Malaysia Kuala Lumpur, Jalan Sultan Yahya Petra (Jalan Semarak), 54100 Kuala Lumpur, Malaysia

azwadi@mail.fkm.utm.my

**Abstract:** The present study investigated influence of formulation methods on the physical properties and heat transfer behaviour of aluminium oxide-car coolant-distilled water nanofluids. The nanofluid solutions were formulated via two methods, namely the conventional method (M1), where nanoparticles were added into the CC-DW mixture and the proposed method (M2), where distilled water was added into the $Al_2O_3$-CC mixture. From the measurement of physical properties, it was observed that the proposed M2 method was more favourable compared to the conventional method because it promoted reductions in density and viscosity values, and also improvement in thermal conductivity. A similar trend was observed when examining nanofluids in the natural convective experiment. The proposed formulation resulted in better dispersion stability when subjected to heat. In addition, the M2 formulation gave higher Grashof ($Gr$), Rayleigh ($R_a$) and Nusselt ($Nu$) numbers. This study demonstrated that dispersion stability, physical properties and thermal performance of nanofluid were remarkably influenced by the preparation process.

**Keywords:** Nanofluid; $Al_2O_3$ nanoparticles; Formulation strategy; Natural convection; Sedimentation

# دراسة تأثير طريقة التركيب على ثبات التشتت والخواص الحرارية للألانوبدات

# Al2O3-CC-DW

**الملخص**: حققت هذه الدراسة تأثير أساليب الصياغة على الخواص الفيزيائية وسلوك نقل الحرارة من نانوفلويد الماء المقطر المبرد بأكسيد الألومنيوم. وقد صيغت الحلول نانوفلويد عبر طريقتين: هما الطريقة التقليدية (م 1)، حيث أضيفت جسيمات نانوية في الخليط (س س . د و) والطريقة المقترحة (م 2)، حيث تمت إضافة الماء المقطر إلى الخليط *Al2O3-CC.* من قياس الخصائص الفيزيائية، لوحظ أن الطريقة (م 2) المقترحة أكثر ملاءمة مقارنة بالطريقة التقليدية لأنها شجعت على تخفيض قيم الكثافة واللزوجة، وأيضا تحسين في الموصلية الحرارية .ولوحظ كذلك اتجاه مماثل عند دراسة نانوفلويد في تجربة الحمل الحراري الطبيعي. الصيغة المقترحة أسفرت عن تحسين استقرار التشتت عند التعرض للحرارة. وبالإضافة إلى ذلك، أعطت الصيغة (م2) عددا أكبر من جراشوف (ج ر)، رايليغ (را)، وأرقام نوسيلت (نو). أظهرت هذه الدراسة أن استقرار التشتت والخصائص الفيزيائية والأداء الحراري للنانوفلويد تأثرت بشكل ملحوظ بعملية التحضير.

## 1. Introduction

In a modern world of today, the current technology of extended surface and conventional heat transfer fluid or coolant have reached their limitation [1,2]. Therefore, modern engineering system demand a new alternative coolant with superior transport properties. Nanofluids as a promising candidate according to most researcher, need to fulfil the requirements of good long-term stability, less viscous solution and large thermal conductivity value before being acknowledged as a future generation coolant. In response to this issue, researcher tend to chemically modify the solution by either introducing a surfactant or acid/alkali into nanofluid solution. In return, the nanosuspension is stable for months. Nonetheless, the addition of surfactant in return dramatically augment viscosity value and transformed the nanofluid into non-Newtonian behaviour as reported in certain studies [3,4]. Yu et al. [4] found that addition of polyvinyl pyrrolidone into pure ethylene glycol enhanced the viscosity value by about threefold. Jarahnejad et al. [5] reported that viscosity of titanium dioxide nanofluid with trioxadecane acid was approximately 61% higher than that of without surfactant. Ravikumar et al. [6] chemically treated copper-water nanofluid with three

different kind of surfactants, namely PVP, sodium dodecyl sulfate (SDS) and cetyl trimethylammpnium bromide (CTAB). Viscosity measurements showed that nanofluid with PVP surfactant exhibited maximum enhancement of 60%, followed by SDS with 22% increment and 12% by CTAB, respectively. in another studies, addition of surfactant like chitosan, SDS and sodium dodecyl benzene sulfonate (SDBS) to improve stability of multiwalled carbon nanotube in water had transformed the solution into non-Newtonian fluid [7]. Similar observation of non-Newtonian behaviour also observed when the amount of alumina nanoparticles dispersed into car engine coolant greater than 0.4% [3]. While for another kind of zinc oxide-ethylene glycol nanofluid, a non-Newtonian behaviour was observed at nanoparticle concentration of 3.0% and above [4]. In another study, Suganthi and Rajan [8] suggested that modified formulation method of nanofluid also could improved dispersion stability of nanoparticles instead of using surfactant.

For natural convection heat transfer, Wen and Ding [9] reported that addition of titanium dioxide nanoparticles and surfactants (nitric acid and sodium hydroxide) into distilled water reduced the value of natural heat transfer coefficient. Such deterioration was found to be increase with nanoparticles concentration between 0.19% and 0.57%. In a subsequence investigation, similar behaviour also observed by Wen and Ding [10] at high $TiO_2$ nanoparticles concentration ranging from 0.8% to 2.5%. For alumina-deionized water ($Al_2O_3$-DI water) nanofluid, Li and Peterson [11] reported that at a given Rayleigh number (*Ra*), deionized water possess the highest Nusselt number (*Nu*) and the lowest values retained by $Al_2O_3$-DI water nanofluid with maximum volume fraction of 6.0%. Ni et al. [12] also claimed that convective heat transfer coefficient of $Al_2O_3$-water nanofluid was found to monotonically decrease. Similar trend also observed by Kouloulias et al. [13] although they did not chemically modify the nanofluid. This deterioration was worsening at maximum concentration of 0.12 % when *Ra* value increased, *Nu* value became nearly constant.

Since less attention is given to the formulation method of nanofluid, the present study investigated the influence of modifying formulation method on dispersion stability and physical properties of $Al_2O_3$-CC-DW nanofluids. Then, heat transfer behaviour of nanofluids that produce through two formulation methods were evaluated in natural convection experiment.

## 2. Materials and Methods

### 2.1 Materials

Aluminium oxide ($Al_2O_3$) nanopowder was commercially purchased from a local supplier. The diameter of primary $Al_2O_3$ particle provided by manufacturer is 30 nm in spherical shape and its density is 3.7 g/cm3. In the present study, $Al_2O_3$ nanoparticle was suspended into a base fluid of car coolant and distilled water (CC-DW) with volume ratio of 50:50. The amount of nanopowder suspended in based liquid was corresponding to 0.5 vol. %, and 2.0 vol. %, in which determined as follows:

$$\text{Concentration of nanoparticle (\%)} = \frac{\frac{m_{np}}{\rho_{np}}}{\frac{m_{np}}{\rho_{np}} + \frac{m_{bf}}{\rho_{bf}}} \times 100\% \quad (1)$$

where *m* and $\rho$ are mass and density, while *np* and *bf* denote to nanoparticle and base fluid.

## 2.2 Formulation of nanofluid

To acquire $Al_2O_3$-CC-DW nanofluid, two formulation methods were employed to produce the solution as elucidated in Figure 1. In first formulation, represented as Method 1 (M1), which is commonly employed by most researchers, involved suspending a predetermined mass of nanoparticles into a mixture of base liquids. While for the second formulation (M2), at first, a quantity of $Al_2O_3$ nanoparticles at certain concentration was first suspended in a coolant and then subjected to mixing process by means of shear homogenizer with operating speed of 11 rpm for 25 minutes. At the end of homogenizing process, the required volume of distilled water was added to the $Al_2O_3$-CC dispersion in order to acquire the final solution of $Al_2O_3$-CC-DW nanofluid.

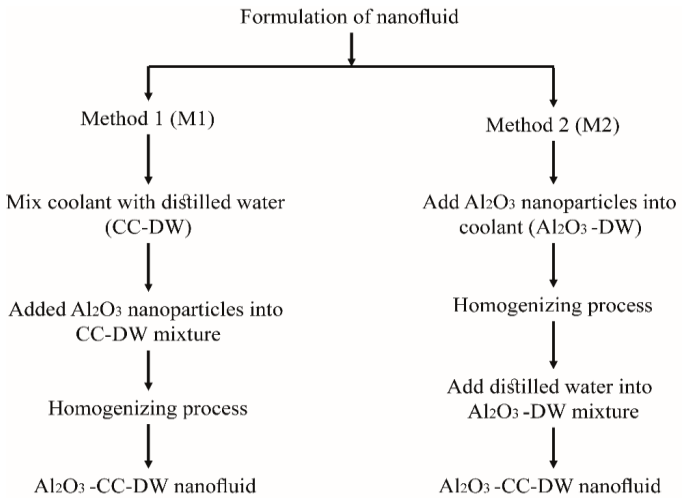


Figure 1. Two types of formulation methods of Al2O3-CC-DW nanofluid.

### 2.3 Physical properties of nanofluid

Density of $Al_2O_3$ nanofluid was measured by using hydrometer at room temperature and reported in kg/m$^3$. Dynamic viscosity was measured using digital rotational viscometer in accordance to ASTM D298 at room temperature. Stability behaviour of $Al_2O_3$ nanoparticles suspensions within based fluid were evaluated by visual inspection analysis over time. This was done by photographed periodically all samples of $Al_2O_3$ nanofluid solutions for 84 days.

### 2.3 Physical properties of nanofluid

A schematic diagram of experimental setup for natural convection heat transfer of $Al_2O_3$ -CC-DW nanofluids is shown in Figure 2. The experimental setup consists of stainless-steel sample holder, an electrical heater, power supply and K-type thermocouples (TC) connected to a data logger. Four TCs were used to measure temperature of the tested fluid at four different locations as illustrated in top view of test rig in Figure 2b. The location of TCs are 30 mm and 52 mm horizontally and vertically from the centre of test rig. The sample holder was insulated using ceramic fibre to minimize heat losses to the surrounding. In order to maintain constant heat flux boundary condition, the fluid sample was heated by supplying constant DC power to the heater. During the experiment, the sample holder was filled with a constant volume of tested fluid and power of 50 Watts was supplied. The temperature of test fluid was directly measure as a function of time for 3000s.

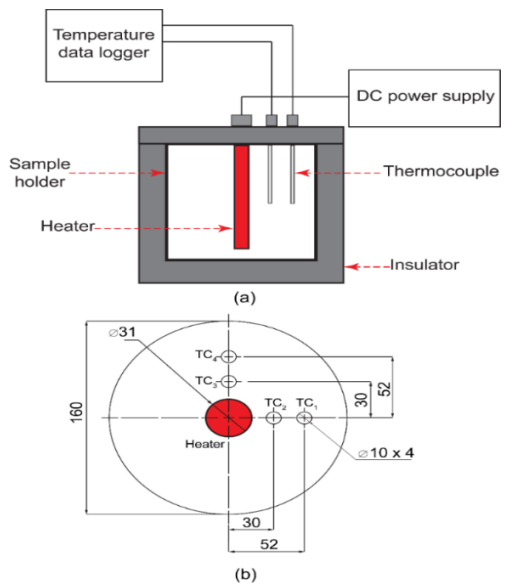


Figure 2. Experimental set up of natural heat transfer experiment.

From the experimental results, thermal conductivity of nanofluid was determined according to the equation:

$$k = \frac{q}{4\,\pi\,(T_2 - T_{1)}} \ln\left(\frac{t_2}{t_1}\right) \tag{2}$$

where $T_1$ and $T_2$ are temperature at different time of $t_1$ and $t_2$, while q is power input to the system, which was assumed constant during natural convective experiment. Moreover, specific heat of the fluid was calculated using the expression of

$$C_p = \frac{Q}{m\,\Delta T} \tag{3}$$

where m is mass of nanofluid, *Q* is flow of heat and ΔT is temperature difference between two time. Next, Grashoff number, *Gr* was determined as

$$Gr = \frac{gB(T_s - T_\infty)L^3}{\nu^2} \tag{4}$$

where L is a characteristic length of heat source, ν is kinematic viscosity, B is thermal expansion coefficient and both Ts and T∞ are defined as instantaneous temperature. For nanofluid solution, thermal expansion coefficient of nanofluid is calculated based on the following formula [15]:

$$B_{nf} = \frac{\phi\,\rho_{np}\,B_{np} + (1-\phi)\left(\rho_{bf}\,B_{bf}\right)}{\rho_{nf}} \tag{5}$$

where subscripts of np, bf and nf are refer to nanoparticle, base fluid and nanofluid and $\rho$ is density value of the constituents. Thermal expansion coefficient of $Al_2O_3$ nanoparticle was taken to be $8.46 \times 10^{-6}$ $K^{-1}$, while for distilled water the value varies between $1.5 \times 10^{-4}$ $K^{-1}$ and $6.2 \times 10^{-4}$ $K^{-1}$

for temperature ranging from 15ºC to 80ºC [16]. Lastly, thermal performance of nanofluid was evaluated based on Nusselt number which is determined according to equation 6 [17]:

$$Nu = \left\{ 0.60 + \frac{0.387Ra^{\frac{1}{6}}}{\left[1 + \left(\frac{0.559}{Pr}\right)^{\frac{9}{16}}\right]^{8/27}} \right\}^2 \quad (6)$$

where *Ra* and *Pr* are Rayleigh number and Prandtl number, where *Pr* number is expressed as $Pr = \frac{C_p}{k}$ and *Ra* = *Gr* x *Pr*. After that, thermal properties of the solution such as thermal conductivity, specific heat, Grashoff number, Rayleigh number and Nusselt number were investigated by plotting those properties as a function of experimental period.

## 3. Results and Discussions

### 3.1 Physical properties of nanofluid

Figure 3 and Figure 4 presented density and viscosity of nanofluids. It can be seen that density of the $Al_2O_3$ -CC-DW nanofluids were conspicuously higher than that of their base fluids, and the augmentation in density value was linear with volume concentration. And this result was consistent with correlation proposed by Pak and Cho [18] as given below:

$$\rho_{nf} = \phi\rho_p + (1-\phi)\rho_{bf} \quad (7)$$

where $\rho_{nf}$ is nanofluid density, $\rho_{bf}$ is fluid density, $\rho_p$ is particles density and $\phi$ is volume concentration of nanoparticles. The density of nanofluid produced via the M2 formulation was consistently lower than that of the nanofluid formulated using M1. At 5.0 vol.% nanoparticle concentration, the difference of density between formulation M1 and M2 is 0.18% and 4.0% for M2, respectively. This observation demonstrated that the density was strongly dependent on the

formulation method, in which the chemical interactions between the constituents had a dramatic influence on the density of nanofluid.

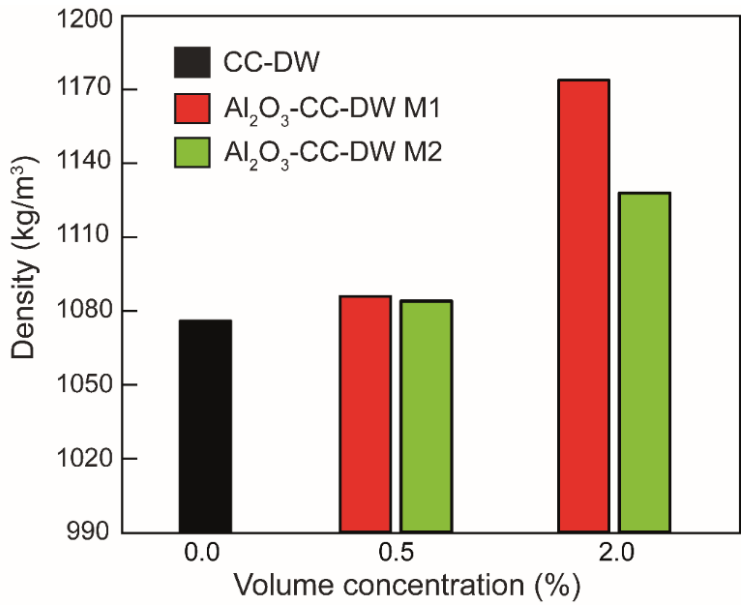


Figure 3. Effect of nanofluid's formulation and concentration on the density.

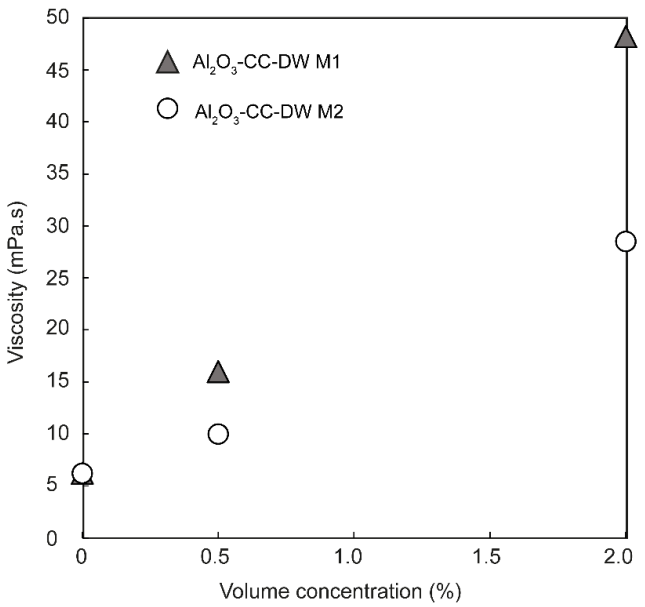


Figure 4. Viscosity of $Al_2O_3$-CC-DW nanofluid with 0.5 and 2.0 wt%.

As can be seen in Figure 4, viscosity of nanofluids were substantially larger than that of its base fluid, a mixture of car coolant with distilled water (CC-DW). This was because the suspended solid particles triggered a change in the velocity profile of base fluid by creating a secondary velocity profile around them and consequently a higher shear stress was generated at solid-liquid interface [14]. Then, the higher shear stress that evolved in a nanofluid system would augment the resistance of the liquid to motion. It was also observed that viscosity of nanofluids enhanced linearly with $Al_2O_3$ concentration. As the amount of $Al_2O_3$ nanoparticles suspended in base liquid escalated from 0.5% to 2.0%, more shear stress was generated at the solid-liquid interface, and this induced more alteration in the velocity profile of base fluid.

Besides, $Al_2O_3$-CC-DW nanofluids formulated by M2 were apparently lower than that of M1. According to [8,19], the addition of distilled water into $Al_2O_3$-CC mixture, as in the formulation M2, led to the disruption of the intermolecular hydrogen bonds in the coolant by water molecules, as elucidated in Figure 5b. Any reordering or disrupting of the hydrogen bonding in ethylene glycol molecules would result in a reduction of viscosity of the bulk solution, as reported in a previous experimental research [8,20]. Suganthi and Rajan [8] reported that the addition of water into zinc oxide-proplyene glycol (ZnO-PG) mixture to acquire ZnO-PG-water nanofluid, led to reduction in viscosity of about 11.4% at 2.0 vol. %. In another study, Christensen et al. [20] studied the effect of suspended iron oxide nanoparticle into various kind of solvents such as ketone, glycerol and water. Among the solvents, only water exhibited a good dispersion due to hydrogen bonding between water molecules. The authors claimed that the strong bonding not only promoted good stability behaviour but also induced the nanofluid became less viscous.

Stability of nanofluids formulated through Method 1 (M1) and Method 2 (M2) are shown in Figure 6 and Figure 7. For the formulation M1, nanofluid with 0.5 vol% was visually stable at day 0 only, while nanofluid with 2.0 vol.% managed to stable up to 3rd day. Meanwhile, for the solution formulated by M2, nanofluids of both concentrations were observed to be stable without any sediment layer at day 0 only. The results conspicuously indicated that sedimentation rate of M1 $Al_2O_3$ nanofluids was substantially slower than the M2 nanofluids. This observation contradicted with the findings reported by Suganthi and Rajan [8]. The researcher inferred that the addition of distilled water into nanoparticle-ethylene glycol (EG) dispersion could improve the stability behaviour as direct contact between water molecules and the nanoparticles had been minimized and this could reduce the aggregation rate and sedimentation rate eventually [8,20].

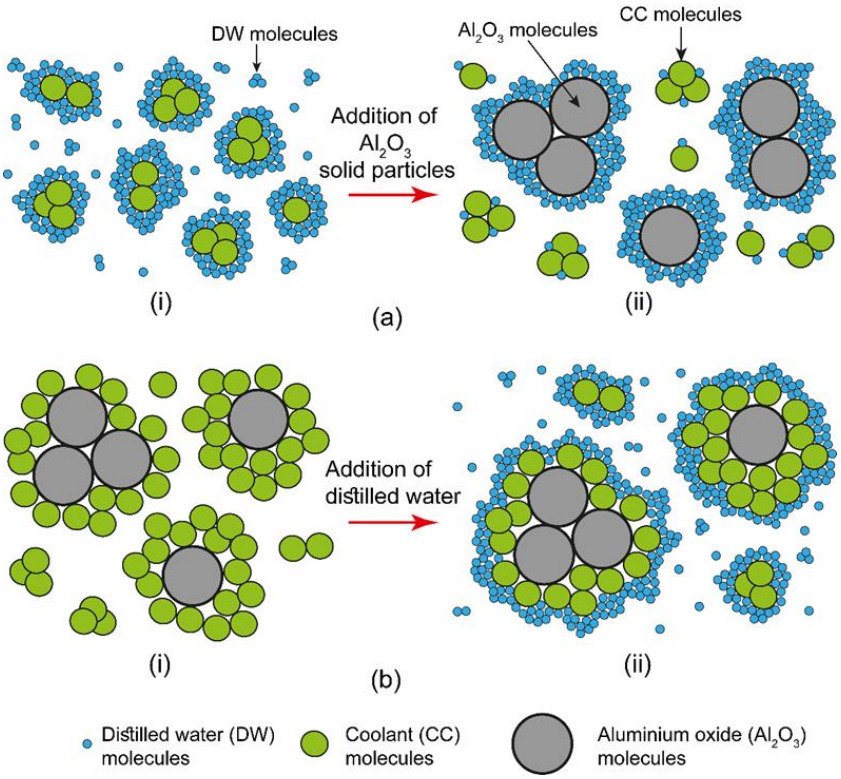


Figure 5. Mechanism of liquid layer in nanofluid when formulated with a) Method 1 and b) Method 2 (ai: CC-DW mixture, aii: $Al_2O_3$-CC-DW-M1 nanofluid, bi: $Al_2O_3$-CC mixture, bii: $Al_2O_3$-CC-DW-M2 nanofluid).

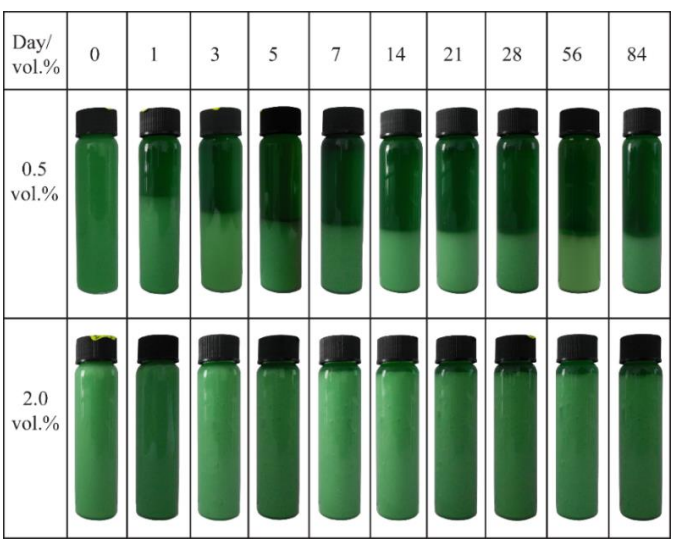


Figure 6. Stability of nanofluid formulated by method 1 as a function of time

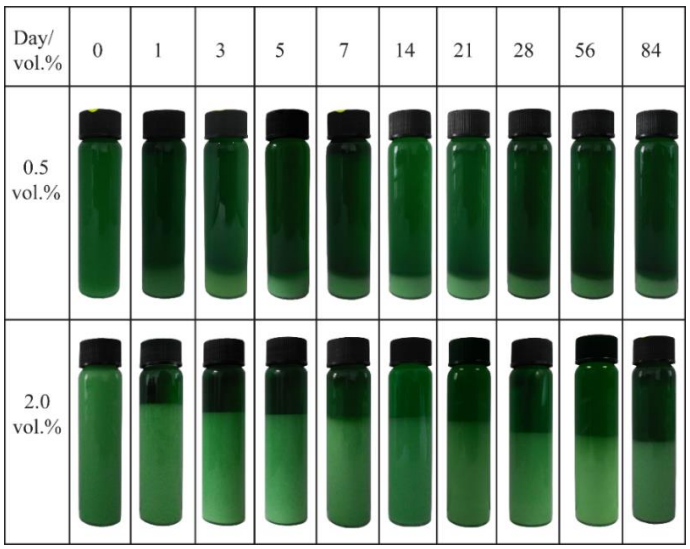


Figure 7. Stability of nanofluid formulated by method 2 over time.

The contradictory result might be attributed to the strong intermolecular forces due to the change of flow behaviour from Newtonian to non-Newtonian characteristic. As found in Figure 4, $Al_2O_3$-CC-DW nanofluids formulated by M1 were highly viscous especially at high concentration of 2.0% and at the same time demonstrated excellent stability behaviour. These results were comparable with observations reported by Kole and Dey [3]. Their rheological studies demonstrated greater than that 0.4%, nanofluid behave like non-Newtonian fluid. They found that nanofluid that demonstrated a non-Newtonian characteristic exhibited a very good stability behaviour for over 80 days in comparison to the nanofluid that demonstrated the Newtonian fluid. Hence, it was strongly believed that the good stability behaviour of the M1 nanofluid compared to that of M2 was due to the non-Newtonian property.

Apart from that, in both formulations, it was found that $Al_2O_3$ -CC-DW nanofluid with 0.5 vol.% exhibited the fastest settling rate compare to that of 2.0 vol.%. This result contradicted with the previous observation reported by [21,31]. The authors claimed that the stability of the $Al_2O_3$-DW nanofluid became worse at high concentration of nanoparticles because when the amount of solid particles increased, the distance between each particles reduced. Hence, there was a higher chance of collisions to occur between the particles, which would trigger rapid aggregation process. However, the interpretation was different from Amrollahi et al. [22] who investigated the effect of sonication time on the settling rate of carbon nanofluids. They observed that at a shorter sonication time less than 10 hours, nanofluid with 2.5 vol. % settled faster than nanofluid with 0.5 vol.%

concentration. Meanwhile, at a longer sonication time of 25 hours, 2.5 vol. % carbon nanofluid was physically stable than the 0.5 vol. % solution. Amrollahi and his co-worker concluded that in order to produce a homogenous and stable suspension, different volume concentrations of nanofluid require different preparation times. Moreover, a prolonged preparation time caused the solution to be unstable due to the excessive energy delivered to the fluid system [23-25]. Hence, the faster sedimentation rate of 0.5% $Al_2O_3$ -CC-DW nanofluid was because of the excessive mixing energy received by the solution. When this happens, nanoparticles are encouraged to re-agglomerate more rapidly and subsequently increased the sedimentation rate.

### 3.2 Thermal Conductivity and Specific Heat Capacity of nanofluid

The thermal conductivity ($k$) of $Al_2O_3$–CC–DW nanofluids is investigated with different formulation methods and volume concentration as presented in Figure 8. It was conspicuous from the figure that $k$ value of nanofluids were relatively larger than that of their base fluid and the trend increased linearly with concentration of nanoparticle. It was also noticeable that $k$ value of nanofluids with formulation M2 were larger in comparison with conventional method of M1. Therefore, the addition of water into the CC-DW mixture not only reduced the viscosity as in Figure 4 but also enhanced the thermal conductivity property of nanofluid.

Figure 9 presents the results of specific heat capacity ($C_p$) $Al_2O_3$–CC–DW nanofluids and its base fluids against experimental time between 500s and 3000s. It was seen that specific heat value of 0.5% and 2.0% $Al_2O_3$–CC–DW nanofluids were increased with heating period. These results exhibited that capability of all solutions to absorb heat enhanced with increasing experimental time along with temperature rise.

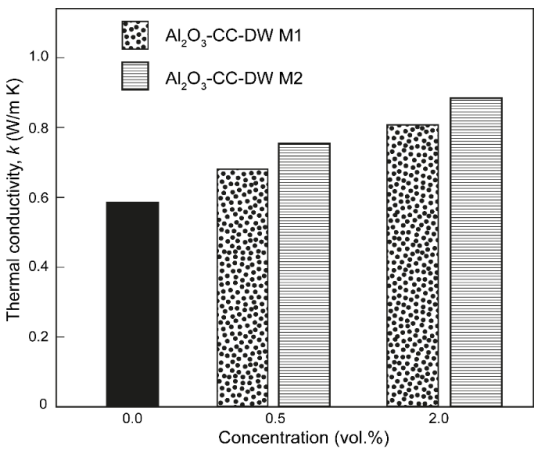


Figure 8. Thermal conductivity of $Al_2O_3$–CC–DW nanofluids.

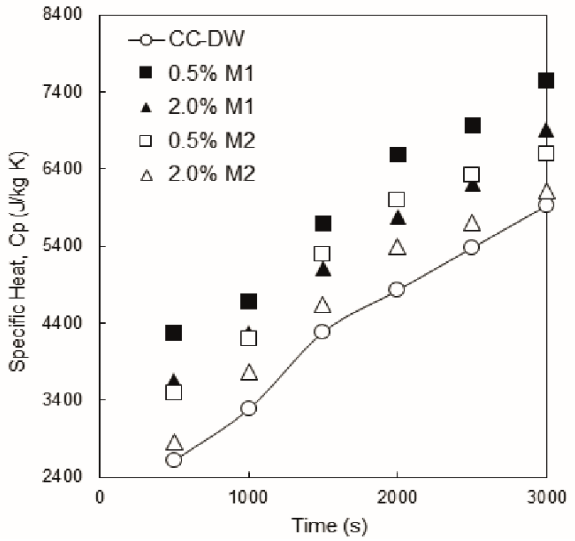


Figure 9. Specific heat capacity of $Al_2O_3$ –CC–DW nanofluids.

Apart from that, it was found that $C_p$ value of fluid containing $Al_2O_3$ nanoparticles was always larger than that of CC–DW base fluid. However, $C_p$ value experienced a reduction in the enhancement when further increased volume concentration of nanoparticles from 0.5% to 2.0%. Such behaviour of $C_p$ over nanoparticle concentration had been observed in other kinds of nanofluid [26,27]. Ijam et al. [26] found that the $C_p$ value of graphene oxide–deionized water–ethylene glycol nanofluid substantially increased with nanoparticle concentration from 0.01 to 0.05 wt.%, but the value decreased when the concentration exceeded 0.07%. Similarly, for multiwall carbon nanotube–water– ethylene glycol nanofluid, Kumaresan and Velraj [27] reported that the reduction in the improvement of $C_p$ occurred at higher concentration of beyond 0.45%. These experimental observations indicated that there was a limit in the amount of nanoparticle suspended in the base fluid, where it become a margin between the enhancement and reduction trend of specific heat capacity.

### 3.3 Thermal Performance: Grashof number, Rayleigh number and Nusselt number

From the natural convective experiment, thermal performance of $Al_2O_3$–CC–DW nanofluid is evaluated in term of Grashof number (*Gr*), Rayleigh number ($R_a$) and Nusselt number (*Nu*) as depicted in Figure 10, Figure 11 and Figure 12, respectively. From Figure 10, it was found that only the base fluids of CC-DW mixture experienced a sharp augmentation of *Gr* value, while all nanofluids behaved contrarily against heating period. Besides that, *Gr* value of nanofluids were lowered than that of base fluid and deteriorated with increasing of nanoparticle concentration.

These results demonstrated that the presence of nanoparticles in the fluid medium retarded the motion of fluid and energy exchange rate driven by buoyancy force.

For nanofluid system, the existence of nanoparticle was expected to augment the temperature gradient and subsequently velocity of fluid flow because the Brownian motion of solid particles became aggressive with increasing temperature. However, from the experimental results, it was observed that the presence of nanoparticles decelerated the velocity of fluid across the enclosure as the *Gr* values were lower than that of base fluid. These findings were absolutely contradicted with the results reported by [15,28,30] as the respective authors inferred that by suspending nanoparticles into base fluid, the fluid flow and velocity distribution were explicitly enhanced, thus leading to the escalation in the rate of energy transfer.

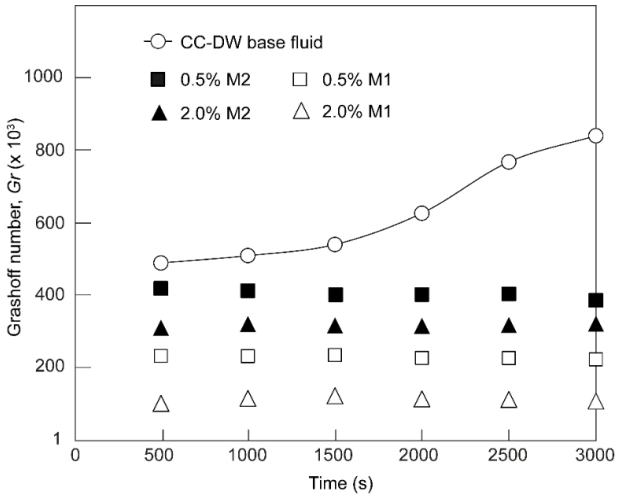


Figure 10. Grashoff number of CC-DW and $Al_2O_3$ nanofluid of formulation M1 and M2.

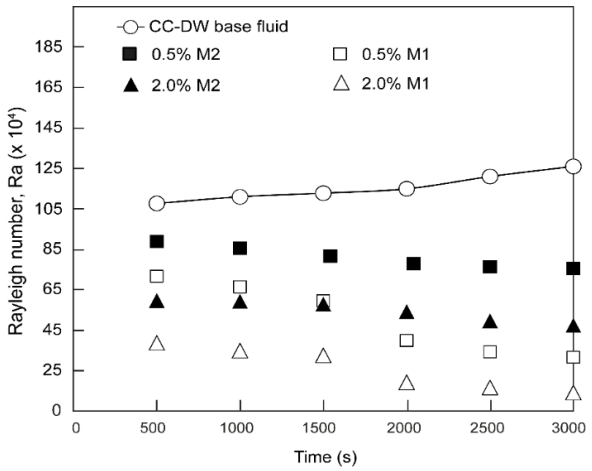


Figure 11. Reduction of Rayleigh number of $Al_2O_3$–CC–DW nanofluids over time.

A similar trend of *Gr* of nanofluid as a function of heating was observed for the Rayleigh number ($R_a$) as presented in Figure 11, where only the base fluid exhibited an increment in $R_a$ value and degradation of $R_a$ of nanofluids became worse with increasing nanoparticle concentration. This result was identical with the numerical study done by Snoussi et al. [29]. The authors suggested that at high nanoparticle concentration, the solution became highly viscous and tend to retard the fluid movement and consequently the convection effect. They inferred that $R_a$ behaviour was very sensitive towards viscosity of nanofluid. For nanofluid, the degradation effect of both *Gr* and $R_a$ became less when formulated with M2 compared to M1. It might be attributed to the enhanced physical properties of nanofluid as a result of the strong liquid layering of hydrogen bonding in formulation M2.

From the *Gr* and $R_a$ graphs, the presence of nanoparticle deteriorated the *Nu* as shown in Figure 12, where *Nu* value of nanofluids were profoundly worsen with increasing of nanoparticle concentration. Experimental investigation done by Kouloulias et al. [13] also demonstrated similar trend, where the suspension of alumina nanoparticle in deionized water had significantly degraded the heat transfer coefficient and the values degenerated with increasing concentration of alumina. The authors claimed that the deterioration of heat transfer performance was attributed to the severe sedimentation of nanoparticles when subjected to the heat as they discovered the deposition of $Al_2O_3$ nanoparticles on the hot plate though the nanofluid was in a good stability condition before the experiment started.

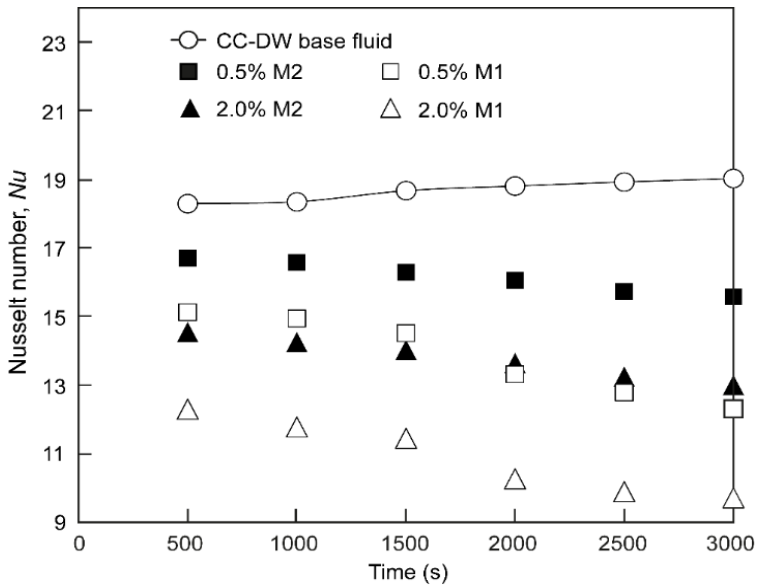


Figure 12. Nusselt number of $Al_2O_3$–CC–DW nanofluids as a function of time.

To prove such occurrence was also present in the present study, a dummy heating test was conducted as shown in Figure 13 since sedimentation phenomenon cannot directly observed during natural convective experiment. It was done by heating the nanofluid at a constant power input for 30 minutes. After 30 minutes of heating, nanofluid with 0.5 and 2.0 vol.% were conspicuously separated into two layers, where the lower layer which closed to the heat source is dominated by the white layer that was believed belong to $Al_2O_3$ nanoparticle. These results obviously showed that imposing heat to the nanofluid would rapidly augment the rate of aggregation process, induced the particles to free themselves from the bulk fluid and eventually deteriorated heat transfer performance of the solution.

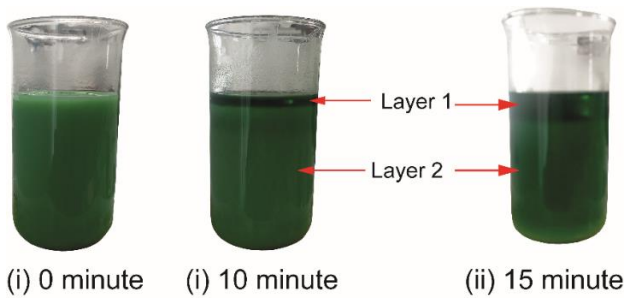


Figure 13. Separation of $Al_2O_3$–CC–DW nanofluids solution when subjected to heat.

## 4. Conclusion

In the present study, $Al_2O_3$ nanoparticles are dispersed in the mixture of car coolant and distilled water (CC-DW). Modifying formulation strategy has been utilized in order to acquire $Al_2O_3$-CC-DW nanofluid with good stability behaviour. The results revealed that liquid layering of molecule has a huge influenced on the stability behaviour, density, viscosity, thermal conductivity and specific heat capacity properties of nanofluid. Enhancement in physical properties were observed in $Al_2O_3$ nanofluid with new formulation of M2. From the natural convection experiment, it was found that the addition of $Al_2O_3$ nanoparticles in CC-DW base fluid has deteriorated the Grashof number, Rayleigh number and Nusselt number. Deposition of nanoparticles when subjected to heat was the main contributory factor of this deterioration. However, the deterioration effect became less when employing nanofluid with new formulation.

## 4. References

[1] R. Saidur, K. Y. Leong, H. A. Mohammad, A review on applications and challenges of nanofluids, Renew. Sust. Energ. Rev. 15 (3) (2011) 1646-1668.

[2] N. A. C. Sidik, M. N. A. W. M. Yazid, R. Mamat, A review on the application of nanofluids in vehicle engine cooling system, Int. J. Heat Mass Transf. 68 (2015) 85-90.

[3] M. Kole, T. K. Dey, Viscosity of alumina nanoparticles dispersed in car engine coolant, Exp. Therm. Fluid Sci. 34 (2010) 677-683.

[4] W. Yu, H. Xie, L. Chen, Y. Li, Investigation of thermal conductivity and viscosity of ethylene glycol based ZnO nanofluid, Thermochimic Acta 491 (2009) 92-96.

[5] M. Jarahnejad, E. B. Haghighi, M. Saleemi, N. Nikkam, R. Khodabandeh, B. Palm, M. S. Toprak, M. Muhammed, Experimental investigation on viscosity of water-based $Al_2O_3$ and $TiO_2$ nanofluids, Rheol. Acta 54 (5) (2015) 411-422.

[6] S. V. Ravikumar, J. M. Jha, K. Haldar, S. K. Pal, S. Chakraborty, Surfactant-Based Cu–Water Nanofluid Spray for Heat Transfer Enhancement of High Temperature Steel Surface, J. Heat Transf. 137 (5) (2015) 051504.

[7] T. P. Teng, Y. B. Fang, Y. C. Hsu, L. Lin, Evaluating stability of aqueous multiwalled carbon nanotube nanofluids by using different stabilizers, J. Nanomater. 2014 (2014) 203.

[8] K. S. Suganthi, K. S. Rajan, A formulation strategy for preparation of ZnO–propylene glycol–water nanofluids with improved transport properties, Int. J. Heat Mass Transf. 71 (2014) 653-663.

[9] D. Wen, Y. Ding, Formulation of nanofluids for natural convective heat transfer applications, Int. J. Heat Fluid Flow 26 (6) (2005) 855-864.

[10] D. Wen, Y. Ding, Natural convective heat transfer of suspensions of titanium dioxide nanoparticles (nanofluids), IEEE Trans. Nanotechnol. 5 (3) (2006) 220-227.

[11] C. H. Li, G. P. Peterson, Experimental studies of natural convection heat transfer of Al2O3/DI water nanoparticle suspensions (nanofluids), Adv. Mech. Eng. 2 (2010) 742739.

[12] R. Ni, S. Q. Zhou, K. Q. Xia, An experimental investigation of turbulent thermal convection in water-based alumina nanofluid, Physics of Fluids, 23 (2) (2011) 022005.

[13] K. Kouloulias, A. Sergis, Y. Hardalupas, Sedimentation in nanofluids during a natural convection experiment, Int. J. Heat Mass Transf. 101 (2016) 1193-1203.

[14] E. E. S. Michaelides, Nanofluidics: thermodynamic and transport properties, Springer, 2014.

[15] K. Khanafer, K. Vafai, M. Lightstone, Buoyancy-driven heat transfer enhancement in a two-dimensional enclosure utilizing nanofluids, Int. J. Heat Mass Transf. 46 (19) (2003) 3639-3653.

[16] C. J. Ho, W. K. Liu, Y. S. Chang, C. C. Lin, Natural convection heat transfer of alumina-water nanofluid in vertical square enclosures: an experimental study, Int. J. Therm. Sci. 49 (8) (2010) 1345-1353.

[17] P. I. Frank, P. D. David, L. E. Theodore, S. L. Adrienne, Foundations of Heat Transfer, 6th ed., Asia: John Wiley & Sons Inc, 2013.

[18] B. C. Pak, Y. I. Cho, Hydrodynamic and heat transfer study of dispersed fluids with submicron metallic oxide particles, Exp. Heat Transf. 11 (2) (1998) 151-170.

[19] K. S. Suganthi, S. Manikandan, N. Anusha, K. S. Rajan, Cerium oxide–ethylene glycol nanofluids with improved transport properties: preparation and elucidation of mechanism, J. Taiwan Inst. Chem. Eng. 49 (2015) 183-191.

[20] G. Christensen, H. Younes, H. Hong, P. Smith, Effects of solvent hydrogen bonding, viscosity, and polarity on the dispersion and alignment of nanofluids containing Fe2O3 nanoparticles, J. Appl. Phys. 118 (21) (2015) 214302.

[21] R. Sadeghi, S. G. Etemad, E. Keshavarzi, M. Haghshenasfard, Investigation of alumina nanofluid stability by UV–vis spectrum, Microfluid. Nanofluidics 18 (5-6) (2015) 1023-1030.

[22] A. Amrollahi, A. A. Hamidi, A. M. Rashidi, The effects of temperature, volume fraction and vibration time on the thermo-physical properties of a carbon nanotube suspension (carbon nanofluid), Nanotechnology 19 (2008).

[23] D. Rouxel, R. Hadji, B. Vincent, Y. Fort, Effect of ultrasonication and dispersion stability on the cluster size of alumina nanoscale particles in aqueous solutions, Ultrason. Sonochem. 18 (1) (2011) 382-388.

[24] Y. Y. Song, H. K. D. H. Bhadeshia, and D. W. Suh, Stability of stainless-steel nanoparticle and water mixtures, Powder Technol. 272 (2015) 34-44.

[25] S. A. Adio, M. Sharifpur, J. P. Meyer, Influence of ultrasonication energy on the dispersion consistency of Al2O3–glycerol nanofluid based on viscosity data, and model development for the required ultrasonication energy density, J. Exp. Nanosci. 11 (8) (2016) 630-649.

[26] A. Ijam, R. Saidur, P. Ganesan, A. M. Golsheikh, Stability, thermo-physical properties, and electrical conductivity of graphene oxide-deionized water/ethylene glycol based nanofluid, Int. J. Heat Mass Transf. 87 (2015) 92-103.

[27] V. Kumaresan, R. Velraj, Experimental investigation of the thermo-physical properties of water–ethylene glycol mixture-based CNT nanofluids, Thermochim. Acta 545 (2012) 180-186.

[28] X. F. Li, X. J. Wang, Z. Z. Li, Grashof number effects on nanofluids in natural convection heat transfer, Appl. Mech. Mater. 468 (2014) 43-48.

[29] L. Snoussi, R. Chouikh, N. Ouerfelli, A. Guizani, Numerical simulation of heat transfer enhancement for natural convection in a cubical enclosure filled with Al2O3/water and Ag/water nanofluids, Phys. Chem. Liq. 4 (6) (2016) 703-716.

[30] M. S. Jaman, S. Islam, S. Saha, M. N. Hasan, M. Q. Islam, Effect of Reynolds and Grashof numbers on mixed convection inside a lid-driven square cavity filled with water-Al 2 O 3 nanofluid, presented at AIP Conference Proceedings (vol. 1754, no. 1, p. 050050), July 12 (2016).

[31] R. Choudhary, D. Khurana, A. Kumar, S. Subudhi, Stability analysis of Al2O3/water nanofluids, J. Exp. Nanosci. 12 (1) (2017) 140-151.

# White Light Interferometry of SOI Deeply-Etched Fully Integrated MEMS Interferometers

**Haitham Omran**

Laboratory of Micro Optic, Faculty of Information Engineering and Technology, German University in Cairo, Egypt

haitham.omran@guc.edu.eg

**Diaa Khalil**

Faculty of Engineering, Ain Shams University, Egypt

diaa.khalil@ieee.org

**Abstract:** In this paper we investigate numerically and experimentally the effect of thin Silicon (Si) splitter parasitic Fabry-Perot and Si/Air splitter Silicon dispersion on the white light interferometry of deeply-etched MEMS interferometers using Silicon On Insulator (SOI) technology. The numerical simulations and practical measurements show that multiple internal reflections inside the thin Silicon splitter form a parasitic Fabry-Perot cavity inside the MEMS interferometer. This results in duplicated side interferograms that practically limits the interferometer maximum optical path difference and hence the resolution of MEMS based FT-IR spectrometer. Silicon dispersion, in case of Si/Air splitter results in a chirped and shifted interferogram that can be compensated using very long travel range electrostatic MEMS actuators.

**Keywords:** White Light, Dispersion, Interferometer, MEMS, SOI, Deeply-Etched.

# قياس تداخل الضوء الأبيض في مقياس تداخل ضوئي كهروميكانيكي ميكرومتري مصنع بتكنولوجيا الحفر العميق على السيليكون

**الملخص:** يقوم هذا البحث بعرض محاكاة رقمية وتجارب عملية تبين تأثير التشتت الضوئي على عمل مقسم ضوئي مصنوع بتكنولوجيا الحفر العميق على السيليكون وتأثير التشتت على عمل مقياس تداخل ضوئي كهروميكانيكي ميكرومتري. وتخلص الدراسة إلى أن التشتت الضوئي الناتج عن استخدام السطح البيني بين الهواء والسيليكون كمقسم ضوئي يمكن التغلب عليه باستخدام محرك كهروميكانيكي ميكرومتري بسعة حركة خطية كبيرة. أما التشتت الضوئى الناتج عن مقسم رفيع من السيليكون فيؤدي إلى ظهور تداخل جانبي غير مرغوم فيه مما يؤثر على دقة مقياس التداخل الضوئي.

## 1. Introduction

Deeply-Etched optical MEMS interferometers and filters using Deep Reactive Ion Etching [1- 5] (DRIE) of SOI [6, 7] wafers have become one of the most enabling technologies for FT-IR micro-spectrometers [8-15] and MEMS based Swept Lasers [16- 18]. Fully integrated deeply-etched Michelson [8] and Mach-Zhender [11] MEMS interferometers have been implemented using this technology and used for MEMS based FT-IR spectroscopy. Two types of deeply-etched splitters have been presented in literature: thin Si splitter [10] and Si/Air beam splitter [8]. A scientific study comparing the performance of deeply-etched interferometers using these two types of splitters with a white light input [23-29] has not been presented in literature, far to our knowledge. The operation of MEMS interferometers with the two splitter types have only been studied using a monochromatic input source [8-13]. The target of this paper is to compare the performance of deeply-etched MEMS interferometers with thin Silicon and Si/air beam splitters with a white light input. The comparison focuses on two main effects: The first is the effect of parasitic Fabry-Perot (FP) cavity formed by the thin Si splitter and the second is the effect of Silicon dispersion in Si/air beam splitter, both on the MEMS interferometer output interferogram.

The comparison is done with the Si/air splitter in a Mach-Zhender Interferometer (MZI) configuration while the thin splitter in a Michelson Interferometer (MSI). The fabrication of MZI

with two thin splitters would double the problem of parasitic FP. The two splitters will not have exact dimensions due to DRIE errors imposing additional unknowns to the study in addition to introducing robustness issues. These reasons motivated the use of two different configurations for the study.

The first section of the paper describes the two MEMS interferometers with the two splitter types. The second section explains the parasitic FP and dispersion effects caused by the two splitters and provides the mathematical representation of the output interferogram. The third section estimates the two effects using numerical simulations and the last section presents the practical measurements of the output interferogram of the two interferometers with white light input and compares the results with the numerical simulations. Part of the numerical results about dispersion in Mach-Zhender interferometry has been presented in MOC2017 Conference in Japan [30]. The numerical analysis of thin Si splitter effect, detailed analysis of Si/Air splitter dispersion effect and all practical results are all new additions.

## 2. Deeply etched interferometers

The two deeply etched interferometers under consideration are a MSI with thin Silicon beam splitter and a MZI with two Si/Air beam splitters. The layouts of the two deeply etched interferometers are shown in figure 1 and figure 2. The fabrication steps have been discussed in our previous work [8, 11]. The Michelson interferometer consists of a moving mirror M1, a fixed mirror M2, thin Silicon splitter BS and two input and output fiber grooves. The optical path (L1,L2) of the two beams is designed to be equal. However after fabrication a mismatch may occur due to DRIE over etching errors. Also misalignment of the input fiber core form mean ray position at the center of the splitter may cause additional optical path mismatch.

The MZI consists of two Si/Air beam splitters BS1 and BS2, two moving mirrors M1 and M2, a total internal reflection (TIR) mirror M3, an input fiber groove and two output fiber grooves [11]. The two mirrors can be moved at the same time using the same MEMS electrostatic comb actuator. Recording the output power with the motion of the moving mirrors gives the interferogram of an FT-IR spectrometer [11].

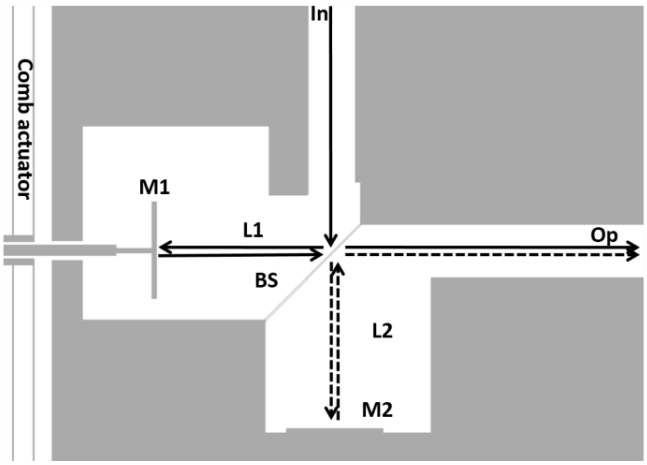


Figure 1. Layout of Deeply-etched Michelson interferometer with thin Silicon beam splitter.

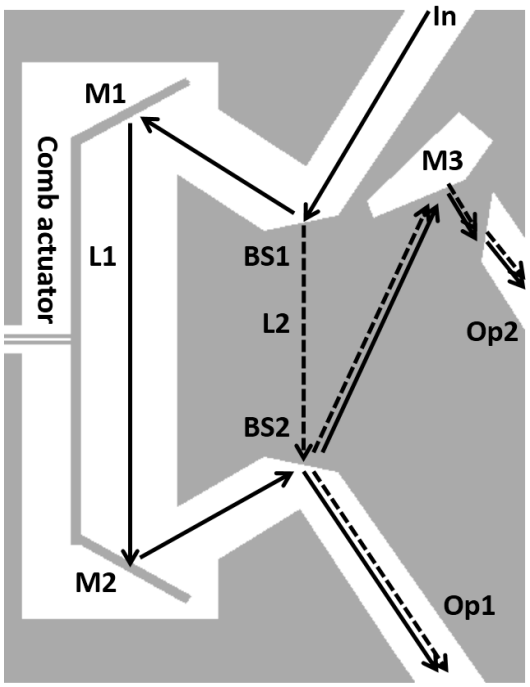


Figure 2. Layout of deeply- etched Mach-Zhender interferometer with two Si/Air beam splitters.

## 3. Description of parasitic Fabry-Perot and Dispersion Effect

### 3.1 Parasitic FP effect in thin Si splitter

The thin silicon splitter has two Si/air interfaces parallel to each other and aligned by optical

lithography with a thin layer of Silicon separating them. The multiple reflections in this thin Silicon layer forms the parasitic Fabry-Perot effect. In conventional bulk spectrometers this can be easily overcome by Antireflection (AR) coating one side of the splitter to match air. This is not feasible in a deeply etched MEMS interferometer fabricated in a one lithography step using DRIE. A subsequent coating step will also coat the micro mirrors in front of the splitter from both sides in addition to introducing uniformity issues in an in-plane deep structure. The complex amplitude of the electric field at output of the Michelson interferometer with thin Si splitter assuming a plane wave model is given by:

$$E_{op} = E_{in} r_{fp} t_{fp} \exp\left[ - j \frac{2\pi}{\lambda} \left( L_{in} + 2L_1 + L_{op} + MOPD \right) - j\pi \right]$$
$$+ E_{in} r_{fp} t_{fp} \exp\left[ - j \frac{2\pi}{\lambda} \left( L_{in} + 2L_2 + L_{op} + OPM \right) - j\pi \right]$$

where $t_{fp}$ and $r_{fp}$ are wavelength dependent transmission and reflection coefficients for a Fabry-Perot cavity with an arbitrary incident angle θ [21]. $t_{fp}$ and $r_{fp}$ are given by:

$$t_{fp} = \frac{t_{12} t_{21} r_{21}}{1 - r_{21}^2 \exp(j\, 2\eta d \, \frac{2\pi}{\lambda} \cos\theta)} \exp(j\, \eta \frac{2\pi}{\lambda} \frac{d}{\cos\theta})$$

$$r_{fp} = r_{12} + \frac{t_{12} t_{21}}{1 - r_{21}^2 \exp(j\, 2\eta d \, \frac{2\pi}{\lambda} \cos\theta)} \exp(j\, 2\eta d \, \frac{2\pi}{\lambda} \cos\theta)$$

L1 and L2 are the length between thin splitter and first and second mirrors respectively as indicated in figure 1. MOPD is the optical path difference due to mirror retardation which is double the comb displacement. Lin and Lop are the length of input and output grooves till fiber tip respectively. OPM is the optical path mismatch between L1 and L2 caused by DRIE errors, fibers misalignment and verticality of deeply-etched surfaces. The π factor accounts for a π phase shift at the mirror [21]. ($r_{12}$,$t_{12}$) and ($r_{21}$,$t_{21}$) are the Fresnel reflection and transmission coefficient from air to Silicon and from Silicon to air respectively [20]. d is thickness of the thin Silicon splitter.

**3.2 Dispersion Effect in Si/Air Splitter**

The dispersion effect in case of the MZI with two Si/Air beam splitter rises from the fact that one of the optical beams has its optical path completely in Silicon with wavelength dependent refractive index while the other beam is completely in air. The monolithic integration of the MZI with thick splitter using DRIE causes this effect to be inherited in the structure. Si cannot be placed in the air path as it will cause multiple parasitic coupled cavities with the moving micro mirrors and loss of power in path L1. At the first output of the MZ interferometer with Si/Air beam splitter the electric field is given by:

$$E_{op1} = E_{in} r_{s1} r_{s2} \exp\left[-j\frac{2\pi}{\lambda}\left(L_{in}+L_1+L_{op}+MOPD+L_{op1}\right)+j\pi\right]$$
$$+E_{in} t_{s1} t_{s2} \exp\left[-j\frac{2\pi}{\lambda}\left(L_{in}+\eta(\lambda)L_2+L_{op}+L_{op1}\right)\right]$$

where ($t_{s1}$,$r_{s1}$), ($t_{s2}$,$r_{s2}$) are the transmission and reflection coefficient at the first Air/Si (BS1) and second Si/Air (BS2) beam splitters, respectively calculated from Fresnel equations [20]. A π /2 phase exists between the reflected and transmitted beams at each beam splitter [21]. The intensity of the interferogram at the output is given by:

$$I_{op1} = \left| E_{op1} \right|^2$$

The wavelength dependent refractive index can be calculated from a temperature dependent Sellmeier model [22]:

$$\eta^2(\lambda,T) = 1+\sum_{i=1}^{3}\frac{S_i(T).\lambda^2}{\lambda^2-\lambda^2{}_i(T)}$$

where Si are the strengths of the resonance features in the material at wavelengths λi and T is the temperature which is assumed to be 300 K.

**4. Numerical model**

**4.1 Numerical estimation of parasitic FP effect**

To numerically investigate the parasitic FP and dispersion effects a simple plane wave model was used based on the equations in the previous section. The new additions in the model are the wavelength dependent refractive index η(λ) and the embedded parasitic FP effect in rfp and tfp. A white light input is assumed in the wavelength range 1.2 um to 1.7 um with equal amplitude for all wavelengths. The numerical simulator computes the electric field for each input wavelength at the output of the interferometers. All field components are then added and intensity is calculated. L1 and L2 of the MSI are designed to be 650 um. The thin splitter thickness after fabrication is estimated to be 2.5 um. Measured MOPD of the comb actuator is 50 um. OPM is estimated to be 26 um to fit with experimental results. This value is reasonable as the error in DRIE process is proportional to the size of the area to be etched [11], fibers misalignment and verticality of the deeply-etched surfaces. The simulated interferogram at the output of the MSI is shown in figure 3. It is clear that the parasitic FP causes duplicated side interferograms to appear limiting the useful optical path difference of the interferometer and hence resolution in case of FT-IR spectroscopy [21]. The location of the duplicated interferograms is function of the splitter thickness.

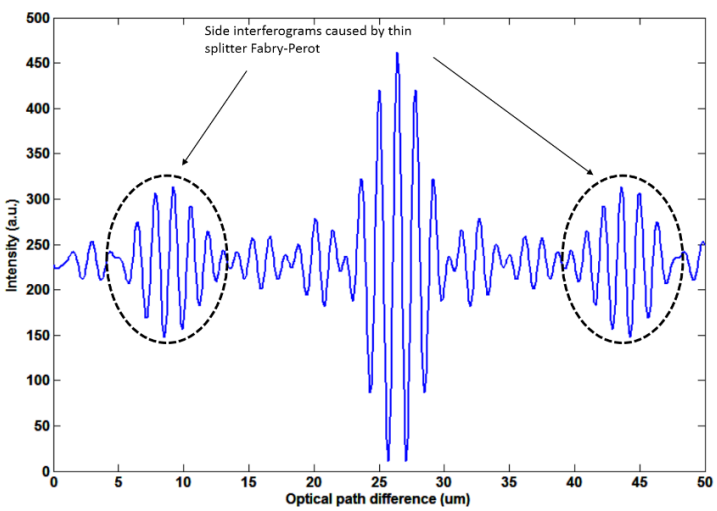


Figure 3.Numerically simulated interferogram of deeply-etched MSI showing duplicated side interferograms.

### 4.2 Numerical Estimation of Dispersion Effect

For the MZI, the comb actuator OPD is 130 um [11]. The interferogram at the first output was simulated for the 130 um OPD that can be practical achieved by the comb and a theoretical extension of 350 um as shown in Figure 4. The Si dispersion effect causes the interfergram to be chirped and shifted. For an OPD of 130 um, part of the intereferogram is practically outside the

achievable 130 um OPD. Thus the dispersion effect of the Si/Air beam splitter needs to be compensated by long travel range electrostatic comb actuators with about 250 um OPD.

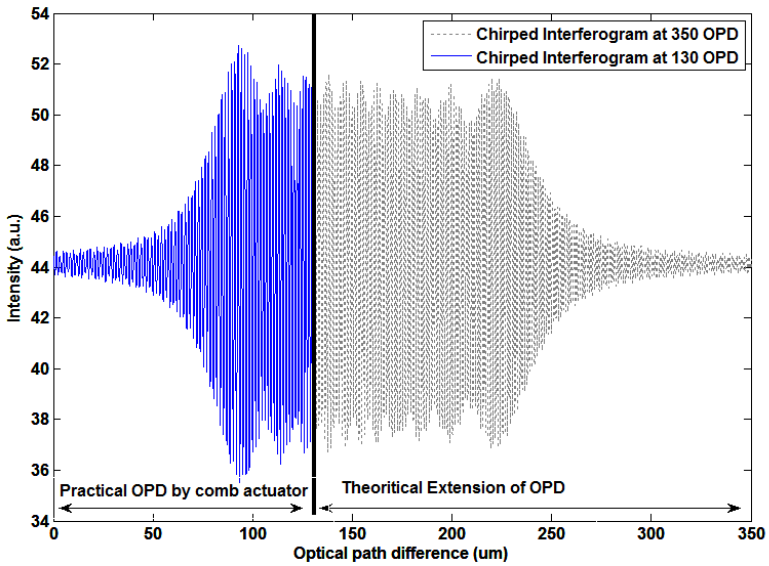


Figure 4. Numerically simulated interferogram of deeply-etched MZI showing chirped and shifted interferogram.

## 5. Practical measurements of white light interferogram

The setup used in the characterization is shown in figure 5. It consist of a white input source with tungsten lamp (1.2 um – 1.7 um), multimode fibers with 62.5 um core inserted into the micromachined grooves aligned with the interferometer splitter, an Agilent optical InGaAs detector connected to a GPIB interface with personal computer and 5 degree-of-freedom micro positioners for fiber alignment.

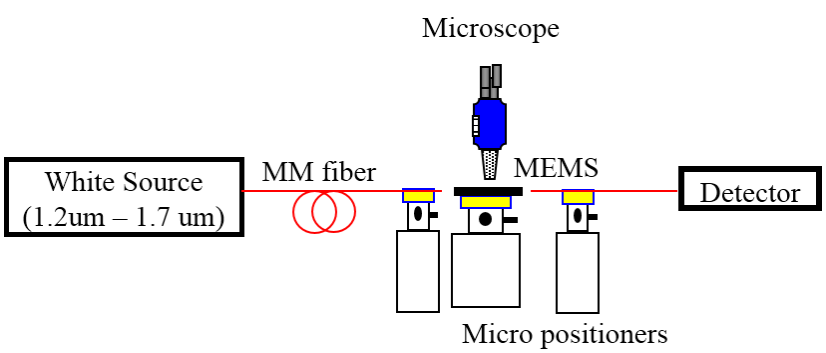


Figure 5. Characterization Setup

Measured interferogram of the MSI is shown in figure 6. The interferogram appears with side

duplicated interferograms caused by parasitic FP effect as expected. Their location depends on real thickness of the thin Si splitter after fabrication. The ZOPD position is shifted by 26 um due to fiber misalignment and etching error as discussed before. The difference between the measured side interferograms and numerical simulation is attributed to the beam divergence in the micro optical structure with increasing OPD which has not been accounted for in the numerical model. The glitches may be caused by mirror vibration at the start of actuation or contamination particles in the structure after words as the interferometer is not caped and tested in a non clean room. For the MZ interferometer the measured interferogram after numerically removing the effect of decay in the measured power with increasing OPD is shown in figure 7.

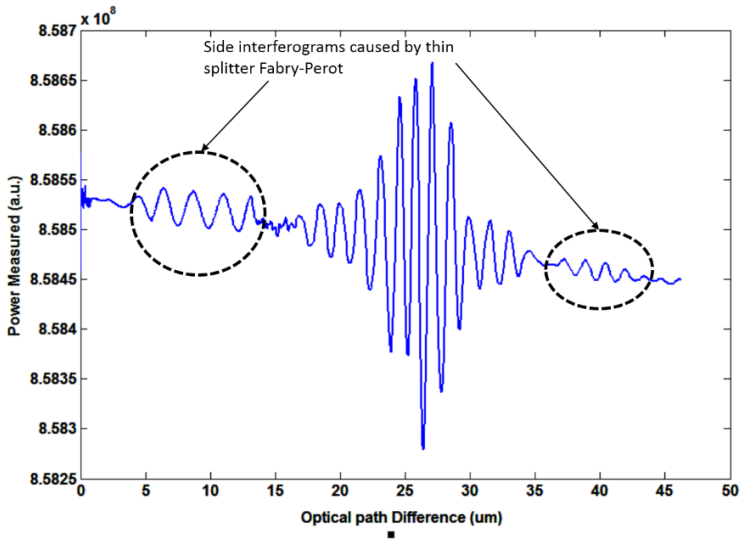


Figure 6. Measured interferogram of MEMS MSI with thin Silicon splitter showing the effect of parasitic FP.

The white light input source power is about -60 dBm and the MZ interferometer loss is around 10 dB [6] causing the amplitude of the output interferogram to be very low and measured power to be comparable to the noise level. The final step is to calculate the absolute of complex Fast Fourier Transform (FFT) to compensate for dispersion effect, and remove undesired noise as shown in figure 8.

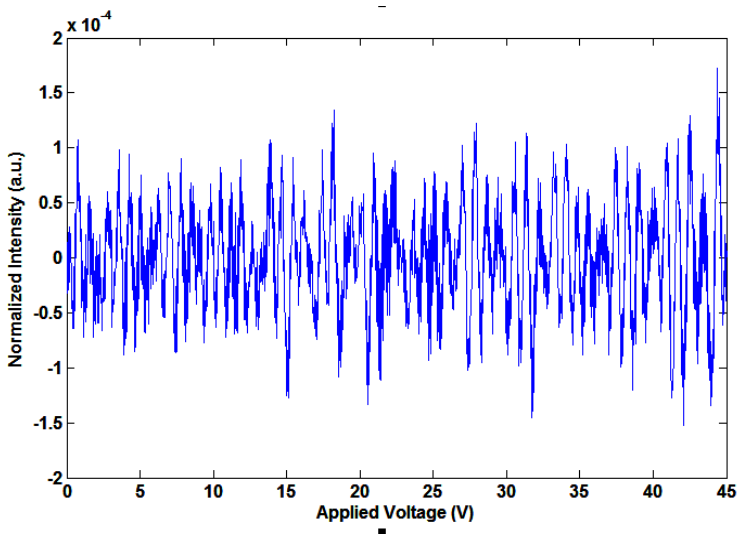


Figure 7. Measured interferogram of MEMS MZI with Si/air splitters showing dispersion effect.

The MZI output Power Spectral Density (PSD) agrees with the MSI PSD for long wavelength while in the short wavelengths some defects appear for the MZI as shown in figure 8. We attribute this to the limited OPD (130 um) of the MZI causing the chirped interferogram to be only partially collected.

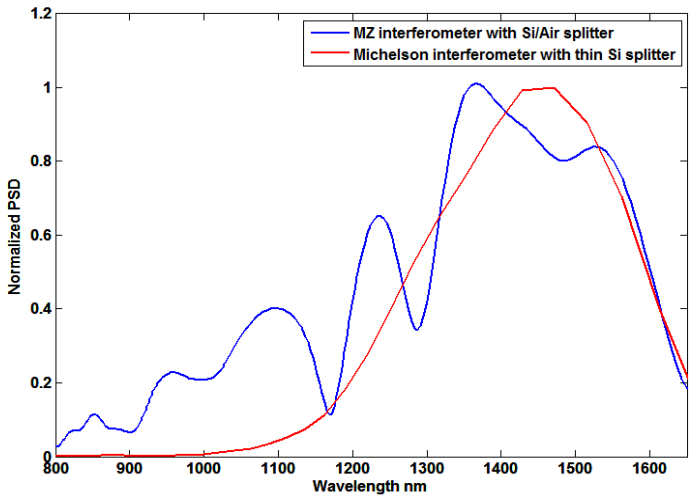


Figure 8. Interferogram FFT for thin Silicon and Si/Air beam splitter interferometers.

## 6. Conclusion

We have presented numerical and practical study on white light interferometry of SOI deeply-etched fully integrated MEMS interferometers. The thin Silicon splitter causes a parasitic Fabry-Perot effect that results in duplicated side interferoargam which limits the useful OPD and hence resolution of an FT-IR spectrometer. The Si/Air splitter suffers from dispersion effect that can be compensated using long travel

range actuators making it the better choice for an FT-IR spectrometer in terms of optical resolution, robustness and reliability.

**7. References**

[1] A. Fathy, Y. M. Sabry, M. Amr, M. Gnambodoe-Capo-chichi, M. Anwar, A. O. Ghoname, A. Amr, A. Saeed, M. Gad, M. Al Haron, M. Erfan, Y. Leprince-Wang, B. Saadany, D.Khalil, and T. Bourouina "MEMS FTIR optical spectrometer enables detection of volatile organic compounds (VOCs) in part-per-billion (ppb) range for air quality monitoring", Proc. SPIE 10931, MOEMS and Miniaturized Systems XVIII, 1093109 (4 March 2019); doi: 10.1117/12.2508239; https://doi.org/10.1117/12.2508239

[2] F. Marty, L. Rousseau, B. Saadany, B. Mercier, O. Français, Y. Mita and T. Bourouina, "Advanced etching of silicon based on deep reactive ion etching for silicon high aspect ratio microstructures and three-dimensional micro-and nanostructures." Microelectronics journal 36.7 (2005): 673-677.

[3] B. Saadany, D. Khalil and T. Bourouina,"Highly efficient micromachined bragg mirrors using advanced DRIE process." MEMS, NANO and Smart Systems, The 2006 International Conference on. IEEE, 2006.

[4] Amr O. Ghoname, Yasser M. Sabry, Momen Anwar, Ahmed Saeed, Bassam Saadany, and Diaa Khalil "Ultra wide band MIR MEMS FTIR spectrometer", Proc. SPIE 10931, MOEMS and Miniaturized Systems XVIII, 109310Z (4 March 2019); doi: 10.1117/12.2509378; https://doi.org/10.1117/12.2509378

[5] Ahmad Mahfouz, Haitham Omran, Yasser M. Sabry, Diaa Khalil, Frédéric Marty, and Tarik Bourouina "Deeply etched silicon optical cavity with curved slotted micromirrors (Conference Presentation)", Proc. SPIE 10931, MOEMS and Miniaturized Systems XVIII, 109310N (4 March 2019); doi: 10.1117/12.2508208; https://doi.org/10.1117/12.2508208

[6] W. Noell, W. Sun, N. de Rooij, H. P. Herzig, O. Manzardo, and R. Dandliker, "Optical mems based on silicon-on-insulator (SOI) for monolithic microoptics." Lasers and Electro-Optics Society (LEOS). The 15th Annual Meeting of the IEEE. Vol. 2. Institute of Electrical and Electronics Engineers (IEEE), 2002.

[7] W. Noell, P.-A. Clerc, L. Dellmann, B. Guldimann, H.-P. Herzig, O. Manzardo, C. R. Marxer, K. J. Weible, R. Dandliker, and N. de Rooij "Applications of SOI-based optical MEMS." IEEE Journal of selected topics in quantum electronics 8.1 (2002): 148-154.

[8] B. Saadany, H. Omran, M. Medhat, F. Marty, D. Khalil, and T.Bourouina,"MEMS tunable Michelson interferometer with robust beam splitting architecture." Optical MEMS and Nanophotonics, 2009 IEEE/LEOS International Conference on. IEEE, 2009.

[9] B. Mortada, M. Erfan, M. Medhat, Y. M. Sabry, B. Saadany and D. Khalil, "Wideband optical MEMS interferometer enabled by multimode interference waveguides." Journal of Lightwave Technology 34.9 (2016): 2145-2151.

[10] Yu, Kyoungsik, Daesung Lee, Uma Krishnamoorthy, Namkyoo Park, and Olav Solgaard, "Micromachined Fourier transform spectrometer on silicon optical bench platform." Sensors and Actuators A: Physical 130 (2006): 523-530.

[11] H. Omran, M. Medhat, B. Mortada, B. Saadany, and D. Khalil, "Fully integrated Mach-Zhender MEMS interferometer with two complementary outputs." IEEE Journal of Quantum Electronics 48.2 (2012): 244-251.

[12] D. Khalil, H. Omran, M. Medhat, B. Saadany, "Miniaturized tunable integrated Mach-Zehnder MEMS interferometer for spectrometer applications." MOEMS and Miniaturized Systems IX. Vol. 7594. International Society for Optics and Photonics, 2010.

[13] H. Omran, M. Medhat, B. Saadany, D. Khalil, "Mach-Zehnder MEMS interferometer with two Si/Air beam splitters." Design and Test Workshop (IDT), 2009 4th International. IEEE, 2009.

[14] Yasser M. Sabry, D. Khalil and T. Bourouina, "Monolithic silicon-micromachined free-space optical interferometers onchip." Laser & Photonics Reviews 9.1 (2015): 1-24.

[15] M. Erfan, Yasser M Sabry, M. Sakr, B. Mortada, M. Medhat and D. Khalil, "On-chip micro–electro–mechanical system fourier transform infrared (MEMS FT-IR) spectrometer-based gas sensing." Applied spectroscopy 70.5 (2016): 897-904.

[16] H. Omran, Y. M. Sabry, M. Sadek, K. Hassan and D. Khalil, "Wideband subwavelength deeply etched multilayer silicon mirrors for tunable optical filters and SS-OCT applications." IEEE Journal of Selected Topics in Quantum Electronics 21.4 (2015): 157-164.

[17] H. Omran, Y. M. Sabry, M. Sadek, K. Hassan, M. Y. Shalaby and D. Khalil, "Deeply-etched optical MEMS tunable filter for swept laser source applications." IEEE Photonics Technology Letters 26.1 (2014): 37-39.

[18] J. Masson, R. St-Gelais, A. Poulin, and Y. A. Peter, "Tunable fiber laser using a MEMS-based in plane Fabry-Pérot filter." IEEE Journal of Quantum Electronics 46.9 (2010): 1313-1319.

[19] R. St-Gelais, A. Poulin and Y. A. Peter, "Advances in modeling, design, and fabrication of deep-

etched multilayer resonators." Journal of Lightwave technology 30.12 (2012): 1900-1908.

[20] K. Iizuka, Elements of Photonics in Free Space and Special Media (John Wiley & Sons, New York, 2002) p. 166.

[21] P. R. Griffiths and De Haseth, Fourier Transform Infrared Spectrometry (John Wiley & Sons, New York, 2007) Vol. 171.

[22] J. Frey Bradley, B. Leviton Douglas, J. Madison Timothy, "Temperature-dependent absolute refractive index measurements of synthetic fused silica." Optomechanical Technologies for Astronomy. Vol. 6273. International Society for Optics and Photonics, 2006.

[23] L. M. Smith and Chris C. Dobson, "Absolute displacement measurements using modulation of the spectrum of white light in a Michelson interferometer." Applied Optics 28.16 (1989): 3339-3342.

[24] KG. Larkin, "Efficient nonlinear algorithm for envelope detection in white light interferometry." JOSA A 13.4 (1996): 832-843.

[25] U. Schnell, R. Dändliker, and S. Gray, "Dispersive white-light interferometry for absolute distance measurement with dielectric multilayer systems on the target." Optics Letters 21.7 (1996): 528-530.

[26] Mark Johnson, "White light interferometry." Fibre Optics' 90. Vol. 1314. International Society for Optics and Photonics, 1990.

[27] Scott Diddams and Jean-Claude Diels, "Dispersion measurements with white-light interferometry." JOSA B 13.6 (1996): 1120-1129.

[28] A. P. Kovács, K. Osvay, Zs. Bor, and R. Szipöcs, "Group-delay measurement on laser mirrors by spectrally resolved white-light interferometry." Optics letters 20.7 (1995): 788-790.

[29] Kentaro Totsu, Yoichi Haga and Masayoshi Esashi, "Ultra-miniature fiber-optic pressure sensor using white light interferometry." Journal of Micromechanics and Microengineering 15.1 (2004): 71.

[30] H. Omran, B. Mortada and D. Khalil, "Numerical estimation of dispersion effect in deeply-etched fully integrated MEMS Mach-Zhender interferometer," 2017 22nd Microoptics Conference (MOC), Tokyo, 2017, pp. 278-279.

# Investigation of the Dynamic Behavior of Coupled Shear Wall Systems

**Hamdy El-Gohary**

College of Engineering, Umm Al-Qura University, Makkah, Saudi Arabia

gohary_h@yahoo.com

**Ayed Eid Alluqmani****

Faculty of Engineering, Islamic University of Madinah, Madinah, Saudi Arabia

dr.ayed@iu.edu.sa**;** eng.ayed@hotmail.com

**** Corresponding Author**

**Abstract:** Coupled shear walls are vertical shear walls or elevator cores with openings connected together by beams or slabs. In the present work, the behavior of the reinforced concrete coupled elevator cores of multistory building has been investigated under the seismic loads. The system consists of two U-shaped in the plan monolithic walls, connected at slab levels by beams. Seismic loads were determined according to the International Building Code, IBC-2015. The elastic analysis of the models, was carried out using finite element method (FEM) and the results were compared with the results obtained using the closed form solution (analytical method). Results show that the rigidity of coupling beams has significant effect on the dynamic behavior of the coupled wall system. The presence of connecting beams and the increase of their rigidity resulted in valuable decrease in the period of vibration and deformations of the coupled wall system in all models. Shear stresses in the cross sections of the connecting beams were calculated in accordance to the American ACI Code and Eurocode. It was observed that in some beams it is possible to use only the minimum required reinforcements, whereas in the majority of the cases, designed shear reinforcement must be provided for the connecting beams.

**Keywords:** Coupled Shear Walls; Dynamic Behavior; Lateral Loads; Elevator Cores, Finite Element Method; Analytical Method; Shear Stresses.

# التحري في السلوك الديناميكي لأنظمة جدران القص المزدوجة

**الملخص**: جدران القص المزدوجة هي جدران قص عمودية أو نوى المصاعد مع فتحات متصلة فيما بينها بواسطة أعمدة أو بلاطات. في العمل الحالي، تمت دراسة سلوك نوى المصاعد المزدوجة من الخرسانة المسلحة في عمائر من عدة طوابق تحت الأحمال الزلزالية. يتكون النظام من جدارين متجانسين بشكل (و) في المخطط متصلين على مستوى البلاطات بواسطة أعمدة. تم تحديد الأحمال الزلزالية وفقا لمعايير البناء العالمي (إ. ب. س) 2015. تم إجراء التحليل المرن للنماذج باستخدام طريقة العناصر النهائية (ف. إ. م) وتمت مقارنة النتائج بالنتائج المتحصل عليها بمساعدة الحل ذو الشكل المغلق (الطريقة التحليلية). توضح النتائج أن صلابة أعمدة الربط المزدوجة لها تأثير كبير على السلوك الديناميكي لنظام الجدران المزدوجة. أسفر وجود أعمدة الربط وزيادة صلابتها عن انخفاض معتبر في مدة اهتزاز وتشوهات نظام الجدران المزدوجة في جميع النماذج. تم حساب ضغوط القص في المقاطع العرضية لأعمدة الربط وفقا للمعيار الأمريكي والمعيار الأوروبي. لوحظ أنه في بعض الأعمدة من غير الممكن الإكتفاء بإستخدام الحد الأدنى من التسليح المطلوب، في حين أنه في معظم الحالات، فإن التسليحات المقصية يجب توفيرها لأعمدة الربط.

## 1. Introduction:

The special feature of the systems in question is the substantial difference between the flexural rigidity of each separate wall and entire system as a whole. In this case, this difference significantly depends on the degree of fixing the beams, which connects the walls. For the case of hinged connection of beams to the mating walls, the flexural rigidity of entire system is equal to the sum of the flexural rigidities of all walls, which forms the system. In the hinged connected beams, the shear does not appear in this case, but they only redistribute the general horizontal loads on the system between its vertical elements proportional to their rigidity.

In the case of rigid connection for beams with the walls, beams contribute to the system by resisting shear forces, which is generated between the coupled walls, and the entire system is deformed as a frame.

Investigation of dynamic behavior of the coupled shear wall system is the focus of interest of many researchers at the present time [1, 2, and 3]

In the present paper the effect of the connecting beam rigidity on the dynamic behavior of the coupled shear wall system under seismic loads was investigated.

## 2. Structural Action of Coupled Shear Wall System

### 2.1 Coupled Shear Wall:

The ratio of the sum of the flexural rigidities of the separate walls of composite system to the horizontal rigidity, which substitutes the composite system of frame, is called the degree of the coupling of walls or the degree of fixing the beams to walls.

The degree of the coupling of walls can be defined just as the ratio of the moment of internal forces in the walls to the moment of the external action:

$$C = \frac{P \cdot L_w}{M} \qquad (1)$$

Where,

$M = \sum F_i \cdot h_i$

$F_i$ = Value of the concentrated load on system at the level "i",

$L_w$ = Distance between centers of gravity of the sections of walls,

$h_i$ = Distance from the base to the level "i", and

P = Axial force in the walls.

The value of pair of internal axial forces in the walls depends on the shear, resisted by the connecting beams. Therefore, the beams which connect the walls substantially influence the systemic reaction of the system, and this influence increases with the increase of the stiffness of the connecting beams. At the same time, in the case of flexible beam connection, the behavior of the system approaches the behavior of separate free walls. Short-span beam connection is more effective, since this increases the shear capacity of the beams. It is considered that in the flexible concrete plates, the steep gradient of the diagram of the bending moments takes place.

In some works, the behavior of systems, which consist of the coupled shear walls, was investigated analytically and numerically [4, 5, and 6]. On the basis of these studies, the conclusion is that the displacements of the connecting beams obtained analytically are frequently more than those ones

measured experimentally for the same beams. It was also noted, that in practice, rigidity of connecting beams frequently exceeds required values compared to the design [7, 8, and 9]. Studies show clear contrary [10, and 11].

The high degree of coupling in the majority of the practical cases causes bending at the supporting zones of the beams. It was found that one characteristic of the degree of coupling does not always satisfy the requirements of the parameter for predicting the spectrum of reactions or determination of the expected behavior of coupled walls [8]. The additional parameters of the rotation at the top of walls, flexibility or relative rigidity of walls and beams, are required for the accurate estimation of the reaction of the coupled shear walls.

*The investigations of the enumerated parameters include:*

1. Evaluating of the role of the critical geometric parameters in the determining characteristics of the coupled shear walls, with the focusing of attention to the requirements of the arrangement of connecting beams;

2. Determining the collection of the characteristic prototypes of constructions for further nonlinear analysis;

3. Determining the additional parameters, which are effectively shown in the coupled structural systems.

The purpose of this study consisted of the development of the parameters, which allows to accurately estimation the initial data, the global behavior of the composite systems, the local behavior of coupling beams and the relation between the global and local behavior.

## 3. Parametric Study:

Aim is to investigate the effect of the enumerated parameters, a core in the form of two monolithic reinforced concrete walls of u-shape, coupled by beams at the opening portion in the lateral wings of walls. Both walls have identical shape and dimensions in the plan and thickness of 400 mm throughout the entire height of the building. The height of floors is considered constant and equals 3.0 m. The coupling beams, in all models, have a span of 1.0 m, a width of 0.40 m and thickness of 0.5, 0.6, 0.7, 0.8, 0.9 and 1.0 m. A row of models of these coupled shear wall systems with number of stories of 10, 15, 20 and 25 is examined. It is considered that because of the symmetry

of the models, torsional moment will not take place. Figure 1 shows coupled shear walls model. Shear walls are considered fixed at base and modeled using shell elements with mesh 1.0 x 1.0 m. The coupling beams are modeled as frame elements.

The weight of the structures at each floor is taken as 15000 KN. The compressive strength of concrete was considered equal to 30 MPa and the concrete modulus of elasticity ($E_c$) was assumed to be 26000 MPa.

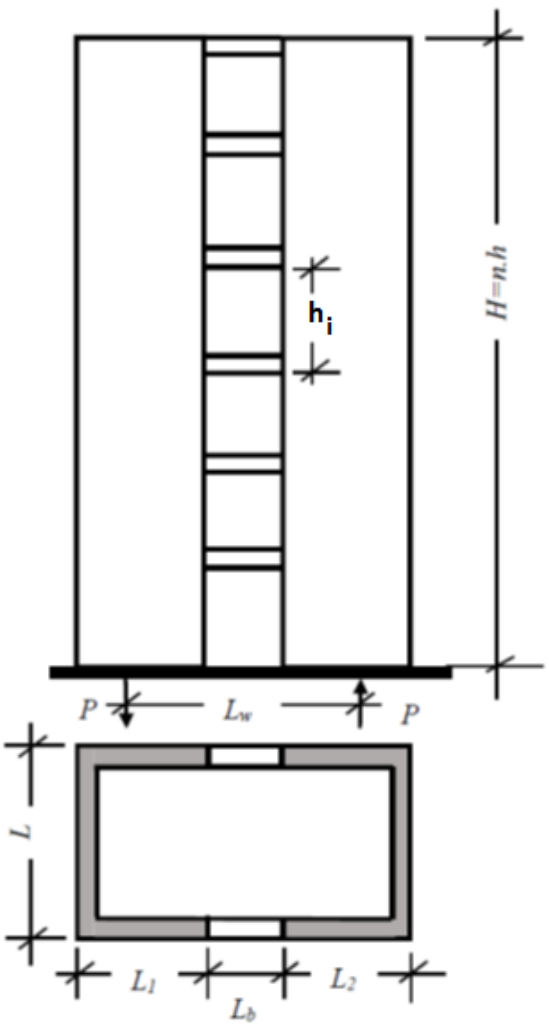


Figure 1. Coupled Shear Walls Model

## 4. Analysis of Models:

The elastic analysis of the models was carried out by FEM and is compared with the calculation by closed form solution (analytical method) [5]. The analytical calculations of continuous systems give the final form of formula for calculating internal forces and displacements. Horizontal seismic load acting on the models is considered in accordance with the IBC [8].

The used values of the period of vibration were determined by the FEM using SAP2000 [12]. All internal forces, reactions and lateral displacements of the models have been determined from SAP2000 models as well.

For the analysis of the behavior of systems, the parameters α, k and H, were used [9, 10 and 11]:

$$\alpha = \sqrt{\frac{12 I_c L_w^2}{L_b^3 \cdot h \cdot I}} \qquad (2)$$

$$K = \sqrt{1 + \frac{(A_1 + A_2) \cdot I}{A_1 \cdot A_2 \cdot L_w^2}} \qquad (3)$$

$$I_c = \frac{I_b}{1 + \frac{12 E I_b}{L_b^2 G A_b} \times 1.2} \qquad (4)$$

Where α and k are analytical parameters which are constant;

$I_b$ = Moment of inertia of the connecting beams;

$I_c$ = Moment of inertia of the walls sections, equal to $I_1$+$I_2$;

$A_1$ and $A_2$ = Cross-sectional areas of the walls.

The parameter 'α' depends on the relation of the rigidity of connecting beams and walls. Low value of α indicates a relative flexibility of the connecting beams of system. In this case, the general behavior of the system of walls will be characterized in essence by the bend of each wall. Higher value of α leads to larger interaction of the walls with each other.

The parameter 'K' characterizes the relation of the bending of the walls of system. This parameter has the lower limit, equal to 1, and it varies in this study from approximately up to 1.2. This parameter usually has a value, which is equal to 1.1, in real structures.

The parameter (degree of coupling) D is defined as:

$$D = K \cdot \alpha \cdot H = \sqrt{\left(1 + \frac{(A_1 + A_2) \cdot I}{A_1 \cdot A_2 \cdot L_w^2}\right) \cdot \frac{12 \cdot I_c \cdot L_w^2}{L_b^3 \cdot h \cdot I} \cdot H^2} \qquad (5)$$

Where, H is the total height of the structure.

The parameter 'D' can be interpreted as a criterion for the stiffness of connecting beams, which is substantially depending on their lengths. If the connecting beams have zero rigidity (D = 0), then external moment bends only walls. In this case, the construction behaves as a pair of walls, connected by beams with hinged ends. If the connecting beams are absolutely rigid (D = ∞), then the behavior of the system approaches a bend of the simple cantilever, fixed at base. Figure 2 shows the increase of degree of coupling with the increase of connecting beam height.

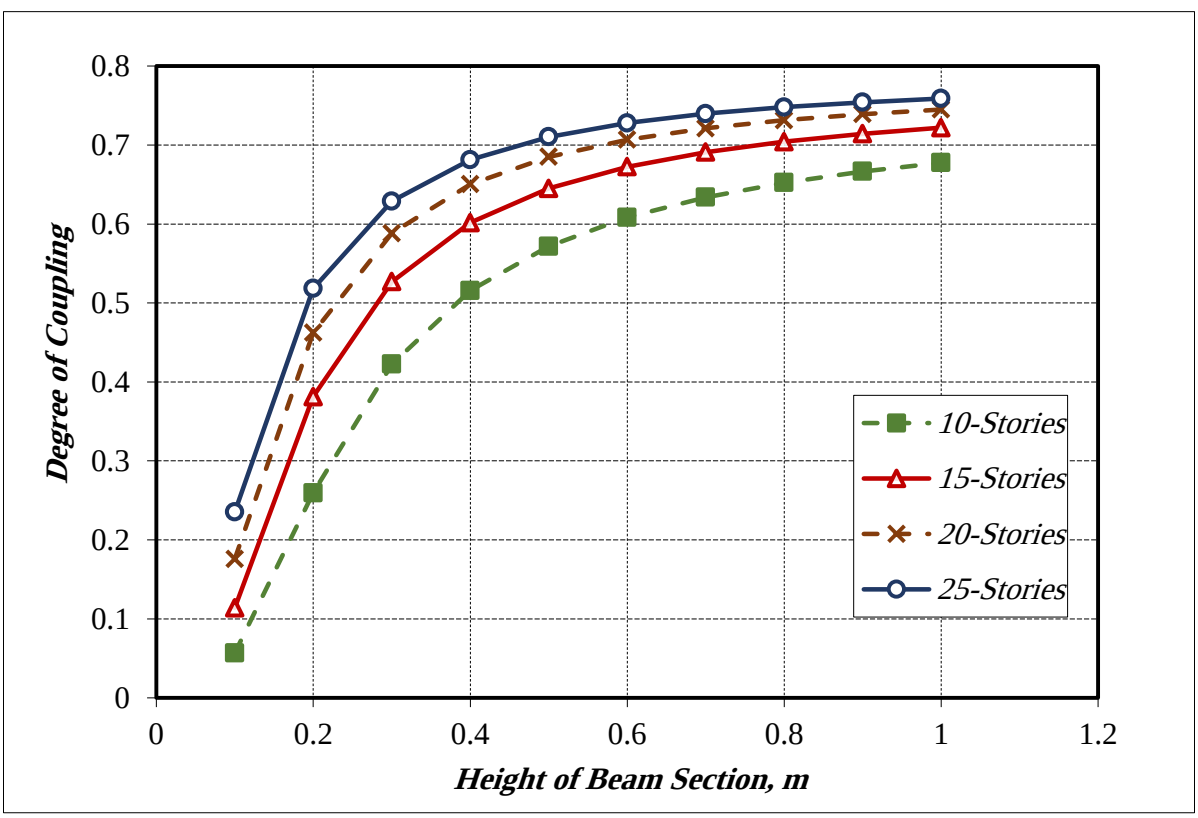


Figure 2. Relation between Degree of Coupling and Height of Connecting Beam

It is obtained that, with an increase in the thickness of the connecting beams (a measure of rigidity), the degree of the coupling "C" increases up to 0.45 in the case of 5-story model and to 0.73 for the 25-story model with the section thickness of 0.6 m as shown later in Figure 5. The increase in connecting beam thickness of more than 0.6 m has small influence on the degree of the coupling "C".

It is acceptable that for D < 1, the structure is considered to have negligible influence on the connecting beams and it will behave as a system of coupled shear walls with hinged connecting beams (C < 20%). With an increase in D up to 8, the connecting beams are considered rigid, and the system responds to domination of one of the walls in accordance with the coefficient 'k'.

The advantage of the coupled shear walls is mainly in the fact that in such systems, a decrease of the period of vibration takes place and it is possible to optimize the horizontal displacements of the system.

## 5. Discussion of Results:

Figure 3 shows the effect of connecting beam rigidity on the fundamental period of vibration of the considered models. It can be observed that, the period of vibration decreases in comparison with case of coupled shear walls connected by hinged beams. This decrease approximately reaches 50% in the case of 10-story model, while it is 60% for the case of 25-story model. The effect of connecting beams rigidity on the fundamental period of vibration of the system increases with the increase of system height.

The relation between top displacement of the coupled shear wall models and the connecting beam rigidity (as indicated by beam section height) is shown in Figure 4. It can be noticed that the top displacement drops more than 50% for the cases of models height 10-stories and more, once the beam thickness is 0.2 m. In most cases the lateral displacement dropped by 70 % from the case of hinged connection. The presence of connecting beams has significant effect on the system lateral rigidity.

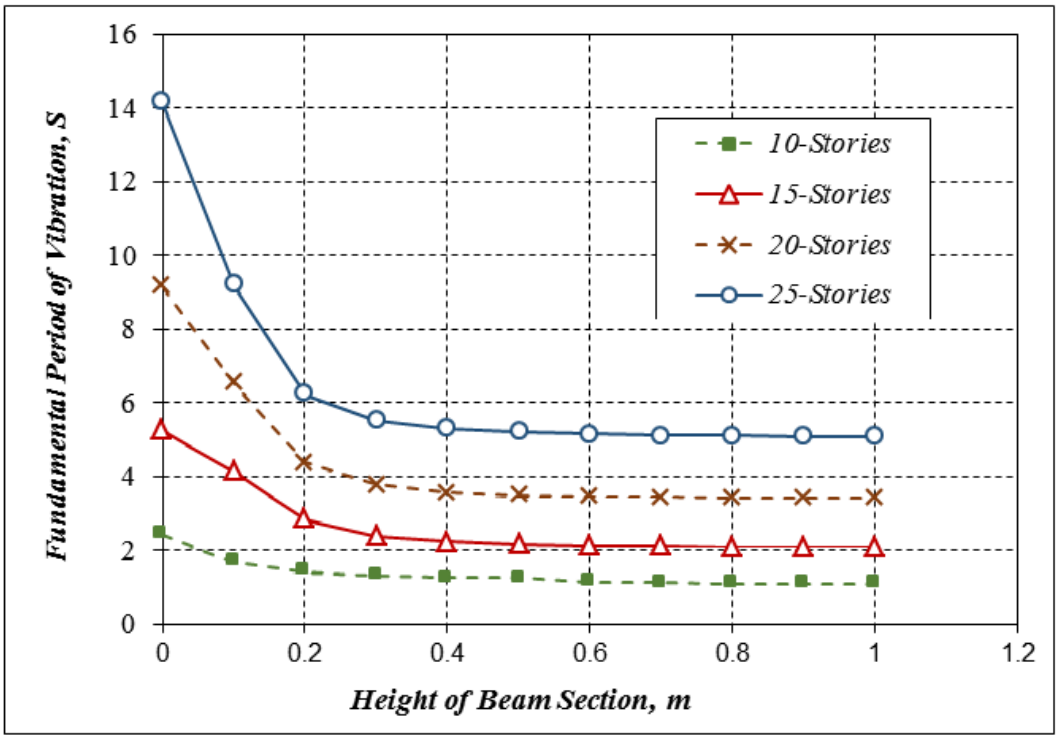


Figure 3. Fundamental Period-Beam Height Relationship

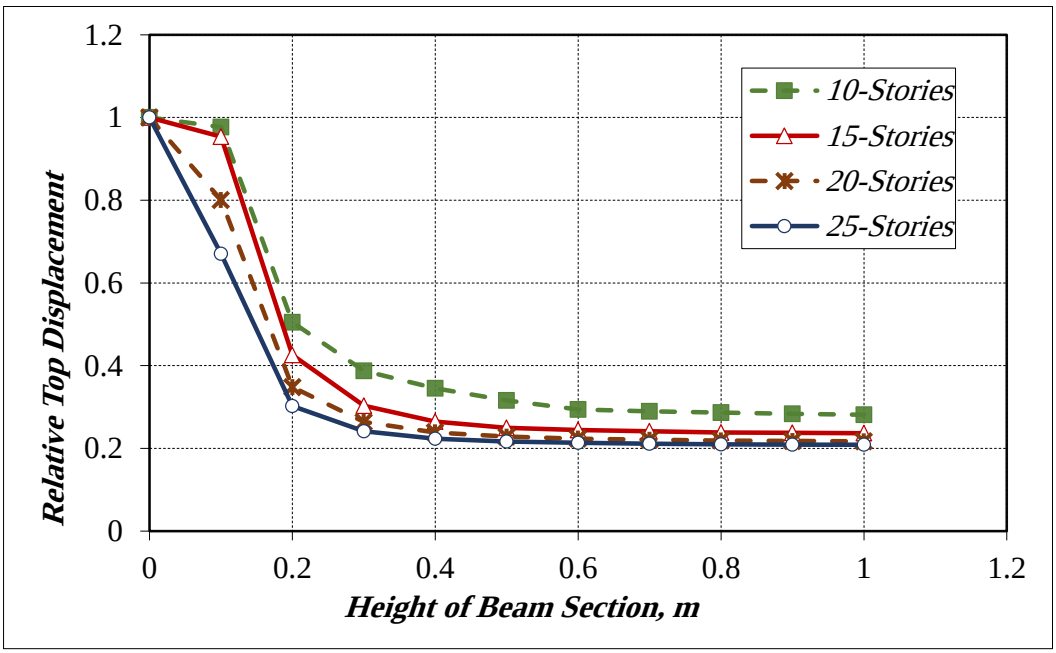


Figure 4. Relative Top Displacement-Connecting Beam Rigidity Relationship

Shear stresses in the cross sections of the connecting beams were calculated and compared with the limiting values of the following Codes: Egyptian Concrete Code (ECC-203), Eurocode for concrete structures (EC-2), American Concrete Institute (ACI-318-14), and Saudi Building Code for reinforced concrete structures (SBC-304) [4, 13, 14, 15 & 16]. The shear design provisions in ACI and SBC-304 are the same, which is the same case for ECC-203 and EC-2. It is clear that in some beams it is possible to use only the minimum required reinforcements, whereas in the majority of the cases designed shear reinforcement must be provided for the connecting beams (Figure 5).

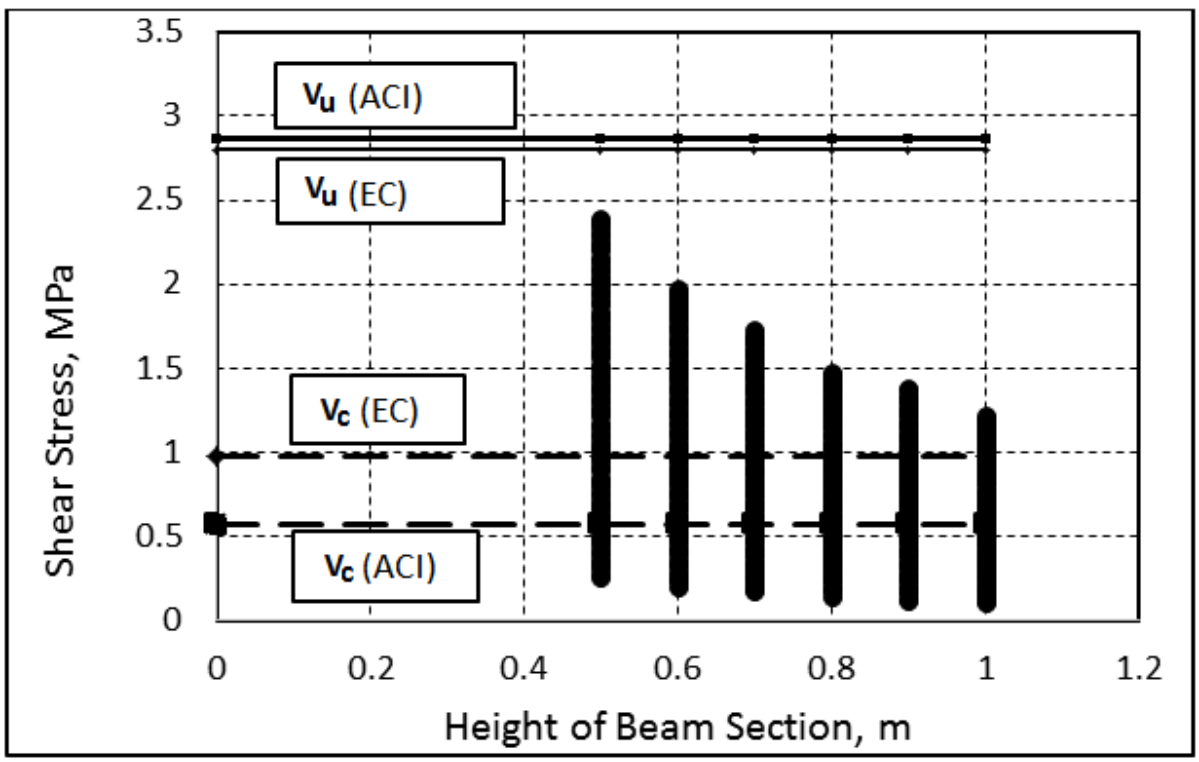


Figure 5. Shear Stresses in Connecting Beams and Codes' Limits

Figure 6 shows the distribution of shear forces in the connecting beams along the height of all models for the case of beams section thickness 0.7 m. Maximum shear force generated in connecting beams at 0.2 to 0.4 of the model height from base. Connecting beams at levels from 0.2 to 0.6 of the total height, carry more than 80% of total shear forces generated in all connecting

beams. With the increase of the height of the model, shear forces in the beams of the lower stories increase and they decrease for the upper stories. This is due to the decrease in shear deformations with the increase of the building height.

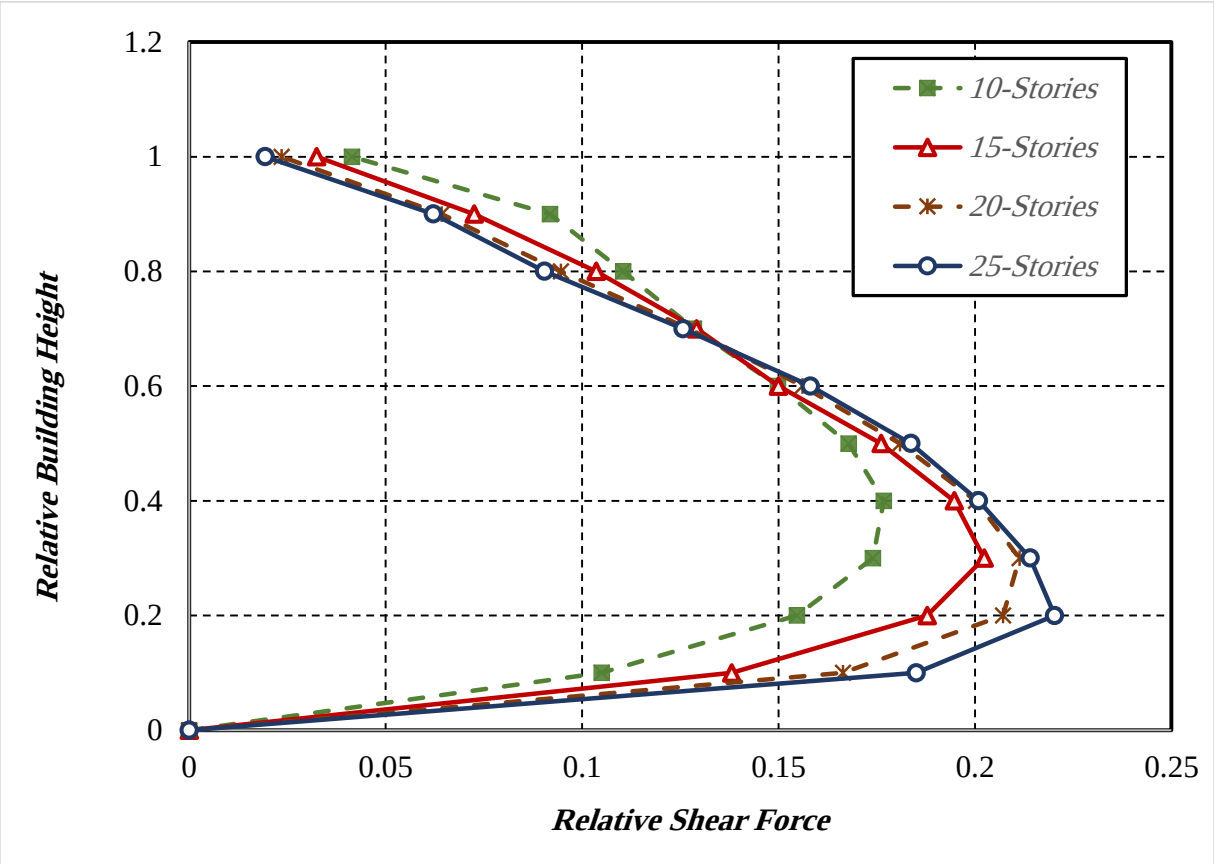


Figure 6: Distribution of Shear Forces in Connecting Beams

## 6. Conclusion

Dynamic behavior of coupled shear wall system has been investigated under seismic loads. The analysis shows that the connecting beam rigidity has great influence on the coupled wall system behavior. The dynamic properties of the system (period of vibration and top displacements) decrease significantly with the increase of the connecting beam rigidity. The shear stresses in connecting beams in all investigated models are within the current Codes' limits. The maximum

shear forces generated in connecting beams are located at 0.2 to 0.6 of the coupled wall system height. The design of connecting beams at these levels need more attention.

**Acknowledgement:** Authors acknowledge the support provided by the Faculties of Engineering at Umm Al-Qura University and Islamic University in Madinah, KSA.

## 7. References

[1] P. S. Lande, V. S. Ankalkote, Evaluation of coupled shear wall in high-rise building, International Research Journal of Engineering and Technology (IRJET), Volume: 05 Issue: 05 | May-(2018).

[2] A. Patil, V. D. Girge, Review on coupled shear wall in multi-story building, International Journal of Research Publications in Engineering and Technology (IJRPET), Volume 3, Issue 4, Apr.-(2017).

[3] S. S. Rangolli, V. Hosur, Analysis of multi-storey building by using coupled shear walls, International Research Journal of Engineering and Technology (IRJET), Volume: 04 Issue: 05 | May –(2017).

[4] Egyptian Code-203 -2017, Design and construction of concrete structures, Housing and Building Research Centre, Cairo, Egypt, (2017).

[5] C. Hung, S. El-Tawil, Seismic behavior of a coupled-wall system with HPFRCC coupling beams. Structures Congress, (2010) 1864-1873.

[6] J. F. Matthew, J. S. Timothy, K. Beyer, Capacity design of coupled RC walls, Journal of Earthquake Engineering, (2014) DOI: 10.1080/13632469.2014.904255.

[7] D. Bhunia, V. Prakash, A. D. Pandey, A conceptual design approach of coupled shear walls, Hindawi Publishing Corporation, ISRN Civil Engineering, Volume 2013, Article ID, (2013) 161502, 28 pages.

[8] International Building Code, IBC (2015).

[9] D. Lehman, J. Turgeon, A. Birely, C. Hart, K. Marley, D. Kuchma, L. Lowes, Seismic behavior of a modern concrete coupled wall. J. Struct. Eng., (2013). 10.1061/ (ASCE) ST.1943-541X.0000853, 1371-1381.

[10] P. V. Patel, S. P. Purohit and K. S. Dash, Static and dynamic behavior of coupled shear wall, International Cconference on Current Trends in Technology, 'NUiCONE – (2010).

[11] R. Rahgozar, M. Malekinejad, M. Jahanshahi, Free vibration analysis of coupled shear walls with axial force effects. The IES Journal Part A: Civil & Structural Engineering, 10.1080/19373260.2011.615493, (2011) 224-231.

[12] SAP2000 Integrated Finite Element Analysis of Building systems, user's manual, Computers and Structures Inc., Berkeley, California, (2000).

[13] ENV 1992-1-1: Eurocode 2 (EC2)-1991, Design of concrete structures, part 1: General Rules and Rules for Buildings, European Prestandard, December, (1991).

[14] ACI Committee 318-2014, Building code requirements for structural concrete (ACI 318-14) and Commentary (ACI 318R-14)," American Concrete Institute, ACI, Farmington Hills, Mich, (2014).

[15] Saudi Building Code SBC-301-2007 – Structural- loading and forces, Saudi Building Code National Committee, (2007).

[16] Saudi Building Code, SBC-304-2018 – Structural- concrete structures requirements, Saudi Building Code National Committee, (2018).

# Studies on Polythiophene Films Prepared by Electropolymerization

**Faiz Mohammad**
Department of Applied Chemistry
Zakir Husain College of Engineering and Technology
Aligarh Muslim University ALIGARH 202002 (India)
faizmohammad54@rediffmail.com

**Abstract:** The electrochemical polymerization of thiophene to $BF_4^-$ doped polythiophene using electrochemical cell fitted with a platinum working electrode and ammonium fluoroborate in propylene carbonate electrolyte showed the efficiency of electropolymerization reaching to 100%. The aqueous ammonia is very commonly used as undoping agent for conducting polymers. The work on the undoping of $BF_4^-$ doped polythiophene by dry ammonia was carried out in order to corroborate the mechanism of undoping vis a vis polyacetylene. The work on the mechanism of the dry ammonia undoping of $BF_4^-$ doped polythiophene ($PTh^{n+}$:$nBF_4^-$) by dry ammonia is novel in the sense the mechanism is strongly supported by our previous works and the scanning electron micrographs showing the formation of $NH_4F$ crystals. The mechanism of irreversible undoping of $BF_4^-$ doped polythiophene by moisture is also proposed. The scanning electron microscopy showed the surface of the $BF_4^-$ doped polythiophene films produced to be extremely smooth while the beautiful microdendrites composed of globules were formed on the edges of the working electrode. The microdendritic growths of such morphology have also been observed in polypyrrole produced by electropolymerization.

**Keywords:** Electropolymerization efficiency, scanning electron microscopy, polythiophene, mechanism of undoping

# دراسات على أفلام البولي إيثيلين التي يتم إعدادها عن طريق التحليل الكهربائي

**الملخص**: أظهرت البلمرة الكهروكيميائية للثيوفين إلى بوليثيوفان المخدر ب (ب ف 4-) باستخدام خلية كهروكيميائية مزودة بقطب كهربائي تعمل بالبلاتينيوم وفليوروبورات الأمونيوم في كربونات البروبيلان المنحل بالكهرباء قد أظهرت فعالية البلمرة التي تصل إلى 100%. الأمونياك المائي شائع الاستخدام كعامل غير متجانس لإجراء البوليميرات. تم العمل على إزالة بوليثيوفان مخدرة ب (ب ف 4) بواسطة الأمونيا الجافة من أجل إثبات آلية إلغاء الانزلاق تجاه البولياسيتيلان. يعد العمل على آلية إزالة الأمونيا الجافة في البوليفين ثنائي الميثان المخدر ب (ب ف 4) (ب ت ح ن+: ن ب ف 4-) بواسطة الأمونيا الجافة جديدة في معنى هذه الآلية المدعومة بقوة من طرف أعمالنا السابقة والصور المجهرية الإلكترونية الممسوحة ضوئيا التي تظهر تشكل الكريستال (ن ح 4 ف). تقترح أيضا آلية إلغاء إزالة البوليفين ثنائي ميثيل ب (ب ف 4) بواسطة الرطوبة. المجهر الإلكتروني المسحي أظهر بأن سطح أفلام البوليثيوفان المخدرة ب (ب ف 4) تم إنتاجه ليكون سلسا للغاية، في حين أن روعة الميكرودوندريت المكونة من كريات كانت مشكلة على حواف القطب الكهربائي العامل. كما لوحظت الزيادات الدقيقة في تشكل بوليبيرول ناتج عن البلمرة الكهربائية.

## 1. Introduction

The conjugated polymers such as polyacetylene (PA), polythiophene (PTh), polyparaphenylene (PPP) etc. show a large increase in their electrical conductivity from insulator through semiconductor to metallic regions on ion-injection by chemical or electrochemical techniques. The conjugated conducting polymers possess the $\pi$-conjugated $sp^2$ hybridized carbon backbone and produced in the *p*-type doped form by chemical or electrochemical polymerization of their monomers. The *p*-type doped forms of such polymers have mobile positive charge carriers (*holes*) generally termed as '*polarons*' and '*bipolarons*' for electrical conduction along the polymer backbone [1, 2].

This is accomplished by removal of electrons from the polymer by an oxidant producing radical cations (holes) on the polymer chain. The movement of the holes on application of voltage causes electrical conduction along the polymer chains provided the electrostatic attraction between the holes and the counter-ions could be overcome by thermal energy or by shielding of charged species. A closely similar is the effect of the interaction between the conjugated polymer chain

and reductant which produces electrons on the polymer chain causing electrical conduction by the movement of electrons. This process of great increase in electrical conductivity of conjugated polymers by interaction with oxidant/reductant is called 'doping' in an extremely poor analogy to that in conventional inorganic semiconductors [3, 4].

For various reasons, doped conducting polymers needed to be undoped which commonly achieved by reacting them with aqueous or dry ammonia. Ammonia neutralizes or compensates the positive charges on the backbone killing the electrical conductivity of the conducting polymer and therefore this undoping process is also called as electrical neutralization or electrical compensation of conducting polymers. Thus the initial insulating state of the polymer could be regained by reverse process called as 'undoping' by chemically or electrochemically neutralizing the charge on the polymer backbone. This process may be perceived as an *n*-type doping of a *p*-type doped polymer in which the undoping reagent neutralizes the electrical charge of the polymer backbone by electron-transfer chemical reaction. The thin films of *p*-type doped polythiophene were found to react rapidly but irreversibly with ammonia and water. The interaction between undoping agents such as ammonia and water with *p*-type doped polythiophene has been examined and the complete mechanism of the undoping process in the form of chemical reactions have been proposed for the first time with the possibility of their use in sensing devices [5. 6-8].

The electrochemical polymerization of thiophene into $BF_4^-$ doped polythiophene ($PTh^{n+}$:$nBF_4^-$) films on platinum electrode and the chemistry of ammonia undoping of polyacetylene (PA), polypyrrole (PPy) and polythiophene (PTh) has already been reported [5, 6, 9] while the mechanism of undoping of polythiophene has yet not been discussed to the compeleteness. This prompted us to carry out the experiments on this aspect of undoping of conducting polymers. In short, the 100% electrochemical polymerization efficiency, certain morphological features in the polythiophene films and the formation of $NH_4F$ crystals were observed for the first time. The detailed characterizations of polythiophene studied in this communication have been reported in several other publications of the author.

## 2. Experimental

An evacuable electrochemical cell with a platinum working electrode and an aluminium counter-electrode was used to produce oxidized polythiophene at a current density of 9–12 mA $cm^{-2}$. Polythiophene films were washed with dry acetonitrile stored over activated molecular sieves and

dried by pumping on a vacuum line for about an hour prior to experimentation. Chemical undoping by moisture and dry ammonia was done in an oxygen-free atmosphere using a specially designed vacuum line fitted with high-vacuum Teflon stopcocks, a Pirani vacuum gauge and a mercury manometer topped with fluorinated oil [5, 6, 9].

## 3. Results and Discussion

In this communication, some observations *viz*. the efficiency of electrochemical polymerization ($E_p$) of thiophene, microdendrite formation on the edge of the $PTh^{n+}:nBF_4^-$ films formed during electropolymerization and the effect of pumping on the electrochemically prepared $PTh^{n+}:nBF_4^-$ undoped by dry ammonia are reported for the first time. A complete mechanism for dry ammonia and moisture undoping of polythiophene is also is presented for the first time.

### 3.1. Efficiency of polymerization

The efficiency of electrochemical polymerization of thiophene ($E_p$) was calculated using the relation ($E_p = 2W_1/W_2$) where $W_1$ is the moles of monomer polymerized and $W_2$ is the moles of electricity passed during polymerization. The efficiency of polymerization was observed to be nearly 100% as evident from the data presented in **Table 1**. Values approaching to 100% for the efficiency of electrochemical polymerization have also been reported by some other workers [10].

Table 1. Efficiency of electropolymerization ($E_p$) of thiophene in different electrolytes.

| **Polymer:Dopant (Mol.Ratio)** | **Current Passed (mA)** | **Duration of Polymerization (s)** | **Mass of Polythiophene (mg)** | **Efficiency ($E_p$) (%)** |
|---|---|---|---|---|
| $PTh^{n+}:nBF_4^-$ (0.1) | 29.95 | 180 | 2.43 | 101 |
| $PTh^{n+}:nBF_4^-$ (0.1) | 29.95 | 180 | 2.35 | 97 |
| $PTh^{n+}:nClO_4^-$ (0.065) | 29.95 | 190 | 2.52 | 100 |
| $PTh^{n+}:nClO_4^-$ (0.065) | 29.95 | 190 | 2.40 | 95 |
| $PTh^{n+}:nAsF_6^-$ (0.07) | 22.70 | 230 | 2.50 | 100 |
| $PTh^{n+}:nAsF_6^-$ (0.07) | 25.70 | 220 | 2.65 | 98 |
| $PTh^{n+}:nAsF_6^-$ (0.07) | 29.95 | 160 | 2.35 | 103 |

### 3.2. Undoping of polythiophene

It has been observed that polyacetylene doped with $AsF_5$ ($PA^{n+}$:$nAsF_6^-$) undergoes undoping by nucleophilic reaction of dry ammonia with the positive charges on the conjugated backbone forming C-N covalent bonds leading to the puncturing in the conjugation and loss of electrical conductivity. In case of electrochemically prepared $BF_4^-$ doped polypyrrole ($PPy^{n+}$:$nBF_4^-$), low pressures of ammonia undopes the positive charges which could be reversed by pumping indicating that covalent bonds are not formed [5, 6, 9]. The charge neutralization via acid-base chemistry involving $N^{\cdots}H^{+\cdots}N$ hydrogen bond bridge between the N atom of ammonia and N atom of pyrrole residues holding positive charges was suggested as was observed by Műnstedt [11] for the interaction of polypyrrole with aqueous hydroxide ions. This has led many workers to study the several types of nanocomposites of polypyrrole for sensor applications in the recent years [12-16]. However, an irreversible reaction of ammonia with polypyrrole at higher pressure and prolonged exposure to ammonia similar to that reported for polythiophene was observed.

As has been said earlier, the process of chemical compensation may be treated as *n*-type doping of a *p*-type doped polymer or vice versa in which the polymer passes through an insulation state. Schöllhörn and Zagefka [17] have suggested a redox reaction for ammonia or amine intercalation into layered metal dichalcogenides which has further been supported by the work of Foot and Shaker on ammonia and amine intercalation into $NiPS_3$ and $CdPS_3$ [18]. The disproportionation reaction of ammonia is given here.

$$8\ NH_3 \rightarrow 6\ NH_4^+ + 6e^- + N_2 \qquad (1)$$

In case of electrochemically prepared $BF_4^-$ doped polythiophene ($PTh^{n+}$:$nBF_4^-$), dry ammonia neutralizes the positive charges on the conjugated backbone of polymer without causing the chemical degradation i.e. the conjugation length of the undoped polythiophene remains unaltered unlike polyacetylene where conjugation length decreases. FTIR spectroscopic and XRD data supported the formation of $NH_4BF_4$ (sublimes ~230$^oC$) and $N_2$. In the light of the disproportionation reaction of ammonia, FTIR spectroscopic and XRD data [5, 6, 9], we suggested the mechanism of undoping of $PTh^{n+}$:$nBF_4^-$ in the following equations.

$$PTh^{n+}{:}nBF_4^- + n\,NH_4^+ + ne^- \rightarrow PTh + n\,NH_4BF_4 \quad (2)$$

(Conducting) (Non-conducting)

On further pumping on the vacuum line, the undoped polythiophene showed the formation of hexagonal crystals of $NH_4F$ on the surface and embedded in the polythiophene films (**Figure 1**). Similar hexagonal structures on the surface of the electrochemically prepared polythiophene have also been observed by Geetha and Trivedi [20]. By attributing the formation of $NH_4F$ (sublimes ~100$^o$C) to the volatilization of $BF_3$ (boiling Point -99.9$^o$C) from $NH_4BF_4$. Therefore, further step into the chemistry of undoping of $PTh^{n+}{:}nBF_4^-$ may be added as given

$$n\,NH_4BF_4 \rightarrow n\,NH_4F + n\,BF_3 \quad (3)$$

$$n\,NH_4F \rightarrow n\,NH_3 + n\,HF \quad (4)$$

A somewhat similar picture has emerged in the case of moisture undoping of $PTh^{n+}{:}nBF_4^-$. An analogous disproportionation reaction of water for the chemical undoping of $PTh^{n+}{:}nBF_4^-$ leading to the formation of HF (Boiling Point ~19.5$^o$C) and $BF_3$ (Boiling Point -99.9$^o$C) via $HBF_4$ (Boiling Point ~130$^o$C) was proposed by us as presented here.

$$6\,H_2O \rightarrow 4\,H_3O^+ + 4e^- + O_2 \quad (5)$$

$$PTh^{n+}{:}nBF_4^- + n\,H_3O^+ + ne^- \rightarrow PTh + n\,HBF_4 + n\,H_2O \quad (6)$$

(Conducting) (Non-conducting)

$$n\,HBF_4 \rightarrow n\,HF + n\,BF_3 \quad (7)$$

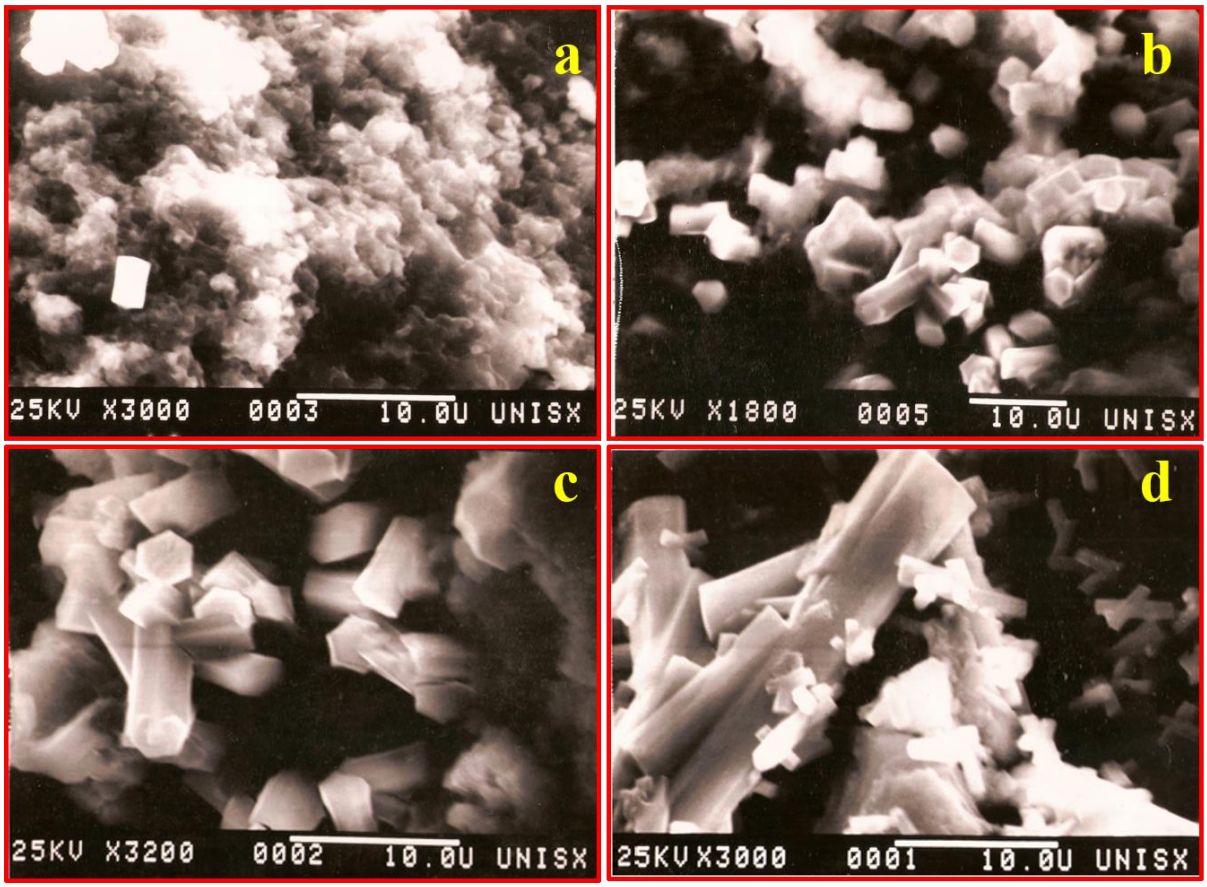


Figure 1. SEM of hexagonal crystals of $NH_4F$ formed during ammonia undoping of $PTh^{n+}:nBF_4^-$ films prepared by electropolymerization.

### 3.3. Morphological studies

The electropolymerization of thiophene produced $PTh^{n+}:nBF_4^-$ films (thickness 3 micron or less) of very high quality. The scanning electron microscopic studies revealed that the surface of the films was very smooth (**Figure 2**) [21-23].

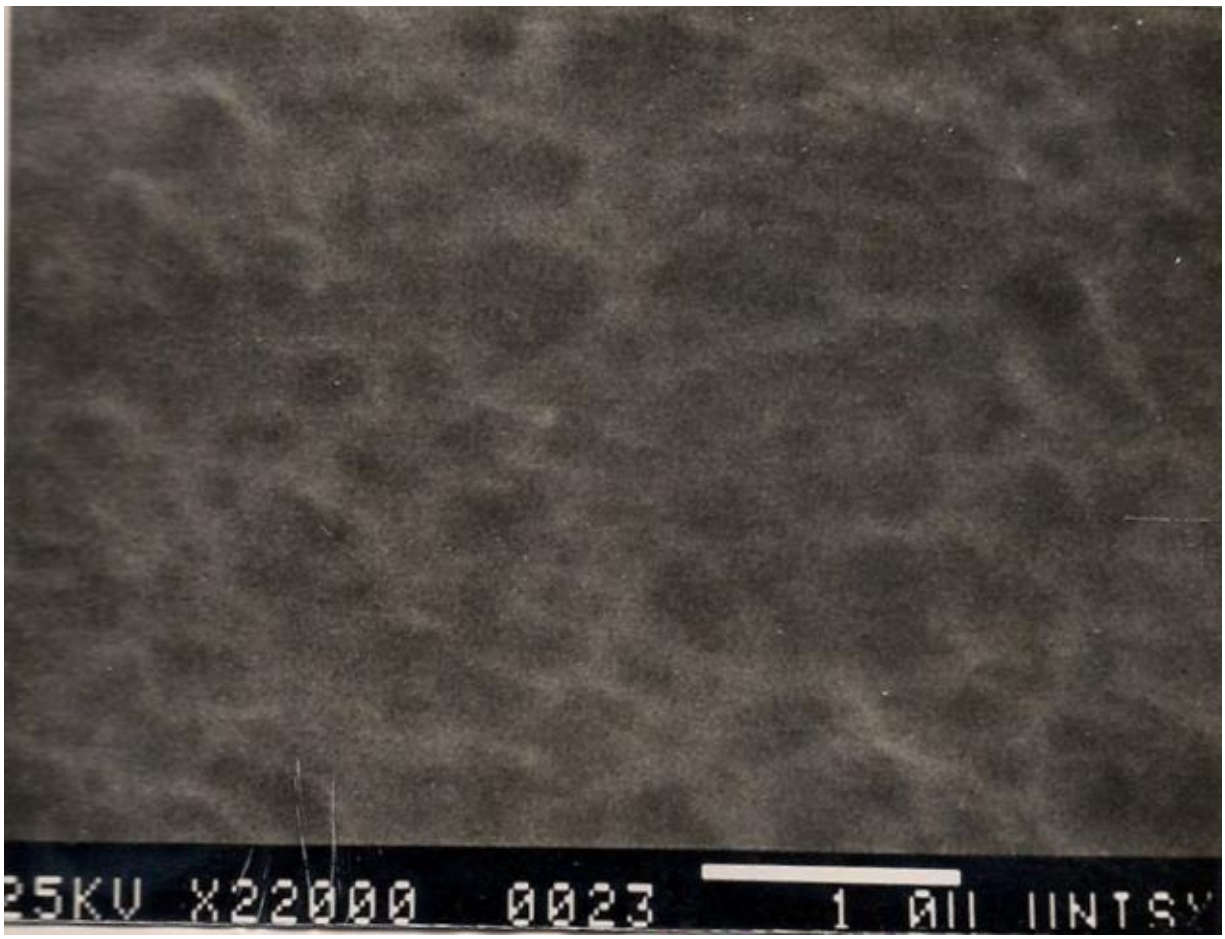


Figure 2. SEM image of the surface of the $PTh^{n+}:nBF_4^-$ films.

At the edge of the films, microdendritic growths of worm-like fibers of different lengths (8-40 micron in diameter) composed of well-organized globules were observed (**Figure 3**). It is typical, where a polymer precipitates after attaining certain threshold chain length into globules forms spherical beads as observed in case of polyethylene [24]. Slightly different types of dendritic growths were observed in polypyrrole during electrochemical polymerization and undoping by others as well [25].

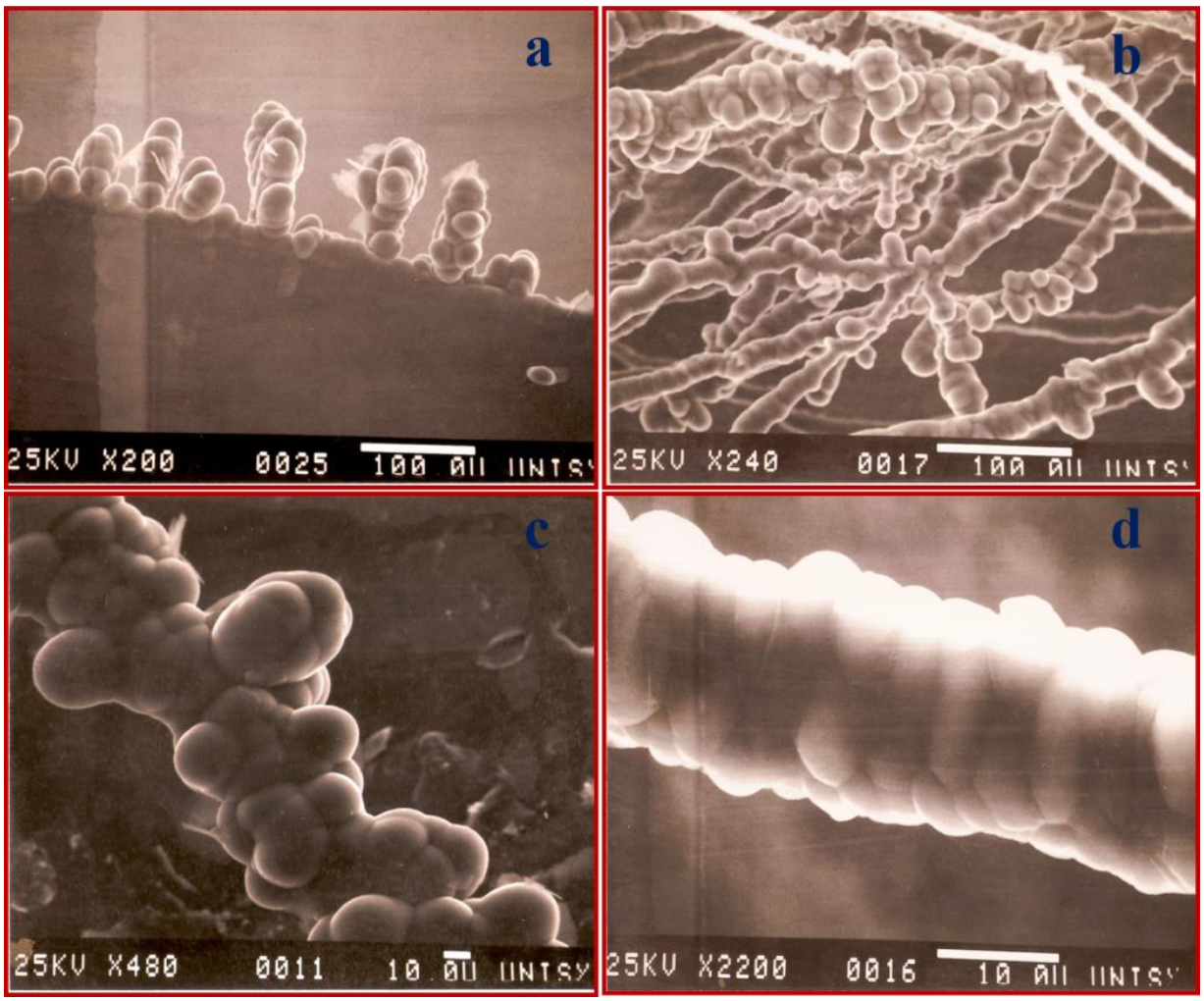


Figure 3. SEM images of the dendritic growths in $PTh^{n+}:nBF_4^-$ films prepared by electropolymerization in different magnifications.

## 4. Conclusion

In conclusion, the electropolymerization of thiophene is a highly efficient process which produces high quality thin films of polythiophene. Microdendritic growths of worm-like fibers of different lengths composed of well-organized globules at the edge of the as-prepared polythiophene films. A complete mechanism of dry ammonia undoping of $PTh^{n+}:nBF_4^-$ films is proposed in the light of our previous work and the formation of hexagonal crystals of $NH_4F$. An analoguous mechanism of moisture undoping of polythiophene is also proposed.

## 5. References

[1] D J Berets, D S Smith, Electrical properties of linear polyacetylene, Trans. Faraday Soc. 64 (1968) 823-828.

[2] H Shirakawa, S Ikeda, Infrared spectra of poly(acetylene) Polymer J. 2 (1971) 231-244.

[3] H Shirakawa, E J Louis, A G MacDiarmid, C K Chiang, A J Heeger, Synthesis of electrically conducting organic polymers: halogen derivatives of polyacetylene, (CH)x, J. Chem. Soc., Chem. Commun. (1977) 578-580.

[4] F Mohammad, Degradation and stability of conductive polymers, in H S Nalwa (ed), Handbook of Organic Conductive Molecules and Polymers, Chichester: Wiley, 1997, pp. 795

[5] F. Mohammad, Compensation behaviour of electrically conductive polythiophene and polypyrrole, J. Phys. D: Appl. Phys. 31 (1998) 951-959.

[6] P. Foot, T. Ritchie, F. Mohammad, Mechanisms of chemical undoping of conducting polymers by ammonia, J. Chem. Soc., Chem. Commun. (1988) 1536-1537.

[7] Lijia Pan, Hao Qiu, Chunmeng Dou, Yun Li, Lin Pu, Jianbin Xu, Yi Shi, Conducting polymer nanostructures: template synthesis and applications in energy storage, Int. J. Mol. Sci. 11 (2010) 2636-2657.

[8] Michael Woodson, Jie Liu, Guided growth of nanoscale conducting polymer structures on surface-functionalized nanopatterns, J. Am. Chem. Soc. 128(11) (2006) 3760-3763.

[9] F Mohammad, P D Calvert and N C Billingham, FT-IR studies on thermal degradation of electrically conducting polymers, Synth. Met. 66(1) (1994) 33-41.

[10] T.R. Jow, K.Y.Jen, R.L. Elsenbaumer, L.W. Shacklette, Electrochemical studies of fused-thiophene systems, Synth. Met. 14 (1986) 53-60.

[11] H. Műnstedt, Properties of polypyrroles treated with base and acid, Polymer 27 (1986) 899-904.

[12] Cuili Xiang, Dadi Jiang, Yongjin Zou, Hailiang Chu, Shujun Qiu, Huanzhi Zhang, Fen Xu, Lixian Sun, Liangjun Zheng, Ammonia sensor based on polypyrrole graphene nanocomposite, Ceramics International: Part A 41(5) (2015) 6432-6438.

[13] Adil Sultan, Faiz Mohammad, Chemical sensing, thermal stability, electrochemistry and electrical conductivity of silver nanoparticles decorated and polypyrrole enwrapped boron nitride nanocomposite, Polymer, 113 (2017) 221-232.

[14] Sharique Ahmad, Adil Sultan, Faiz Mohammad, Liquefied petroleum gas sensing and dc electrical conductivity studies of polythiophene/silicon carbide nanocomposite. RSC Advances 6(64) (2019) DOI: 10.1039/C6RA12655C.

[15] Adil Sultan, Sharique Ahmad, Faiz Mohammad, A highly sensitive chlorine gas sensor and enhanced thermal dc electrical conductivity from polypyrrole/silicon carbide nanocomposites, RSC Advances, 6 (2016) 84200-84208.

[16] A Sultan, S Ahmad, T Anwer, F Mohammad, Binary doped polypyrrole and polypyrrole/boron nitride nanocomposites: preparation, characterization and application in detection of liquefied petroleum gas leaks, RSC Advances, 5(128) (2015) 105980-105991.

[17] R. Schöllhorn, H. D. Zagefka, Angew. Chem., Intercalation compounds of low-dimensional transition metal chalcogenides (Chapter 7), Annu. Rep. Prog. Chem., Sect. C: Phys. Chem. 90 (1993) 177-213.

[18] P.J.S. Foot, N.G. Shaker, Amine intercalates of lamellar compounds NiPS3 and CdPS3, Materials Research Bulletin 18(2) (1983) 173-180.

[19] W. Feng, S. Rangan, Y. Cao, E. Galoppini, R. A. Bartynski, E. Garfunkel, Energy level alignment of polythiophene/ZnO hybrid solar cells, J. Mater. Chem. A 2 (2014) 7034-7044.

[20] S. Geetha, D.C. Trivedi, A new route to synthesize high degree polythiophene ia room temperature melt medium, Synth. Met. 155 (2005) 232–239.

[21] Reena S. Futane, V.M. Raut, S.D. Khandare, Study of Undoped and V2O5 Doped Polythiophene thin Films by Chemical Bath Deposition Technique, International Journal of Advanced Research in Chemical Science (IJARCS) 3(11) (2016) 32-37.

[22] M. Faisala, Farid A. Harraza, Adel A. Ismail, Ahmed Mohamed El-Tonib, S.A. Al-Sayaria, A. Al-Hajrya, M.S. Al-Assiria, Polythiophene/mesoporous SrTiO3 nanocomposites with enhanced photocatalytic activity under visible light Separation and Purification Technology 190 (2018) 33–44.

[23] Kornelia Kadac, Jacek Nowaczyk, Polythiophene nanoparticles in aqueous media, J. Appl. Polym. Sci. (2016) DOI: 10.1002/APP.43495.

[24] A. Akar, N.C. Billingham, P.D. Calvert, The morphology of polyethylenes produced by alumina-supported zirconium tetrabenzyl, Polymer J. 24 (1983) 889-897.

[25] L.C. Scienza, G.E. Thompson, TEM and SEM investigations of polypyrrole films on aluminium, 17º CBECIMat - Congresso Brasileiro de Engenharia e Ciência dos Materiais, 15 a 19 de Novembro de 2006, Foz do Iguaçu, PR, Brasil, 8613-8622.

# Tribo-corrosion Performance of Plasma Sprayed $Al_2O_3$ on Aluminum Alloy for Thermal Barrier Coatings

**Essam R.I. Mahmoud**

Department of Mechanical Engineering, Faculty of Engineering, Islamic University of Madinah, Saudi Arabia

emahoud@iu.edu.sa

**Ali Algahtani**

Department of Mechanical Engineering, Faculty of Engineering, King Khalid University, Saudi Arabia

Research Center for Advanced Materials Science (RCAMS), King Khalid University, Saudi Arabia

alialgahtani@kku.edu.sa

**Abstract:** Aluminium alloys have attractions to be used for a wide range of applications due to its lower density and the formation of passive film which provide corrosion protection. At high temperature (more than 250 $^0$C), the passive film may be destroyed, thermally corroded and it will easily be failed by thermal fatigue failures. This work has investigated the enhancements of plasma sprayed $Al_2O_3$ coating on the performance of 6082-T6 aluminium alloy surface against erosion and corrosion test environments. The study investigates the macro/microstructure and the formed phases of the plasma sprayed $Al_2O_3$ formed layer. The erosion resistance of the coated layer, in particular, the effect of sand concentration and temperature variations to the aqueous slurry impingement against material properties such as adhesion, ductility, and roughness were investigated. In addition, a series of electrochemistry tests have been conducted to verify the corrosion performance. As a reference, the un-coated 6082-T6 aluminium substrate was instigated in all the experiments. The resulted showed that plasma sprayed $Al_2O_3$ coating layer had lamellar structure of approximately 86% $\gamma$-$Al_2O_3$ and 14% $\alpha$-$Al_2O_3$ phases and contained many voids and porosity. The coated layer shows good corrosion resistance at ambient temperature. At 80 $^o$C, small amount of ions penetrations was recorded. The coated layer was completely removed after polarizing the solution up to 400 mV for 24 hours. Although there was no stability of the current in the coating during the polarization test, the coating shows lower corrosion current density under static anodic polarization tests compared to the aluminium substrate indicates better corrosion

resistance. It has been shown that the erosion of the coated layer shows linear erosion rate. The erosion rates observed for the coating in elevated temperature are much lower than aluminium substrate. As a result, the erosion resistance of aluminium alloy can be highly improved by plasma sprayed $Al_2O_3$ coating, especially at high temperature.

**Keywords:** 6082 Aluminium Alloy; plasma sprayed coating; erosion resistance; Microstructure; Wear resistance; polarization test.

# دراسة أداء سبائك الألومنيوم المطلية بحبيبات الألومينا الصلبة عن طريق البلازما في درجات الحرارة العالية

**الملخص**: تعتبر سبائك الألومنيوم من المواد الصناعية الهامة وذلك لاستخدامها في مجموعة واسعة من التطبيقات بسبب كثافتها المنخفضة وتشكل طبقة طبيعية رقيقة على سطحها توفر لها الحماية من التآكل الكيميائي. في درجات الحرارة العالية أكثر من 250 درجة مئوية، سيتم تدمير هذه الطبقة، وتتآكل حرارياً خاصة عندما تتعرض لعوامل الفشل الحراري في هذه الظروف الصعبة. في هذا العمل ترسيب حبيبات الألومينا **Al2O3** وذلك عن طريق الرش بالبلازما على سطح إحدى سبائك الألومنيوم المهمة واختبار كفاءتها عن طريق اختبار التآكل والبري الميكانيكي. تمت دراسة البنية المجهرية لمعدن الأساس وكذلك البنية المجهرية للطبقة المشكَّلة بالبلازما. تم فحص مقاومة التآكل للطبقة المترسبة، وكذلك تأثير تركيز الرمال وتغيرات درجات الحرارة على خصائص المواد المختلفة، تم إجراء سلسلة من اختبارات التآكل الكيميائي عن طريق سلسلة من الاختبارات للتحقق من أداء المواد المصنعة عند درجات حرارة مختلفة. أظهرت النتائج أن طبقة الطلاء **Al2O3** التي تم رشها بالبلازما كانت لها بنية صفائحية تقارب 86٪ **γ–Al2O3** و14٪ **α–Al2O3** وتحتوي على العديد من الفراغات والمسامية. تُظهر الطبقة المطلية مقاومة جيدة للتآكل في درجة الحرارة العالية. عند 80 درجة مئوية، تم تسجيل كمية صغيرة من اختراقات الأيونات. تمت إزالة الطبقة المطلية بالكامل بعد استقطاب المحلول حتى 400 ملي فولت لمدة 24 ساعة. على الرغم من عدم وجود استقرار للتيار الموجود في الطلاء أثناء اختبار الاستقطاب، إلا أن الطلاء يظهر انخفاض كثافة تيار التآكل في ظل اختبارات الاستقطاب الأنودي الثابت مقارنة مع الركيزة المصنوعة من الألومنيوم، مما يشير إلى مقاومة أفضل للتآكل. لقد ثبت أن تآكل الطبقة المطلية يظهر معدل تآكل خطي. معدلات التآكل التي لوحظت للطلاء في درجة حرارة مرتفعة أقل بكثير من معدن الأساس غير المطلي. نتيجة لذلك، يمكن تحسين مقاومة التآكل لسبائك الألمونيوم بشكل كبير من خلال طلاء **Al2O3** الرش بالبلازما، خاصة في درجات الحرارة العالية.

## 1. Introduction

Aluminium is a metallic element which has a natural corrosion resistance at room temperature due to the formation of very thin oxide layer (few nanometre thick) on its surface [1]. This dense layer is formed quickly when it is exposed to the environment. The thickness of the layer is dependent

on the environment parameters. Some of the aluminium alloys also possess attractive properties such as strength to weight ratio, low-cost material and good weldability which make them good candidate for wide range of applications such as aerospace, automotive structures, renewable energy, extraction systems, internal combustion engines and gas turbines sectors. The operation temperature of some of these applications is relatively high. When the surface of the aluminium alloys exposed to high temperature for long time, it will easily be oxidized and wearied. Also, relatively amount of heat losses is expected due to their high thermal conductivity [2-4].

Under aggressive environments, aluminium is subjected to different types of severe corrosion like intergranular corrosion, pitting corrosion, and many other cracks such as stress corrosion cracking [5-6]. Pitting corrosion usually attacks aluminium surfaces causing localised holes in the protective film under chloride corrosive environments which affect the mechanical properties of the metal like reducing the tensile stress and causing fatigue and stress corrosion cracks [7]. For some applications, the materials are suffered from many severe conditions of erosion/wear and corrosion. It led to an irreversible materials degradation, and whenever they take place simultaneously, the process is known as tribo-corrosion. Tribo-corrosion involves a synergism between wear and corrosion, since the total material loss when the two processes occur simultaneously is greater than when they act alone [8]. Insufficient resistance to tribo-corrosion limit the application of aluminium alloys [9]. For that reason, a thin layer called “thermal barrier coatings” can be formed on the surface subjected to high temperature for long time, to protect it from thermal damage. These thermal barrier coatings, usually consisting of ceramics, will protect the surface and reduce heat loss from inside to outside due to its lower thermal conductivity.

Many technologies were used to form a protective layers/coating on aluminium alloys to enhance the tribo-corrosion resistance properties of the alloy, such as laser cladding, traditional welding processes, hard anodization, plasma electrolytic oxidation and plasma-spray ceramic coatings etc. [10].

Plasma-spray ceramic (PSC) coating is considered a famous and cheap technique for cladding many metallic surfaces. It can be used to deposit metals, ceramics or even plastics on the surface of most of the metallic surfaces. Also, the thickness of the coating varies from a few micrometres to several millimetres [11–12]. Plasma Spray Ceramic Coating is a coating produced by process in which molten or softened particles are applied by impact onto a substrate [13, 14]. It was first addressed by Schoop when he studied the production of metallic particles from a molten metal to

be used as a coating at the beginning of the last century [15]. There are three main stages to form this coating. Firstly, plasma particles are created as small droplets stream [16]. Secondly, these particles are subjected to high temperature using heat source generating thermal energy. The particles' compositions get changed due to the chemical reaction between the droplet material and the flame [17]. After that, they are flattened then striking a cold surface at high velocities generating kinetic energy. A common feature of lamellar grain structure will be formed as a result of the rapid solidification and cooling processes. The general behaviours of PSC coating are considered to be porous lamellar structures [18] composed of splats with columnar grain structures and have voids and pores areas.

Among many ceramics, $Al_2O_3$ are the most widely used for cladding the aluminum alloys through plasma spraying. Besides its low density, high hardness & wear resistance, low cost and its wide range of available grades, it has excellent thermal stability. The $Al_2O_3$ coating can protect its substrate form severe and harsh environment when wear and corrosion are presented [19]. Beauvais et al., [20] studied the microstructure of plasma sprayed coating using different ceramic powders ($Al_2O_3$–$TiO_2$, $Al_2O_3$, $ZrO_2$–$Y_2O_3$ (YSZ) and $Cr_2O_3$) on 316 stainless substrates. It was found that the PSC microstructure was homogenous with low porosity. Also, micro-cracks in the $Al_2O_3$ coating were detected as a result of the thermal stresses developed during the process [20]. Song et al., [21] deposited $Al_2O_3$ and $TiO_2$ powders using plasma spraying method with different powers on 6063 aluminium alloy substrate. The coating has high porosity at low power source, since the parts of the particles did not completely melt and were embedded in the melted lamellar structure. As the power source increased, the un-melted particles decreased, and lamellar structure was formed with less particle sizes. Abdel-Salam et al., [22] improved the corrosion resistance of the 2014 Al alloy through hard anodizing in sulphuric acid electrolyte. They found that the addition of sulphonate significantly improve the corrosion resistance. Tabakoff and Shanov [23] studied the erosion behaviour of the plasma ceramic coating that used in compressors and turbines at high temperature. They reported that TiC coating shows better erosion resistance when exposed to fly ash and chromite particles. Wang et. al. [24] sealed the plasma sprayed alumina coating through aluminum phosphate. The results showed that the phosphate penetrates through the interface between the alumina coating and the substrate and improves the sliding wear resistance.

Most of the previous works [19-26] were focused on the wear or corrosion behaviors of plasma ceramic coating. In this research work, we planned to characterize both erosion and corrosion of

the plasma ceramic coating layer that deposited on Al 6082 alloy. The microstructure of the coating layer was investigated in detail. The hardness, erosion resistance, and corrosion behavior of the coating layer was evaluated in detail at ambient and high temperatures.

## 2. Experimental work

The substrate used for PSC coating was 6082-T6 aluminum alloy. The substrate specimens' discs were cut with a diameter of 25.40 mm and a thickness of 10 mm ± 0.01 mm to be fitted in the holder for erosion and electrochemistry experiments suitable for the rig available in the lab. The samples were coated using a conventional 100 kW atmospheric plasma spraying system. The powder of grey alumina contains 2.5% of titanium dioxide was feed at constant rate of 15 gm/min, using a turntable type volumetric powder feeder. The feeding and spraying distances were 24 mm and 300 mm, respectively. The microstructures of the PSC coating were investigated using scanning electron microscope equipped with EDX analyzer. The database (ICDD, International Centre for Diffraction Data) entries used were 00-046-1212 and 01-074-4629 for alpha and gamma respectively. The area of the peaks was determined using the software XPert Highscore Plus. The PSC coated layer were analyzed by X-ray diffractometer (XRD). Surface roughness of the coated surface was measured using Veeco-Wyko NT 3300S Interferometer. An Inductive Coupled Plasma (ICP) test was performed to assess the amount of ions ($Al^{3+}$) released from the 3.5%NaCl solution after 24 hours (for temperatures of 20°C and 80°C) of immersing the samples into the solution at different test conditions. Then, the samples were polarized up to 400 mV against the reference electrode for another 24 hours. This polarization test was theoretically compared with Faraday's Law of electropolsity that gives an indication of corrosion process of these coatings on the basis of ion movements across the coating layers. The erosion tests were performed using sand particles through Recirculation Jet Impinging Rig. These sand particles have round shape and sharp edges with an average diameter between 200 µm and 250 µm as shown in the SEM image in Figure 1. Two sand loadings (200 mg/l & 1000mg/l) and two temperatures (20°C & 70°C) were selected as the main experimental variables to go gradually from medium to highly severe erosion conditions. After erosion experiments, the weight loss measurements were recorded after 2, 5, 8 and 10 hours followed by profilometry and microscopic analysis on the surfaces of the coated samples to analyze the surface of the coated samples after erosion experiments using "Form Talysurf 120L" equipment in order to measure the surface shape, texture, profile of volumetric damage and to identify the depth of the attack and the zones which suffer the greatest degradation.

The microhardness of the coated layer and the substrate were measured (before and after the erosion test) using Knoop indenter. The shape of this type of indenter is an elongated diamond pyramid and it is more sensitive to surface conditions than Vickers test which is more suitable for the thin coatings [27].

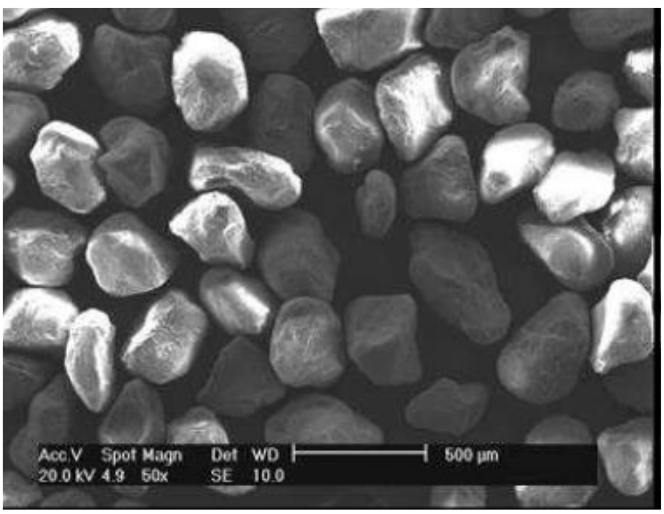


Figure 1. SEM image of sand particles used for erosion test.

## 3. Results and Discussions

### 3.1 Macro/microstructure analysis

The coated plasma spray ceramic (PSC) consisted of three different layers of about 350 µm thick, starting with a loose layer in the interface region of 87 µm as shown in Figure 2 (a). This layer is followed by the intermediate layer of approximately 250 µm and finally the top porous layer of 55 µm. The intermediate layer contains many laminar structures with white colours which could be the aluminium alloy 6082-T6. Similarly, the SEM cross-sectional image of PSC sample, shown in Figure 2 (b), reveals that the average coating thickness is about 275 – 280 µm. The dark layer (gap) at the interface is probably due to debonding of the PSC coating from the substrate. Although it is due to metallographic preparation (sectioning / polishing), it also indicates a poorer bond with the substrate.

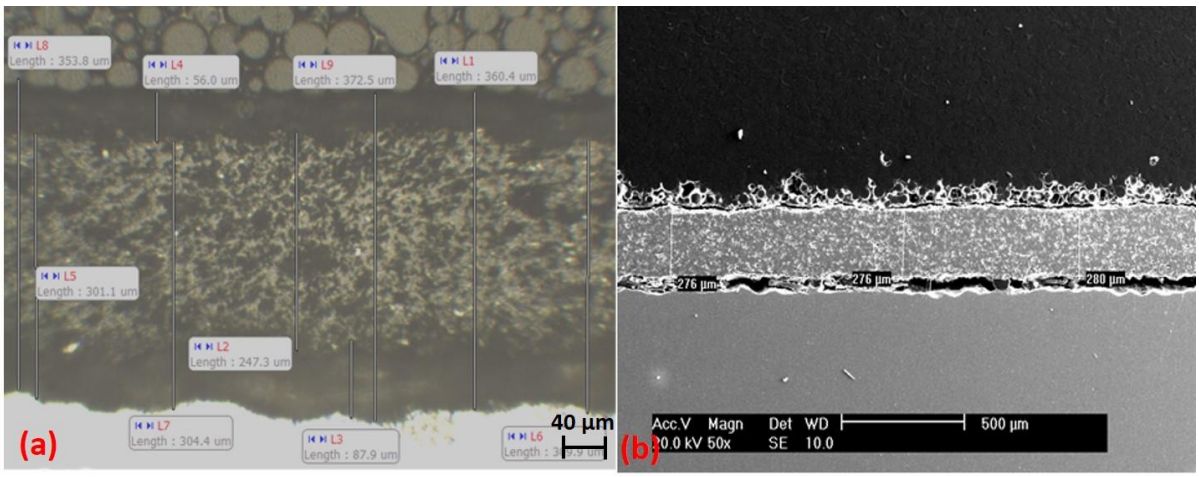


Figure 2. Cross-sectional view of PSC coating.

Microscopically, the microstructure of the plasma spray ceramic coating (Figure 3) exhibits a lamellar structure and has many porous regions. The EDX analysis (Figure 4) detected the elements of aluminium, oxygen and titanium. The PSC coating was prepared using grey alumina powder which contains 2.5% of titanium dioxide according to the supplier. According to XRD spectra shown in Figure 5, PSC coating has $\alpha$-$Al_2O_3$ and $\gamma$-$Al_2O_3$ phases but with lower intensity peaks. The relative proportions of alpha alumina ($\alpha$-$Al_2O_3$) and gamma alumina ($\gamma$-$Al_2O_3$) phases can be estimated from the intensity (area) of the peaks in the XRD plots for the material. Conventionally, this is achieved using the most intense peaks for each phase and using an RIR (Reference Intensity Ratio) for each phase. RIR values are normalised against corundum (alpha alumina, which has a value of 1.0). Due to peak overlap and strong scattering from the substrate, it was not possible to use the most intense peaks. Therefore, to gauge the relative proportions, less intense, but unobstructed peaks were used at 25.578° for and 19.318° for gamma. The area of the peaks was then divided by the product of the RIR and the relative intensity of the peak (from the database). The amount of alumina phases ($\alpha$-$Al_2O_3$) available in PSC coating was 14% and Gamma alumina ($\gamma$-$Al_2O_3$) was 86%.

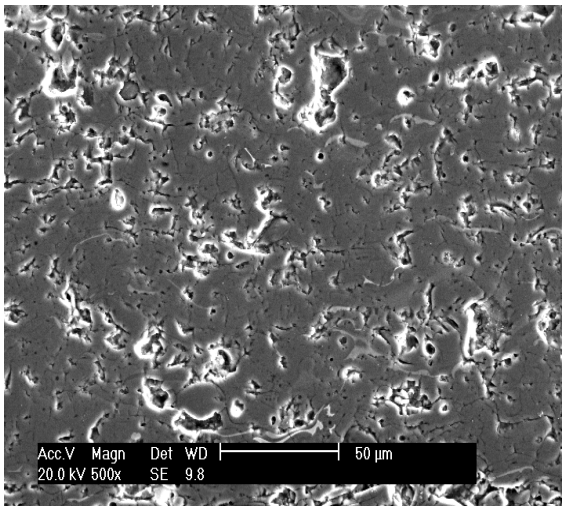


Figure 3. Microstructure of PSC.

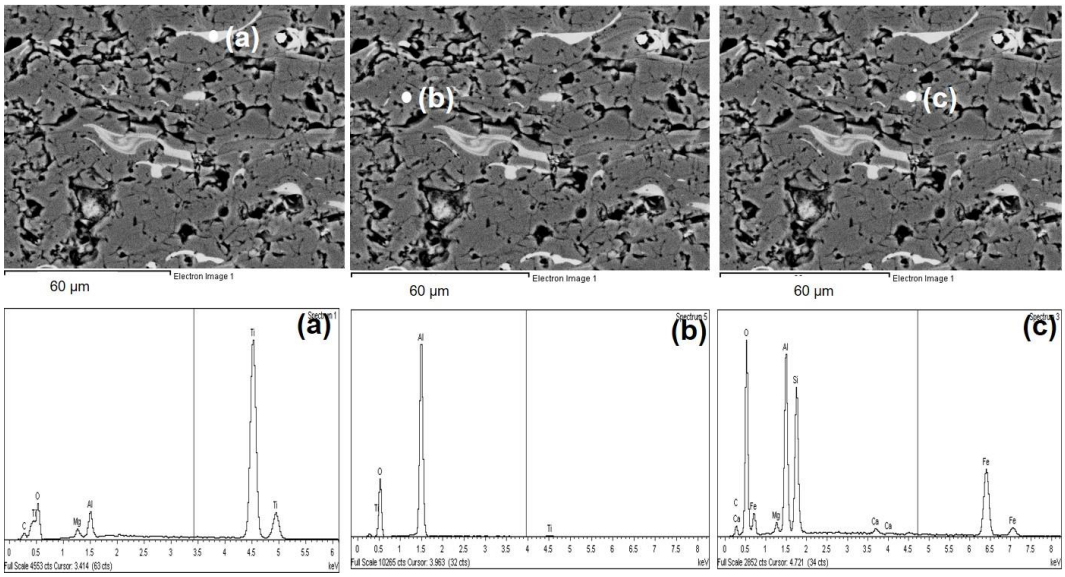


Figure 4. Detection of elements of PSC using EDX analysis.

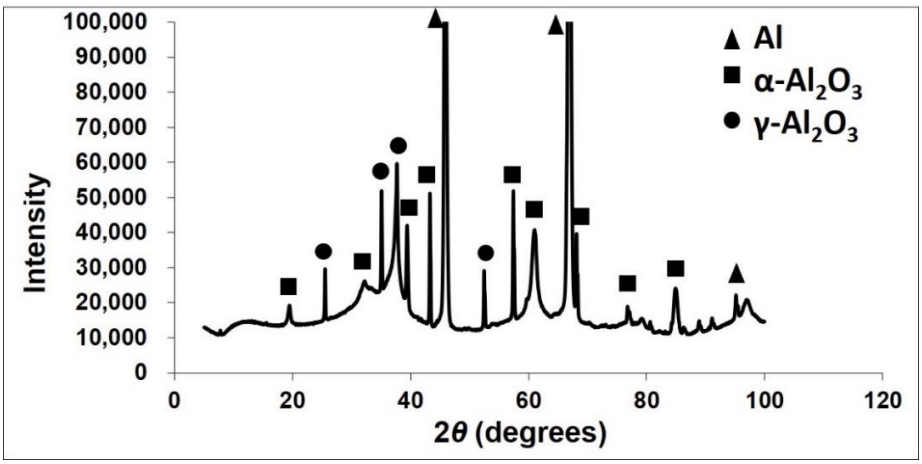


Figure 5. XRD for PSC sample; (a) full plot and (b) Zoomed scale.

## 3. 2. Electrochemistry

### 3.2.1 Inductive Coupled Plasma (ICP) Test Results

Figure 6 show the potential current versus time plots to calculate charge transfer at 400 mV for PSC sample. There was no stability of the current in the PSC sample as many variations of the curve occurs during the 24 hours polarization test and the currents were relatively high. The first increase of the current occurs at about 1000 seconds from 1.5 x $10^{-2}$ A/cm$^2$ to 3.0 x $10^{-2}$ A/cm$^2$ which could be attributed to high movements of $Al^{3+}$ movement through the coating due to its high porosity. The current fluctuation on the polarisation curves could be attributed for electrochemistry activities taking place on the surfaces such as localised pitting corrosion in the substrate/coating interface region [28]. However, the current increases also from about 2.5 x $10^{-2}$ A/cm$^2$ to 5.0 x $10^{-2}$ A/cm$^2$ around 7000 seconds where it is expected that the PSC coating has completely removed from the substrate as shown in Figure 7. This is due to the low adhesion between the substrate and the coating where ions penetrate between them.

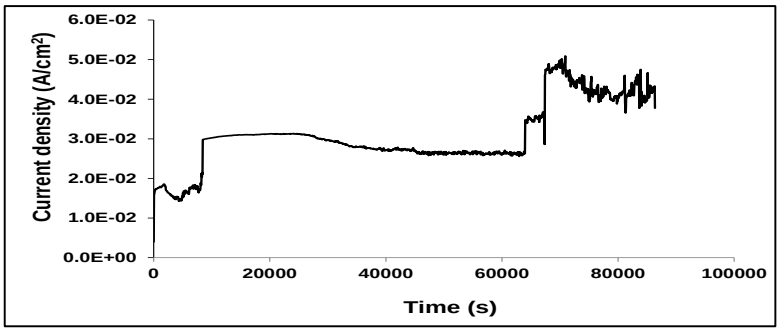


Figure 6. Current density versus time plots to calculate charge transfer for PSC at +400 mV (Ag/AgCl).

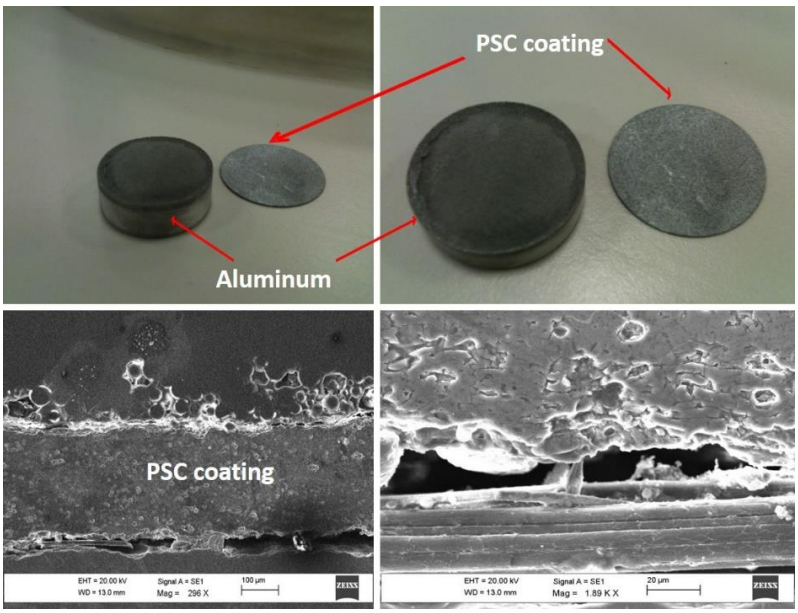


Figure 7. PSC sample after 24 hours ICP polarization Test.

### 3.2.2 Anodic Polarization (AP) Measurements

Figure 8 shows the results of the anodic polarization resistance for PSC sample together with Al substrate. The breakdown voltages for all materials can be determined from the anodic polarization curves at the potential value where the current increased rapidly and deviated from the initial growing rate. The values of the breakdown potentials of the materials were determined from the Excel plots and the red lines in these graphs are just to show the method and not indicating the exact $E_b$ values. The breakdown potential ($E_b$) is the potential where the passive film of the surface breaks down. $E_b$ for the ceramic materials indicate the penetration of the electrolyte ions through the coating defects to the substrate metal. It is expected that the coating would decrease the possibility of breaking down the aluminium passive film and consequently decrease the current density and improve the corrosion resistance [29-30].

The corrosion current densities for the materials were determined from the logarithmic scale of the current density in the anodic polarization curves as shown in Figure 9. The potential was shifted from the OCP value of the material to 250 mV in the opposite direction to ensure that the cathodic and anodic currents are different to measure the corrosion current density on the sample by extrapolating the anodic branch with the line from OCP value. Table 1 summarises the main corrosion parameters of the materials that were determined from the DC electrochemistry plots

(anodic polarisation curves). Therefore, PSC coating has lower corrosion current density (2.6E-07 A/cm$^2$) under static anodic polarization tests.

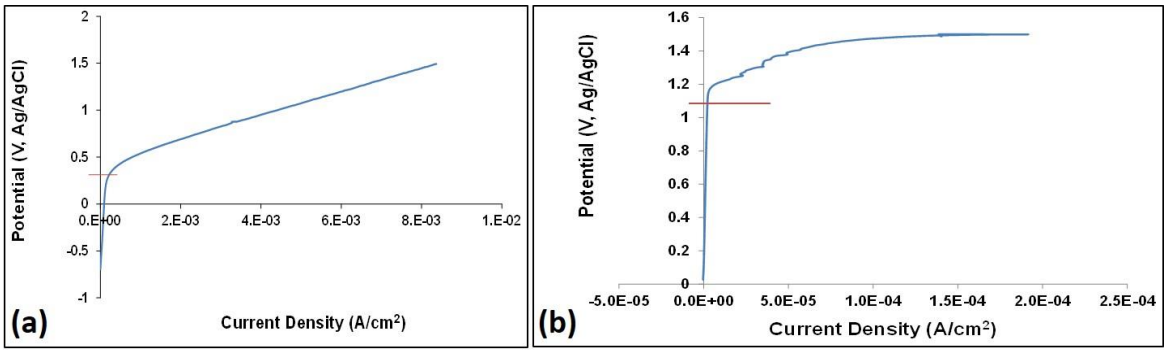


Figure 8. AP Measurements for (a) aluminium substrate and (b) PSC coating.

Table 1. Summary of corrosion parameters of the materials.

| **Corrosion Parameter** | **PSC** | **Al** |
|---|---|---|
| Open circuit potential *(*OCP*)* [V] | -0.76 | -0.7 |
| Breaking down potential ($E_b$) [V] | 1.12 | 0.2 |
| Corrosion current density ($i_{corr}$) [A/cm$^2$] from AP Curve | 2.6E-07 | 1.2E-05 |

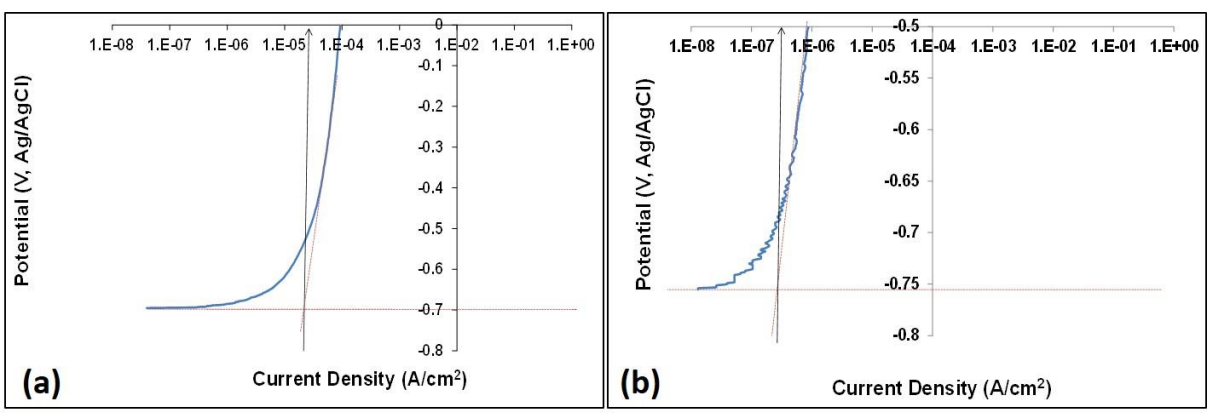


Figure 9. Determination of corrosion current density for (a) Al substrate and (b) PSC.

### 3.2.3 AC Impedance Plots for Plasma Spray Ceramic (PSC) Surface

The arc radius in the Nyquist plot of PSC coating was slightly increased after the full period of immersion test (Figure 10 (a)). This corresponds to the minimal change in the total resistance from the Bode plot shown in Figure 10 (b). The aluminium substrate can be seen after the corrosion test which indicates that relatively high amount of PSC coating degradation has occurred due to this chemical reaction.

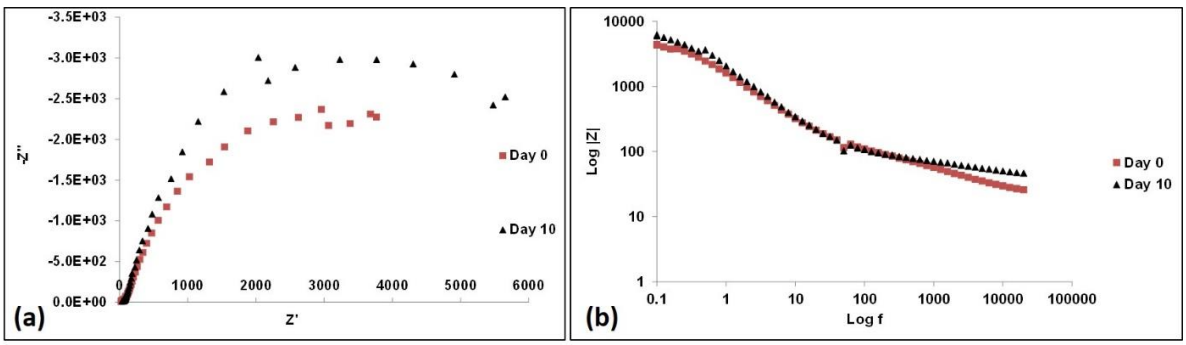


Figure 10. (a): Nyquist plots and (b): Bode plots for PSC at different immersion times.

The AC impedance data was fitted using the circuit model (Figure 11) and the results are shown in Figure 12 for Day 10 of the immersion period. Although there is no significant change in the arc radius of the Nyquist plot of PSC after the full period of immersion test, the total resistance was fluctuating between these two end points as shown in Figure 13. The increase of the resistance between day 2 and day 5 corresponds to the formation of the corrosion products at the coating/substrate interface that initiated due to ions transfer in the pores regions of PSC surface. The resistance and phase constant element were fluctuating during the period of the test (Figure 13) which indicate that part of the PSC coating was delaminated [31].

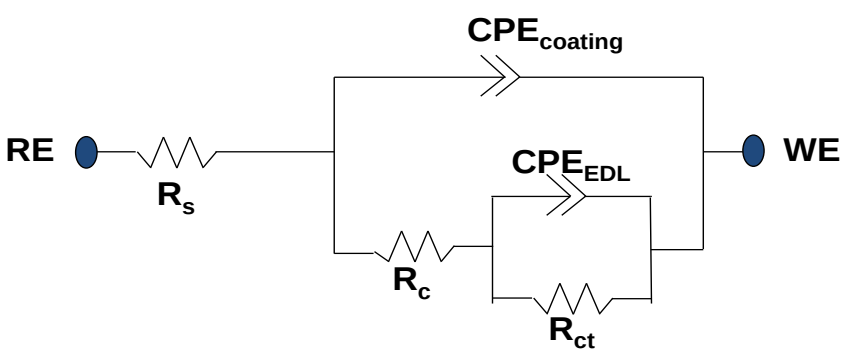


Figure 11. Modified circuit model for PSC coating.

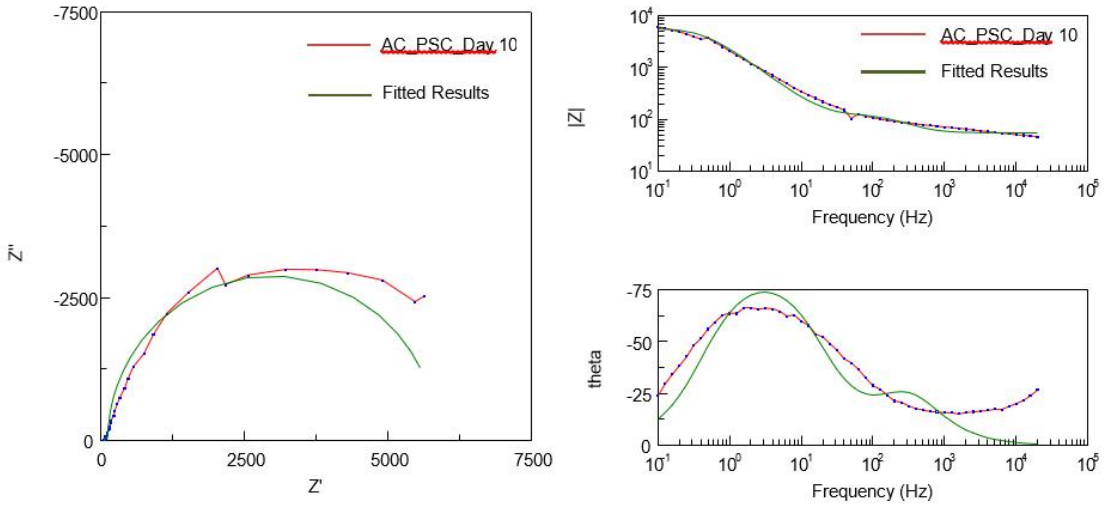


Figure 12. Fitted data for PSC coating at day 10.

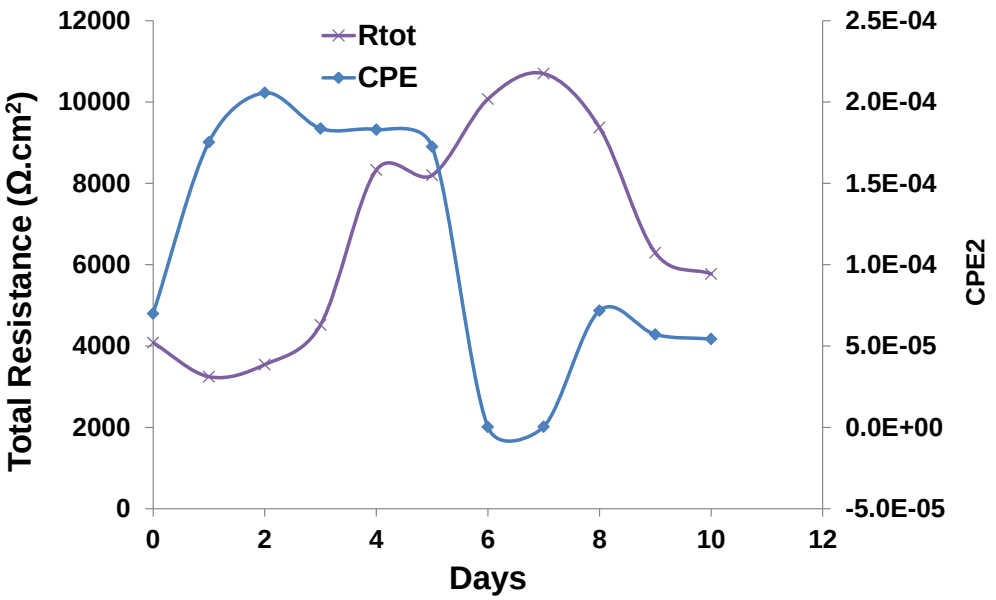


Figure 13. Time dependence of the $R_{tot}$ and $CPE_2$ for PSC coating after different exposure times.

### 3.4. Erosion Test Results

This part presents the results of erosion experiments performed on the samples of the aluminium substrate and the PSC coatings. Figure 14 shows the weight loss measurements of the materials for ten hours experiments under low (200 mg/l) and high (1000 mg/l) sand loadings at temperatures

of 20 and 70 ºC. The weight loss measurements were recorded after 2 hours, 5 hours, 8 hours and 10 hours to observe how the wear rate of the materials changes with time. The data points have been fitted with either linear regression line or polynomial curve according to the weight loss trend for each material. A consistent increase in the wear losses has been observed with increasing both time and sand loading as expected. Generally, the PSC coating exhibits poor erosion resistance in the test conditions when compared to aluminium substrate at both sand loading 200 mg/l and 1000 mg/l. The PSC coating has high erosion rate and its weight loss is more than the aluminium substrate after five hours at low sand loading and four hours at high sand loading. Moreover, the erosion rates observed in elevated temperature tests are higher than in room temperature tests for the PSC coated samples and aluminium substrate.

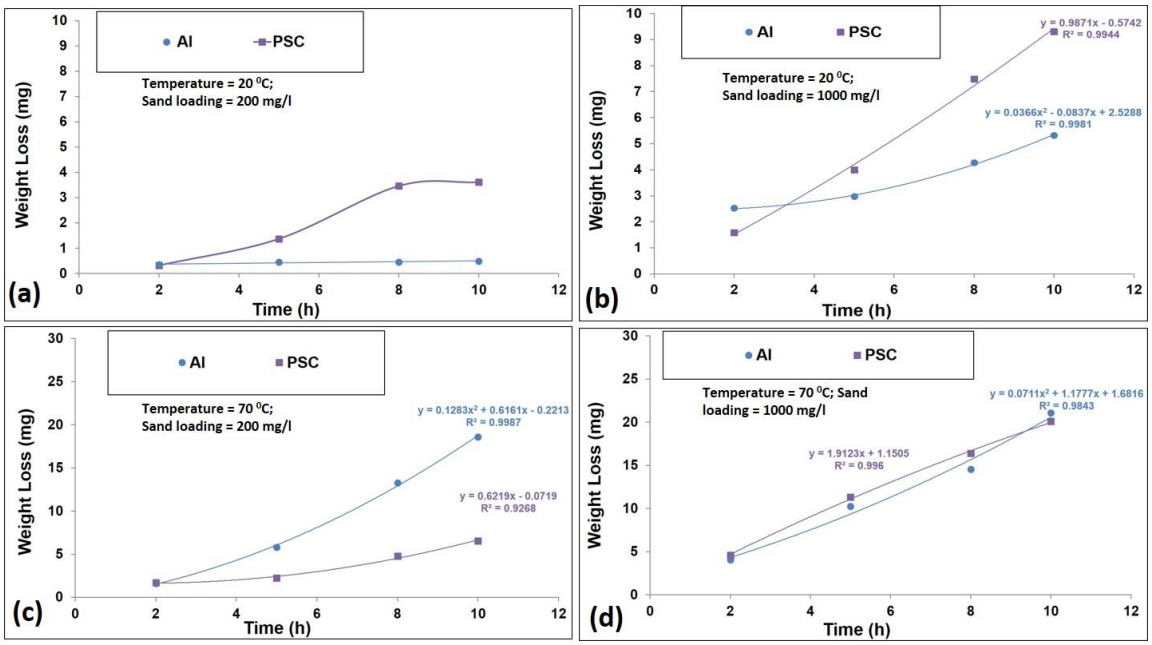


Figure 14. Weight loss measurements at different conditions after 10 hours.

It has been observed that the aluminium substrate has good erosion resistance and has a linear wear rate at low sand loading and low temperature. When the sand lading was increased to 1000mg/l, large amount of material loss was observed, which match the results of Zhang et al., [32] and Costa et. Al. [33]. It is noticed that a large amount of PSC material has been removed due to the impact loading. Also, its wear loss rate increases sharply compared to aluminium sample where the erosion rate increases gradually. This indicates that the removed materials of PSC take place as cracks on the surface followed by chipping off the coating since its surface exhibits brittle material

fracture. This could be attributed to the low adhesion bonding and pores as shown between the PSC coating and the substrate in Figure 15.

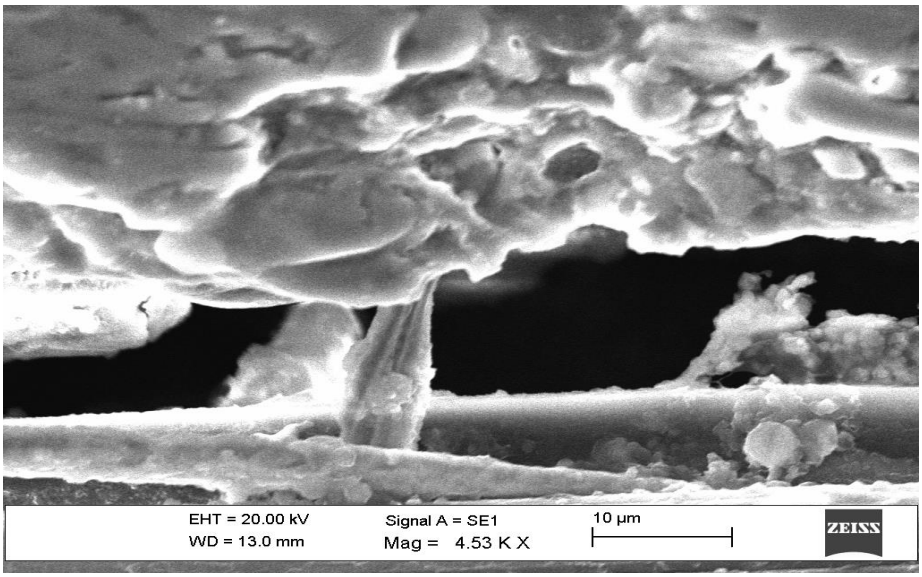


Figure 15. High gap size between PSC coating and Al substrate.

### 3.5. Hardness measurements

The hardness values of the tested materials were obtained before performing the erosion tests to study the effect on the wear response and the results shown in Figure 16. Before the erosion test, the micro-hardness values for the coating layer are much harder than the Al substrate. The coating layer hardness increases as the distance from the substrate increases until near the middle of the coating (100 μm). After that, the hardness decreases as the distance approaches the resin side of the coating. Also, the hardness measurements of the eroded regions of the coatings were compared with the un-eroded surfaces after the test and it is obvious that the hardness for the eroded surface is higher for all materials. The increase of the material's hardness after the erosion tests is expected since there is a work hardening undergoing on the surface due to the effect of the impact particles loading.

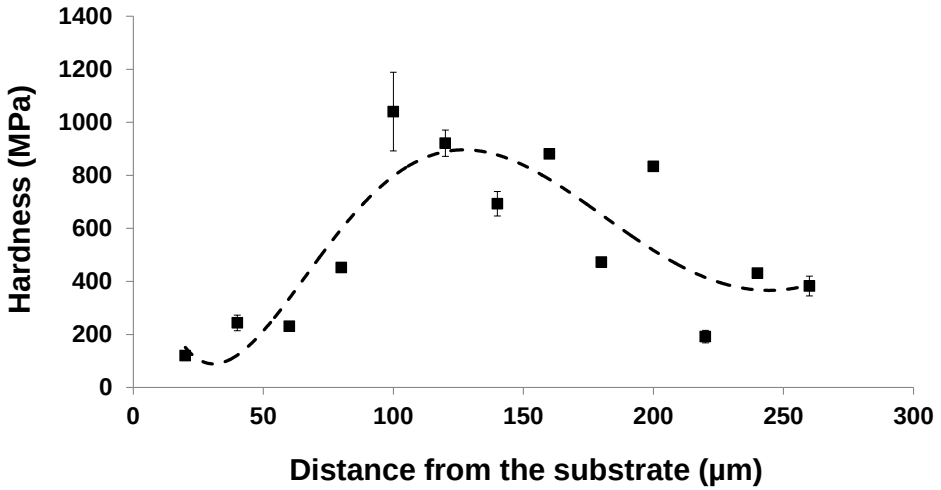


Figure 16: Distribution of hardness values across PSC coating (Knoop Test, Load = 25 g).

### 3.6. Talysurf Tests

Figure 17 shows the surface textures of the tested samples after ten hours tests for different sand loadings (200 and 1000 mg/l) and different temperatures (20 ©C and 70 ©C). The 3-D profile of the sample was captured to show the affected zone of the surface and its type in terms of the deformation type such as plastic deformation, cutting chip, etc. As clearly shown in Figure 17 (b) and (d), the sand lading had a greater effect on the erosion rate more than the temperature. Also, the materials' volume loss due to impact particles were calculated to be compared with the weight loss measurements.

Regarding the coating density, it has been approximately determined by coating porosity which can be studied from optical or SEM images. Limited studies have measured the coating density. For example, Curran and Clyne [34] has suggested that the PEO density is summation of phase densities in the coating ($\alpha$-$Al_2O_3$, $\gamma$-$Al_2O_3$ and amorphous alumina) which theoretically equals to 3.69±0.25 g/cm$^3$. However, this will depend on the phases available in the coating and also affected by the thickness of the coating.

The density of the removed materials after erosion can be calculated by dividing the measured weight loss over the volume loss data as shown in Figure 18. There are two reasons that can explain the anomalous densities of the removed materials against their theoretical values (2.7 g/cm$^3$ for the aluminium substrate and approximately 3.69±0.25 g/cm$^2$ for the coatings). Firstly, it should be

noted the removed materials sometimes consists of the coating part and the substrate which have different densities. Secondly, the porosity has main effect of the density of the material as the pore space in the eroded material will increase due to the impact of solid particles [35]. As a result, the volume of the material will decrease and consequently increase its density as shown in Figure 18. Thirdly, it is assumed that the measured volume loss from the Talysurf analysis is less than the actual volume loss of the material. The volume of the removed top layer could not be determined using this technique. Therefore, most of the measured densities of the materials under different test conditions are higher than their actual density values.

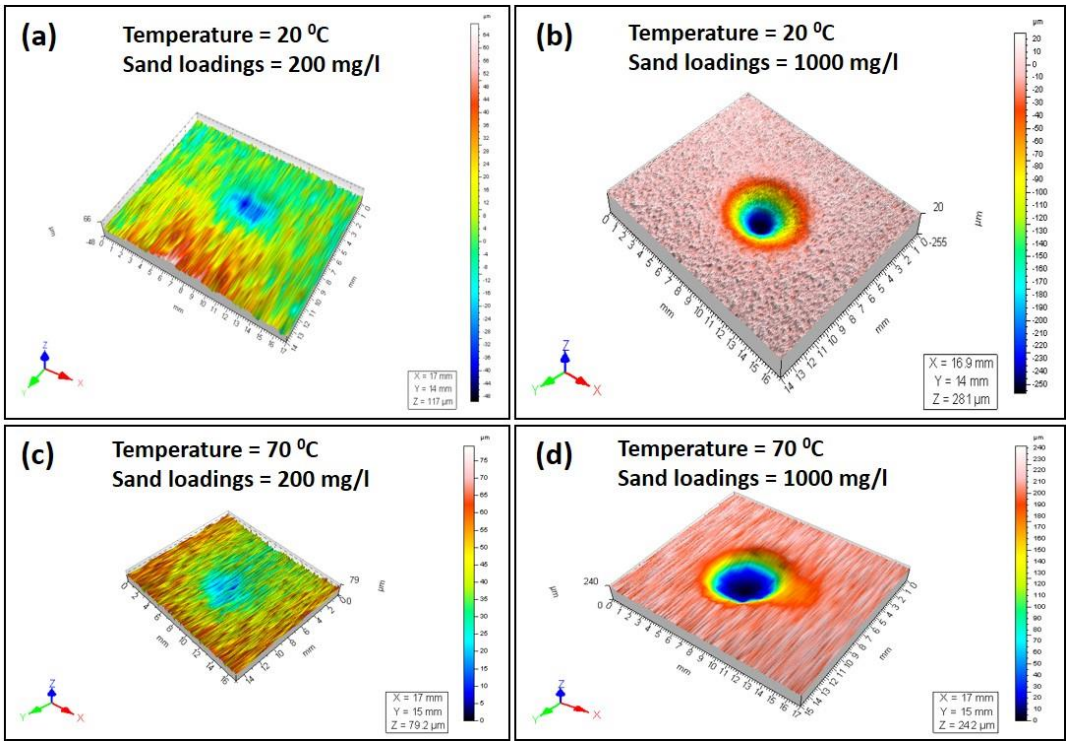


Figure 17. 3-D Profilometry tests for PSC coating after erosion test of 10 hours.

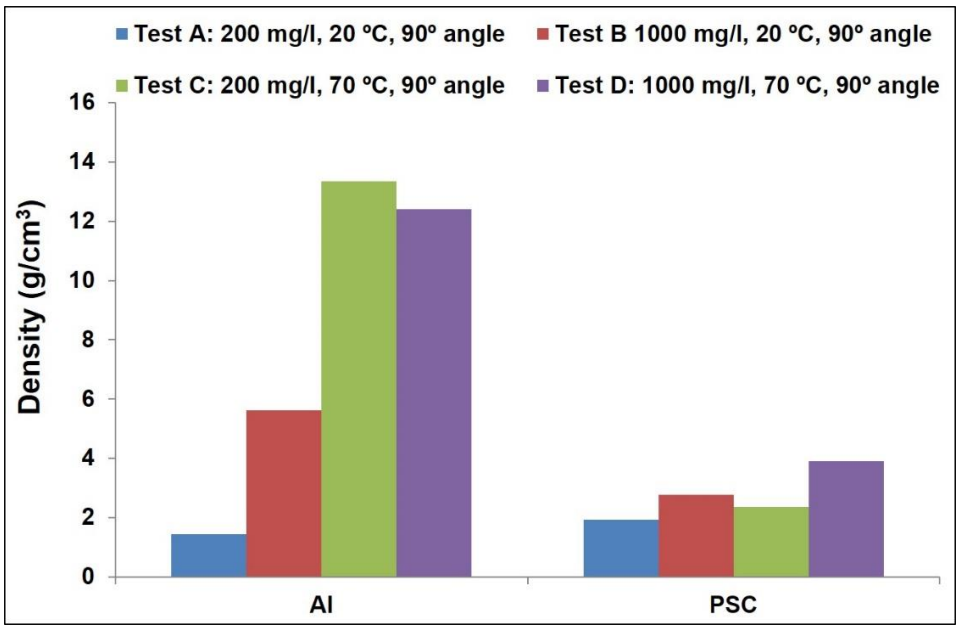


Figure 18. Density of the removed materials after 10 hours erosion tests.

## 4. Conclusions

In this work, aluminum 6082-T6 was cladded with the plasma sprayed $Al_2O_3$ coating process. The macro/microstructures of the coated specimens were investigated using optical and scanning electron microscopes. An inductively coupled plasma test was performed after immersion in 3.5% NaCl solution for 24 hours (for temperatures of 20°C and 80°C). The erosion tests were performed with water carrying sand particles at different sand loadings (200mg/l and 1000mg/l) and two temperatures (20°C and 70°C). After erosion experiments, the weight loss measurements were recorded followed by profilometry and microscopic analysis. The micro-hardness of the coated layer and the substrate were measured. The results of this study led to the following conclusions:

- The coated layer consisted of three different layers of about 350 µm thick, starting with a loose layer in the interface region followed by laminar intermediate layer and finally top porous layer. The hard-anodizing coating has a higher roughness value compared with the Al substrate.
- The coated layer was consisted of approximately 86% Gamma alumina ($\gamma$-$Al_2O_3$) and 14% alumina phases ($\alpha$-$Al_2O_3$).
- There was no stability of the current in the coating during the polarization test. The coating shows lower corrosion current density under static anodic polarization tests.

- During the erosion test, a consistent increase in the wear losses has been observed with increasing both time and sand loading.
- Compared to the aluminium substrate, the PSC coating exhibits poor erosion resistance at low temperature, while the erosion rates observed for the PSC coating in elevated temperature are much lower than aluminium substrate.
- The coating showed higher hardness values compared to aluminum substrate.

## 5. References

[17] H. Mraied, W. Cai, and A. A. Sagüés, "Corrosion resistance of Al and Al–Mn thin films," Thin Solid Film. Vol. 615, pp. 391-401, 2016. doi.org/10.1016/j.tsf.2016.07.057.

[18] R.W. Revie, and H.H. Uhlig, "Corrosion and Corrosion Control: An Introduction to Corrosion Science and Engineering, fourth edition, Wiley-Interscience, 2008, [Online]. Available: http://onlinelibrary.wiley.com/book/10.1002/9780470277270. [Accessed: July. 15, 2018].

[19] A.W. Momber, T. Marquardt, "Protective coatings for offshore wind energy devices (OWEAs)," J. Coat. Technol. Res. Vol. 15, pp. 13–40, 2018. https://doi.org/10.1007/s11998-017-9979-5.

[20] A. López, R. Bayón, F. Pagano, A. Igartua, A. Arredondo, J.L. Arana, and J.J. González, "Tribocorrosion behaviour of mooring high strength low alloy steels in synthetic seawater," Wear Vol. 338-339, pp. 1-10, 2015. https://doi.org/10.1016/j.wear.2015.05.004.

[21] G. A. El-Mahdy, and K.B. Kim, "AC impedance study on the atmospheric corrosion of aluminium under periodic wet-dry conditions," Electrochim. Acta. Vol. 49(12), pp. 1937-1948, 2004. doi:10.1016/j.electacta.2003.12.022

[22] M. Navaser, and M. Atapour, "Effect of Friction Stir Processing on Pitting Corrosion and Intergranular Attack of 7075 Aluminum Alloy.," J. Mater. Sci. Technol. Vol. 33 (2), pp. 155-165, 2017. doi: 10.1016/j.jmst.2016.07.008

[23] M. de Bonfils-Lahovary, L. Laffont, and C. Blanc, "Characterization of intergranular corrosion defects in a 2024 T351 aluminium alloy." Corros. Sci. vol.119, pp. 60-67, 2017. doi:10.1016/j.corsci.2017.02.020

[24] C.N. Panagopoulos, and E.P. Georgiou, "Corrosion and wear of 6082 aluminium alloy," Tribol. Int. vol. 42(6), pp. 886-889, 2009. doi.org/10.1016/j.triboint.2008.12.002

[25] A. López-Ortega, R. Bayón, J.L. Arana, A. Arredondo and A. Igartua, "Influence of temperature on the corrosion and tribocorrosion behaviour of high-strength low alloy steels used in offshore applications," Tribol. Int. vol. 121, pp. 341–352, 2018. https://doi.org/10.1016/j.triboint.2018.01.049.

[26] H. Li, Z. Ke, J. Li, L. Xue, and Y. Yan, "An effective low-temperature strategy for sealing plasma sprayed Al2O3-based coatings," Journal of the European Ceramic Society 38, pp.1871–1877, 2018. http://dx.doi.org/10.1016/j.jeurceramsoc.2017.09.051

[27] P. Wang and J. P. Li, "The formation mechanism of the composited ceramic coating with thermal protection feature on an Al-12Si piston alloy via a modified PEO process," J. Alloys Compd. Vol. 682, pp. 357–365, 2016.

[28] J. Yamabe, S. Matsuoka and Y. Murakami, "Surface coating with a high resistance to hydrogen entry under high-pressure hydrogen-gas environment," Int. J. Hydrogen Energy vol. 38, pp. 10141–10154, 2013.

[29] R. Kromer, S. Costil, C. Verdy, S. Gojon, and H. Liao, "Laser surface texturing to enhance adhesion bond strength of spray coatings – Cold spraying, wire-arc spraying, and atmospheric plasma spraying," Surf. Coat. Technol. Vol. 352, pp. 642–653, 2018. doi.org/10.1016/j.surfcoat.2017.05.007

[30] K. Yang, J. Rong, C.G. Liu, H.Y. Zhao, S.Y. Tao and C.X. Ding, "Study on erosion–wear behavior and mechanism of plasma-sprayed alumina-based coatings by a novel slurry injection method," Tribo. Int. vol. 93, pp.29–35, 2016.

[31] H. Singh, and B. S. Sidhu, "Use of plasma spray technology for deposition of high temperature oxidation/corrosion resistant coatings-a review," Mater. Corros. VOL. 58(2), PP. 92-102, 2007. DOI: 10.1002/maco.200603985

[32] S. Kumar, A. Kumar, D. Kumar, and L. Jain, "Thermally sprayed alumina and ceria-doped-alumina coatings on AZ91 Mg alloy," Surf. Coat. Tech. vol. 332, pp. 533-541, 2007. doi:10.1016/j.surfcoat.2017.05.09

[33] D. Thirumalaikumarasamy, K. Shanmugam, and V. Balasubramanian, "Corrosion performances of atmospheric plasma sprayed alumina coatings on AZ31B magnesium alloy under immersion environment," J. Asian Ceram. Soc. vol. 2(4), pp. 403-415, 2014. doi.org/10.1016/j.jascer.2014.08.006

[34] T. Q. Nakamura, G. Berndt, and C. Christopher "Effects of Pores on Mechanical Properties of Plasma-Sprayed Ceramic Coatings," Journal of the American Ceramic Society, vol 83(3), pp. 578-584, 2000.

[35] S.H. Yao, "Comparative study on wear performance of traditional and nanostructured Al2O3-13 wt.% TiO2 air plasma spray coatings," Ceramics- Silikáty vol. 59, pp. 59–63, 2015.

[36] S. Beauvais, and V. Guipont, "Process-microstructure-property relationships in controlled atmosphere plasma spraying of ceramics," Surf. Coat. Technol., vol. 183(2-3), pp. 204-11, 2004.

[37] R. G. Song, and C. Wang,"Microstructure and properties of Al2O3/TiO2 nanostructured ceramic composite coatings prepared by plasma spraying," J. Alloys Compound., vol. 544(0), pp. 13-18, 2012.

[38] O. E.Abdel-Salam, M. A. Shoeib, and H. Ashour Elkilany, "Characterization of the hard anodizing layers formed on 2014-T3 Al alloy, in sulphuric acid electrolyte containing sodium lignin sulphonate," Egyptian Journal of Petroleum, Article in Press, https://doi.org/10.1016/j.ejpe.2017.07.014

[39] W. Tabakoff, and V. Shanov. "Erosion rate testing at high temp. for turbo machinery use." Surf. Coat. Technol. Vol. 76 – 77, Part I, pp. 75 –80, 1995.

[40] Q. Wang, C. S. Ramachandran, G. M. Smith, S. Sampath, "Sliding wear behavior of air plasma sprayed Al2O3 coatings sealed with aluminum phosphate," Tribo. Int., vol. 116, pp. 431–439, 2017. http://dx.doi.org/10.1016/j.triboint.2017.08.002

[41] M. Daroonparvar, M. Yajid, N. Yusof, and H. Rad, "Fabrication and properties of triplex NiCrAlY/nano Al2O313%TiO2/nano TiO2 coatings on a magnesium alloy by atmospheric plasma spraying method," J. Alloys Compd. Vo. 645, pp. 450–466, 2015.

[42] E. Colonetti, E. Kammer, and A. Junior, "Chemically-bonded phosphate ceramics obtained from aluminum anodizing waste for use as coatings," Ceram. Int. vol. 40, pp. 14431–14438, 2014.

[43] C. Sujaya, H. Shashikala, G. Umesh and A. C. Hegde, (2012). "Hardness and electrochemical behaviour of ceramic coatings on Inconel." J. Electrochem. Sci. Eng. Vol. 2(1), pp. 19-31. 2012.

[44] M. Thammachart, “Corrosion Mechanisms of Chemically Bonded Composite Sol-Gel (CB-CSG) Al2O3 Coated Systems in Aqueous Environment,” Edinburgh, Heriot-Watt University, PhD: 297, 2005.

[45] H. Lee, J. K. Singh, and M. A. Ismail, “An effective and novel pore sealing agent to enhance the corrosion resistance performance of Al coating in artificial ocean water, Sci Rep. 2017; 7: 41935. Published online 2017 Feb 3. doi: 10.1038/srep41935

[46] Y. Shi, B. Yang and P. K. Liaw, “Corrosion-Resistant High-Entropy Alloys: A Review,” Metals, vol. 7, pp. 43-61, 2017. doi:10.3390/met7020043.

[47] A. A. Olajire, “Corrosion inhibition of offshore oil and gas production facilities using organic compound inhibitors - A review,” J. Mol. Liq. Vol. 248, pp. 775-808, 2017. doi:10.1016/j.molliq.2017.10.097

[48] G. A. Zhang, and L. Y. Xu, "Investigation of erosion-corrosion of 3003 aluminium alloy in ethylene glycol-water solution by impingement jet system," Corrosion Science, vol. 51(2), pp. 283-290, 2009.

[49] A. Costa, and G. Macedonio, “Viscous heating in fluids with temperature-dependent viscosity: implications form agma flows,” Nonlinear Processes in Geophysics, vol. (20), pp. 101-111, 2003.

[50] J.A. Curran, and T.W. Clyne, “Thermo-physical properties of plasma electrolytic oxide coatings on aluminium,” Surf. Coat. Technol. Vol.199(2-3), pp. 168-176, 2005. doi:10.1016/j.surfcoat.2004.09.037.

[51] A. Nandi, and I. Lufman, "Erosion Related Changes to Physicochemical Properties of Ultisols Distributed on Calcareous Sedimentary Rocks." Journal of Sustainable Development, vol. 5(8), pp.52-68, 2012.

# An FTIR Spectroscopic Study of a Novel Kaolinite-NPK Mixture

**Ehab Alshamaileh Mohammad R. Al-Rbaihat**

Department of Chemistry, The University of Jordan, Jordan

ehab@ju.edu.jo, Moh.irbeihat83@hotmail.com

**Bety Al-Saqarat**

Department of Geology, The University of Jordan, Jordan

B.saqarat@ju.edu.jo

**Beatrix Udvardi**

Geological and Geophysical Institute of Hungary, Stefánia U. 14, Hungary

Udvardi.beatrix@mfgi.hu

**Aiman Eid Al-Rawajfeh**

Department of Chemical Engineering, Tafila Technical University, Tafila, Jordan

aimanr@yahoo.com

**Abstract:** In the present study, Fourier Transform Infrared (FTIR) spectroscopic characterization of a novel mixture of kaolinite-NPK is described. Kaolinite is an environmentally friendly substance that exhibits good structural properties when used as a carrier of chemical fertilizers. Mixtures of kaolinite and NPK fertilizer were prepared by mechanochemical ball milling with three different mass ratios (Kaolinite : NPK = 1:3, 1:1 and 3:1). The milling parameters were varied in order to obtain the best mixture consistency. These include milling time (60, 120, and 180 min) and rotational speed (200, 400 and 700 rpm). The studied NPK fertilizers are urea ($CON_2H_4$), ammonium phosphate ($(NH_4)_2HPO_4$), and potassium dihydrogen phosphate ($KH_2PO_4$). The result indicated that a mass ratio of kaolinite: NPK of 3:1 and a milling duration of 120 min at a rotational speed of 600 rpm represent the most suitable conditions to synthesize a novel kaolinite-NPK mixture. A possible application of this mixture is the use as a slow-release fertilizer.

**Keywords:** NPK fertilizers, Kaolinite, Mechanochemical, Milling, FTIR.

# دراسة التوصيف الطيفي بتقنية فورير لتحويل الأشعة تحت الحمراء لمزيج جديد من الكاولين والسماد الكيميائي المكون من النيتروجين والفسفور والبوتاسيوم

**الملخص**: تم في هذه الدراسة دراسة التوصيف الطيفي بتقنية فورير لتحويل الأشعة تحت الحمراء (ف.ت.أ.ت.ح) لمزيج جديد من الكاولين والسماد الكيميائي المكون من النيتروجين والفسفور والبوتاسيوم (ن.ف.ب). تعتبر مادة الكاولين مادة صديقة للبيئة وكذلك فإنها تُظهر خصائص هيكلية جيدة عند استخدامها كحامل للأسمدة الكيماوية. في هذا البحث، تم تحضير خلطات من الكاولين والأسمدة النيتروجينية بواسطة الطحن الميكانوكيميائي بالكرات لثلاثة نسب ذات كتلة مختلفة (نسبة الكاولين إلى سماد (ن.ف.ب) = 1:3 و1:1 و3:1). وقد استخدمت عوامل طحن مختلفة للحصول على أفضل تناسق للخليط واشتملت على ما يلي: وقت الطحن (60 و120 و180 دقيقة) وسرعة الدوران (200 و400 و700 دورة في الدقيقة). كانت أسمدة (ن.ف.ب) المستخدمة في الدراسة هي اليوريا ($CON2H4$) وفوسفات الأمونيوم ($(NH4)2HPO4$) وفوسفات البوتاسيوم ثنائي الهيدروجين ($KH2PO4$). أوضحت نتائج الدراسة أن نسبة الكتلة 3:1 من الكاولين إلى سماد (ن.ف.ب) خلال مدة الطحن 120 دقيقة بسرعة دوران 600 دورة في الدقيقة تمثل الظروف الأكثر ملاءمة لتجميع خليط جديد من الكاولين والسماد والذي يمكن استخدامه كسماد بطيء التحلل في التربة.

## 1. Introduction

With the population growth and rapid urbanization, controlled and efficient fertilization is essential in modern agriculture in order to improve crop yields. However, conventional and commonly used chemical fertilizers tend to dissolve in the soil at a much faster rate than plants intake. The resulting imbalanced fertilization leads to a rapid release of nutrients from the soil into groundwater. In addition to the loss of valuable fertilizers, the leak is found to cause many environmental concerns [1]. For a sustainable agriculture, slow-release fertilizers (SRF) in which nutrients are slowly released and hence synchronized with the growth rate and physiological need of plants is one of the alternative solutions to fertilization issues.

NPK fertilizers comprise primarily of the three primary nutrients required for healthy plant growth (Nitrogen, Phosphorus and Potassium). The Jordanian agriculture industry relies heavily on the use of DAP (di ammonium phosphate) and other NPK fertilizers to meet the demanding food supply and ensure healthy crops.

Most studies on SRF have pointed out that the required amount of nutrients is significantly reduced compared to conventional fertilizers [2-9]. Some researchers recommended the use of SRF in order to reduce $N_2O$ emissions from the agricultural fields in an attempt to reduce its role in climate change [10-11].

Several types of SRF have been prepared based on a wide range of physical and chemical methods including dispersion of fertilizer in a matrix. Among them, Noh et al. described a mineral-based SRF that exhibits charge and crystal structure frameworks protecting nutrients from rapid degradation and hence contributing to the long-term fertility in the soil [12]. To this type of fertilizer, various inorganic clays including kaolinite are used as a nutrient-carrier through a mechanochemical processes, like milling, to produce highly reactive amorphous materials that are capable of reacting with soluble fertilizers such as urea [13-17].

A mechanochemical process is a simple, environment friendly, low-cost milling and mixing technology that does not require chemical solvents. The effectiveness of the mechanochemical synthesis is highly dependent on the mass ratio of carrier to fertilizer and on the milling parameters such as milling speed and milling duration. However, these practical variables have not been extensively tested with SRFs and, to our knowledge, no previous work has been carried out on kaolinite-NPK mixtures as an SRF. In this study, we use the abundantly available and low-cost Jordanian kaolinite as a carrier for our SRF.

In the present study, we use Fourier transform infrared (FTIR) spectroscopy as a reliable technique to study the degree of bonding of NPK chemical fertilizers (NPK) within a mixture of kaolinite-NPK. Since all bonds within molecules vibrate at temperatures above absolute zero as bending and/or stretching, FTIR spectroscopy is a precise overview of the presence of different molecular functional groups and hence molecules. Therefore, different peaks account for different molecules. This is proven by FTIR in the case of dehydroxylation of kaolinite (loss of OH groups).

The mass ratios and milling parameters were varied and tested by FTIR in order to establish the optimal conditions for the mechanochemical synthesis of a novel kaolinite-NPK fertilizer mixture.

The studied chemical fertilizers are urea ($CON_2H_4$), ammonium phosphate ($(NH_4)_2HPO_4$), and potassium dihydrogen phosphate ($KH_2PO_4$). The results showed very similar results proving the validity of our technique to synthesize a novel formulation of a slow-release fertilizer (SRF).

## 2. Experimental

Kaolinite ($Al_2(Si_2O_5)(OH)_4$), as a hydrated aluminum silicate, was obtained from Wadi Araba in Jordan [18-19]. The NPK fertilizers used in this study were of chemical grade reagents: urea ($CON_2H_4$), diammonium phosphate ($(NH_4)_2HPO_4$), potassium sulfate ($K_2SO_4$) from Merck and potassium phosphate ($KH_2PO_4$) from Panreac PRS.

The samples were prepared by co-grinding the kaolinite and one of the different fertilizers at dry conditions using a planetary ball mill (Pulverisette-7, Fritsch, Germany), which had two mill pots (45 $cm^3$ inner volume each) made of zirconia ($ZrO_2$) with 7 zirconium-balls of 15 mm diameter. Five grams of the starting materials was put into the vial with the balls, and milled under ambient atmosphere.

Three sets of experiments were designed and performed to observe the effect of different mixing ratios of kaolinite to fertilizer, milling speed and duration on the infrared spectra of synthesized mixtures (Table 1).

To avoid any chemical complications resulting from the excessive heating during the milling processes, the operation was programmed to include a 5-minute rest time for every 10 minutes of continuous milling.

Table 1. Mixture ratios and milling parameters used in the different experiments.

| Set | (kaolinite: NPK) mass ratio | Milling speed (rpm) | Milling time (min) |
|---|---|---|---|
| Exp. 1 | 1:3, 1:1, 3:1 | 600 | 120 |
| Exp. 2 | 3:1 | 200, 400, 700 | 120 |
| Exp. 3 | 3:1 | 600 | 60, 120, 180 |

Infrared spectra of all synthesized samples were recorded using a Fourier transform infrared spectrometer (FTIR, Thermo Nicolet Nexus 870). The samples were diluted in powdered solid KBr (Spectroscopic grade, Sigma-Aldrich). KBr background spectrum was obtained before

running each sample. IR spectra were collected in the mid-IR region (500-4000 $cm^{-1}$) with a spectral resolution of 4 $cm^{-1}$.

## 3. Results and Discussion

The IR spectra of kaolinite, NPK and their mixtures are discussed in the first part. The second part presents the results for the effect of varying mass ratios of kaolinite to NPK. The third and fourth parts deal with results of the milling parameters: milling speed and milling duration, respectively.

### 3.1 IR Characteristics of Kaolinite, NPK And Their Mixtures:

Figure 1 displays the infrared spectra of kaolinite-NPK mixtures. Two types of the hydroxyl functional group can be assigned for kaolinite. The stretching of the inner surface hydroxyl groups occurs at 3688 and 3655 $cm^{-1}$, whereas the band at 3619 $cm^{-1}$ belongs to the inner hydroxyl group that lie within lamellae in plane common to both tetrahedral and octahedral sheets. The intensity and location of the inner surface hydroxyl groups usually change upon intercalation, whereas the band at 3619 $cm^{-1}$ remains unaffected by intercalation [20-21].

In an ordered kaolinite, four distinct IR bands can be assigned, whereas poorly ordered kaolinite, displays only three bands [22], as can be seen in this study. The Si-O stretching region comprises of stretching bands at 1113, 1000-1003 and 1025 $cm^{-1}$, and the Si-O bending vibrations at 790, 751 and 688 $cm^{-1}$. The Al-OH bending vibration at 912 $cm^{-1}$ assigned to the inner hydroxyls.

The most intense bands of urea ($CON_2H_4$) are the N-H stretchings at 3427, 3339 and 3254 $cm^{-1}$, the N-H bending vibration at 1591 $cm^{-1}$ and the C-N stretching at 1459 $cm^{-1}$ (Figure 1 A). The band at 1677 $cm^{-1}$ is assigned as the amide vibration, while the band at 1147 $cm^{-1}$ is attributed to $NH_2$ vibration [23-24].

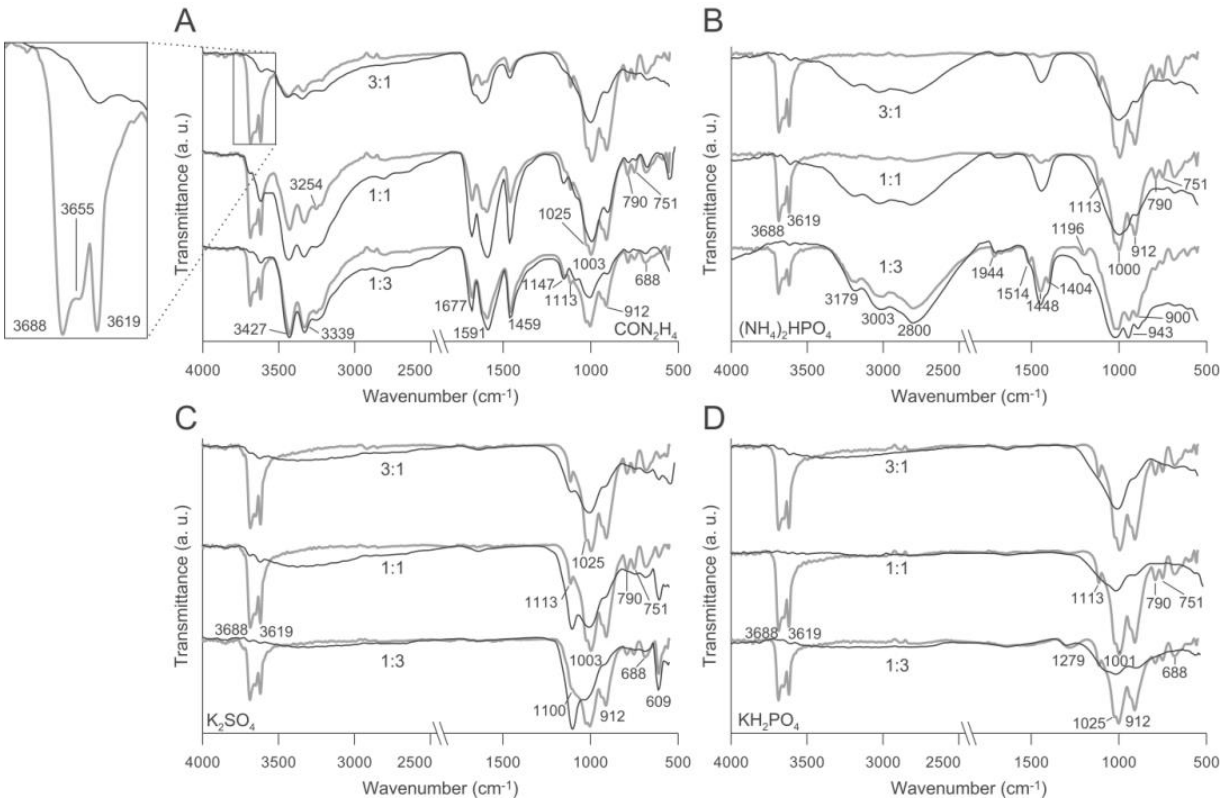


Figure 1. Infrared spectra of original kaolinite-NPK mixtures (light-faced) and the milled samples (bold-faced) are shown. A: urea, B: DAP, C: $K_2SO_4$, D: $KH_2PO_4$. The characteristic peaks and the ratios of the kaolinite-NPK (1:3, 1:1, 3:1) are also displayed.

From the IR spectra of DAP ($(NH_4)_2HPO_4$), the presence of vibration due to $NH_4$ groups is noticed. Two strong bands are observed at 3179 and 3003 $cm^{-1}$ and a mid-band upto 1448 $cm^{-1}$ (Figure 1 B). The band at 2800 $cm^{-1}$ corresponds to the O-H stretching vibration. The O-H bending vibration can be seen at 1196 $cm^{-1}$. The peak of the $PO_4^{3-}$ group is found at 943 $cm^{-1}$ [25].

The bands of $K_2SO_4$ appearing at ~1100 and 609 $cm^{-1}$ are assigned to stretching and bending of the sulfate ($SO_4$) groups [26] as seen in (Figure 1 C).

Figure 1 D shows the spectral profile of $KH_2PO_4$ with three smooth band peaks at 1279 $cm^{-1}$, at 1077 $cm^{-1}$ (PO4 vibrations) and at 877 $cm^{-1}$ ($(PO_2(H_2)$ vibration) with increasing transmittance values from the highest to the smallest wavenumber regions [27].

### 3.2 The Effect of Kaolinite-NPK Fertilizer Mass Ratio:

For this part of the experiment, the milling speed and duration were kept constant. Three different mass ratios were studied (kaolinite : NPK = 1:3, 1:1 and 3:1). IR spectra were collected for the mixtures. The spectra show that characteristic peaks of the individual studied fertilizers occur in each mixture.

The peak intensity of kaolinite appear to be reduced after 120 minutes of grinding at 600 rpm (Figure 1 A-D). It is noticed that the intensity of the kaolinite bands at 3688 and 3655 $cm^{-1}$ are less than that at 3619 $cm^{-1}$. Bands of the inner surface hydroxyl groups completely disappear in the mixtures with different ratio of kaolinite and one of the following fertilizers: urea, DAP or $KH_2PO_4$.

Previous studies reported that the intensity loss of IR peaks is attributed to the degradation of the hydroxyl groups in kaolinite during the mechanochemical process [13-14, 16]. Therefore, the mechanochemical amorphization of kaolinite in our study accounts for the intensity loss of the inner surface hydroxy groups at 3688, 3655 $cm^{-1}$ and the deformation mode at 912 $cm^{-1}$.

The inner surface hydroxyl band at 3688 $cm^{-1}$, however, appears in each $K_2SO_4$ containing kaolinite, and its intensity in the samples with 50-75% kaolinite is higher than in the sample with the 1:3 mass ratio. This suggests that kaolinite partially remained in the crystalline phase.

On the other hand, the major intensity of the $K_2SO_4$ at ~1100 $cm^{-1}$ and 609 $cm^{-1}$ decreases with the increased amount of kaolinite in the sample (Figure 1 C). When kaolinite content was increased to 75%, the vibration intensities of the fertilizers slightly decrease both in urea and $K_2SO_4$ (Figure 1 A-C). This indicates that milling results in amorphization of both the kaolinite and the fertilizer [13-15, 17].

At low kaolinite content (25%), Solihin et al. (2011) showed that the amorphous structure is not large enough to incorporate ions from fertilizers, but when the amount of kaolinite is increased, more ions are incorporated into the amorphous structure of kaolin. The ratio of carrier and fertilizer, therefore, is a critical parameter for maintaining high nutrients in a SRF, the less silica added, the better [16].

### 3.3 The Effect of Milling Speed:

In this part of the study, the mass ratio of (kaolinite : NPK) is fixed at 3:1 and the milling duration of 120 min is used for all the experiments. The milling rotational speed (milling speed) was varied (200, 400 and 700 rpm). All the spectra of kaolinite-NPK mixtures show that the stretching vibration of the hydroxyl groups at 3688 and 3619 $cm^{-1}$ decrease as the milling speed is increased and disappeared from the samples prepared at 700 rpm.

The disappearance of the hydroxyl bending vibration at 912 $cm^{-1}$ and the decrease in the intensity of the Si-O band at ~1000 $cm^{-1}$ also indicate the mechanochemical decomposition of kaolinite at 700 rpm. Band intensities of the studied fertilizers also decrease with increasing the milling speed. These results indicate that higher milling speeds are required to reduce the starting materials to the amorphous phase and allow the incorporation of the nutrients into the kaolinite structure.

According to a previous study [14], a milling process at a minimum of 400 rpm rotational speed is required to incorporate nutrients such as $KH_2PO_4$ and $NH_4H_2PO_4$ into the amorphous kaolinite structure.

The major contributing factor to the release of nutrients can be the rate of rotation [17]. Our study highlights, that a rotational speed between 400 and 700 rpm would be optimum for the mechanochemical synthesis of kaolinite-NPK fertilizers.

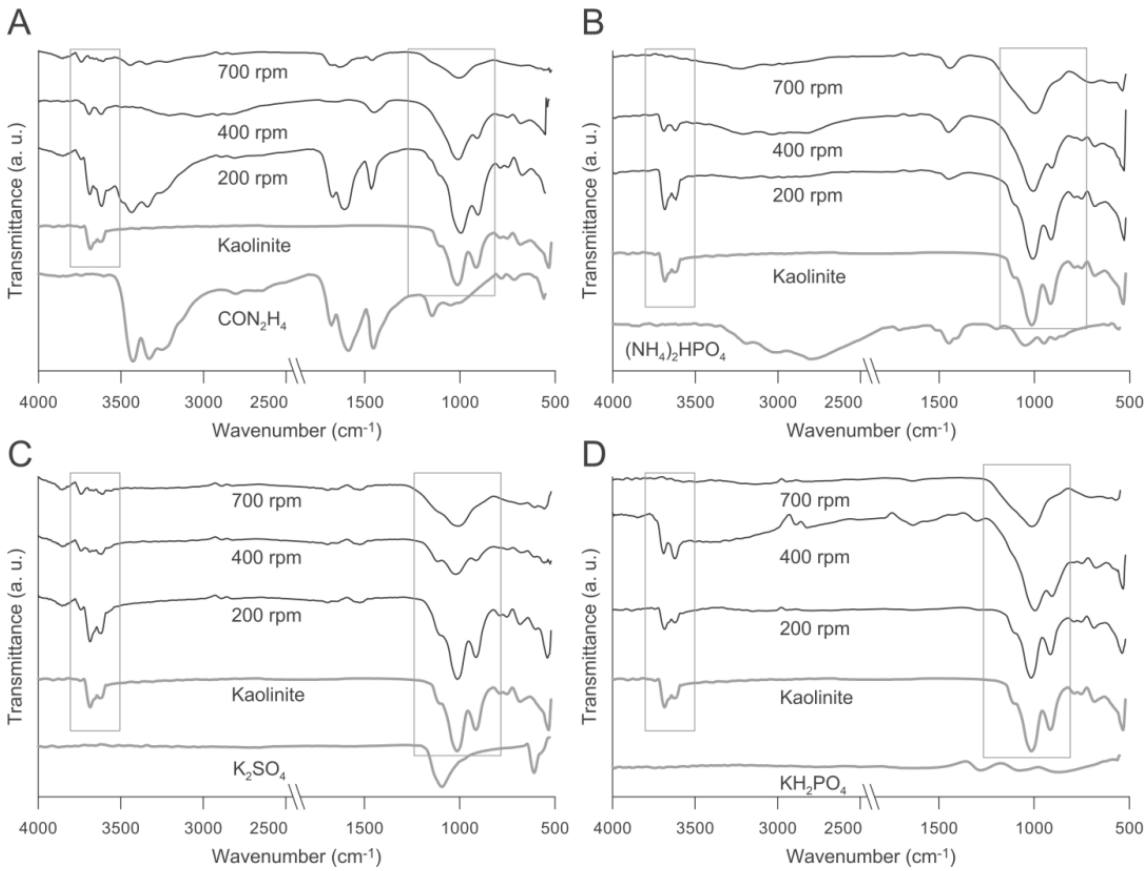


Figure 2. Infrared spectra of kaolinite-NPK mixtures (3:1 ratio) milled at different speeds for 120 min. A: urea, B: DAP, C: $K_2SO_4$, D: $KH_2PO_4$.

### 3.4 The Effect Of Milling Duration:

Figure 3 A-D displays the FTIR spectra of kaolinite-NPK (3:1) mixtures milled at 600 rpm for 60, 120 and 180 min.

The intensities of characteristic bands at 3688, 3655 and 3619 $cm^{-1}$ markedly decrease in each spectrum of the mechanochemically treated samples, indicating the scission of O-H bonds. The weak bands at 3688 and 3619 $cm^{-1}$ indicate that after 60 minutes of milling, some OH groups remained bonded between the adjacent kaolinite layers, evidencing that some residual kaolinite phase still existed. However, on prolonging the milling time up to 120 min, these bands completely disappeared, implying completion of the mechanochemical dehydroxylation process and amorphization.

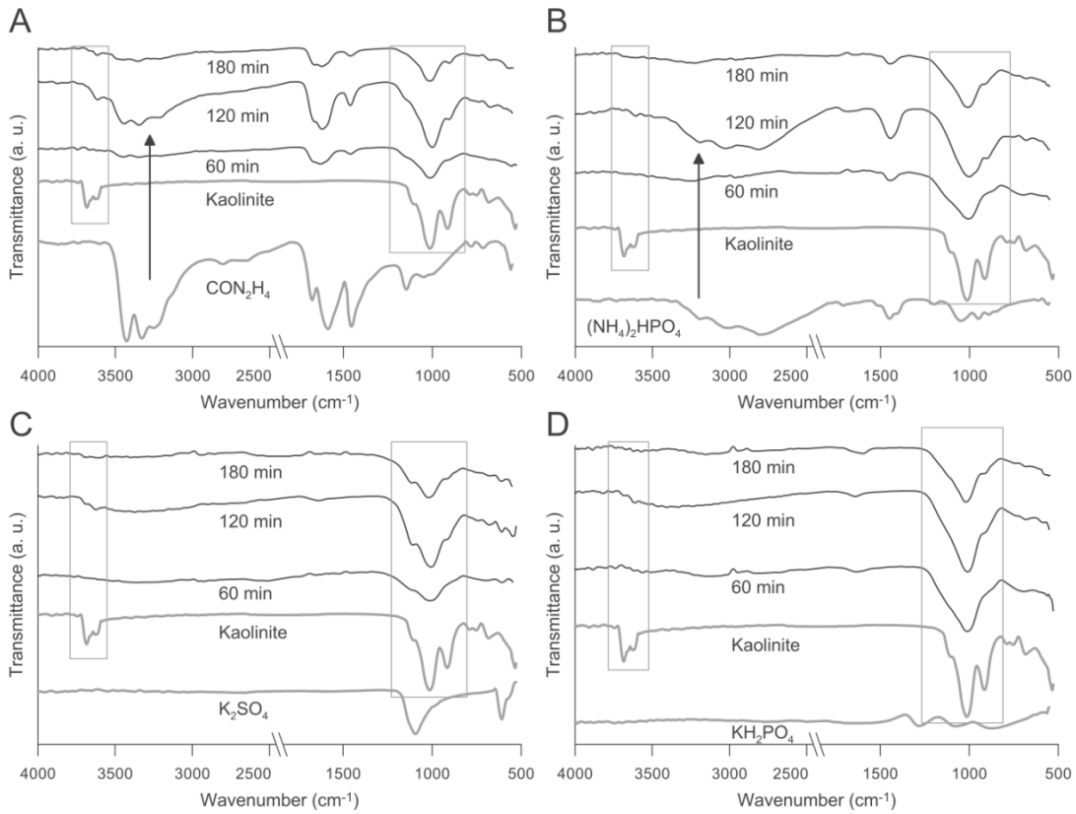


Figure 3. Infrared spectra of kaolinite-NPK mixtures (3:1 ratio) milled at speed 600 rpm for different duration. A: urea, B: DAP, C: $K_2SO_4$, D: $KH_2PO_4$.

By comparing intensity of the Si-O band at ~1000 $cm^{-1}$ in the spectra of mixtures after 60 min and 120 min milling, it can be seen that prolonged milling duration strengthens the intensity (Figure 3 A-D). The Si-O stretching vibration increases when the duration of milling reaches 120 min. After 180 min of milling, however, the infrared intensities both of the Si-O network and the fertilizers decrease. Therefore, the incorporation of nutrients into the short order of the Si-O network is complete after 120 min of co-grinding.

Similar results were found in a previous study on urea intercalated kaolinite [24]. Sahnoun et al. (2015) also demonstrated on kaolin-potassium phosphate mixtures that two hours of milling is sufficient to achieve the distortion of the crystalline network of kaolinite in order to insert additive [28].

## 4. Conclusions

This study investigated the influence of the milling operating parameters (speed and duration) and different mass ratios of kaolinite-NPK mixtures as a slow-release fertilizer using infrared spectroscopy. The selected fertilizers were the most used in agriculture, namely: $CON_2H_4$, $(NH_4)_2HPO_4$, $K_2SO_4$, and $KH_2PO_4$. Incorporation of fertilizers into the structure of kaolinite was successfully carried out by dry co-grinding of kaolinite-NPK mixtures in a planetary ball mill. Infrared spectroscopic results confirmed the mechanochemical dehydroxylation of kaolinite (loss of OH groups), and show that amount of kaolinite, milling speed and milling duration play an important role in the mechanochemical treatment of kaolinite-NPK mixtures. It is recommended to synthesize a slow-release fertilizer with the kaolinite as a carrier to the fertilizer at a mass ratio of 3:1 (kaolinite : fertilizer). The optimum time of milling was found to be 120 minutes at 600 rpm milling speed. Mechanochemical treatment offers an easy access to develop slow-release fertilizers.

**Acknowledgment**

The authors acknowledge the financial support from the Deanship of Scientific Research at the University of Jordan (Project No. 2007, Year: 2016).

## 5. References

[1] F. Khan, S. Khan, S. Fahad, S. Faisal, S. Hussain, S. Ali, A. Ali, Effect of different levels of nitrogen and phosphorus on the phenology and yield of maize varieties. Am J Plant Sci. 5 (2014) 2582–2590.

[2] D. Qiao, H. Liu, L. Yu, X. Bao, G.P. Simon, E. Petinakis, L. Chen, Preparation and characterization of slow-release fertilizer encapsulated by starch-based superabsorbent polymer. Carbohydrate polymers 147 (2016) 146-154.

[3] A. Shaviv, Advance in controlled-release fertilizers. Adv Agron. 71 (2001) 1–49.

[4] RD. Hangs, JD. Knight, KCJ. Van-Rees, Nitrogen accumulation by conifer seedlings and competitor species from nitrogen-labeled controlled-release fertilizer. Soil Sci Soc Am J. 67 (2003) 300–308.

[5] D. Chen, HC. Suter, A. Islam, R. Edis, JR. Freney, Prospects of improving efficiency of fertilizer nitrogen in Australian agriculture: a review of enhanced efficiency fertilizers. Aust J Soil Res. 46 (2008) 289–301.

[6] S. Sato, KT. Morgan, Nitrogen recovery and transformation from a surface or subsurface application of controlled-release fertilizer on a sandy soil. J Plant Nutr. 31 (2008) 2214–2231.

[7] CR. Hyatt, RT. Venterea, CJ. Rosen, M. Mcnearney, ML. Wilson, MS. Dolan, Polymer-coated urea maintains potato yields and reduces nitrous oxide emissions in a Minnesota loamy sand. Soil Sci Soc Am J. 74 (2010) 419–428.

[8] ML. Wilson, CJ. Rosen, JF. Moncrief. Effects of polymer-coated urea on nitrate leaching and nitrogen uptake by potato. J Environ Qual. 39 (2010) 492–499.

[9] R. Borges, V. Prevot, C. Forano, F. Wypych. Design and Kinetic Study of Sustainable Potential Slow-Release Fertilizer Obtained by Mechanochemical Activation of Clay Minerals and Potassium Monohydrogen Phosphate. Ind Eng Chem Res. 56 (2017) 708–716.

[10] WG. Cheng, S. Sudo, H. Tsuruta, K. Yagi, A. Hartley. Temporal and spatial variations in N2O emissions from a Chinese cabbage field as a function of type of fertilizer and application. Nutr Cycling Agroecosyst. 74 (2006) 147–155.

[11] J. Jingyan, H. Zhenghua, S. Wenjuan, H. Yao. Nitrous oxide emissions from Chinese cropland fertilized with a range of slow release nitrogen compounds. Agric, Ecosyst Environ. 135 (2010) 216–225.

[12] YD. Noh, S. Komarneni, M. Park, Mineral-Based Slow Release Fertilizers: A Review. Korean J Soil Sci Fert. 48 (2015) 1–7.

[13] Solihin, QW. Zhang, W. Tongamp, F. Saito. Mechanochemical route for synthesizing KMgPO4 and NH4MgPO4 for application as slow-release fertilizers. Ind Eng Chem Res. 49 (2010) 2213–2216.

[14] Solihin, QW. Zhang, W. Tongamp, F. Saito. Mechanochemical synthesis of kaoline–KH2PO4 and kaoline–NH4H2PO4 complexes for application as slow release fertilizer. Powder Technol. 212 (2011) 354–358.

[15] F. Mahdavi, SBA. Rashid, MK. Zusop. Intercalation of urea into kaolinite for preparation of controlled release fertilizer. Chem Ind Chem Eng Q. 20 (2014) 207−213.

[16] W. Yuan, Solihin, QW. Zhang, J. Kano, F. Saito. Mechanochemical formation of K–Si–Ca–O compound as a slow-release fertilizer. Powder Technol. 260 (2014) 22–26.

[17] R. Borges, SF. Brunatto, AA. Leita, GS. De Carvalho, F. Wypych. Solid-state mechanochemical activation of clay minerals and soluble phosphate mixtures to obtain slow-release fertilizers. Clay Miner. 50 (2015) 153–162.

[18] J. Ala'li. Evaluation and Beneficiation of Silica Sand and Kaolinitic Sandstone in South of Jordan. Ph.D. Thesis, Nottingham University, U.K (2001).

[19] M. Barjous. Pre-processing Investigation of the Kaolin minerals of the Disi Sandstone Formation from the Wadi Araba-Jordan. In: The Second Jordanian Mining Conference. Jordan (1997).

[20] L. Vaculíková, E. Plevová, S. Vallová, I Koutnik. Characterization and differentiation of kaolinites from selected Czech deposits using infrared spectroscopy and differential thermal analysis. Acta Geodyn. Geomater. 8 (2011) 59-67.

[21] JE. Gardolinski, LCM. Carrera, MP. Cantao, FJ. Wypych, Layered polymer-kaolinite nanocomposites. J Mater Sci. 35 (2000) 3113–3119.

[22] J. Madejová, I. Kraus, D. Tunega, E. Šamajová. Fourier transform infrared spectroscopic characterization of kaolin group minerals from the main Slovak deposits. Geol Carp Clays 1 (1997) 3–10.

[23] MM. Mortland, Urea complexes with montmorillonite: an infrared absorption study. Clay Miner. 6 (1966) 143–156.

[24] É. Makó, J. Kristóf, E. Horváth, V. Vágvölgyi. Mechanochemical intercalation of low reactivity kaolinite. Appl Clay Sci. 83–84 (2013) 24–31.

[25] M. Gargouri, C. Chtara, P. Sharrock, A, Nzihou, H. El Feki. Purification of an industrial fertilizer (diammonium phosphate) using design of experiments. Int J Mater Eng. 4(6) (2014) 185–191.

[26] A. Periasamy, S. Muruganand, M. Palaniswamy. Vibrational studies of Na2SO4, K2SO4, NaHSO4 and KHSO4 crystals. Rasayan J Chem. 2 (2009) 981–986.

[27] NS. Meshram, NM. Gahane, RN. Kakde, BA. Shingade, KG. Rewatkar. Rapid growth of potassium dihydrogen phosphate (KDP) single crystal by rotating crystal method. Int J Knowl Eng. 3 (2012) 175–177.

[28] RD. Sahnoun, K. Chaari, J. Bouaziz. Mechanochemical Synthesis of Kaolin-Potassium Phosphates Complexes for Application as Slow-Release Fertilizer. Mediterr J Chem. 4 (2015) 156–162.

# Investigation of Interfacial Magnetic Properties of Co/$C_{60}$ Hybrid Interface

**Mohd Taukeer Khan  Abdullah Almohammedi**

Department of Physics, Faculty of Science, Islamic University of Madinah, Saudi Arabia

Corresponding author,

khanmtk@iu.edu.sa, arda@iu.edu.sa

**Abstract:** The present work demonstrates a detail investigation of interfacial magnetic properties of cobalt (Co)/fullerene ($C_{60}$) based ferromagnetic/organic (F/O) hybrid interface. The interfacial structural properties of Co, $C_{60}$ and hybrid interface have been analyzed by X-ray reflectivity (XRR), both computationally and experimentally. The results shows that the grown films have smooth surface (roughness < 0.5 nm) and intermixing at the interface between organic and inorganic layers is less than 1 nm. The spin injection at the hybrid interface was studied by recording the magnetic hysteresis loop at 100 K and photoemission of hybrid interface under the applied bias and magnetic field. It has been observed that due to interfacial spin polarized electron transfer at F/O interface, the photoemission of $C_{60}$ reduces, coercivity of the cobalt increases which give about 18% spin polarization of the carriers injected in $C_{60}$. Finally, the performance of $C_{60}$ based tunnel junction have been studied in the device configuration viz. Co/$Al_2O_3$/$C_{60}$/Py. The magneto resistance (MR) of up to 10 % is obtained for device which having $C_{60}$ layer of thickness 10 nm.

**Keywords**: Organic spintronics, fullerene, X-ray Reflectivity, magnetoresistance, spin-polarized current

# دراسة الخصائص المغناطيسية البينية للواجهة الهجينة Co / C60

**الملخص**: يوضح العمل الحالي دراسة تفصيلية للخصائص المغناطيسية البينية للكوبالت / (Co) الفوليرين (C60) استنادًا إلى الواجهة الهجينة المغناطيسية / العضوية (ف/ و). لقد تم تحليل الخصائص الهيكلية البينية لCo ، C60 والواجهة الهجينة بواسطة انعكاس الأشعة السينية (خ ر ر) ، على حد سواء حسابيا وتجريبيا. أظهرت النتائج أن الأفلام المزروعة لها سطح أملس (خشونة <0.5 نانومتر) والتداخل في الواجهة بين الطبقات العضوية وغير العضوية أقل من 1 نانومتر. تمت دراسة الحقن الدوراني في الواجهة الهجينة عن طريق تسجيل حلقة التباطؤ المغناطيسي عند 100 كلفن والإنتاج الضوئي للواجهة الهجينة تحت الجهد المطبق والمجال المغناطيسي. لقد لوحظ أنه نظرًا لنقل الإلكترونات المستقطبة فإن الدوران بين الأقطاب في واجهة ف/ و، يقلل التصوير الضوئي لـ C60 وتزيد قهرية الكوبالت مما يؤدي إلى استقطاب حوالي 18٪ من الناقلات التي تم حقنها في C60. أخيرًا، تمت دراسة أداء تقاطع النفق القائم على C60 في اختبار تكوين الجهاز Co/Al2O3/C60/Py. يتم الحصول على مقاومة مغناطيسية (م ر) تصل إلى 10 ٪ للجهاز الذي يحتوي على طبقة C60 بسمك 10 نانومتر.

## 1. Introduction

Since past few decades, organic semiconductors (OSCs) have shown auspicious performance in the area of light emitting diodes [1-3], field effect transistors [4-6], photovoltaics [7-11] and spintronics [12-15] due to their small intrinsic size, easy processing, possibility of the fabrication of device in large area, tenability of energy levels according to device requirement. The main attractive aspects of OSCs for spintronics applications is long spin diffusion length (up to 110 nm) due to weak spin-orbit coupling in these materials [16].

Fullerene is very interesting OSCs because it possess numerous properties which make it ideal for organic spintronics devices. Due to absence of hydrogen atom in fullerene, the hyperfine interactions between electron and nuclear spins is very weak and hence reduce the spin-flipping events. Z. G. Yu theoretically predicted that more than 430 nm spin dependent transport length can be achieved for $C_{60}$ at room temperature [17]. It has high electron mobility compare to other OSCs of the order of 1-10 $cm^2/V.s$ [18]. The Fermi levels of commonly used ferromagnetic metals

in spintronic device are quite well matched with lowest unoccupied molecular orbital (LUMO) level of C60 which give rise to a large spin injection from ferromagnetic electrode to $C_{60}$.

Moreover, $C_{60}$ molecules are very robust and sustain the top ferromagnetic electrode without being damage its surface and hence it can be efficiently sandwiched between ferromagnetic electrodes in spin devices [19].

Although there are many advantages for introducing $C_{60}$ molecules in vertical spin device, but there are still many unresolved questions about the working mechanisms of these devices are yet to known. Previously a lot of work has been done to understand the charge transport in organic semiconductors [20-23]. But they have not considered the effect of magnetic field and spin coupling in their studies. The device performance of the OSVs depends upon the reliability of spin injection at F/O interface, spin transport in organic semiconductor and preserving the spin polarized signal. Therefore, the structural and magnetic properties of F/O interface as well as spin transport are the most vital parameters. Henceforth, understanding the structural, magnetic, spin injection and spin polarization and various other spin transport parameters for a spin valve is very vital. The present project aims to study the structural, magnetic properties of $Co/C_{60}$ interface and understand the spin injection, spin transport $Co/C_{60}$/Py based spin valve.

## 2. Experimental

The spin valve were fabricated on $Si/SiO_2$ substrates by using a computerised sputtering system which contains dc magnetron and thermal evaporator in the same chamber. Prior to deposition of thin films, the $Si/SiO_2$ substrate have been carefully cleaned with propanol then followed by acetone and dried under oxygen flow. The dried substrates were placed inside a sputtering system operated under ultra high vacuum conditions. As a first step tantalum (Ta) seed layer deposited. On top of Ta layer, Co as a bottom ferromagnetic electrode was deposited and then an Al layer was sputtered. To get $Al_2O_3$ of desired thickness Al layer was oxidised for optimised time. Fullerene layer was thermally evaporated on top of Co. Finally Permalloy (Py) as a top electrode was deposited. The devices were protected from environmental by depositing a capping layer on top of Py electrode.

## 3. Results and discussions

### 3.1 X-ray Reflectivity (XRR)

X-ray reflectivity give the information about the roughness, thicknesses, as well as interfacial mixture of a multilayer film [17]. Figure 1 (a-c) shows the XRR spectra of $C_{60}$, Co, and [$C_{60}$/Co]×5 multilayers, respectively. The Kiessig fringes in XRR spectra shown in Fig. 6(a) and (b) extend up to an angle of 3 degrees which confirm the high quality of grown Co and $C_{60}$ surface. The detailed analysis of XRR curves has been performed by using GenX software. GenX is a scientific program to refine XRR using the differential evolution algorithm. The fit to the data for $C_{60}$ shown in Fig. 1 (a) by red line provides the film thickness ~ 26.7 nm, surface roughness $\sigma_{rms}$ = 5.3 Å and density of layer of 1.6 g/cm$^3$. The fit to the data for Co shown in fig. 1 (b) by red line give film thickness ~32.4 nm, surface roughness $\sigma_{rms}$ = 3.4 Å and density of Co of 8.8 g/cm$^3$.

The XRR spectra of [$C_{60}$/Co]×5 multilayers is shown in Figure 1 (c). The spectra shows well-defined Kiessig fringes extend up to an angle of 1.5 degrees, intensity decreases uniformly with increase of angle, and well resolved Bragg peak indicates that the bilayer film thickness is uniform through the entire surface. The fit result was obtained by dividing the multilayer in to three layer: $C_{60}$/Co bilayer/($C_{60}$/Co)×3 multilayer/$C_{60}$/Co bilayer. The fit to the XRR data of the $C_{60}$/Co multilayers is shown by red line in Fig. 1 (c). From the fitted curves, we obtain the density for the $C_{60}$ layer of 1.63 g/cm$^3$, and layer thickness of 19.5 nm. The layer thickness of Co in multilayer is found to be 7.8 nm with a density of 8.75 g/cm$^3$. These results are in good agreement with the expected values. The fitted interface parameters for Co, $C_{60}$ and [$C_{60}$/Co]×5 multilayer are presented in Table I.

**Table 1** Fitting parameters obtained for Co, $C_{60}$ and [$C_{60}$/Co]×5.

| **Layer** | | **Thickness t (Å)** | **Density** d **(g/cc)** | **Surface Roughness $\sigma_{rms}$ (Å)** | **Interface Roughness (Å)** |
|---|---|---|---|---|---|
| **$C_{60}$** | | 265 | 1.60 | 5.3 | --- |
| **Co** | | 324 | 8.8 | 3.4 | ---- |
| **[$C_{60}$/Co]x5** | **Co** | 78 | 8.75 | 5-8 | 1-2 |
| | **$C_{60}$** | 195 | 1.63 | 8-12 | 5-9 |

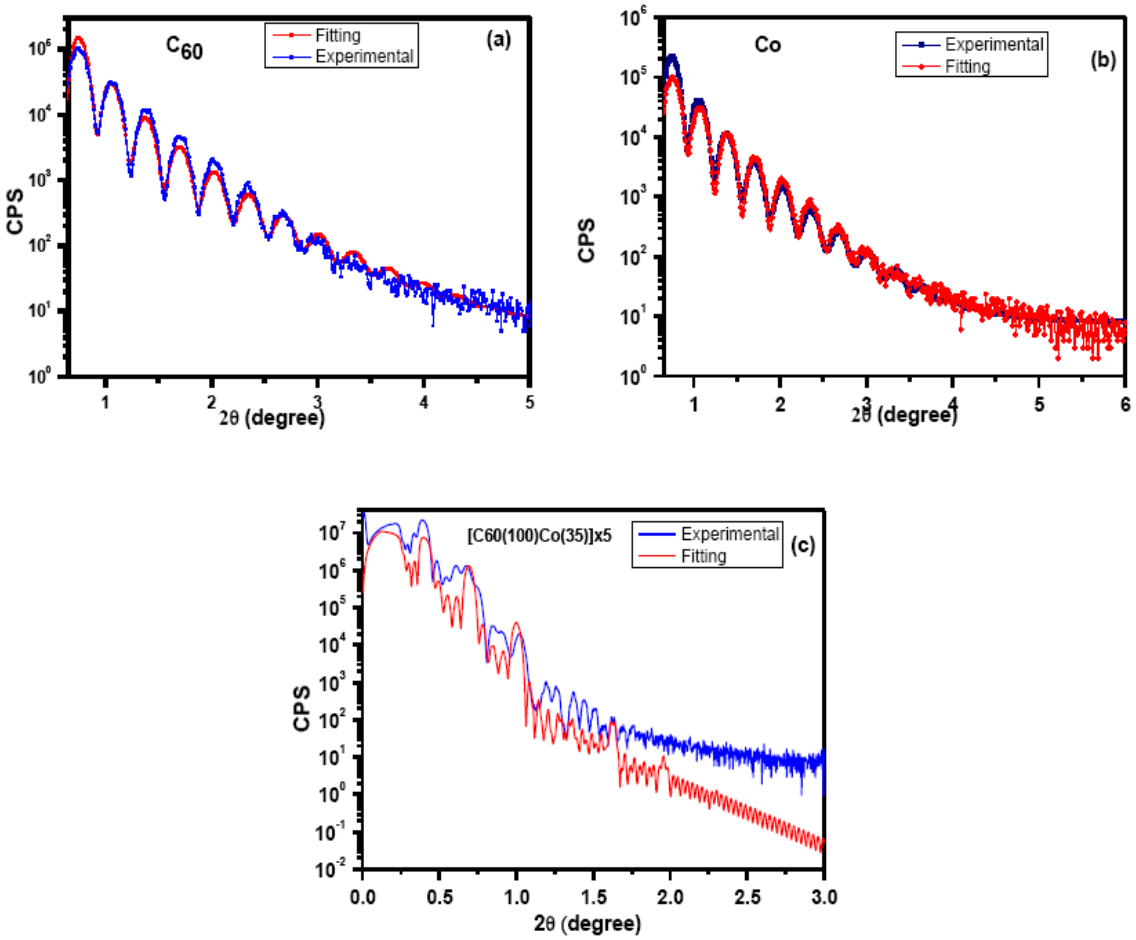


Figure 1: X-ray reflectivity of (a) a $C_{60}$ single layer, (b) a Co single layer, and (c) a [$C_{60}$/Co]x5 multilayers. Blue lines show the experimental data and red line the fitted line.

### 3.2 Magnetic Properties of Co/$C_{60}$ Bilayer

After discussing the structural properties of Co and $C_{60}$ layers, our next attention is to analyse the magnetic properties of Co layer when it deposited either above or below the $C_{60}$ layer. For the fabrication of an optimal device, the Co layer must preserve its magnetic properties when it is deposited in a vertical spin device. To understand the effect of molecular layer on the effect of magnetic properties of Co, we have measured the hysteresis loop of different $C_{60}$/Co and extracted the coercive field ($H_c$) and the saturation magnetization ($M_S$).

Figure 2 shows magnetic hysteresis loops, for a 8 nm Co thin film with on top of $C_{60}$ layer with different thickness at 100 K. It has been observed from the Fig. 2 that the $M_S$ value of Co/$C_{60}$ bilayers decreased by 270±10 emu/cc while $H_C$ value increased relative to cobalt layer alone. The

decrease in the value of $M_S$ can be understood as the transfer of spin polarised electron from the Co to the organic. The ferromagnetic properties of Co is due to spin-polarized electron population on 3d band [18]. LUMO of $C_{60}$ molecule is about 4.5 eV and when it comes in contact with the 3d (up) orbital of Co they make a hybridization induced states. When a 20 nm thick $C_{60}$ layer was deposited on top 8 nm Co film, the magnetization of Co layer was reduce about 15%. Moreover increase in $H_C$ value may be result of the local pinning sites caused by surface defects between the organic and the ferromagnet layer [19-21].

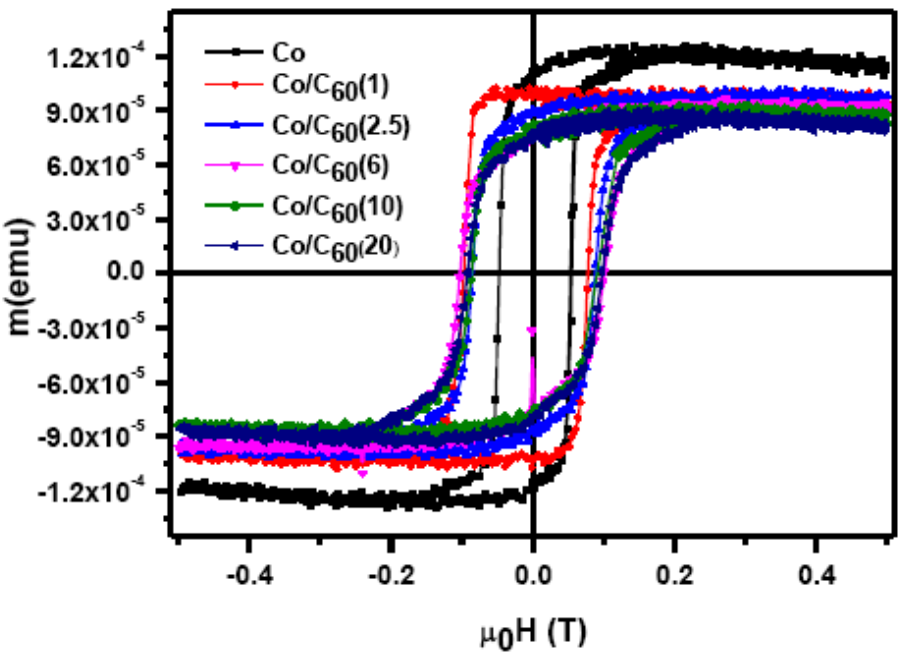


Figure 2: Hysteresis loop of 8 nm Co thin film with on top of C60 layer with different thickness at 100 K. Thickness of C60 are given in bracket.

### 3.3 Spin-Polarization in $C_{60}$

To further understand the spin injection from ferromagnet to organic, we have studied the photoemission of $C_{60}$ layer sandwiched between the magnetic electrodes Co and Py. For this purpose we fabricated devices in the configuration viz Ta(5)Co(8)/$AlO_x$(1.5)/$C_{60}$(20)/Py(20) (device A) and Ta(5)Co(8)/$C_{60}$(20)/Py(20) (device B).Under the influence of applied bias charge carrier recombination decreases which results in decrease of photoemission. This is known as negative luminescence (NPL) [22]. Photoemission of device A and device B are shown in Fig. 3(a) and (b), respectively. When a small current of 1μA/cm$^2$ and small field of 5 mT was applied across device B, the intensity of photoemission $_0$ remains nearly constant in device B as shown in Figure

3(b). However, in device A when a small current of 1μA/cm$^2$ was applied, there is drop in the photoluminescence (PL) [Fig. 3(a)]. Furthermore, in device A when a small current of 1μA/cm$^2$ as well as small field of 5 mT was applied, there is an 18% drop in the PL [Fig. 3(a)].

.

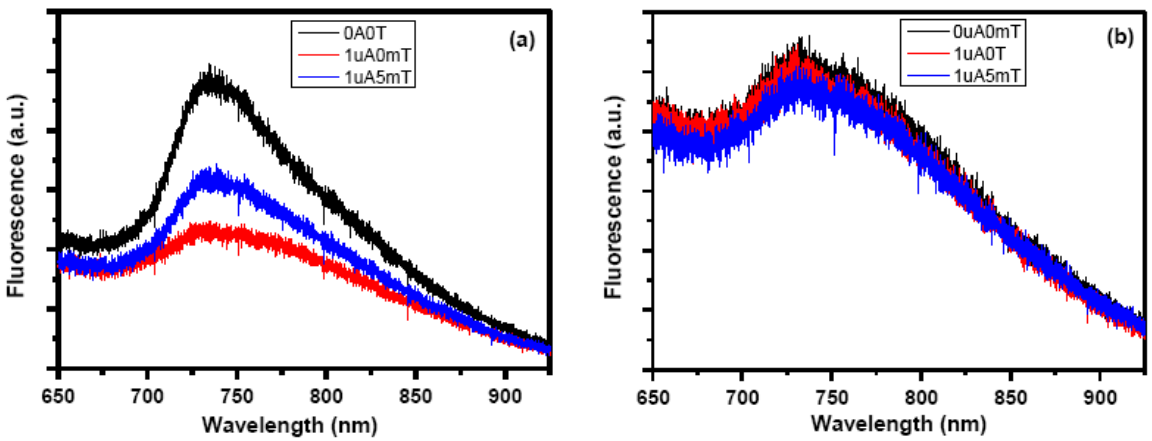


Figure 3: Field dependent florescence spectra of (a)Ta(5)Co(8)/C60(20)/Py(20) (b) Ta(5)Co(8)/AlOx(1.5)/C60(20)/Py(20) excited at wavelength of 532 nm.

This NPL can be understood by the Figure 4. Photoluminescence in organic materials is a spin-dependent phenomenon. As both electron and hole have spins, then according to quantum mechanics, four different combinations of spin are possible: one antiparallel combination of spins, giving a singlet, which emit fluorescence light. On the other hand there are three different combinations of parallel spins are possible, giving a triplet state, and its excitation transferred into heat. When we apply small current in device A, spin polarized electrons are injected by magnetic electrode Co into C60 layer as a results reduction of singlets and increase of triplet electron Figure 4 (b) and hence drops in PL. With the introduction of magnetic field along with current no of singlet electrons further go down and hence PL Figure 4(c). On the other hand when we have $Al_2O_3$ barrier between FM/Organic interfaces PL is almost constant due to the fact that barrier layer stops the injection of spin polarized electrons from FM electrode to organic layer and hence no of singlet and triplet electrons remains same and hence no NPL.

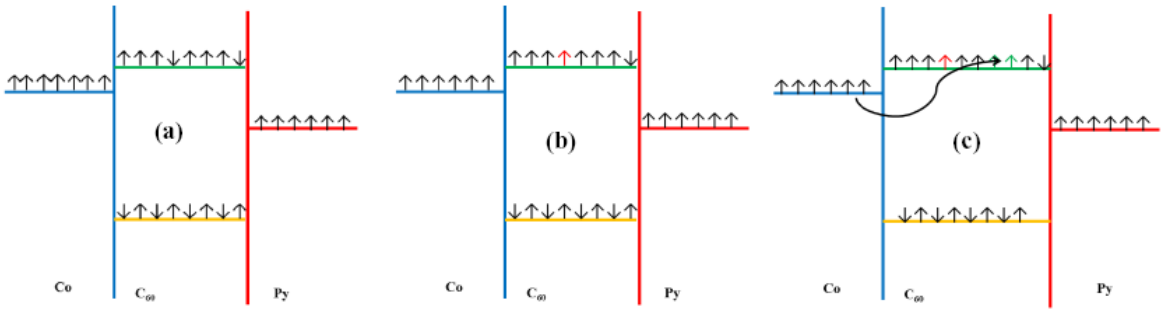


Figure 4: Mechanism of spin transport from Co to C60 in device structure Ta(5)Co(8)/C60(20)/Py(20) (a) without bias and without field (b) 1 μA current and no field (c) 1 μA current and 5 mT field.

### 3.4 Magnetic Tunnel Junction

We have studied the magneto-transport properties of Co/$Al_2O_3$/$C_{60}$/permalloy (Py) multilayer junctions with different thickness of $C_{60}$ layer. $C_{60}$ thickness were taken 0 nm, 10 nm and 20 nm and the corresponding devices are namely, device A, device B and device C, respectively. Due to dissimilar magnetic properties, Py and Co are most common choice of magnetic electrodes for magnetic tunnel junction devices. Py is a nickel–iron magnetic alloy (80% Ni and 20% Fe), with small coercivity (5 Oe for 15-nm thick layer) and high permeability ($\mu=10^5 - 10^6$) while Co is a hard magnetic material with coercivity of about 22 Oe (8 nm thick Co layer) and relatively small permeability. Dissimilar coercivity of Py and Co offers a "window" for changing the orientation of the magnetizations of these two layers, which is a main feature required to achieve the tunnel magneto resistance (TMR).

The fabricated spin valve devices have a cross-bar geometry. These devices were fabricated on Si/$SiO_2$ (300 nm) substrates by depositing all required layers by sequential deposition inside a sputtering chamber under a high vacuum of ~ $10^{-7}$ $10^{-8}$ torr. The final devices configuration of fabricated devices is: Tantalum (Ta, 7.5 nm)/Co(8 nm)/$Al_2O_3$(1.5nm)/$C_{60}$(0 or 10 or 20 nm)/Py(15 nm)/Ta(7.5 nm). The Ta layer was deposited on top of Py to prevent the oxidation of it from ambient environment. The Co electrode is used as a spin injector, the spin polarized current is propagated along the organic $C_{60}$ layer and finally detected by the Py electrode. The room temperature resistance as a function of applied magnetic field, at 1 V of fabricated devices (device A, B and C) are displayed in Figure 5 (a-c). The resistance of materials depend on the orientation of net magnetic moment of the electrodes. When both electrodes have parallel configuration of net magnetic moment, the device show low resistance called $R_P$. On the other hand, when magnetic

electrodes have antiparallel configuration of net magnetic moment, the device shows high resistance $R_{AP}$. The relative change of resistance is called tunnel magnetoresistance (TMR), is given by equation [23, 24]:

$$TMR = \frac{R_{AP} - R_P}{R_P} \quad (1)$$

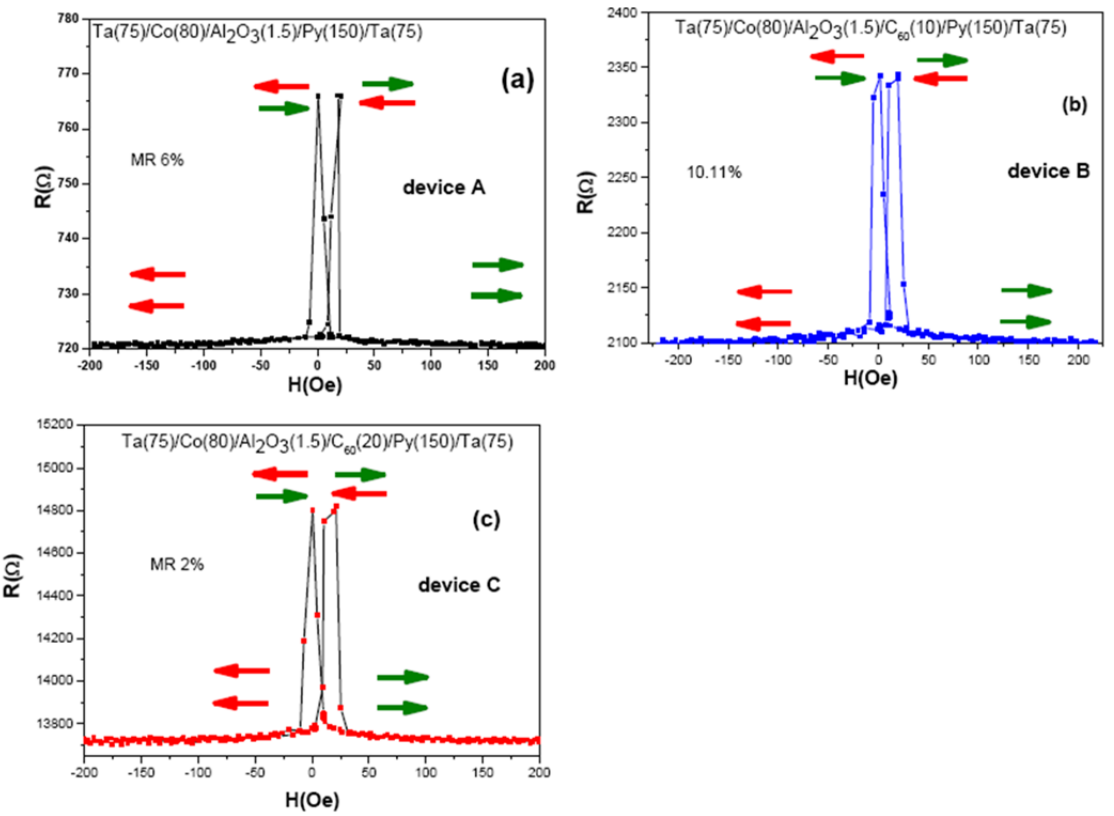


Figure 5 MR measured in (a) device A, (b) device B, and (c) device C.

Figure (5) shows a clear and reproducible TMR, which correspond to the coercive fields of the ferromagnetic layers. For applied field higher than 50 Oe, the two electrodes have parallel configuration of magnetic moments, therefore devices shows low resistance. When magnetic field changes from positive to negative, the magnetic moments of Py switch its orientation due to low coercivity, resulting an antiparallel configuration of magnetic moment and hence devices shows high resistance. When field increases more than 50 Oe in opposite direction, the two electrodes again returns to parallel configuration and device resistance decreases. The reference device A without $C_{60}$ shows MR value about 6%. The maximum MR value of 10.1% is obtained for device B. for device C with the thicker $C_{60}$ (20 nm) layer the MR value goes down 2%. Resistance of

device also depends upon the thickness of organic layer. With the increase of the thickness the resistance of device increases due to the fact of lower mobility in organics.

## 4. Conclusions

In conclusion, we have successfully analysed the interfacial properties in Co/$C_{60}$ hybrid interface by using multiple structural, photoemission and spin-dependent measurement technique. It has been observed that grown Co, $C_{60}$ and [Co/$C_{60}$]×5 multilayers have low surface roughness and the intermixing between organic/inorganic interface is less than 1 nm. The coercivity of the cobalt increases when $C_{60}$ is deposited on top of Co which confirm the formation of spin induced hybridization state at F/O interface. With the application of magnetic field and electric current in $C_{60}$ based magnetic device it was found that the photoluminescence of $C_{60}$ was drops by 18%. Finally, the device based on 20 nm thick $C_{60}$ shows >10% of room temperature MR.

## 5. References

[1] J. Burroughes, C. Jones, and R.H. Friend, New semiconductor device physics in polymer diodes and transistors, Nature, 335 (1988) 137.

[2] J. H. Burroughes, D. D. C. Bradley, A. R. Brown, R. N. Marks, K. Mackay, R. H. Friend, P. L. Burn, and A. B. Holmes. Light-emitting diodes based on conjugated polymers, Nature, 347 (1990) 539.

[3] A. Zampetti A. Minotto F. Cacialli, Near-Infrared (NIR) Organic Light-Emitting Diodes (OLEDs): Challenges and Opportunities, Adv. Funct. Sci., January (2019) https://doi.org/10.1002/adfm.201807623

[4] M. Ahles, A. Hepp, R. Schmechel, and H. V. Seggern, Light emission from a polymer transistor, Appl. Phys. Lett., 84 (2004)428.

[5] L.-L. Chua, J. Zaumseil, J.-F. Chang, E. C.-W. Ou, P. K.-H. Ho, H. Sirringhaus, and R. H. Friend, General observation of n-type field-effect behaviour in organic semiconductors, Nature, 434 (2005)194.

[6] Y. Kim, S. Chung, K. Cho, D. Harkin, W.-Taek Hwang, D. Yoo Jae-Keun, Kim W. Lee Y. Song, H. Ahn, Y. Hong, H. Sirringhaus, K. Kang, T. Lee, Enhanced Charge Injection Properties of Organic Field-Effect Transistor by Molecular Implantation Doping, Adv. Mater., 31, (2019) 1806697.

[7] 17.3% is organic solar cell efficiency record, https://www.electronicsweekly.com/news/research-news/17-3-organic-solar-cell-efficiency-record-2018-08/ .

[8] J. Hou, O. Inganäs, R. H. Friend & F. Gao, Organic solar cells based on non-fullerene acceptors, Nature Materials, 17 (2018) 119–128.

[9] C. Yan, S. Barlow, Z. Wang, H. Yan, A. K.-Y. Jen, S. R. Marder & X. Zhan, Non-fullerene acceptors for organic solar cells, Nature Rev. Mat. 3, (2018) 18003.

[10] M. T. Khan, R. Bhargav, A. Kaur, S.K. Dhawan, S. Chand. Effect of cadmium sulphide quantum dot processing and post thermal annealing on P3HT/PCBM photovoltaic device, Thin Solid Films 519 (2010) 1007.

[11] M. T. Khan, A. Kaur, S K Dhawan and S. Chand, In-Situ growth of cadmium telluride nanocrystals in poly(3-hexylthiophene) matrix for photovoltaic application, J. Appl. Phys 110 (2011) 044509.

[12] Haoliang Liu, Chuang Zhang, Hans Malissa, Matthew Groesbeck, Marzieh Kavand, Ryan McLaughlin, Shirin Jamali, Jingjun Hao, Dali Sun, Royce A. Davidson, Leonard Wojcik, Joel S, Organic-based magnon spintronics. Miller, Christoph Boehme & Z. Valy Vardeny, Nature Materials, 17 (2018) 308–312.

[13] Haoliang Liu, Jingying Wang, Matthew Groesbeck, Xin Pan, Chuang Zhang and Z. Valy Vardeny, Studies of spin related processes in fullerene $C_{60}$ devices, J. Mater. Chem. C, 2018,6, 3621-3627.

[14] Srijani Mallik, Stefan Mattauch, Manas Kumar Dalai, Thomas Brückel & Subhankar Bedanta Effect of magnetic fullerene on magnetization reversal created at the Fe/C60 interface, Scientific Reports, 8 (2018) 5515.

[15] Lidan Guo Xianrong Gu Xiangwei Zhu Xiangnan, Sun Recent Advances in Molecular Spintronics: Multifunctional Spintronic Devices, Adv. Mat. (2019), 1805355, https://doi.org/10.1002/adma.201805355

[16] Shiheng Liang, Rugang Geng, Baishun Yang, Wenbo Zhao, Ram Chandra Subedi, Xiaoguang Li, Xiufeng Han & Tho Duc Nguyen, Curvature-enhanced Spin-orbit Coupling and Spinterface Effect in Fullerene-based Spin Valves, Scientific Reports, 6, (2016) 19461.

[17] Xianmin Zhang, Shigemi Mizukami, Takahide Kubota, Qinli Ma, Mikihiko Oogane, Hiroshi Naganuma, Yasuo Ando & Terunobu Miyazaki, Observation of a large spin-

dependent transport length in organic spin valves at room temperature, *Nat. Commun.* 4 (2013) 1392.

[18] Z. G Yu, Spin-orbit coupling and its effects in organic solids, Phys. Rev. B 85 (2012) 115201.

[19] Roderick C. I. MacKenzie, Jarvist M. Frost, and Jenny Nelson, A numerical study of mobility in thin films of fullerene derivatives, J. Chem. Phys. 132 (2010) 064904.

[20] Marco Gobbi Federico Golmar Roger Llopis Fèlix Casanova Luis E. Hueso, Room-Temperature Spin Transport in C60-Based Spin Valves, Adv. Mater. 23 (2011) 1609.

[21] Mohd Taukeer Khan, V. Agrawal, Abdullah Almohammedi, V. Gupta, Effect of Traps on the Charge Transport in Semiconducting Polymer PCDTBT, Solid State Electronics, 145 (2018) 49–53. 4)

[22] Mohd Taukeer Khan, and Abdullah Almohammedi, Effect of CdS nanocrystals on charge transport mechanism in poly(3-hexylthiophene), J. App. Phy., 122 (2017) 075502.

[23] Mohd Taukeer Khan, Amarjeet Kaur, S K Dhawan and Suresh Chand, Hole transport mechanism in organic/inorganic hybrid system based on in-situ grown CdTe nanocrystals in poly(3-hexylthiophene), J. Appl. Phys. 109 (2011) 114509.

[24] Mohd Taukeer Khan, Manisha Bajpai, Amarjeet Kaur, S. K. Dhawan, Suresh Chand, Electrical, optical and hole transport mechanism in thin films of poly(3-octylthiophene-co-3-hexylthiophene): Synthesis and characterization, Synthetic Metals 160 (2010) 1530.

[25] Elements of Modern X-ray Physics, by J. Als-Nielsen and Des McMorrow, 2nd Edition wiley, (2001).

[26] Handbook of Thin Film Materials: Nanomaterials and Magnetic Thin Films by H. S. Nalwa, Academic Press, (2002).

[27] Y.-L. Chan, Y.-J. Hung, C.-H. Wang, Y.-C. Lin, C.-Y. Chiu, Y.-L. Lai, H.-T. Chang, C.-H. Lee, Y. J. Hsu, and D. H. Wei, Magnetic Response of an Ultrathin Cobalt Film in Contact with an Organic Pentacene Layer, Physical Review Letters 104 (2010) 177204.

[28] A. A. Sidorenko, C. Pernechele, P. Lupo, M. Ghidini, M. Solzi, R. De Renzi, I. Bergenti, P. Graziosi, V. Dediu, L. Hueso, and a. T. Hindmarch, Interface effects on an ultrathin Co film in multilayers based on the organic semiconductor $Alq_3$, App. Phy. Let. 97 (2010) 162509.

[29] I. Bergenti, a. Riminucci, E. Arisi, M. Murgia, M. Cavallini, M. Solzi, F. Casoli, and V.

Dediu, Magnetic properties of Cobalt thin films deposited on soft organic layers, Journal of Magnetism and Magnetic Materials 316 (2007) e987.

[30] Y-J., L.Y.-L. Hsu, C-H. Chen, Y-H. Lin, H-Y. Chien, J-H.Wang, T-N. Lam, Y-L. Chan, D. H. Wei, H-J. Lin and C-T. Chen, Self-Assembled Graphene/Carbon Nanotube Hybrid Films for Supercapacitors, The J. Phy. Chem. Lett., 4 (2012) 310.

[31] J. S. Moodera and G. Mathon, Spin polarized tunneling in ferromagnetic junctions, J. Magn. Magn. Mater., 200 (1999) 248–273.

[32] M. Julliµere, Tunneling between ferromagnetic films, Phys. Lett. 54, (1975) 225.

# Mixed Vector Equilibrium Problems with Fuzzy Mappings

Mohd. Akram
Department of Mathematics, Faculty of Science, Islamic University in Madinah
Madinah, KSA
akramkhan_20@rediffmail.com

## Abstract

In this paper, we study fuzzy generalized mixed vector equilibrium problem and fuzzy mixed vector equilibrium problem. We prove existence results for fuzzy generalized mixed vector equilibrium problem and fuzzy mixed vector equilibrium problem by using some basic tools as KKM theory and Maximal element lemma. We provide sufficient conditions that ensure the existence of the solution of these problems. The results presented in this paper generalize, improve and unify the previously known results in this area. An example is given.

## keywords

Vector equilibrium problem, KKM theory, Maximal element lemma, Fuzzy setting, Existence, AMS Subject Classification: 47J22; 47J25; 47S40

# اتزان المتجه الغامض المعمم المدمج ومشكلة حالة اتزانه

**الملخص:** في هذا البحث, نحن ندرس مسألة حالة اتزان المتجه الغامض المعمم المدمج ومشكلة حالة اتزان المتجه الغامض المدمج, نحن نثبت وجود نتائج لمسألة حالة اتزان المتجه الغامض المعمم المدمج ومسألة حالة اتزان المتجه الغامض المدمج باستخدام بعض الطرق الأساسية مثل نظرية(ك م م) ونظرية العنصر الأقصى.

كما نوفر شروط كافية لضمان وجود حلول لهذه المسألة. النتائج التي تقدم في هذا البحث معممة وتحسن وتوحد النتائج المعروفة السابقة في هذا المجال, وأيضًا أُعطيت أمثلة.

# 1 Introduction

Equilibrium problems have been the subject of considerable research and have profound contributions in large variety of problems of practical interest arising in nonlinear analysis, optimization, economics, finance and game theory. It includes many mathematical problems as particular cases such as mathematical programming problems, complementarity problems, variational inequality problems, fixed point problems, minimax inequality problems and Nash equilibrium problems in noncooperative games, see for example, [8, 14, 18, 30]. The foundation of (scalar) equilibrium theory has been laid down by Ky Fan [17], his minimax inequality still being considered one of the most notable results in this field. The classical scalar equilibrium problem in [17], described by a bifunction $f : K \times K \to R$ consists in finding $x \in K$ such that

$$f(x,y) \geq 0, \ \ \forall\, y \in K.$$

It was Blum and Oettli [8], who used the term equilibrium problem for the first time. Starting with the pioneering work of Giannessi [18], several extensions of the scalar equilibrium problem to the vector case have been considered. These vector equilibrium problems, much like their scalar counterpart, offer a unified framework for treating vector optimization, vector variational inequalities or cone saddle point problems, see for examples [2, 3, 4, 6, 19, 21]. Let $X$ and $Z$ be locally convex Hausdorff topological vector spaces, $K \subseteq X$ be a nonempty set and let $C \subseteq Z$ be a convex and pointed cone. Assume that the interior of the cone $C$, denoted by $intC$, is nonempty and consider the mapping $f : K \times K \to Z$. The vector equilibrium problem, consists in finding $x \in K$, such that

$$f(x,y) \notin -intC, \ \forall\, y \in K.$$

Because of its applications and interests, vector equilibrium problems have been studied by many authors in different directions using variant techniques, see, for example, [5, 20, 29]. The concept of fuzzy set theory was introduced by Zadeh [36] and penetrates almost all branches of mathematics. Fuzzy set theory have been applied to many fields including information science, artificial intelligence, computer science, management science and control engineering, etc., see [32, 37].

In 1981, Heilpern [22] proved a fixed point theorem for fuzzy contraction mapping which is fuzzy analogue of Nadlar's fixed point theorem for set-valued mapping. In 1989, Chang and Zhu [9] introduced the concept of variational inequalities for fuzzy mappings in abstract spaces and investigated the existence problem for solutions of some class of variational inequalities for fuzzy mappings. Since then several classes of variational inequalities (inclusions) and vector variational inequalities with fuzzy mappings were considered by Chang and Huang [10], Ding and Park [15], Chang and Salahuddin [12], Anastassio and Salahuddin [1], Lan and Verma [26] and Lee et al. [28]. Recently, Huang and Lan [23] considered non linear equations with fuzzy mappings in

fuzzy normed spaces. Very recently, Rahaman and Ahmad [31] studied fuzzy vector equilibrium problem. They proved some existence results by using particular forms of results of Kim and Lee [25] and Tarafdar [34]. Motivated by the research mentioned above and ongoing research in this direction, in this paper, we study some mixed vector equilibrium problems in fuzzy setting.

# 2 Preliminaries

Now, we mention some definitions, notations and conclusions which are needed in the sequel.
A mapping $F$ from $E$ into the collection $\mathscr{F}(E)$ of all fuzzy sets of $E$ is called fuzzy mapping. If $F : E \to \mathscr{F}(E)$ is a fuzzy mapping, then $F(x), x \in E$ (denoted by $F_x$, in the sequel) is a fuzzy set in $\mathscr{F}(E)$, which is a function from $E$ to $[0,1]$. For each $y \in E, F_x(y)$ is the degree of membership of $y$ in $F_x$. Let $A \in \mathscr{F}(E)$ and $\alpha \in [0,1]$, then the set
$A_\alpha = \{x \in E : A(x) \geq \alpha\}$ is called an $\alpha$-cut set of $A$.
**Definition 2.1** A mapping $f : K \to Z$ is said to be convex, if for any $x_1, x_2 \in K$ and $t \in [0,1]$,

$$f(tx_1 + (1-t)x_2) \leq_{C(x)} tf(x_1) + (1-t)f(x_2),$$

which is equivalent to

$$tf(x_1) + (1-t)f(x_2) - f(tx_1 + (1-t)x_2) \in C(x).$$

**Definition 2.2** (see, [35]) Let $X, Y$ be two topological vector spaces, $T : X \to 2^Y$ be a set-valued mapping and $T^{-1}(y) = \{x \in X : y \in T(x)\}$. Then

(*i*) $T$ is said to be upper semi-continuous, if for each $x \in X$ and each open set $V$ in $Y$ with $T(x) \subset V$, then there exists an open neighbourhood $U$ of $x$ in X such that $T(u) \subset V$, for each $u \in U$.

(*ii*) $T$ is said to be closed, if for any net $\{x_\alpha\}$ in $X$ such that $x_\alpha \to x$ and any net $\{y_\alpha\}$ in $Y$ such that $y_\alpha \to y$ and $y_\alpha \in T(x_\alpha)$ for any $\alpha$, we have $y \in T(x)$.

(*iii*) $T$ is said to have a closed graph, if the graph of $T, Gr(T) = \{(x,y) \in X \times Y : y \in T(x)\}$ is closed in $X \times Y$.

**Definition 2.3** (see, [27]) Let $X, Y$ be topological spaces and $T : X \to \mathscr{F}(Y)$ be a fuzzy mapping. $T$ is said to have fuzzy set-valued, if $T_x(y)$ is upper semi-continuous on $X \times Y$ as a real ordinary function.
**Lemma 2.1** If $A$ is a closed subset of a topological space $X$, then the characteristic function $\mathscr{X}_A$ of $A$ is an upper semi-continuous real-valued function.

**Lemma 2.2** (see, [24]) Let $K$ be a non-empty closed convex subset of a real Hausdorff topological vector space $X$, $E$ be a non-empty closed convex subset of a real Hausdorff topological vector space $Y$ and $a : X \to [0,1]$ be a lower semi-continuous function. Let $T : K \to \mathscr{F}(E)$ be a fuzzy mapping with $(Tx)_{a(x)} \neq \emptyset, \forall\, x \in X$ and $\bar{T} : K \to 2^E$ be a multi-function defined by $\bar{T}(x) = (Tx)_{a(x)}$. If $T$ is a closed set-valued mapping, then $\bar{T}$ is a closed multi-function.

**Definition 2.4** (see, [13]) Let $K$ be a convex subset of a topological vector space $E$ and $Z$ be a topological vector space. Let $C : K \to 2^Z$ be a set-valued mapping. For any given finite subset $\{x_1, x_2, \cdots, x_n\}$ of $K$ and any $x = \sum_{i=1}^n t_i x_i$ with $t_i \geq 0$ for $i = 1, 2, \cdots, n$ and $\sum_{i=1}^n t_i = 1$,

($i$) a single valued mapping $M : K \times K \to Z$ is said to be vector 0-diagonally convex in the second variable, if

$$\sum_{i=1}^{n} t_i M(x, x_i) \notin -intC(x);$$

($ii$) a set-valued mapping $M : K \times K \to 2^Z$ is said to be generalized vector 0-diagonally convex in the second variable, if

$$\sum_{i=1}^{n} t_i u_i \notin -intC(x),\ \forall\, u_i \in M(x, x_i).$$

**Lemma 2.3** (see, [33]) Let $X, Y$ be two topological spaces and $T : X \to 2^Y$ be an upper semi-continuous set-valued mapping with compact values. Suppose $\{x_\alpha\}$ is a net in $X$ such that $x_\alpha \to x_0$. If $y_\alpha \in T(x_\alpha)$ for each $\alpha$, then there exists $y_0 \in T(x_0)$ and a subnet $\{y_\beta\}$ of $\{y_\alpha\}$ such that $y_\beta \to y_0$.

**Lemma 2.4** (see, [7]) Let $X$ and $Y$ be two topological spaces. If $T : X \to 2^Y$ is an upper semi-continuous set-valued mapping with closed values, then $T$ is closed.

**Lemma 2.5** (see, [11], Maximal Element Lemma) Let $X$ be a non-empty convex subset of a topological vector space $E$ and $T : X \to 2^X$ be a set-valued mapping satisfying the following conditions:

($i$) for each $x \in X, x \notin CoT(x)$ and for each $y \in X, T^{-1}(y)$ is open-valued in $X$;

($ii$) there exist a non-empty compact subset $A$ of $X$ and a non-empty convex subset $B$ of $X$ such that

$$Co(T(x)) \cap B \neq \emptyset,\ \forall\, x \in X \setminus A.$$

Then there exists $x_0 \in X$ such that $T(x_0) = \emptyset$.

**Definition 2.5** (KKM Mapping) Let $K$ be a subset of a topological vector space $X$. A set-valued mapping $A : K \to 2^X$ is said to be KKM-mapping, if for each finite subset $\{x_1, x_2, ...., x_n\}$ of $K$, $Co\{x_1, x_2, \cdots, x_n\} \subseteq \bigcup_{i=1}^{n} A(x_i)$, where $Co\{x_1, x_2, \cdots, x_n\}$ denotes the convex hull of $\{x_1, x_2, \cdots, x_n\}$.

**Lemma 2.6** (see, [16], KKM-Fan Theorem) Let $K$ be a subset of a Hausdorff topological vector space $X$ and let $A : K \to 2^X$ be a KKM mapping. If for each $x \in K, A(x)$ is closed and if for at least one point $x \in K, A(x)$ is compact, then $\bigcap_{x \in K} A(x) \neq \emptyset$.

Let $Y$ be a locally convex Hausdorff topological vector space and $X$ be a Hausdorff topological vector space, $L(X,Y)$, the space of all continuous linear operators from $X$ into $Y$ be a locally convex space being equipped with $\sigma$-topology. Let $K$ be a non-empty convex subset of a Hausdorff topological vector space $X, C : K \to 2^Y$ be a set-valued mapping such that $intC(x) \neq \emptyset,\ \forall\ x \in K$. Let $T : L(X,Y) \times L(X,Y) \times L(X,Y) \to 2^{L(X,Y)}, f : K \times K \to 2^Y$, $g : K \to K$ and $\phi : X \times X \to 2^Y$ be the vector-valued mappings. Let $P, Q, R : K \to \mathscr{F}(L(X,Y))$ be the fuzzy mappings and $a, b, c : K \to [0,1]$ are the functions. The partial order relation $\leq_{C(x)}$ in $Y$ with the convex cone $C(x)$ is defined as

$$y_1 \leq_{C(x)} y_2 \Leftrightarrow y_2 - y_1 \in C(x),\ \forall y_1, y_2 \in Y.$$

In this paper, we consider the following fuzzy generalized mixed vector equilibrium problem: Find $x \in K, u \in (Px)_{a(x)}, v \in (Qx)_{b(x)}$ and $w \in (Rx)_{c(x)}$ such that

$$f(x,y) + \langle T(u,v,w), y - g(x)\rangle + \phi(x,y) - \phi(x,x) \notin -intC(x),\ \forall\ y \in K \tag{1}$$

and the fuzzy mixed vector equilibrium problem: Find $x \in K, u \in (Px)_{a(x)}, v \in (Qx)_{b(x)}$ and $w \in (Rx)_{c(x)}$ such that

$$f(x,y) + \langle T(u,v,w), y - x\rangle + \phi(x,y) - \phi(x,x) \notin -intC(x),\ \forall\ y \in K. \tag{2}$$

In support of problem (1), we construct the following example.

**Example 2.1** Let $X = Y = K = C = [0,1]$, we define the fuzzy mappings $P, Q, R : K \to \mathscr{F}(L(X,Y))$, for all $u, v, w \in [0,1]$ as follows:

$P_x(u) = \begin{cases} 0, & \text{if } x \in [0, \frac{1}{2}); \\ \frac{x+u}{2}, & \text{if } x \in [\frac{1}{2}, 1], \end{cases}$ $Q_x(v) = \begin{cases} 0, & \text{if } x \in [0, \frac{1}{3}); \\ \frac{x+v}{3}, & \text{if } x \in [\frac{1}{3}, 1], \end{cases}$ $R_x(w) = \begin{cases} 0, & \text{if } x \in [0, \frac{1}{4}); \\ \frac{x+w}{4}, & \text{if } x \in [\frac{1}{4}, 1], \end{cases}$ and the mapping $a, b, c : K \to [0,1]$ as follows:

$a(x) = \begin{cases} 0, & \text{if } x \in [0, \frac{1}{2}); \\ \frac{x}{2}, & \text{if } x \in [\frac{1}{2}, 1], \end{cases}$ $b(x) = \begin{cases} 0, & \text{if } x \in [0, \frac{1}{3}); \\ \frac{x}{3}, & \text{if } x \in [\frac{1}{3}, 1], \end{cases}$ $c(x) = \begin{cases} 0, & \text{if } x \in [0, \frac{1}{4}); \\ \frac{x}{4}, & \text{if } x \in [\frac{1}{4}, 1]. \end{cases}$

Clearly, $P_x(u) \geq a(x), Q_x(v) \geq b(x)$ and $R_x(w) \geq c(x), \forall x \in K$, i.e., $u \in (P_x)_{a(x)}, v \in (Q_x)_{b(x)}$ and $w \in (R_x)_{c(x)}$.

Now, we define the mappings $f : K \times K \to Y, \phi : X \times X \to Y, g : K \to K$ and $T : L(X,Y) \times L(X,Y) \times L(X,Y) \to Y$ as follows:

$f(x,y) = \frac{x+y}{2}, \phi(x,y) = \frac{x-y}{2}, g(x) = x^2$ and $T(u,v,w) = \begin{cases} 0, & \text{if } x \in [0, \frac{1}{2}); \\ \frac{1}{2}\sin^2(uvw), & \text{if } x \in [\frac{1}{2}, 1]. \end{cases}$ Then, one can verify that

$f(x,y) + \langle T(u,v,w), y - g(x)\rangle + \phi(x,y) - \phi(x,x) \notin -intC(x), \forall y \in K$. Thus, fuzzy generalized mixed vector equilibrium problem (1) is satisfied.

# 3 Existence Results

In the following theorem, we prove the existence of solution for fuzzy generalized mixed vector equilibrium problem (1).

**Theorem 3.1** Let $Y$ be a locally convex Hausdorff topological vector space, $K$ be a non-empty convex subset of a Hausdorff topological vector space $X$. Let $P,Q,R : K \to \mathscr{F}(L(X,Y))$ be the fuzzy mappings and $\mathscr{P},\mathscr{Q},\mathscr{R} : K \to 2^{L(X,Y)}$ be upper semi-continuous set-valued mappings with non-empty compact values induced by fuzzy mappings $P,Q$ and $R$, respectively, i.e.,

$$\mathscr{P}(x) = (Px)_{a(x)}, \mathscr{Q}(x) = (Qx)_{b(x)}, \mathscr{R}(x) = (Rx)_{c(x)}, \forall x \in K.$$

Let $T : L(X,Y) \times L(X,Y) \times L(X,Y) \to 2^{L(X,Y)}, f : K \times K \to 2^Y, \phi : X \times X \to 2^Y$ be the set-valued mappings and $g : K \to K$ be the single-valued mapping such that the following conditions hold:

(*i*) $f$ is generalized vector 0-diagonally convex and affine in the second argument;

(*ii*) $g$ is continuous mapping with $x - g(x) = 0, \ \forall \ x \in K$;

(*iii*) $\phi$ is affine in the second argument;

(*iv*) $C : K \to 2^Y$ be a convex set-valued mapping and $Y \setminus \{-intC(x)\}$ is upper semi-continuous ;

(*v*) for all $y \in K$, $f(\cdot,y) + \langle T(\cdot,\cdot,\cdot), y - g(\cdot)\rangle + \phi(\cdot,y) + \phi(\cdot,\cdot)$ is upper semi-continuous with compact values;

(*vi*) there exists a non-empty compact subset $A$ of $K$ and a non-empty compact convex subset $D$ of $K$ such that for all $x \in K \setminus A$, there exists $\bar{y} \in D$ such that

$$f(x,\bar{y}) + \langle T(u,v,w), \bar{y} - g(x)\rangle + \phi(x,\bar{y}) - \phi(x,x) \in -intC(x),$$

$$\forall \ u \in \mathscr{P}(x) = (Px)_{a(x)}, v \in \mathscr{Q}(x) = (Qx)_{B(x)}, w \in \mathscr{R}(x) = (Rx)_{c(x)}, \ \forall \ x \in K.$$

Then the fuzzy generalized mixed vector equilibrium problem (1) has a solution.

*Proof.* We define a set-valued mapping $M : K \to 2^K$ by

$$M(x) = \{y \in K : f(x,y) + \langle T(u,v,w), y - g(x)\rangle + \phi(x,y) - \phi(x,x) \in -intC(x),$$

$$\forall \ u \in \mathscr{P}(x) = (Px)_{a(x)}, v \in \mathscr{Q}(x) = (Qx)_{b(x)}, w \in \mathscr{R}(x) = (Rx)_{c(x)}\}, \ \forall \ x \in K.$$

Now, we have to show that $x \notin coM(x), \forall \ x \in K$. Suppose to the contrary that there exists $\bar{x} \in K$ such that $\bar{x} \in coM(\bar{x})$, then there exists a finite set $\{y_1, y_2, \cdots, y_n\}$ such that $\bar{x} \in co\{y_1, y_2, \cdots, y_n\}$,

we have

$$f(\bar{x},y_i)+\langle T(u,v,w),y_i-g(\bar{x})\rangle+\phi(\bar{x},y_i)-\phi(\bar{x},\bar{x})\in -intC(\bar{x}),\ i=1,2,\cdots,n,$$

$$\forall\ u\in\mathscr{P}(\bar{x})=(P\bar{x})_{a(\bar{x})},v\in\mathscr{Q}(\bar{x})=(Q\bar{x})_{b(\bar{x})},w\in\mathscr{R}(\bar{x})=(R\bar{x})_{c(\bar{x})}.$$

Since $intC(\bar{x})$ is a convex set, for each $i=1,2,\cdots,n$ with $\sum_{i=1}^{n}t_i=1,t_i\in[0,1],\bar{x}=\sum_{i=1}^{n}t_iy_i$, then it follows from affinity of $f,\phi$ in the second argument and by condition $(ii)$ that

$$\begin{array}{rcl} f(\bar{x},\sum_{i=1}^{n}t_iy_i) & + & \langle T(u,v,w),\sum_{i=1}^{n}t_iy_i-g(\bar{x})\rangle+\phi(\bar{x},\sum_{i=1}^{n}t_iy_i)-\phi(\bar{x},\bar{x}) \\ & = & \sum_{i=1}^{n}t_if(\bar{x},y_i)+\langle T(u,v,w),\bar{x}-g(\bar{x})\rangle+\phi(\bar{x},\bar{x})-\phi(\bar{x},\bar{x}) \\ & = & \sum_{i=1}^{n}t_if(\bar{x},y_i)\in -intC(\bar{x}), \\ & = & \sum_{i=1}^{n}t_iu_i\in -intC(\bar{x}),\forall u_i\in f(\bar{x},y_i),i=1,2,\cdots,n, \end{array}$$

which is a contradiction to the generalized vector 0-diagonal convexity of $f$ in the second argument and hence $x\notin coM(x),\ \forall\ x\in K$.

Next, we prove that for each $y\in K,M^{-1}(y)$ is an open set. To prove this, we need to show that the complement $[M^{-1}(y)]^c$ of $M^{-1}(y)$ is closed, i.e.,

$$[M^{-1}(y)]^c=\{x\in K:\{f(x,y)+\langle T(u,v,w),y-g(x)\rangle+\phi(x,y)-\phi(x,x)\}\cap Y\setminus\{-intC(x)\}\neq\emptyset,$$

$$\forall\ u\in\mathscr{P}(x)=(Px)_{a(x)},v\in\mathscr{Q}(x)=(Qx)_{b(x)},w\in\mathscr{R}(x)=(Rx)_{c(x)}\}$$

is a closed set in $K$. Let $\{x_\alpha\}$ be a sequence in $[M^{-1}(y)]^c$ such that $x_\alpha\to x_0$, then there exist $u_\alpha\in\mathscr{P}(x_\alpha)=(Px_\alpha)_{a(x_\alpha)},v_\alpha\in\mathscr{Q}(x_\alpha)=(Qx_\alpha)_{b(x_\alpha)},w_\alpha\in\mathscr{R}(x_\alpha)=(Rx_\alpha)_{c(x_\alpha)}$ such that

$$\{f(x_\alpha,y)+\langle T(u_\alpha,v_\alpha,w_\alpha),y-g(x_\alpha)\rangle+\phi(x_\alpha,y)-\phi(x_\alpha,x_\alpha)\}\cap Y\setminus\{-intC(x_\alpha)\}\neq\emptyset.$$

Since $\mathscr{P},\mathscr{Q},\mathscr{R}:K\to 2^{L(X,Y)}$ are compact valued upper semi-continuous mappings induced by the fuzzy mappings $P,Q,R:K\to\mathscr{F}(L(X,Y))$, respectively, then by Lemma 2.3, $\{u_\alpha\},\{v_\alpha\}$ and $\{w_\alpha\}$ have the subsequences $\{u_{\alpha_n}\},\{v_{\alpha_n}\}$ and $\{w_{\alpha_n}\}$, respectively, such that $u_{\alpha_n}\to u_0,v_{\alpha_n}\to v_0$ and $w_{\alpha_n}\to w_0$ and $u_0\in\mathscr{P}(x_0)=(Px_0)_{a(x_0)},v_0\in\mathscr{Q}(x_0)=(Qx_0)_{b(x_0)},w_0\in\mathscr{R}(x_0)=(Rx_0)_{c(x_0)}$. Suppose that

$$v_\alpha\in\{f(x_\alpha,y)+\langle T(u_\alpha,v_\alpha,w_\alpha),y-g(x_\alpha)\rangle+\phi(x_\alpha,y)-\phi(x_\alpha,x_\alpha)\}\cap Y\setminus\{-intC(x_\alpha)\}.$$

Since $f(\cdot,y)+\langle N(\cdot,\cdot,\cdot),y-g(\cdot)\rangle+\phi(\cdot,y)-\phi(\cdot,\cdot)\cap Y\setminus\{-intC(x_\alpha)\}$ is upper semi-continuous and compact values, it follows from Lemma 2.3 that there exists $v_0\in f(x_0,y)+\langle T(u_0,v_0,w_0),y-g(x_0)\rangle+\phi(x_0,y)-f(x_0,x_0)$ and a subsequence $\{v_{\alpha_n}\}$ of $\{v_\alpha\}$ such that $v_{\alpha_n}\to v_0$. Since $Y\setminus\{-intC(x)\}$ is an upper semi-continuous with closed values, hence by Lemma 2.1, $v_0\in Y\setminus$

$\{-intC(x_0)\}$, thus we have

$$\{f(x_0,y)+\langle T(u_0,v_0,w_0),y-g(x_0)\rangle+\phi(x_0,y)-f(x_0,x_0)\}\cap Y\setminus\{-intC(x_0)\}\neq\emptyset.$$

Hence $[M^{-1}(y)]^c$ is a closed subset in $K$ and therefore $M^{-1}(y)$ is an open set for all $y\in K$. It follows from the condition $(vi)$ of the theorem that for each $x\in K\setminus A$, there exists $\bar{y}\in D$ such that $x\in intM^{-1}(\bar{y})$. Thus, all the conditions of the Lemma 2.5 are satisfied, hence there exists $x\in K$ such that $M(x)=\emptyset$, i.e., there exists $x\in K$, $u\in\mathscr{P}(x)=(Px)_{a(x)}$, $v\in\mathscr{Q}(x)=(Qx)_{b(x)}$, $w\in\mathscr{R}(x)=(Rx)_{c(x)}$ such that

$$f(x,y)+\langle T(u,v,w),y-g(x)\rangle+\phi(x,y)-\phi(x,x)\notin -intC(x),\ \forall\, y\in K.$$

This completes the proof.

In the following theorem, we prove the existence of solution for the fuzzy mixed vector equilibrium problem (2), which is obtained by taking $g\equiv I$, the identity mapping in Theorem 3.1.

**Theorem 3.2** Let $Y$ be a locally convex Hausdorff topological vector space, $K$ be a non-empty convex subset of a Hausdorff topological vector space $X$. Let $P,Q,R:K\to\mathscr{F}(L(X,Y))$ be the fuzzy mappings and $\mathscr{P},\mathscr{Q},\mathscr{R}:K\to 2^{L(X,Y)}$ be upper semi-continuous set-valued mappings with non-empty compact values induced by fuzzy mappings $P,Q$ and $R$, respectively, i.e.,

$$\mathscr{P}(x)=(Px)_{a(x)},\mathscr{Q}(x)=(Qx)_{b(x)},\mathscr{R}(x)=(Rx)_{c(x)}.$$

Let $T:L(X,Y)\times L(X,Y)\times L(X,Y)\to 2^{L(X,Y)}$, $f:K\times K\to 2^Y$ and $\phi:X\times X\to 2^Y$ be the set-valued mappings such that the following conditions hold:

$(i)$ $f$ is generalized vector 0-diagonally convex and affine in the second argument;

$(iii)$ $\phi$ is affine in the second argument;

$(iii)$ $C:K\to 2^Y$ be a convex set-valued mapping and $Y\setminus\{-intC(x)\}$ is upper semi-continuous;

$(iv)$ for all $y\in K$, $f(\cdot,y)+\langle T(\cdot,\cdot,\cdot),y-(\cdot)\rangle+\phi(\cdot,y)-\phi(x,x)$ is upper semi-continuous with compact values;

$(v)$ there exists a non-empty compact subset $A$ of $K$ and a non-empty compact convex subset $D$ of $K$ such that for all $x\in K\setminus A$, there exists $\bar{y}\in D$ such that

$$f(x,\bar{y})+\langle T(u,v,w),\bar{y}-x\rangle+\phi(x,\bar{y})-\phi(x,x)\in -intC(x),$$

$$\forall\, u\in\mathscr{P}(x)=(Px)_{a(x)},v\in\mathscr{Q}(x)=(Qx)_{B(x)},w\in\mathscr{R}(x)=(Rx)_{c(x)},\ \forall\, x\in K.$$

Then the fuzzy mixed vector equilibrium problem (2) has a solution.

*Proof.* We define a set-valued mapping $M : K \to 2^K$ by

$$M(x) = \{y \in K : f(x,y) + \langle T(u,v,w), y-x\rangle + \phi(x,y) - \phi(x,x) \in -intC(x),$$

$$\forall\, u \in \mathscr{P}(x) = (Px)_{a(x)}, v \in \mathscr{Q}(x) = (Qx)_{B(x)}, w \in \mathscr{R}(x) = (Rx)_{c(x)}\},\ \forall\, x \in K.$$

Now, we have to show that $x \notin coM(x), \forall\, x \in K$. Suppose to the contrary that there exists $\bar{x} \in K$ such that $\bar{x} \in coM(\bar{x})$. Then there exists a finite set $\{y_1, y_2, \cdots, y_n\}$ such that $\bar{x} \in co\{y_1, y_2, \cdots, y_n\}$, then we have

$$f(\bar{x}, y_i) + \langle T(u,v,w), y_i - \bar{x}\rangle + \phi(\bar{x}, y_i) - \phi(\bar{x}, \bar{x}) \in -intC(\bar{x}),\ i = 1, 2, \cdots, n,$$

$$\forall\, u \in \mathscr{P}(x) = (Px)_{a(x)}, v \in \mathscr{Q}(x) = (Qx)_{b(x)}, w \in \mathscr{R}(x) = (Rx)_{c(x)}.$$

Since $intC(\bar{x})$ is a convex set, for each $i = 1, 2, \cdots, n$ with $\sum_{i=1}^n t_i = 1, t_i \in [0,1], \bar{x} = \sum_{i=1}^n t_i y_i$, then it follows from the affinity of $f$ and $\phi$ in the second argument that

$$\begin{aligned} f(\bar{x}, \textstyle\sum_{i=1}^n t_i y_i) &+ \langle T(u,v,w), \textstyle\sum_{i=1}^n t_i y_i - \bar{x}\rangle + \phi(\bar{x}, \textstyle\sum_{i=1}^n t_i y_i) - \phi(\bar{x}, \bar{x}) \\ &= \textstyle\sum_{i=1}^n t_i f(\bar{x}, y_i) + \langle T(u,v,w), \bar{x} - \bar{x}\rangle + \phi(\bar{x}, \bar{x}) - \phi(\bar{x}, \bar{x}) \\ &= \textstyle\sum_{i=1}^n t_i f(\bar{x}, y_i) \in -intC(\bar{x}), \\ &= \textstyle\sum_{i=1}^n t_i u_i \in -intC(\bar{x}), \forall u_i \in f(\bar{x}, y_i), i = 1, 2, \cdots, n, \end{aligned}$$

which is a contradiction to generalized vector 0-diagonally convexity assumptions of $f$ and hence $x \notin coM(x),\ \forall\, x \in K$.

Next, we prove that for each $y \in K, M^{-1}(y)$ is an open set. To prove this, we need to show that the complement $[M^{-1}(y)]^c$ of $M^{-1}(y)$ is closed, i.e.,

$$[M^{-1}(y)]^c = \{x \in K : \{f(x,y) + \langle T(u,v,w), y-x\rangle + \phi(x,y) - \phi(x,x)\} \cap Y \setminus \{-intC(x)\} \neq \emptyset,$$

$$\forall\, u \in \mathscr{P}(x) = (Px)_{a(x)}, v \in \mathscr{Q}(x) = (Qx)_{b(x)}, w \in \mathscr{R}(x) = (Rx)_{c(x)}\}$$

is a closed set in $K$. Let $\{x_\alpha\}$ be a sequence in $[M^{-1}(y)]^c$ such that $x_\alpha \to x_0$. Then there exist $u_\alpha \in \mathscr{P}(x_\alpha) = (Px_\alpha)_{a(x_\alpha)}, v_\alpha \in \mathscr{Q}(x_\alpha) = (Qx_\alpha)_{b(x_\alpha)}, w_\alpha \in \mathscr{R}(x_\alpha) = (Rx_\alpha)_{c(x_\alpha)}$ such that

$$\{f(x_\alpha, y) + \langle T(u_\alpha, v_\alpha, w_\alpha), y - x_\alpha\rangle + \phi(x_\alpha, y) - \phi(x_\alpha, x_\alpha)\} \cap Y \setminus \{-intC(x_\alpha)\} \neq \emptyset.$$

Since $\mathscr{P}, \mathscr{Q}, \mathscr{R} : K \to 2^{L(X,Y)}$ are compact valued upper semi-continuous mappings induced by the fuzzy mappings $P, Q, R : K \to \mathscr{F}(L(X,Y))$, respectively, then by Lemma 2.3, $\{u_\alpha\}, \{v_\alpha\}$ and $\{w_\alpha\}$ have the subsequences $\{u_{\alpha_n}\}, \{v_{\alpha_n}\}$ and $\{w_{\alpha_n}\}$, respectively, such that $u_{\alpha_n} \to u_0, v_{\alpha_n} \to v_0$

and $w_{\alpha_n} \to w_0$ and $u_0 \in \mathscr{P}(x_0) = (Px_0)_{a(x_0)}, v_0 \in \mathscr{Q}(x_0) = (Qx_0)_{b(x_0)}, w_0 \in \mathscr{R}(x_0) = (Rx_0)_{c(x_0)}$. Suppose that

$$v_\alpha \in f(x_\alpha, y) + \langle T(u_\alpha, v_\alpha, w_\alpha), y - x_\alpha \rangle + \phi(x_\alpha, y) - \phi(x_\alpha, x_\alpha)\} \cap Y \setminus \{-intC(x_\alpha)\}.$$

Since $f(\cdot, y) + \langle T(\cdot, \cdot, \cdot), y - (\cdot)\rangle + \phi(\cdot, y) - \phi(\cdot, \cdot)$ is upper semi-continuous and compact values, it follows from Lemma 2.3 that there exists $v_0 \in f(x_0, y) + \langle T(u_0, v_0, w_0), y - x_0\rangle + \phi(x_0, y) - \phi(x_0, x_0)$ and a subsequence $\{v_{\alpha_n}\}$ of $\{v_\alpha\}$ such that $v_{\alpha_n} \to v_0$. Since $Y \setminus \{-intC(x)\}$ is an upper semi-continuous with closed values, hence by Lemma 2.1, $v_0 \in Y \setminus \{-intC(x_0)\}$, thus we have

$$\{f(x_0, y) + \langle T(u_0, v_0, w_0), y - x_0\rangle + \phi(x_0, y) - \phi(x_0, x_0)\} \cap Y \setminus \{-intC(x_0)\} \neq \emptyset.$$

Hence $[M^{-1}(y)]^c$ is a closed subset in $K$ and therefore $M^{-1}(y)$ is an open set for all $y \in K$. It follows from the condition $(v)$ of the theorem that for each $x \in K \setminus A$, there exists $\bar{y} \in D$ such that $x \in intM^{-1}(\bar{y})$. Thus, all the conditions of the Lemma 2.5 are satisfied, hence there exists $x \in K$ such that $M(x) = \emptyset$, i.e., there exists $x \in K, u \in \mathscr{P}(x) = (Px)_{a(x)}, v \in \mathscr{Q}(x) = (Qx)_{b(x)}, w \in \mathscr{R}(x) = (Rx)_{c(x)}$ such that

$$f(x, y) + \langle T(u, v, w), y - x\rangle + \phi(x, y) - \phi(x, x) \notin -intC(x), \ \forall\, y \in K.$$

This completes the proof.

# 4 Competing Interests

The authors declare that there is no competing interests regarding the publication of this article.

# References

[1] G.A. Anastassiou, Salahuddin, Weakly set valued generalized vector variational inequalities, J. Comput. Anal. Appl. 15(4) (2013) 622-632.

[2] Q.H. Ansari, W. Oettli, D. Schlager, A generalization of vectorial equilibria, Math. Methods Oper. Res. 46 (1997) 147–152.

[3] Q.H. Ansari, I.V. Konnov, J.C. Yao, Existence of a solution and variational principles for vector equilibrium problems, J. Optim. Theory Appl. 110 (2001) 481–492.

[4] Q.H. Ansari, I.V. Konnov, J.C. Yao, Characterizations of solutions for vector equilibrium problems, J. Optim. Theory Appl. 113 (2002) 435–447.

[5] Q.H. Ansari, F. Flores-Bazan, Recession methods for generalized vector equilibrium problems, J. Math. Anal. Appl. 321 (2006), 132–146.

[6] Q.H. Ansari, Vector equilibrium problems and vector variational inequalities. In: F. Giannessi (Ed.), Vector Variational Inequalities and Vector Equilibria, Kluwer Academic Publishers, Dordrecht (2000), pp. 1–15.

[7] J.P. Aubin, Applied Functional Analysis, John Wiley & Sons, New York, 2000.

[8] E. Blum, W. Oettli, From optimization and variational inequalities to equilibrium problems, Math. Stud. 63 (1994) 123–145.

[9] S.S. Chang, Y.G. Zhu, On variational inequalities for fuzzy mappings, Fuzzy Sets Syst. 32 (1989) 359–367.

[10] S.S. Chang, N.J. Huang, Generalized complementarity problem for fuzzy mappings, Fuzzy Sets Syst. 55 (1993), 227–234.

[11] S.S. Chang, K.K. Tan, Equilibria and maximal elements of abstract fuzzy economics and qualitative fuzzy games, Fuzzy Sets Syst. 125 (2002) 389–399.

[12] S.S. Chang, Salahuddin, Existence theorems for vector quasi variational-like inequalities for fuzzy mappings, Fuzzy Sets Syst. 233 (2013) 89–95.

[13] Y. Chiang, O. Chadli, J.C. Yao, Generalized vector equilibrium problems with trifunctions, J. Glob. Optim. 30 (2004) 135–154.

[14] X.P. Ding, Quasi-equilibrium problems in noncompact generalized convex spaces, Appl. Math. Mech. 21(6) (2000) 637—644.

[15] X.P. Ding, J.Y. Park, A new class of generalized nonlinear implicit quasi-variational inclusions with fuzzy mapping, J. Comput. Appl. Math. 138 (2002) 243–257.

[16] K. Fan, A generalization of Tychonoff's fixed point theorem, Math. Ann. 142 (1961) 303–310.

[17] K. Fan, A minimax inequality and its applications. In: O. Shisha (Ed.), Inequalities, Vol. (3), Academic Press, New York, 1972, pp. 103–113.

[18] F. Giannessi, Vector Variational Inequalities and Vector Equilibria, Mathematical theories, Kluwer, Dordrecht, 2000.

[19] X. Gong, Efficiency and Henig efficiency for vector equilibrium problems, J. Optim. Theory Appl. 108 (2001) 139–154.

[20] X. Gong, Strong vector equilibrium problems, J. Global Optim. 36 (2006) 339–349.

[21] A. Gopfert, H. Riahi, C. Tammer, C. Zalinescu, Variational Methods in Partially Ordered Spaces, Springer, New York, 2003.

[22] S. Heilpern, Fuzzy mappings and fixed point theorems, J. Math. Anal. Appl. 83 (1981) 566–569.

[23] N.J. Huang, H.Y. Lan, A couple of nonlinear equations with fuzzy mappings in fuzzy normed spaces, Fuzzy Sets Syst. 152 (2005), 209–222.

[24] M.F. Khan, S. Husain, Salahuddin, A fuzzy extension of generalized multi-valued $\eta$-mixed vector variational-like inequalities on locally convex Hausdorff topological vector spaces, Bull. Cal. Math. Soc. 100(I) (2008) 27–36.

[25] W.K. Kim, K.H. Lee, Generalized fuzzy games and fuzzy equilibria, Fuzzy Sets Syst. 122 (2001), 293–301.

[26] H.Y. Lan, R.U. Verma, Iterative algorithms for nonlinear fuzzy variational inclusions with $(A, \eta)$-accretive mappings in Banach spaces, Adv. Nonlinear Var. Inequal. 11(1) (2008) 15–30.

[27] G.M. Lee, D.S. Kim, B.S. Lee, Vector variational inequality for fuzzy mappings, Nonlinear Anal. Forum 4 (1999) 119–129.

[28] B.S. Lee, M.F. Khan, Salahuddin, Fuzzy nonlinear set-valued variational inclusions, Comput. Math. Appl. 60(6) (2010) 1768–1775.

[29] J. Li, N. J. Huang, J. K. Kim, On implicit vector equilibrium problems, J. Math. Anal. Appl. 283 (2003), 501–502.

[30] A. Moudafi, Mixed equilibrium problems: sensitivity analysis and algorithmic aspect, Comput. Math. Appl. 44 (2002) 1099–1108.

[31] M. Rahaman, R. Ahmad, Fuzzy vector equilibrium problems, Iranian J. Fuzzy Syst. 12(1) (2015) 115–122.

[32] E. Shivanan, E. Khorram, Optimization of linear objective function subject to fuzzy relation inequalities constraints with max-product composition, Iranian J. Fuzzy Syst. 7(5) (2010), 51–71.

[33] C.H. Su, V.M. Sehgal, Some fixed point theorems for condensing multi-functions in locally convex spaces, Proc. Natl. Acad. Sci. USA 50 (1975) 150–154.

[34] E. Tarafdar, Fixed point theorems in $H$-spaces and equilibrium points of abstract economies, J. Austral. Math. Soc. Ser. A 53 (1992), 252–260.

[35] G. Xiao, Z. Fan, R. Qi, Existence results for generalized nonlinear vector variational-like inequalities with set valued mapping, Appl. Math. Lett. 23 (2010) 44–47.

[36] L.A. Zadeh, Fuzzy sets, Inf. Control 8 (1965) 338–353.

[37] H.J. Zimmermann, Fuzzy set Theory and Its Applications, Kluwer Academic Publishers, Dordrecht, 1988.

# Charging Connected and Autonomous Electric Vehicles in Smart Cities

Binod Vaidya and Hussein T. Mouftah
School of Electrical Engineering and Computer Science,
University of Ottawa, Ottawa, ON, Canada
bvaidya|mouftah@uottawa.ca

**Abstract**

In coming years, attraction to alternative urban mobility paradigms such as Connected and Autonomous Electric Vehicles (CAEVs) will increase as CAEVs can significantly contribute to not only optimize traffic flow and improve road safety but also minimize dependence on fossil fuel and reduce carbon emission in urban areas. Nonetheless, there are several barriers towards widespread adoption of CAEVs. In order to have significant growth of CAEVs in urban areas, adequate number of charging facilities in urban areas is needed. However, getting information of the available charging stations is still challenging. Furthermore, the waiting time at the charging stations may be unpredictable. Thus an efficient smart CAEV charging management is required for managing and allocating charging station resources from different charging operators. In this paper, we have designed and implemented a CAEV charging management system that utilizes automated reservation based charging strategies which include effective reservation management and efficient allocation of time slots of wireless charging stations. And we have conducted preliminary evaluations on various charging parameters.

**Keywords**

Connected and Autonomous Electric Vehicles (CAEVs); Smart city; Smart CAEV charging; Automated reservation.

# شحن السيارات الكهربائية المتصلة والمستقلة في المدن الذكية

**الملخص**: في السنوات القادمة، سيزداد الجذب على نماذج التنقل الحضرية البديلة مثل السيارات الكهربائية المتصلة والحركية (ج ا إ ف) حيث يمكن أن تساهم بشكل كبير في تحسين تدفق حركة المرور وتحسين السلامة على الطرق ولكن أيضًا تقليل الاعتماد على الوقود الأحفوري وتقليل انبعاثات الكربون في المناطق الحضرية. ومع ذلك، هناك العديد من الحواجز التي تحول دون اعتمادها على نطاق واسع. من أجل تحقيق نمو كبير في المناطق الحضرية، هناك حاجة إلى عدد كاف من مرافق الشحن في المناطق الحضرية. ومع ذلك، فإن الحصول على معلومات حول محطات الشحن المتاحة لا يزال يمثل تحديًا. علاوة على ذلك، وقت الانتظار في محطات الشحن قد لا يمكن التنبؤ بها. وبالتالي، فإن إدارة الشحن الذكية تتسم بالكفاءة لإدارة وتخصيص موارد محطة الشحن من مشغلي الشحن المختلفين. في هذه الورقة، قمنا بتصميم وتنفيذ إدارة شحن (ج ا إ ف) النظام الذي يستخدم استراتيجيات الشحن الآلي القائمة على الحجز والتي تشمل الإدارة الفعالة للحجز والتخصيص الفعال للفواصل الزمنية لمحطات الشحن اللاسلكي. وقمنا بإجراء تقييمات أولية على معايير الشحن المختلفة.

# 1 Introduction

More than half of the world's population live in urban areas now, and it is anticipated to reach 80% by 2050 [1].

With rapid urbanization, transportation related issues have posed a major impediment to sustainable development for many cities. For instance, the increasing demand for mobility yields significant greenhouse gas (GHG) emissions and thus causes environmental problems (i.e. air pollution, climate change) due to the transportation using internal combustion engines (ICEs) [2].

Futhermore, urban transportation systems are confronting significant challenges owing to the drastic increase in vehicle ownership that yields increased road congestion, longer travel times, growing parking demand as well as larger carbon footprint.

Smart cities, from a transport perspective, should effectively tackle the mobility challenge of rapid urbanization and growing traffic congestion [1, 3].

Connected and Autonomous Electric Vehicles (CAEVs) [4] could be a potential solution to urban transportation problems and thus for mitigating the impact of carbon emissions and climate change.

CAEVs that use emerging communication technologies, deep learning techniques, and highly efficient batteries could transport people more efficiently, without the need for drivers or fossil-fuel based ICEs [5].

Wide adopation of CAEVs could reduce environmental degradation through reduced $CO_2$ emissions while furnishing beneficial economic and social outcomes through improved efficiency, traffic flow, road safety, and greater access [6].

Given the advantages of cleaner and reliable transport, CAEVs could potentially accelerate significantly greenhouse gas emissions reductions in the transport sector and would be beneficial for urban environments such that to improve quality of life in urban area.

Though CAEVs may have the capacity to change the landscape of transportation, recharging CAEVs in the urban area might be challenging.

For the wide-scale deployment of CAEVs in urban areas, significant number of charging facilities should be deployed in urban areas such that CAEVs can recharge whenever they desire.

Although fast charging facilities are emerging, still charging is almost limited to chargers at homes, businesses and public places where recharging takes hours compared to refuelling the ICE-enabled vehicle which takes just a couple of minutes. So CAEVs may have to face longer waiting time at the charging stations. Thus, an efficient smart CAEV charging management is required for managing and allocating charging station resources.

This paper presents automated reservation based charging strategies and depicts implementation of a system that can provide effective automated reservation for CAEVs. One of

the objectives is to minimize waiting time at the charging stations.

Other significances of this system are to alleviate the challenges related to allocation of charging station resources in dense urban area, especially during peak (rush) hour and to assure convenience of automated and coordinated charging strategies.

The remainder of this paper is organized as follows. Section II highlights Related works while Section III describes Connected and Autonomous Electric Vehicles. Similarly, Section IV introduces CAEV Charging Management System. Automated Reservation Mechanism is described in Section V, while deployment of SecCharge CAEV system is depicted in Section VI. Finally, Section VII provides conclusions.

## 2 Related Works

Autonomous vehicle (AV) technologies have been progressing at a very rapid pace over the past decade. Typically, the technological advancement for AV accelerated in 2015. And in recent years, Connected and Autonomous Vehicle (CAV) as well as Connected and Autonomous Electric Vehicle (CAEV) technologies are considered as highly appealing automotive technologies.

Many companies are heavily investing in CAVs and adopting different approaches to bring the change in automotive industry. Typically, the companies working on CAVs can be categorized into Traditional Original Equipment Manufacturer (OEM) players and disruptive players. Traditional OEM players are companies that are already in the automotive business and disruptive players are those that have no significant background in automotive industry such as Waymo, Uber.

In recent years, there have been many researches and studies undertaken in the transportation domain related to CAVs and CAEVs [6, 7, 8]. Some of them focus on CAEV applications, for instance, the paper [9] proposes a secure automated valet parking using privacy-preserving reservation scheme for AVs.

It can be observed that the charging management of Battery Electric Vehicles (BEVs) [10, 11, 12] are well studied. For instance, in the paper [13], the authors have proposed smart charging strategies that incorporate unified Grid-to-Vehicle and Vehicle-to-Grid charging framework in order to provide optimal integration of plug-in electric vehicles (PEVs) within the existing distribution system infrastructure. Similarly, in [14, 15, 16], optimal scheduling mechanisms for charging electric vehicles (EVs) are depicted. However, these techniques may not suitable for CAEVs since CAEVs have unique characteristics such as vehicle autonomy.

Studies in charging management of CAEVs [17, 18, 19] are still in early stage. Major challenge in the charging management of CAEVs is due to the fact that there is less or no human intervention.

The paper [20] proposes an effective, autonomous proportional control scheme for charging EVs, which does not require any real-time communication between the EV and the utility. Whereas in the paper [21], the authors have proposed a multi-class dispatching and charging scheme which can be used for autonomous electric mobility on-demand (AEMoD) services. And the paper [22] investigates electricity use of fully autonomous electric vehicle (AEV) fleets in cities, which is based on a dial-a-ride system. Similarly, the paper [23] presents an AV public transportation system that supports point-to-point services with ride sharing capability as well as manages a fleet of AVs and accommodates a number of transportation requests. The authors focus on two major problems in the system: scheduling and admission control. However, these papers neither deal with reservation of the charging stations nor address issues of waiting time at the charging stations.

# 3 Connected and Autonomous Electric Vehicles

## 3.1 Overviews

Connected and Autonomous Electric Vehicles (CAEVs) are complex automotive systems, combining basically connected vehicles (CV), autonomous vehicle (AV) and electric vehicle (EV).

A connected vehicle (CV) is a vehicle with technology that enables it to communicate with nearby vehicles, infrastructure, as well as objects; but may not be automated nor electrically operated. While, an autonomous vehicle (AV) is a vehicle that is, in the broadest sense, capable of driving itself without human intervention. And electric vehicle (EV) is a vehicle that powers up and operates with energy stored in the battery.

Typically, CAEV is an electric vehicle that is capable of sensing its environment and navigating with little or no human input. CAEV senses its environment using various sensing devices including Radar, LiDAR (Light Detection and Ranging), image sensors, and 3D camera etc. Basically, CAEV is composed of five major components [5].

- Perception system which is responsible for sensing the environment to understand its surroundings.
- Localization and mapping system that enables the vehicle to know its current location.
- Driving policy refers to the decision making capability of a CAEV under various situations, such as negotiating at roundabouts, giving way to vehicles and pedestrians, and overtaking vehicles.
- Communication system: As CAVs will be connected to the surrounding environment such as vehicles with Vehicle to Vehicle connectivity (V2V), to the infrastructure with

Vehicle to Infrastructure (V2I) and to anything else such as the internet: Vehicle to Anything (V2X), through wireless communications links

- Storage Battery System: This system includes charger and battery packs in the vehicle. Basically State of Charge (SoC) level determines the amount of charge stored in the battery.

## 3.2 Need of CAEVs

CAEVs definitely transform existing mobility paradigm. It can be observed that technological advancements in driving assistants and network connectivity yield further opportunities and services and meet the sustainable development for cleaner, safer, and smarter mobility.

CAEVs offer many potential advantages in terms of sustainable development for environment friendly urban mobility, which are as follows.

- Improved safety: may eliminate many of the accidents caused by human error, estimated at about 90% of all accidents.
- Greater mobility: for those who cannot drive, including elderly, disabled, and youth.
- Reduced parking needs: passengers can be dropped off at their destinations without needing a nearby parking space.
- Relaxed drivers: drivers can rest, work, or entertain themselves during a trip.
- Increased car-sharing: reduced need for individually-owned cars.
- Increased road capacity: through fleet platooning, more predictable traffic flow, and reduced congestion
- Fewer $CO_2$ emissions and pollutants: using electric power to operate, can reduce GHG emissions as well as air pollution; minimized environmental impact; improve quality of life in urban area.
- Less fuel costs: Fossil fuel will not be consumed to run CAEV, so fuel consumption is significant reduced.

With wide adoptation of the CAEVs, it is expected to improve road safety, optimize traffic flow, help reduce fuel consumption, and minimize $CO_2$ emissions in the urban environments.

## 3.3 Vehicle Automation

Society of Automotive Engineers (SAE) released SAE International Standard J3016 that sets out taxonomy and standard to define different levels of autonomy [24]. SAE updated its classification in 2016 as SAE J3016_201609.

Basically, vehicle automation has been categorized into various levels of autonomous vehicle technology ranging from Level 0, corresponding to no automation, to Level 5, corresponding to full automation. For instance, automated driver-assistance systems such as adaptive cruise control correspond to lower automation levels, while fully automated driverless vehicles correspond to higher automation levels.

The SAE defined levels of vehicle automation is depicted as follows.

Level 0 – No Automation: In this level, the human driver is responsible for all the driving tasks including control of the car as well as monitoring the road and environment around the car. Level 1 – Driver Assistance: In this level, the human driver is assisted with either steering or acceleration/ deceleration by the driver assistance system but not both. For instance, adaptive cruise control. Level 2 – Partial Automation: In this level, the driver assistance system take care of both acceleration/ deceleration and steering control of the car, while the human driver monitors the road and environment around the car. It includes more advanced levels of driver assistance and requires continuous supervision of the driver. Level 3 – Conditional Automation: In this level, the automated driving system undertakes all aspects of the dynamic driving task with the expectation that the human driver will respond appropriately to a request to intervene. Thus it requires partial supervision of the driver. Level 4 – High Automation: In this level, the automated driving system undertakes all aspects of the dynamic driving task, even if a human driver does not respond appropriately to a request to intervene. This level is basically unsupervised. Level 5 – Full Automation: In this level, the automated driving system undertakes all aspects of the dynamic driving tasks in all roadway and environmental conditions. This level does not require driver at all.

Figure 1 shows SAE defined level of vehicle automation.

| SAE Level | Name | Execution of steering & acceleration/ deceleration | Monitoring of driving environment | Fallback performance of dynamic driving task | System capability (Driving modes) |
|---|---|---|---|---|---|
| Human Driver monitors the Driving Environment | | | | | |
| 0 | No Automation | | | | N/A |
| 1 | Driver Assistance | | | | Some Driving Modes |
| 2 | Partial Automation | | | | Some Driving Modes |
| Automated System monitors the Driving Environment | | | | | |
| 3 | Conditional Automation | | | | Some Driving Modes |
| 4 | High Automation | | | | Some Driving Modes |
| 5 | Full Automation | | | | All Driving Modes |

Figure 1: SAE defined Level of Vehicle Automation

## 3.4 CAEVs in Smart Cities

Smart cities will contain fully-integrated infrastructure, including smart transport services, smart water/ electric grid systems, smart environment monitoring services and others. In turn, these smart systems shall accelerate efficiency and productivity, while improving quality of life.

One of the key components of smart cities are intelligent transportation solutions including CAEVs. For these vehicles to effectively and efficiently travel in the city, several infrastructure changes are required in order to accommodate them. One major change will be the implementation of Road Side Units (RSUs) along streets and highways. The RSUs, which are vital components of Intelligent Transportation Systems (ITSs), use public or private networks to send vital information to the CAEVs. With the help of these RSUs, CAEVs will be able to visualize activities far ahead on their routes.

Smart cities, able to integrate living space with efficient mobility solutions like CAEVs, will necessitate faster and better connectivity, as well as improved data storage. Through the use of emerging communication such as 5G, infrastucture that is complete with sensors will be able to capture surrounding information (such as traffic information) and transmit this data to CAEVs on the road. For instance, a sensor-equipped traffic light would be able to send information about light changes to CAEVs, allowing the latter to act properly.

Other major changes of smart cities will be alterations to the use of parking spaces and traffic flows. The smart cities will most likely see the benefits of intelligent transport if CAEVs are used shared services. With deployment of shared CAEVs, not only the demand for parking or garages will drastically decrease but also the traffic flows in the smart cities will be reduced, in turn, reducing traffic congestions.

# 4 CAEV Charging Management System

In this section, CAEV charging management system based on the SecCharge platform is presented. It consists of following key components: SecCharge CAEV server, Wireless charging station operators (WCSOs), and Energy service providers (ESPs). Figure 2 depicts a high level diagram for CAEV charging management system.

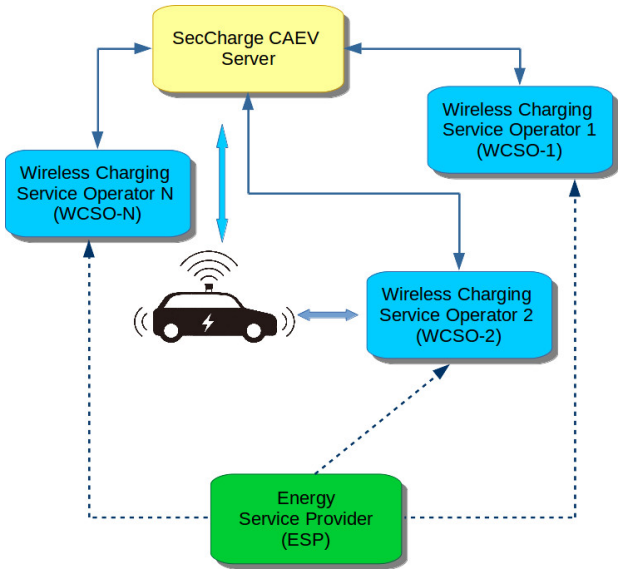


Figure 2: High level diagram for CAEV charging management system

ESPs are autonomous entities producing and distributing energy to the consumers. These consumers may be private (i.e. homeowners) or public (i.e. charging stations operators). Whereas, WCSOs are fundamentally accountable for operation and maintenance of wireless charging stations (WCSs). Typically, WCSOs may manage multiple WCSs at various charging sites/locations. As shown in Figure 2, a particular electric vehicle (EV) charging network may have several WCSOs such as WCSO-1, WCSO-2..,WCSO-N.

A SecCharge CAEV system, which is a central component of the system architecture, acts as a Smart Management Center (SMC) for EV charging. It is designed for facilitating charging services to the CAEVs by providing effectual coordination with various WCSOs in EV charging networks.

On one hand, SecCharge server may provide charging related services to CAEVs including finding WCS location, assigning reservation and managing CAEV information and financial transactions. On another hand, SecCharge server is responsible for interacting with WCSOs for efficient smart charging. The SecCharge CAEV system may establish agreements with different WCSOs in the EV network such that CAEVs can charge in the entire EV charging infrastructure.

Consequently, the SecCharge CAEV system is based on a centralized server that smartly

manages charging related activities. In case of scheduling and reservation services, the system maintains reservation allocation information including occupied and available time slots, so that CAEVs may reserve the WCSs operated by different WCSOs. In the SecCharge CAEV charging management system, automated reservation mechanism is one of the main components.

### 4.1 System Functionality

Main functionality of the SecCharge CAEV Charging management system includes Data collection, Route/Trip planning, and Scheduling and Reservation services.

- Data collection service: CAEVs can obtain information on wireless charging stations (location, technical characteristics, current status). The system also obtains information (i.e. current State-of-charge, current location) from the CAEV and CAEV owner.
- Scheduling and reservation services: CAEVs can reserve the wireless charging stations operated by various WCSOs. The system collects all the information about the reservation. Reservation allocation information including occupied time slot and available time slots can be retrieved. Reservation can be modified, or deleted by the CAEV owner. CAEV owner can also view the historical data of his previous reservations. Detail explanation of automated reservation mechanism is provided in Section 5.

## 5 Automated Reservation Mechanism

In this section, automated reservation mechanism is proposed for SecCharge CAEV Charging Management System [25].

For the wide deployment of the battery electric vehicles (BEVs) as well as CAEVs, a range anxiety is one of the major issues. In order to minimize such an anxiety, charging CAEV in a timely fashion is imperative to guarantee a certain degree of its mobility. However, for EV/CAEV charging, the waiting time at the charging stations is still challenging issue.

Similar to EVs, CAEVs are concerned with charging process as the charging time is still significantly long especially with Level 2 charger. As wireless charging being in very early stage, the charging time is same as with Level 2 charger. Possibly, long charging times may cause considerable delays, owing to not only the CAEV charging process, but also the waiting times due to busy charging stations.

Furthermore, unlike EVs, CAEVs especially level 4 and 5 would driver assistance system shall take most of the tasks, so CAEVs would be responsible for timely charging as well.

In the future, number of CAEVs will increase significantly in the urban areas, then they may experience congestion at several WCSs. Since waiting in queue at the charging stations

may not be convenient for CAEVs, the system should be able to provide current waiting time for the WCSs such that the CAEVs would recharge accordingly. This would help to curtail queuing time at the WCSs.

In this paper, we have proposed a novel automated reservation mechanism for charging CAEVs. By deploying an automated reservation mechanism, the CAEVs can reserve recharging schedule ahead of time, so such a strategy can not only minimize waiting time but also alleviate congestion at the charging stations (i.e. recharging congestion).

Primarily, SecCharge CAEV system embraces charging strategies based on slotted reservation where, a 24-hour period is divided into time slot intervals, for instance, $\delta$ is set at 15 min in our case. Table 1 shows the notations used in the scheme.

Table 1: Notations used in the scheme

| **Symbol** | **Description** |
|---|---|
| $SoC_{\max}$ | Upper limit of SoC level |
| $SoC_{\text{cr}}$ | Critical SoC level |
| $SoC_{\text{th}}$ | Threshold SoC level for a given CAEV |
| $SoC_{\text{tar}}$ | Targeted SoC level for a given CAEV |
| $\epsilon$ | Total energy gained from $SoC_{\text{th}}$ to $SoC_{\text{tar}}$, kWh |
| $t_{\text{tar}}^{\text{th}}$ | Charging time required from $SoC_{\text{th}}$ to $SoC_{\text{tar}}$ |
| $t_{\text{tra}}$ | Travel time to the WCS |
| $t_{\text{arr}}$ | Arrival time at the WCS |
| $t_{\text{wa}}$ | Waiting time at the WCS |
| $t_{\text{s}}^{\text{r}}$ | Reservation start time |
| $t_{\text{f}}^{\text{r}}$ | Reservation finish time |
| $\tau^{\text{r}}$ | Reservation duration |
| $\eta$ | Number of time slots |
| $\delta$ | Time slot interval |
| $Loc_{\text{cur}}$ | Current location of a given CAEV |
| $Dest$ | Destination to be reached by a given CAEV |

Automated reservation allocation scheme is a strategic constituent of the charging strategies. The automated charging module gets information from the sensing unit to determine the state of charge (SoC) of the CAEV. A threshold SoC for a CAEV $SoC_{\text{th}}$, say 25%, is an initial desired SoC level for recharging a particular CAEV. A critical SoC $SoC_{\text{cr}}$ is bare minimum SoC level in the CAEV. It should be noted that $SoC_{\text{th}}$ must be greater than $SoC_{\text{cr}}$.

Thus as soon as current SoC reaches $SoC_{\text{th}}$, it will send an alert and triggers Reservation Request (Reserve_Req).

In automated reservation allocation scheme, the CAEV sends Reserve_Req, which has 3-tuple $\{SoC_{\text{th}}, Loc_{\text{cur}}, Dest\}$, to the SecCharge CAEV system indicating that the CAEV needs recharging. Figure 3 depicts message flows for CAEV Charging.

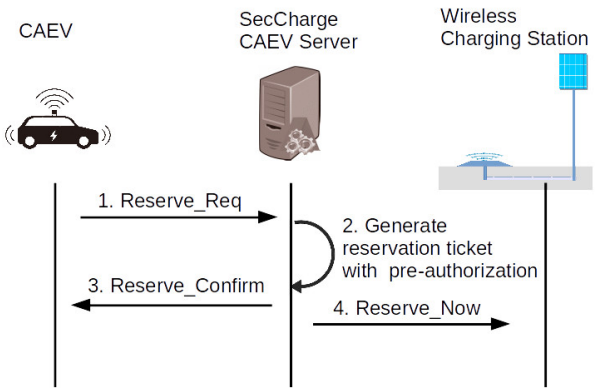


Figure 3: Message Flows for CAEV Charging

Upon receiving Reserve_Req, the SecCharge CAEV Server shall deploy an algorithm for determining appropriate SoC level and reserving time slots with an appropriate charging station. Figure 4 depicts an algorithm flow for the automated reservation.

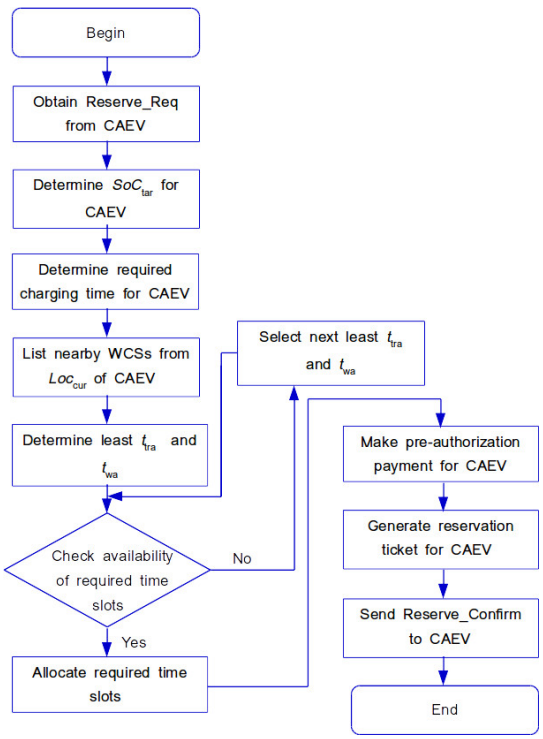


Figure 4: Flow for Automated Reservation Algorithm

Target SoC level for recharging is given by:

$$SoC_{\text{tar}} = \alpha\left(SoC_{\max} - SoC_{\text{cur}}\right)$$

where $\alpha$ is a coefficient for recharging, such that $\alpha \in \{0,1\}$.

Determination of $\alpha$ depends on various factors such as distance to be travelled, a location of a WSC (i.e. downtown or suburb) and time of day (peak hour or wee hour). As SecCharge CAEV server is responsible for determining $\alpha$, in turn, $SoC_{\text{tar}}$ for each CAEV, a slot allocation in WSC will be optimal.

Required charging time $t_{\text{char}}$ is computed as:

$$t_{\text{char}} = SoC_{\text{tar}} \times \frac{Q}{CR_x \times \mu}$$

where $Q$ is CAEV's battery capacity (kWh); $CR_x$ is charge rate; $\mu$ is CAEV charging efficiency, typically, $\mu = 0.9$.

While computing $t_{\text{char}}$, $CR_x$ should be considered with lower value of either the vehicle's acceptance rate or the WSC power output rate.

With the list of nearby WSCs, the SecCharge CAEV Server shall compute travel time ($t_{\text{tra}}$) to each WCS as well as waiting time ($t_{\text{wa}}$). The waiting time ($t_{\text{wa}}$) is the time between the arrival time ($t_{\text{arr}}$) of the CAEV to the WSC and the time that the CAEV starts to receive charging service.

Then the SecCharge CAEV Server shall determine the WSC with the least $t_{\text{tra}}$ and $t_{\text{wa}}$ and check if the required time slots are available in the given WSC.

If the required time slots are not available, then the SecCharge CAEV Server shall choose the next WSC with lower $t_{\text{tra}}$ and $t_{\text{wa}}$.

After allocating the time slots in the given WSC, the SecCharge CAEV Server shall generate Reservation ticket, which has reservation information. At least, the reservation information for the CAEV shall have Reservation start time($t_{\text{s}}^{\text{r}}$), Reservation finish time ($t_{\text{f}}^{\text{r}}$) and information on WSC location.

Reservation finish time and reservation duration can be computed as follows.

$$t_{\text{f}}^{\text{r}} = t_{\text{s}}^{\text{r}} + \eta \times \delta$$
$$\tau^{\text{r}} = t_{\text{f}}^{\text{r}} - t_{\text{s}}^{\text{r}}$$

After successful pre-authorization payment with help of the Payment gateway, the status changes to 'payment pre-authorized'. Upon successful generation of the reservation ticket, the SecCharge CAEV server shall send a confirmation for automated reservation (Reserve_Confirm) to the CAEV. In the meantime, the SecCharge CAEV server shall also send the automated reservation details (Reserve_Now) with $\tau^{\text{r}}$ in order to reserve time

slot(s) at the given WCS.

Upon receiving Reserve_Confirm, the CAEV can obtain a desired route to re-route via the given WCS.

# 6 Deployment of SecCharge CAEV System

This section describes the deployment of SecCharge CAEV Charging Management system. It includes real-world implementation in a testbed as well as case studies and analysis.

## 6.1 Implementation in Testbed

SecCharge CAEV system utilizes combination of client-server, web-based and mobile architecture. It has several key components such as back-end servers, Control center server, and payment gateway modules.

At the back-end, it consists of Application server, Database server and Authentication server. The back-end system is connected to the payment gateway for financial transaction. The client can access to the back end system through mobile or web applications.

The back-end server has connection to the Control center server for accessing wireless charging stations. Figure 5 depicts system architecture for SecCharge CAEV Charging Management System.

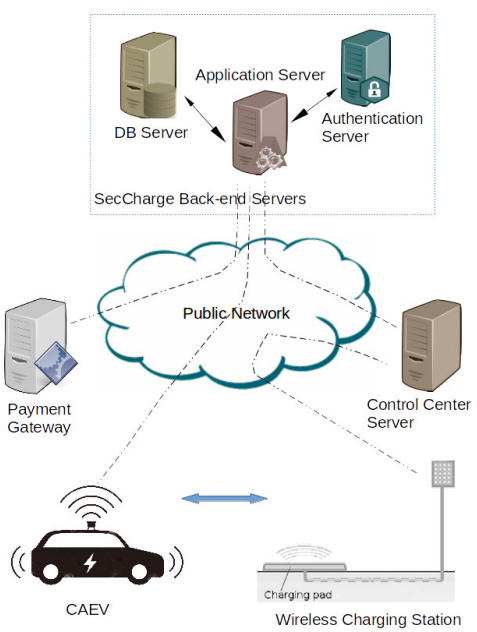


Figure 5: Testbed for SecCharge CAEV Charging Management System

The technical specifications of the SecCharge CAEV system are discussed as follows.

The SecCharge application is built on Model View Controller (MVC) architecture. MVC architecture divides application into three parts which are interconnected and have loose coupling. Loose coupling among these three components allows code reuse and easy code modification.

- Model: A model stores information that is recovered from the controller and showed in the perspective user interface view.
- View: A view is graphical user interface that creates a yield presentation to the client in light of changes in the model.
- Controller: A view controller creates a yield perspective and an inserted controller. It manages the interaction between the view and model.

The MVC architecture is implemented using the Spring framework which is generally referred as Spring MVC.

Oracle Express edition has been used as the database for application due to its highperformance speed and multiple databases support. Hibernate is an ORM (Object Relational Mapping) API which abstracts the SQL from developers. This allows developers to focus primarily on developing business logic thus speeding up the software development.

Apache Tomcat provides a light weight web container to host SecCharge application. Primarily Tomcat was used because it supports Java and is compatible with Spring MVC and consumes less memory.

And Eclipse is deployed as a fundamental Integrated Development Environment (IDE) for web application development, while Android Studio is used as IDE for Android platform development.

Being open source operating system and Linux distribution based on Debian, Ubuntu is considered as underlying operating system in the SecCharge system.

Representational State Transfer (REST) is an architectural style that specifies constraints to induce desirable properties like performance, scalability and modifiability. These desirable properties make a web service work best on the web. RESTful web services are the web services which implements REST architecture. In SecCharge system, web services are implemented using REST API provided by Spring framework. All HTTP/ HTTPS calls in the application are performed over RESTful web services. And being lightweight data-interchange format, JavaScript Object Notation (JSON) is used.

As Open Charge Point Protocol (OCPP) is an application protocol for communication between wireless charging stations and a central management system, the OCPP is considered as communication protocols between WCSs and the SecCharge CAEV server in our implementation. Being an open protocol, the OCPP would allow wireless charging stations and central systems from different vendors to easily communicate with each other.

For the testbed deployment, the SecCharge CAEV platform uses miniture CAEV. The miniture CAEV is built with remote controlled (RC) car that has been modified using Raspberry Pi 3 along with a Pi camera and $I^2C$-bus Pulse-width modulation (PWM) controller, namely PCA9685. In order to achieve an automated driving capability, it uses various software libraries including OpenCV (Open Source Computer Vision) and machine learning tools such as Tensorflow and Keras.

Google Map platform is used to compute a distance to be travelled and a time taken for that distance.

## 6.2 Case Studies and Analysis

In order to provide an efficient automated reservation service, charging parameters should be properly adjudicated. However, determining the charging time may not be straightforward, since it may take long time for full charge. Especially, when the CAEV has limited time for recharging, the required charging time should be determined with pertinent $SoC_{\text{tar}}$.

Furthermore, during daytime, the charging stations in the urban areas may be very demanding. So determining appropriate number of time slots for charging BEVs/CAEVs may be challenging. With efficient allocation of the time slots, the waiting time at the charging stations can be significantly minimized.

For the testbed implementation, we have considered several assumptions in case of the electric vehicles and charging stations.

Since technical details for fully-fledged CAEVs (i.e. Level 4 and 5) are not available till the date, we have determined to utilize the technical specifications of the existing Battery Electric Vehicles (BEVs) for the testbed implementation. Table 2 shows the technical specifications of BEVs that are considered for the testbed implementation.

Table 2: Technical Specifications of BEVs [26]

| Make, Model, Year | Battery capacity | Onboard charger | Total range (EPA rating) | Charging time for full charge | Avg Fuel consumption rating |
|---|---|---|---|---|---|
| | kWh | kWh | km | h | kWh/100km |
| Smart fortwo 2017 | 17.6 | 7.2 | 93 | 3 | 19.6 |
| Nissan Leaf 2017 | 30 | 6.6 | 172 | 6 | 18.6 |
| BMW i3 94Ah 2017 | 33 | 7.4 | 183 | 5 | 17.8 |
| Ford Focus Electric 2017 | 33.5 | 6.6 | 185 | 5.5 | 19.6 |
| Chevrolet Bolt 2017 | 60 | 6.6 | 383 | 9.3 | 17.6 |
| Tesla Model S 75D 2017 | 75 | 10 | 417 | 12 | 20.3 |

Environmental Protection Agency (EPA) has specified a total range (EPA rating) covered

by a BEV with full charge, shown in the Table 2.

Charging time for full charge is shown in the Table 2. Basically, the charging time for BEV may depend on following parameters:

- Current SoC level or Energy stored in its battery pack.
- Size of battery pack or Battery capacity.
- On-board charger capacity or Vehicle acceptance rate
- Output of a charging station

For the convenience, plug-in charging outlets such as the International Electrotechnical Commission (IEC) 62196-2 chargers are considered. Typically, in the testbed implementation, we have considered three Level 2 chargers, namely, a) charger with 240V, 3.6kW, 16A; b) charger with 240V, 7.3kW, 32A; and c) charger with 400V, 11kW, 16A.

**Case I**

Case I depicts the analysis of BEV charging parameters with the given $SoC_{\text{tar}}$.

With the assumption of plug-in charging outlet with 7.3kW, 32A, several sessions of charging process were conducted for the selected BEVs.

Assuming $SoC_{\text{th}}$ at 25%, $SoC_{\text{tar}}$ is computed such that SoC level reaches at 60%. Then we have obtained various BEV charging parameters including $\epsilon$, $t_{\text{tar}}^{\text{th}}$, $\tau^{\text{r}}$, and $\eta$. Table 3 shows various BEV charging parameters for the selected BEVs.

Table 3: BEV charging parameters

| Make, Model, Year | $\epsilon$, kWh | $t_{\text{tar}}^{\text{th}}$, h | $\tau^{\text{r}}$, h | $\eta$ |
|---|---|---|---|---|
| Smart fortwo 2017 | 6.2 | 0.97 | 1 | 4 |
| Nissan Leaf 2017 | 10.5 | 1.73 | 1.75 | 7 |
| BMW i3 94Ah 2017 | 11.5 | 1.73 | 1.75 | 7 |
| Ford Focus Electric 2017 | 11.7 | 1.94 | 2 | 8 |
| Chevrolet Bolt 2017 | 21.0 | 3.18 | 3.25 | 13 |
| Tesla Model S 75D 2017 | 26.3 | 3.93 | 4 | 16 |

It can be seen that eventhough the bigger BEVs yield larger $\epsilon$ than the smaller BEVs, the formers need more $\eta$ than the latters. With the appropriate charging time for different types of BEVs, the system shall be able to efficiently manage the time slots $\eta$ from various WCSs.

## Case II

Case II delineates variation of BEV charging parameters for the specified range. In this case, we have selected two representative BEVs, namely, BMW i3 94Ah 2017 and Tesla Model S 75D 2017.

In order to accumulate similar range, about 100 km, during charging process, $SoC_{\text{tar}}$ for BEV should be appropriately computed. It can be observed that determination of $\alpha$ depends on the distance to be travelled.

Assuming intial SoC is $SoC_{\text{th}}$, $SoC_{\text{tar}}$ is computed with proper selection of $\alpha$. Then various BEV charging parameters (i.e. $\epsilon$, $t_{\text{tar}}^{\text{th}}$, $\eta$) are obtained for that specified range. Table 4 shows the BEV charging parameters for the specified range.

Table 4: BEV charging parameters for the specified range

| Make, Model, Year | $SoC_{\text{tar}}$, % | $\epsilon$, kWh | $t_{\text{tar}}^{\text{th}}$, h | $\eta$ |
|---|---|---|---|---|
| BMW i3 94Ah 2017 | 79 | 17.8 | 2.73 | 11 |
| Tesla Model S 75D 2017 | 52 | 19.5 | 3.13 | 12 |

To achieve similar added distance, $SoC_{\text{tar}}$ for BMW i3 is significantly higher than that for Tesla Model S. However, BMW i3 requires slightly lesser $t_{\text{tar}}^{\text{th}}$, in turn, $\eta$ than Tesla Model S.

## Case III

Case III illustrates the effect of the charging outlet outputs on the BEV charging parameters.

Appropriate selection of the Level 2 charging outlet may be desirable since with higher charger output, the charging time and the number of time slots can be reduced drastically.

Figure 6 depicts charging time and number of time slots required for various Level 2 chargers.

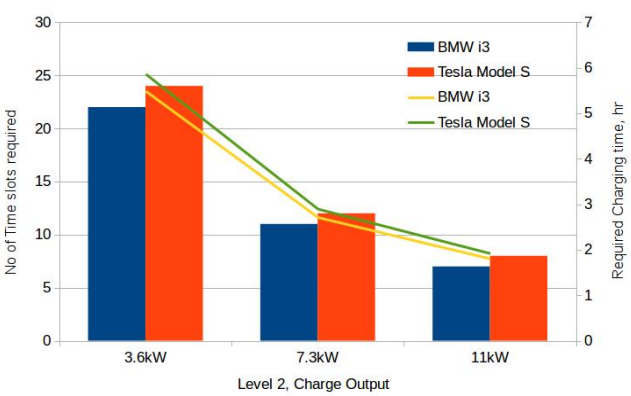


Figure 6: Charging time and number of time slots required for various Level 2 chargers

It can be observed that the charging time decreases with the increase in the charger output. Furthermore, with 7.3kW charger, $\eta$ for BMW i3 and Tesla Model S are 11 and 12 respectively, whereas with 11kW charger, $\eta$ for BMW i3 and Tesla Model S are 7 and 8 respectively.

The system shall choose the charging outlet with appropriate charger output for efficient management of the WCSs.

**Case IV**

Case IV depicts the selection of appropriate targeted SoC level. In order to provide efficient allocation of the time slots at the charging stations, precise computation of $SoC_{\text{tar}}$ is essential, which mainly relies upon $\alpha$.

Determining proper targeted SoC level might be challenging since on one hand, CAEVs do not need to recharge more frequently, but another hand, CAEVs do not have to spend lot of time at the charging stations.

Figure 7 shows the charging time with respect to various $SoC_{\text{tar}}$. With increasing $SoC_{\text{tar}}$, the required charging time increases significantly. In order to provide efficient time slot allocation, $SoC_{\text{tar}}$ needs to be computed precisely.

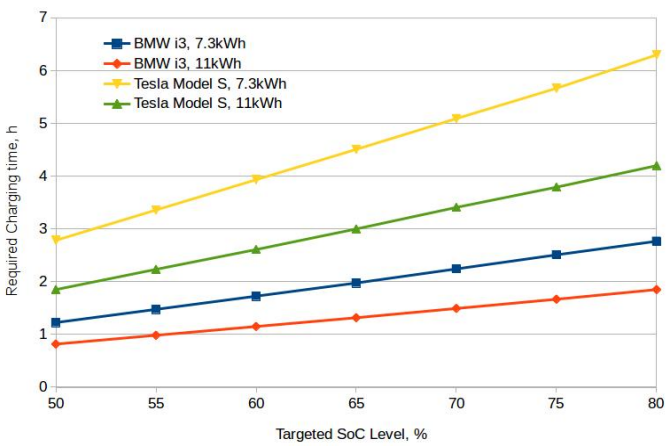


Figure 7: Charging time with respect to various targeted SoC levels

Figure 8 illustrates the energy gained with respect to various $SoC_{\text{tar}}$. The energy gained for Tesla Model S is distinctly greater than that of BMW i3 for all $SoC_{\text{tar}}$. For instance, at $SoC_{\text{tar}} = 60\%$, Tesla Model S has gained 26.3kWh, whereas BMW i3 has gained only 11.5kWh.

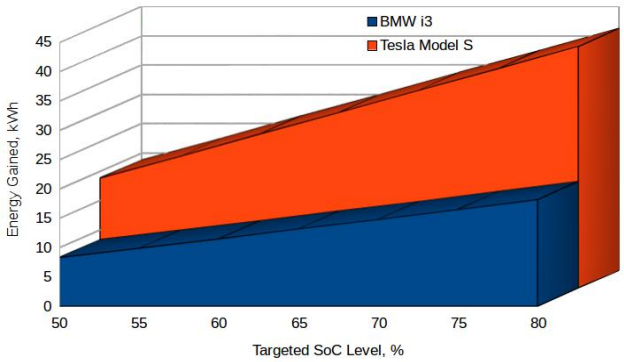


Figure 8: Energy gained with respect to various targeted SoC levels

Figure 9 characterizes the range added with respect to various $SoC_{\text{tar}}$. The range added for Tesla Model S is significantly higher than that of BMW i3 for every $SoC_{\text{tar}}$. For example, at $SoC_{\text{tar}} = 60\%$, BMW i3 has added only 64.4km, while Tesla Model S has added 146.4km.

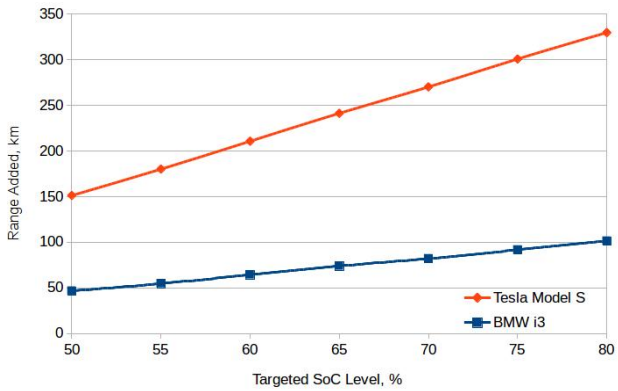


Figure 9: Range added with respect to various targeted SoC levels

# 7 Conclusions

Connected and Autonomous Electric Vehicles (CAEVs) are getting attention due to the fact that they can provide significant benefits such as improved traffic flow, improved road safety, reduced carbon emission in urban areas and minimized dependency on fossil fuel.

For greater penetration of CAEVs in the smart cites, the deployment of charging facilities in urban areas should be well considered. However, getting information on the availability of charging stations and duration of waiting time at the charging stations is still challenging. In order to manage and allocate the charging station resources from different WCSOs, an efficient and smart CAEV charging management is necessitated. We have designed a system utilizing automated reservation based charging strategies that include effective reservation management and efficient allocation of time slots of wireless charging stations. In this system,

charging strategies based on automated reservation are used, which encompass optimum WCS selection in terms of waiting time and charging time as well as scheduling including reservation slot allocation and pre-authorized payment.

The test-bed was built using Backend servers and modified RC cars built on Raspberry Pi. And case studies are carried out along with the analysis to verify the efficient allocation of the time slots in WCSs.

## Acknowledgement

This research work is supported by Smart Grid Fund (SGF), Ministry of Energy, The Ontario Government and Canada Research Chair (CRC) Fund, Canada.

## References

[1] H. S. M. Lim and A. Taeihagh, "Autonomous vehicles for smart and sustainable cities: An in-depth exploration of privacy and cybersecurity implications," *Energies*, vol. 11, no. 5, 2018.

[2] S. Huang, L. He, Y. Gu, K. Wood, and S. Benjaafar, "Design of a mobile charging service for electric vehicles in an urban environment," *IEEE Transactions on Intelligent Transportation Systems*, vol. 16, no. 2, pp. 787–798, 2015.

[3] E. Paffumi, M. De Gennaro, G. Martini, and H. Scholz, "Assessment of the potential of electric vehicles and charging strategies to meet urban mobility requirements," *Transportmetrica A: Transport Science*, vol. 11, no. 1, pp. 22–60, 2015.

[4] S. A. Bagloee, M. Tavana, M. Asadi, and T. Oliver, "Autonomous vehicles: challenges, opportunities, and future implications for transportation policies," *Journal of Modern Transportation*, vol. 24, no. 4, pp. 284–303, 2016.

[5] D. Gonzalez, J. Perez, V. Milanes, and F. Nashashibi, "A review of motion planning techniques for automated vehicles," *IEEE Transactions on Intelligent Transportation Systems*, vol. 17, no. 4, pp. 1135–1145, 2016.

[6] Y. Zhang, G. Zhang, R. Fierro, and Y. Yang, "Force-driven traffic simulation for a future connected autonomous vehicle-enabled smart transportation system," *IEEE Transactions on Intelligent Transportation Systems*, vol. 19, no. 7, pp. 2221–2233, 2018.

[7] A. M. Taha and N. AbuAli, "Route planning considerations for autonomous vehicles," *IEEE Communications Magazine*, vol. 56, no. 8, pp. 78–84, 2018.

[8] R. W. L. Coutinho, A. Boukerche, and A. A. F. Loureiro, "Design guidelines for information-centric connected and autonomous vehicles," *IEEE Communications Magazine*, vol. 56, no. 8, pp. 85–91, 2018.

[9] C. Huang, R. Lu, X. Lin, and X. Shen, "Secure automated valet parking: A privacy-preserving reservation scheme for autonomous vehicles," *IEEE Transactions on Vehicular Technology*, 2018.

[10] R. Wang, G. Xiao, and P. Wang, "Hybrid centralized-decentralized (hcd) charging control of electric vehicles," *IEEE Transactions on Vehicular Technology*, vol. 66, no. 8, pp. 6728–6741, 2017.

[11] Y. Qiao, K. Huang, J. Jeub, J. Qian, and Y. Song, "Deploying electric vehicle charging stations considering time cost and existing infrastructure," *Energies*, vol. 11, 2018.

[12] Y. Cao, T. Wang, O. Kaiwartya, G. Min, N. Ahmad, and A. H. Abdullah, "An ev charging management system concerning drivers' trip duration and mobility uncertainty," *IEEE Transactions on on Systems, Man, and Cybernetics: Systems*, vol. 48, no. 4, pp. 596–607, 2018.

[13] R. Mehta, D. Srinivasan, A. M. Khambadkone, J. Yang, and A. Trivedi, "Smart charging strategies for optimal integration of plug-in electric vehicles within existing distribution system infrastructure," *IEEE Transactions on Smart Grid*, vol. 9, no. 1, pp. 299–312, 2018.

[14] A. Gusrialdi, Z. Qu, and M. A. Simaan, "Distributed scheduling and cooperative control for charging of electric vehicles at highway service stations," *IEEE Transactions on Intelligent Transportation Systems*, vol. 18, no. 10, pp. 2713–2727, 2017.

[15] Y. Zhang, P. You, and L. Cai, "Optimal charging scheduling by pricing for ev charging station with dual charging modes," *IEEE Transactions on Intelligent Transportation Systems*, 2018.

[16] Y. Zheng, Y. Song, D. J. Hill, and K. Meng, "Online distributed mpc-based optimal scheduling for ev charging stations in distribution systems," *IEEE Transactions on Industrial Informatics*, vol. 15, no. 2, pp. 638–649, 2019.

[17] J. Paska, M. Klos, L. Roslaniec, R. Bielas, and M. Bledzinska, "Autonomous electrical vehicles' charging station," *Acta Energetica*, vol. 3, no. 28, pp. 109–115, 2016.

[18] V. D. Doan, H. Fujimoto, T. Koseki, T. Yasuda, H. Kishi, and T. Fujita, "Allocation of wireless power transfer system from viewpoint of optimal control problem for autonomous driving electric vehicles," *IEEE Transactions on Intelligent Transportation Systems*, vol. 19, no. 10, pp. 3255–3270, 2018.

[19] Z. Yi and M. Shirk, "Data-driven optimal charging decision making for connected and automated electric vehicles: A personal usage scenario," *Transportation Research Part C*, vol. 86, pp. 37–58, 2018.

[20] G. M. A. Akhtar, A. T. Al-Awami, E. Sortomme, M. A. Abido, and M. W. Ahmed, "Autonomous electric vehicle charging management over real time digital simulator," in *Proc. 2014 IEEE PES General Meeting Conference & Exposition*, Washington, DC, USA, Jul 2014.

[21] S. Belakaria, M. Ammous, S. Sorour, and A. Abdel-Rahimyz, "A multi-class dispatching and charging scheme for autonomous electric mobility on-demand," in *Proc. 2017 IEEE 86th Vehicular Technology Conference (VTC-Fall)*, Toronto, Canada, Sep 2017.

[22] J. Munkhammar and M. Shepero, "Autonomous electric vehicle fleet charging in cities: Optimal utility estimates and monte carlo simulations," in *Proc. 2017 IEEE PES Innovative Smart Grid Technologies Conference Europe (ISGT-Europe)*, Torino, Italy, Sep 2017.

[23] A. Y. S. Lam, Y. W. Leung, and X. Chu, "Autonomous-vehicle public transportation system: Scheduling and admission control," *IEEE Transactions on Intelligent Transportation Systems*, vol. 17, no. 5, pp. 1210–1226, 2016.

[24] T. Inagaki and T. B. Sheridan, "A critique of the sae conditional driving automation definition, and analyses of options for improvement," *Cognition, Technology & Work*, 2018.

[25] B. Vaidya and H. T. Mouftah, "Automated reservation mechanism for charging connected and autonomous evs in smart cities," in *Proc. 2018 IEEE 88th Vehicular Technology Conference (VTC2018-Fall) Workshop*, Chicago, USA, Aug 2018.

[26] "2017 model year electric vehicles," Natural Resources Canada (NRCan), Government of Canada, Ottawa, Canada. [Online]. Available: https://www.nrcan.gc.ca/energy/efficiency/transportation/21365

# Spatio-Temporal Database Modeling And Applications For Assistance Of Huge Crowd In Hajj

**Kashif Rizwan**
Department of Computer Science, {Federal Urdu University of Arts, Science & Technology, Pakistan & University of Karachi, Pakistan}
kashifrizwan@fuuast.edu.pk

**Nadeem Mahmood**
Department of Computer Science, University of Karachi, Karachi, Pakistan
nmahmood@uok.edu.pk

**Adnan Nadeem**
Faculty of Computer and Information System,
Islamic University in Madinah, KSA
adnan.nadeem@iu.edu.sa

**Ali Mousa G. A lzahrani**
Faculty of Computer and Information System,
Islamic University in Madinah, KSA
alnaashi1@gmail.com

**Abstract:** The annual Islamic pilgrimage, Hajj has become very easy and planned in this era. Authorities in the Kingdom considering to make this Holy event more secure, convenient and controlled by planning strategically and comprehensively. For this, Government launched a program, called Vision 2030. This program intends to facilitate and serve Muslims who gathered annually in Makkah-tul-Mukarramah. Presented research proposes a model and architecture for the Hujjaj monitoring and tracking using a mobile based application. This application can function as a guide or facilitator for Hujjaj whilst performing Hajj (The Fifth pillar of Islam). The gathering of hujjaj for Hajj is taken into account as, the most important annual gathering of Muslims on earth. Hajj is a demonstration of the cohesion of the Muslim brotherhood, and their submission to ALLAH, entirely. The word Hajj is a manner of ritual or to intend a journey, which connotes each, the outward act of a journey and the inward act of intentions. Theme of this proposed application is to make sure that the Haji perform rituals (manasik) without a doubt, in accordance with the Sunnah. Presented application at the one hand is capable to improve Hajj services, and at the other hand, it additionally make sure that Haji is aware of that, 'wherein he/she is and in wherein he/she supposed to be'. We used the foundation

of spatio-temporal concepts and theory to model data, operators and functions. These spatio-temporal constructs are then integrated with geofence information to the proposed framework as a conceptual model for system. Presented application has the potential to increase the modern strategies in the way to offer assistance and provided quality of services.

**Keywords:** Spatio-Temporal Modelling, Hajj, Pilgrims, Huge Crowd Management System, Realtime Tracking and assistance, Mobile applications

# نمذجة قاعدة البيانات المكانية والزمانية وتطبيقات مساعدة الحشود الضخمة في الحج

**الملخص**:الحج الإسلامي السنوي ، أصبح سهلا للغاية على غرار السنوات السابقة لعصر التكنولوجيا . تفكر السلطات في المملكة في جعل هذا الحدث المقدس أكثر أمانًا وملاءمة والقدرة على التحكم بهذا الحدث من خلال التخطيط الاستراتيجي والشامل. ومن اجل ذلك أطلقت الحكومة بما يسمى رؤية 2030. وتهدف الرؤية إلى تسهيل وخدمة المسلمين المجتمعين سنويًا في مكة المكرمة. وعلى صعيد نتائج البحوث المقدمة و المقترحة لرصد الحجاج والمساعدة في استخدام وانشاء تطبيقات الهواتف الذكية التي تخدم الحجاج . ومن الممكن أن تعمل التطبيقات كدليل للحجاج أثناء أداء الحج (الركن الخامس من الإسلام). مع الاخذ في الاعتبار العدد الكبير للحجاج المتزايد على مر السنين ، وهو يعد أهم تجمع سنوي للمسلمين على الأرض. الحج دليل على تماسك المسلمين ، وخضوعهم لله. كلمة الحج هي تعني طقوس أو رحلة ، والتي تدل على كل فعل خارجي وداخلي . فكرة انشاء التطبيق هي التأكد من أن الحجاج يؤدون طقوسهم بشكل كامل وسهولة وبلا شك او نقصان ، وفقًا للسنة. البرنامج المقدم قادر على زيادة الربحية وتحسين خدمات الحجيج. من ناحية أخرى ، والتأكد أيضًا من أن الحجاج لديهم العلم بذلك. وتم بناء التطبيق على عدد من الاسس و المفاهيم النظرية و المكانية و الزمانية لتجميع البيانات. ثم سيتم دمج هذه البنى المكانية والزمانية مع معلومات السور الجغرافي للإطار المقترح والنموذج المفاهيمي لنشر قاعدة البيانات. وسيزيد التطبيق من الاستراتيجيات الحديثة في طريقة تقديم المساعدة والرضا للسماح للعملاء بالتفاعل بأسهل طريقة ممكنة

## 1. Introduction

It is considered that the Hajj is most important pillar of Islam, covers all kinds of rituals. In the last month of Hijri calendar Hajj is done once in a year. In the Kingdom of Saudi Arabia Makkah, Hajj is performed by the Muslims. It is the duty of every healthy and wealthy Muslim to perform Hajj once in a life. All those Muslims who has a great health and good finance should perform Hajj. There are five pillars of Islam and Hajj is set on 5th. The word “Hajj” is to make intention to a Holy journey. Muslims start to perform Hajj from the 8 ZilHajjah to 12 ZilHajjah (13 ZilHajjah for other case). A man who pilgrims called Haji and Hajjah for female. Very large number of Muslims approximately three million of Hijjaj perform this sacred rituals of Hajj by gathering in Makkah. When the second last month of Islam ZilQadah starts the Hujjaj arrives to Saudi Arabia. With good preparation and great intention in their heart the Muslims enter in Meeqat. It takes a week to gather in Mecca. Every Muslim starts to walk seven times clock wise around the Ka’ba.

They run back between the hills Al-Safa and Al-Marwah where the drink zamzam well, then they move towards Mount Arafat where in the plain of Muzdalifa they spend a night, They through stones at evil three pillars which is also the part of Hajj. Then the time comes when they shave their heads and sacrifice animal and also celebrate three days of Eid-ul-Adha. There is also a details for the places they visited which is also has to follow. Now the Hajj is performed which starts 8$^{th}$ Zil Hajj to 12$^{th}$ Zil Hajj.

One of the main aims of this paper is to propose a novel definition of Hajj as spatio-temporal event. Hajj is defined as an event where Pilgrim has a mandatory religious obligation to move into a specific place at specific time and stay for a specific period; and leave a specific place at a specific time and perform rituals as per Quran and Sunnah". In this perspective, a Pilgrim (called Moving Object) is bound to move (enter into or depart) a specific place (a Spatial attribute) at specific time ( Valid Time VT, or Transaction Time TT) for a specific period (time interval) during the course of Hajj (called Event). Therefore, the event of Hajj may be defined as spatio-temporal event where Pilgrim is the spatio-temporal object.

### 1.1 Problems Faced by Pilgrims during Hajj

In Islam Hajj is set of all rituals. Every year Not only the Hundreds or Thousands of Pakistani but also people of all over the world performs Hajj. These are not enough the facilities that are provided to Pakistani pilgrims, Major problems are also present especially for Pakistani not distant residence like stampede, lack of guidance etc. For performing Hajj millions of Muslims are gathered in Makkah_tul_Mukarramah every year. It becomes a challenge for the Kingdom authorities to give best security to pilgrims. Events are disturbed during this occasion with accidents and tragedies. Some of them are listed in (**Table 1)**.

Table 1: Accidental events and tragedies during Hajj [5]

| Date | No. of Martyrs | Place | Reason |
|---|---|---|---|
| 24-09-2015 | 310 | Mina | Stampede |
| 12-01-2006 | 360 | Jamaraat | Stampede |
| 22-01-2005 | 3 | Mina | Stampede |
| 01-02-2004 | 250 | Mina | Stampede |
| 11-02-2003 | 14 | Jamaraat | Stampede |
| 05-03-2001 | 35 | Mina | Stampede |
| 09-04-1998 | 118 | Mina | Stampede |
| 15-04-1997 | 343 | Mina | Fire Spread |
| 24-05-1994 | 270 | Jamaraat | Stampede |
| 02-07-1990 | 1426 | Mina | Suffocation in Tunnel |

The capacity of Haram for Hujjaj is being increased very fast. During performing of rituals see **(Table 2)** pilgrims may face various types of problems for instance lost and found scenarios.

Table 2: Spatio-Temporal-Event based application support [8]

| Important Movements of Haji w.r.t Space, Time and Event | Application Support |
|---|---|
| Meeqaat Entrance and/or Exit | Location based notification to Haji using App. before and after entrance and / or exit |
| Perform Umrah | Notifies Haji step by step as per selection of Hajj Type and Classifies accordingly before entering into Meeqaat |
| Perform Tawaaf | Assist Haji by Automatic Tawaaf Counter |
| Perform Sa'ee | Assist Haji by Automatic Sa'ee Counter |
| Move to Mina | Location based notification to Haji using App. before and after entrance and / or exit with respect to date and time |
| Move to Arafaat | Location based notification to Haji using App. before and after entrance and / or exit with respect to date and time |
| Move to Muzdlifah | Location based notification to Haji using App. before and after entrance and / or exit with respect to date and time |
| Go to Jamaraat | Notifies Haji with respect to Location, date and time |
| Go to Building/Hotel | Notifies Haji with respect to Location, date and time |

### 1.2 Primary Logical Flow Of Start Of Hajj Application (In Perspective Of UI Screens And Messages)

*1)* First residence select the type of Hajj.
*2)* Now it will check the Haji's current location that it is right or wrong based on above description.
*3)* Now next information is displayed.
*4)* Meqaat is validated.
*5)* Residence is validated.
*6)* With respect to event, location and time validate NEAR/IN/OUT of all other fences.
*7)* As per event, location and time information is displayed.

### 1.3 Application's Description:

It is worked as a remedial application by the proposed application to the problems which is defined above. To ensure the smooth performance of Ibadat the following three parameters of the application are focused by our application.

### 1.3.1 Monitoring

Aware that a right person is at the right place at right time.

### 1.3.2 Assistance


(a) The Nymi [4]


(b) Hajj QR wristband

Fig. 1: Wrist band approaches

Second measure feature of application is Assistance. On the basedof current location, date and time will be guided by Haji.

### 1.3.3 Tracking

Update the location of pilgrime by tracking them on server, for security reason it is reviewed the location of Hijaj.

Providing above facilities, several features will be able to provide by our application in future. Currently in our application it is focused on limited features. Key functions includes:

1. Location Based Routing and Assistance for Hujjaj
2. Immediate Monitoring and Controlling of Hujjaj as
3. Transportation Facilitation
4. Improved Disaster Management
5. uide/ Route Hujjaj for Load Balancing To Avoid Extreme Rush

6. Manage Every Single Person in Hujjaj for Timely Fulfillment of Every Activity (As Per 'Sunnah' صلى الله عليه وسلم)
7. Planning Hujjaj's Food
8. Making Prompt Decision Support
9. Improved Quality of Services during Hajj
10. Monitor and Track Hujjaj
11. Assist Hujjaj in His/her Native Language
12. Healthcare Management and Control

Hujjaj has been allotted QR wrist band (See Fig. 1b) first time in year 2016 that has following information printed:

1. Gender
2. QR code for location in Mina
3. QR code for location in Arafaat
4. Maktab Number
5. Muallim details
6. Jamaraat Timings
7. Tent Number

It has the only yet very strong power to passively assist hujjaj upon a manual trigger a smart phone application using Hajj Bracelets Reader to check the current location of Haji from its one of two destination locations during Hajj days i.e., Mina camp and Arafaat. Moreover, it has mentioned the date and time of Rami and Gender classification containing the tent number and Maktab number, region Haji belongs to, Mu'allim's name and finally the seven color code. In Mina, the location of bed for each Haji (i.e., around one square meter) is marked and valley of Mina is divided in these seven color codes. This can be visualized imply in a grid of 11x8 squares on a digital map (like google map).

### 1.4 NYMI Band

Nymi [4] is experimentaly used for identifying Hujjaj in this study but unsuccessful to fully integrate with obtaining unique heart ID of person as it has claimed, using the procured wrist bands. It claims a unique heart ID capturing function of every person with wearable wristband that exploit the features of Nymi that uses heart ID for identifying Haji. Person using his/her unique cardiac rhythm ECG by Nymi authentication. It is worked with sensors that is shown in **Fig. 1(a)**.

Table 3: Space vs Time[8]

| Space | Time |
|---|---|
| Objects or containers for objects | Objects exist (move) in space with respect to time point or time interval |
| Spatial domains may be discrete, dense or continuous | Temporal domain may be discrete, dense or continuous |
| Random or predictable movement of objects in space | Time is not random, it is unidirectional |
| Spatial object in space is dynamic but static in case of container | Time is dynamic |
| Limited definition | Unlimited definition |
| Follows non-linear order | Follows linear order (T,<) |
| Limited dimensions | Unlimited dimensions |

This module uses two electrodes one is on top and the other is on bottom. By opposite hand When the user touches the topside electrode ECG data can be captured, when the user touches the topside electrode with the opposite hand. For avoiding the Hassle and bussle in the days of Hajj NYMI band with improved, enhanced, more-adaptable, extensible version or alike gadget may be provided to pilgrim prior to departure for Hajj.

Table 4: Various mobile applications and features [8]

| Application Name | Developer | Operating Mode | Monitoring | Tracking | Assistance | Spatio-Temporal features |
|---|---|---|---|---|---|---|
| Al Sirat | Zerone Innovations | Manual | No | No | Partial | No |
| سلام Salam | EtcAndroid | Manual | No | Partial | Partial | No |
| Hajj Organizer منظمالحج | project hajj | Automatic | No | Yes | Yes | No |
| Tawaf | GIS Technology Innovation Center | Manual | No | No | Yes | No |
| Tawaf and Sai in Hajj and Umra | Islamic Solutions | Manual | No | No | Yes | No |
| Hajj and Umrah | I.T. Department of DawateIslami | Manual | No | No | Yes | No |
| Labbaik: Hajj and Umrah Audio | AMPlified | Manual | No | No | Yes | No |
| Hajj player I ENGLISH | YUSUF YİĞİTALP | Manual | No | No | Partial | No |
| Manasik | Brainstorm Technologies Sdn Bhd | Manual | No | No | Partial | No |
| HajjSalam | Hajjnet FZE | Automatic | No | Yes | Yes | No |
| Tawaf and Sai Auto Counter | AboAdam | Automatic | No | Yes | Yes | No |
| My Tawaaf | TCMCORE | Automatic | No | Yes | Yes | No |
| SOFTnet Solat Times | Abu Bakar Hj Hasan | Manual | No | Yes | Yes | No |
| إحسانطواف IHSEN Tawaf | Generation IT | Automatic | No | Yes | Yes | No |
| Hajj Guider | Daira Tech FZCO, DTEC, Dubai Silicon Oasis | Automatic | Claims | Yes | Yes | No |

## 2. Related work in Mobile Application Perspective and Analysis

We now analyze our literature review to identify the gap. In terms of components and functionalities Table 5 demonstrate the components and functionalities that would be given by various spatio-temporal data models.

Table 5: Comparitive analysis of various spatio-temporal models

| Spatio-Temporal Data Models | Temporal Granularity | Temporal operations | Temporal Density Discrete: D Continious: C | Lifespan | Spatio-Temporal Ontology | Object-Relational Support for Moving Objects, Time and Moving Events | Event Handling Support | Transaction TT vs VT vs BT | Expendably | Type of Change All 8 types: A/N Discrete: D/N Continuous: C/N Movement: M/N | Application |
|---|---|---|---|---|---|---|---|---|---|---|---|
| Snapshot | Multiple | NO | D | NO | NO | NO | NO | VT | NO | N-N-N-N | LIS |
| STC | Multiple | NO | D | NO | NO | NO | NO | BT | NO | N-D-N-N | LIS |
| Simple Time-stamping | Multiple | YES | D | YES | NO | NO | Temporal | VT | NO | N-D-N-N | Historical Cadastral database |
| Event Oriented | Multiple | NO | D | YES | NO | NO | Spatial | VT | NO | N-D-N-N | LIS |
| 3-Domain | Multiple | YES | D | YES | NO | NO | Temporal | BT | NO | A-D-C-N | LIS |
| History Graph | Multiple | NO | D/ C | YES | NO | NO | Temporal | BT | NO | N-D-C-M | LIS |
| STER | Multiple | NO | D | YES | NO | NO | Temporal | BT | NO | A-D-C-N | Cadastral Application |
| O-R | Multiple | NO | D/ C | YES | NO | NO | Partial | BT | NO | A-D-C-N | Rural –Urban Land Use application |
| O-O | Multiple | YES | D/ C | YES | NO | NO | Partial | BT | NO | A-D-C-M | LIS |
| STUML | Multiple | NO | D/ C | YES | NO | NO | Temporal | BT | NO | A-D-C-M | Regional Healthcare |
| Moving Objects | Multiple | YES | D/ C | YES | NO | NO | Partial | BT | NO | A-D-C-M | multimedia, forest fire controls |

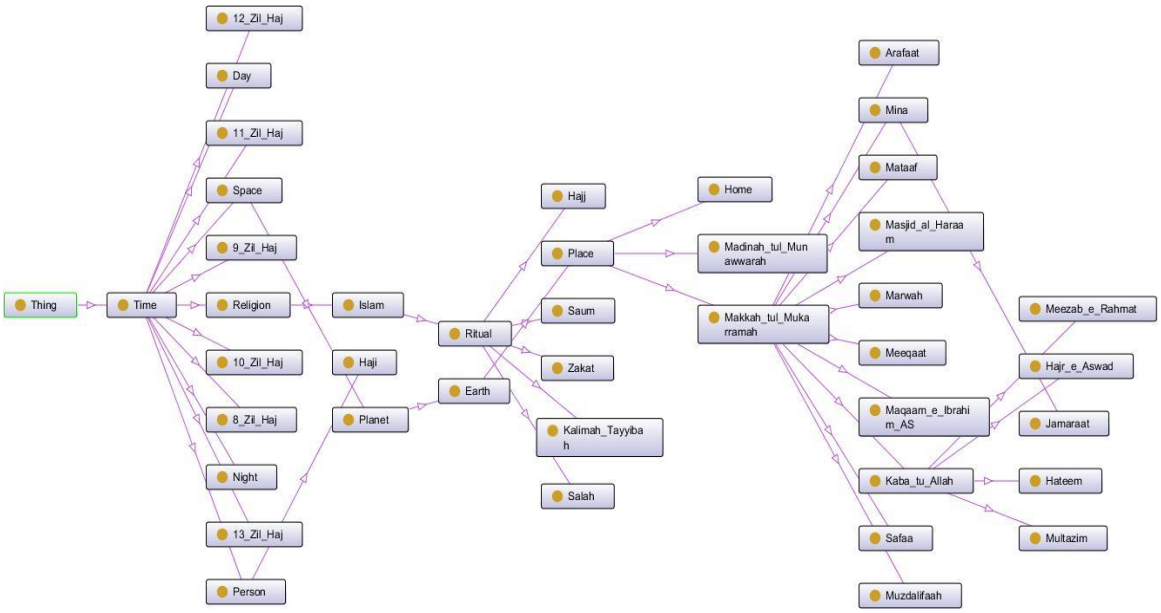


Fig. 2: A Brief ontology of Hajj [8]

We review the existing literature of Hajj through mobile applications and modeling like [7] [8] [9] in this section. There are various services and mobile phone applications are present, tracking and assistance applications are included. For assisting and tracking are listed in **(Table 4)** at some level.

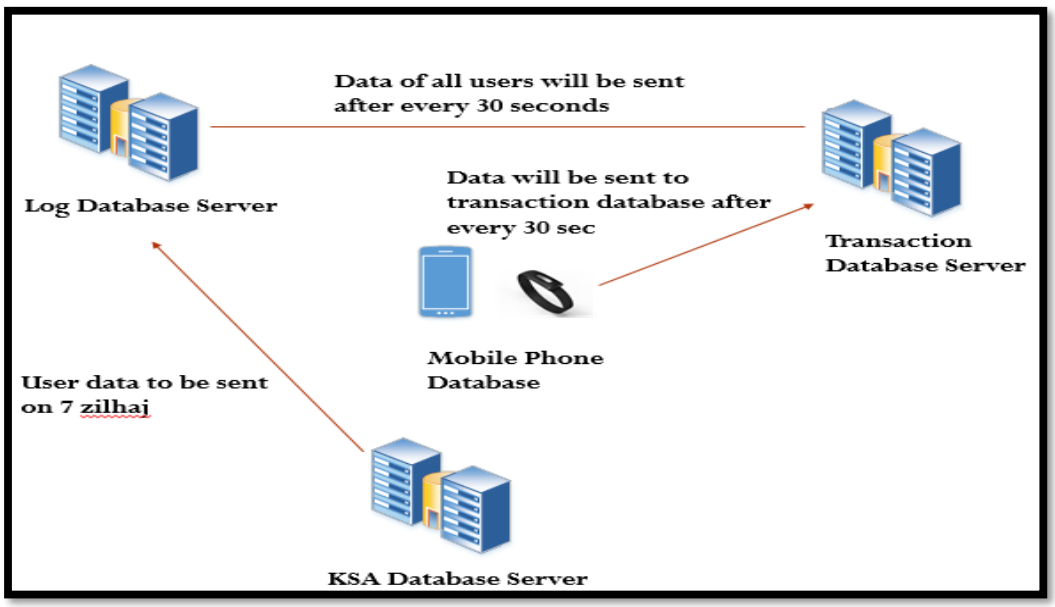


Fig. 3: Proposed Framework for application-database connectivity [7]

For instance, the easy interface to access the content publicity is *Al Sirat ,The Salam, Hajj Organizer, SoftnetSolat Times, Tawaf and Sai Auto Counter and Tawaf and Sai* in Hajj and Umra are the other additional features. It providesDu'a and keep you in Tawaf track by Tawaf counter, your progress also tracked by Sa'ee. The direction of Qiblah also determined by this program and counts the number of Tawaf rounds. It helps to remind the duties of his/her time to time and also helps to pilgrim the important steps of Hajj and keep them alert. The complete knowledge of Hajj and Umrah is provided by the *Hajj and Umra* which include Ihram, types of Hajj, The prayer assistance [31 application of tracking are IhsenTawaf, Hajj Guider' and *My Tawaaf* but except Hujjaj there is no any integrated monitoring and tracking avaibility. The applications *Tawaf and Sai in Hajj and Umra* used in collecting future data. So in monitoring, tracking and assistance for government control there is no any mobile applications, services and runtime facilitation are available. From the 1st Day our application guides the pilgrim based on his/her current location for addressing the problem. User is known at any instant by watching on screen all the supplications,

Table 6: Sptio-Temporal Existence of Hujjaj during Hajj Days with Application Assistance [8]

| Date | Time | Current location | Notification |
|---|---|---|---|
| 8 ZIL HAJJ | 6:05 AM | Makkah | You have to move towards Mina after sunrise |
| 8 ZIL HAJJ | 6:36 AM | Makkah | Now move towards Mina. |
| 9 ZIL HAJJ | 4:20 AM | Mina | You have to move towards Arafat after Fajar prayer. |
| 9 ZIL HAJJ | 4:52 AM | Mina | Now move towards Arafat before zawal time. |
| 9 ZIL HAJJ | 11:57 AM | Arafat | Waqoof is started at the beginning of zawal time. |
| 9 ZIL HAJJ | 5:05 AM | Arafat | You have to move towards Muzdalifah after sunset. |
| 9 ZIL HAJJ | 5:36 AM | Arafat | Now move towards Muzdalifah. |
| 10 ZIL HAJJ | 6:00 AM | Muzdalifah | You have to move towards Mina when sun is about to rise. |
| 10 ZIL HAJJ | 6:25 AM | Muzdalifah | Now move towards Mina. |
| 10 ZIL HAJJ | 10:00 AM | Mina | Move towards HARAM to perform Tawaf-e-Ziarat after Qurbani and Halq or Qasr. |
| 10 ZIL HAJJ | 3:30 PM | Mashid-al-Haraam | Return to Mina for overnight stay. if tawaf-e-ziarat and sa'ee has done |
| 11 ZIL HAJJ | 11:57 AM | Mina | Perform Rami after zawal time. |
| 11 ZIL HAJJ | 3:30 PM | Mina | Perform tawaf-e-ziarat if you have not done yet and return to mina for overnight stay. |
| 12 ZIL HAJJ | 11:57 AM | Mina | Perform rami after zawal time if you have not done. |
| 12 ZIL HAJJ | 3:30 PM | Mina | Must Perform tawaf-e-ziarat before sunset and return to Mina for overnight stay. |
| 12 ZIL HAJJ | 7:00 AM | Mina | Return to Makkah for performing tawaf-e-Wida |

salah timings, upcoming rituals etc by applications. . The complete knowledge of Hajj and Umrah is provided by the Hajj and Umra which include Ihram, types of Hajj, The assistance application of tracking are IhsenTawaf, Hajj Guider' and My Tawaaf but except Hujjaj there is no any integrated monitoring and tracking availability. The applications Tawaf and Sai in Hajj and Umra used in collecting future data. So in monitoring, tracking and assistance for government control there is no any mobile applications, services and runtime facilitation are available. GISTIC have developed applications [11] [12] [13] [14] for the service of pilgrims.

We discussed some applications above by studying various applications, for getting a pedestal support based on these applications it has no architecture, framework or model for presenting **(Fig. 3)**. It has not been presented, pointed and discussed the spatio-temporal ontology [1] [2] of Hajj see **(Fig. 2)** as per our best knowledge and belief. Founding this gap by us and spatio-temporal architecture presented it. Theory and the strength of spatio-temporal using this foundation. Their features are being offered and explored by various applications.

## 3. Spatio-Temporal Semantics

The concept of spatial and temporal aspect of Hajj is shown in (Table 3 and Table 6) by Spatio-temporal semantics (ontology) [6]. These concept incorporated by STDB model during its implementation. For creating STDB system it is so important to comprehending the data base. Realizing independently for the spatial and temporal's researches in first step. With the objects it focuses on design, modeling and querying dimensions (geometries) and it keeps in database. So these are static databases. Information is expanded by temporal databases, it helps to kept object of previous states along with the current state.

### 3.1 Spatio-Temporal database features

Managing the database applications is the capacity of STDBs that attributes both spatial (space coordinates) and temporal (timestamps) are possessed. Spatial database models are often the extensions of STDB's in which temporal features, in order to deal with complex dynamic environment, like moving objects, traffic flow etc. are also included. As a natural fact in a single application of both spatial and temporal data are needed to join.

### 3.1.1 Valid Time (VT)

$\overset{\Psi}{V}_x$ in the modelled reality the fact of time t is true. In Hijre calendar 8 Zil Hajj to 13 Zil Hajj is considered the valid time of Hajj. Time of entrance into Meeqat in KSA till the exit is considered as the valid time of Haji.

### 3.1.2 Transaction Time (TT)

$\overset{\Psi}{T}_{Z_e}$ in database the current element is $Z_e$. (e may be an object or event or time). 8 Zil Hajj to 13 Zil Hajj of Hijre present as a transaction time of Hajj. So during the valid time of Hajj an event moves form one place to another. When Haji enters it is set as a valid time for Haji. During this time they stay or leave.

### 3.1.3 Existence Time

$\overset{\Psi}{\exists}_O = \overset{\Psi}{V}_{\exists_o}$ is applied as a valid time of object's existence.

The time of Manasik is the existence time for Hajj ( which starts the starting till exit time of Hajj) in this time we stay in Mina, Arafaat and Muzadlifah during Hajj. Transaction time is also the existence time of Hajji which is considered as IN valid.

### 3.2 Spatio-Temporal Modelling Requirements

a. In the literature many data is considering in modeling spatio-temporal [4][11][30]. Some requirements are given below.

b. The existence in time , the identification of object and spatial coordinates (attributes) representation.

c. Changing in object movement with respect to time need capturing.

d. Spatial attributes and organization definition sets into layers.

e. Changing of spatial attributes need capturing over the time.

f. Association of spatial attributes to objects.

g. It is the representation of spatial relationship with respect to time among different objects.

h. It is the representation of spatial attributes relationship in time.

i. For the data correctness spatio temporal integrity's specification is used.

### 3.3 Spatio-Temporal Query Languages

In the database environment for managing the spatio-temporal data, existing query languages have most of extended versions. There is an extension of DEAL called HQL (Hibernate Query Language) in which all the programming constructs is provided (nesting, loop, conditional sructure, functions etc). These operations similar to spatical relationship operators that handling the spatio-temporal query. In this context of Spatial query languages that includes Geo-Quel and GeoQ, STQL (extention of SQL)[10], and for query handling that is considered for Spatio-temporal. For the both spatial and temporal charactereistics which served a forementioned lanuages and also offers paradigms of spatial-temporal query lanugage. However, it is the big weakness of STQL represented for the objects that move continuously.

## 4. Proposed Framework and Application

- An ID is generated for each Haji with firebase with his complete details, for the identification purpose the details we get convey to the Hajj monitoring.With firebase this app is for

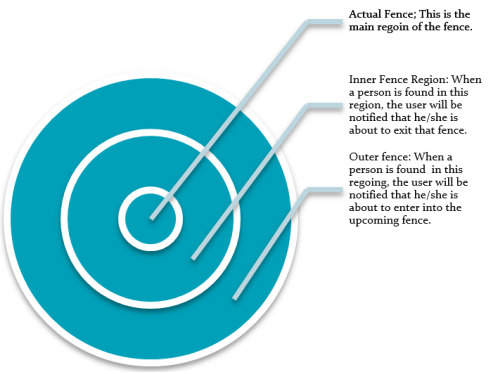


Fig. 4: Topology of fences used for mobile **application** [8]

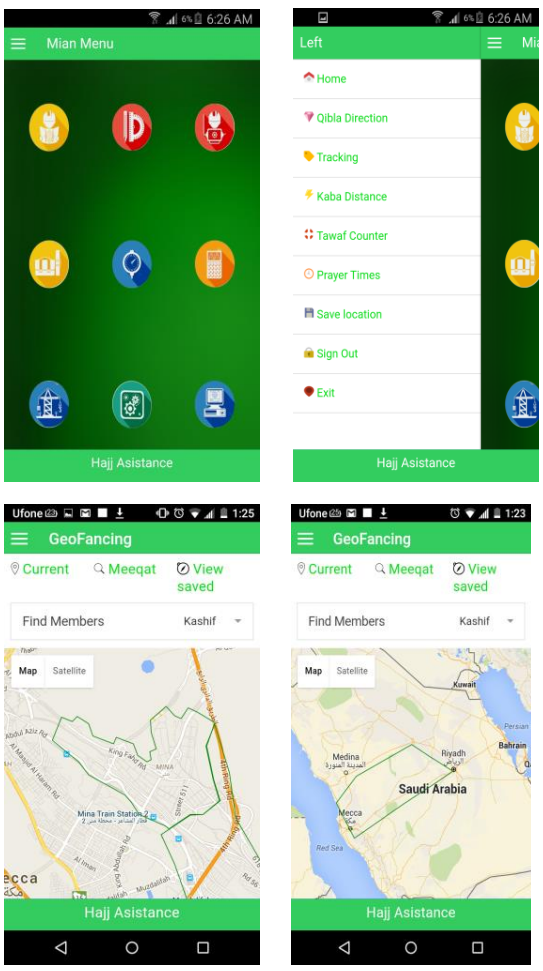


Fig. 5: Hajj App's screenshots (User + Admin) modules [7]

Hajj is integrated, On the basis of country, city the details we get is useful for the identification of Haji.

- The current and last locations of Haji's details uses in monitoring of hajj and it has been shared also to the team of Saudi Arabia.
- The hajj monitoring team will use this data if any tragedy or misfortune would be happen to haji to rescue.
- The risk of missing haji will be reduced during hajj with the cooperation of hajj monitoring team of Saudi Arabia.

Tawaaf is one of the most important ritual in Hajj. During Tawaaf hujjaj are being assisted,

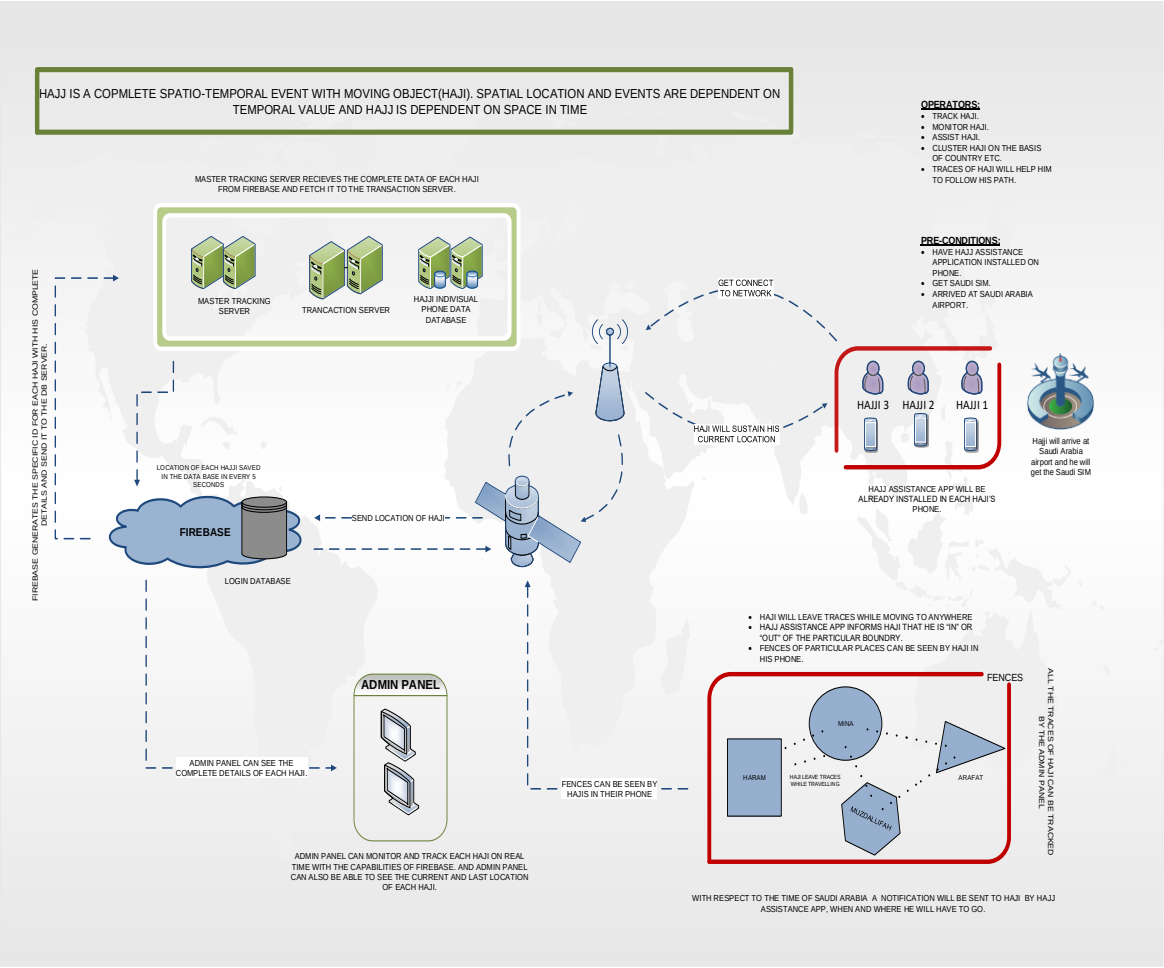


Fig. 6: Work flow model of proposed system [7]

monitored and tracked by automatic rounds counting. There is a Hajr-e-Aswad in the corner where Tawaf starts.

### 4.1 Smart Hajj Assistant

Two modules (user and admin) responsible to notify the user in our application about Haji's current location and keep monitoring to alert using spatio-temporal opertors **(Fig. 5)**. If Haji crosses any fence and get far from place during Hajj. There are three fences as a copy fences of each, shown in **(Fig. 4).** Key functions includes:


Fig. 8: View of Fence for Arafaat [3]

- *Location Based Routing and Assistance for Hujjaj*
- *Immediate Monitoring and Controlling of Hujjaj as*
- *Transportation Facilitation*
- *Improved Disaster Management*
- *Guide/ Route Hujjaj for Load Balancing To Avoid Extreme Rush*
- *Manage Every Single Person in Hujjaj for Timely Fulfillment of Every Activity (As Per 'Sunnah' صلى الله عليه وسلم)*
- *Planning Hujjaj's Food*
- *Making Prompt* Decision Support
- *Improved Quality of Services during Hajj*
- *Monitor and Track Hujjaj*
- *Assist Hujjaj in His/her Native Language*
- *Healthcare Management and Control*

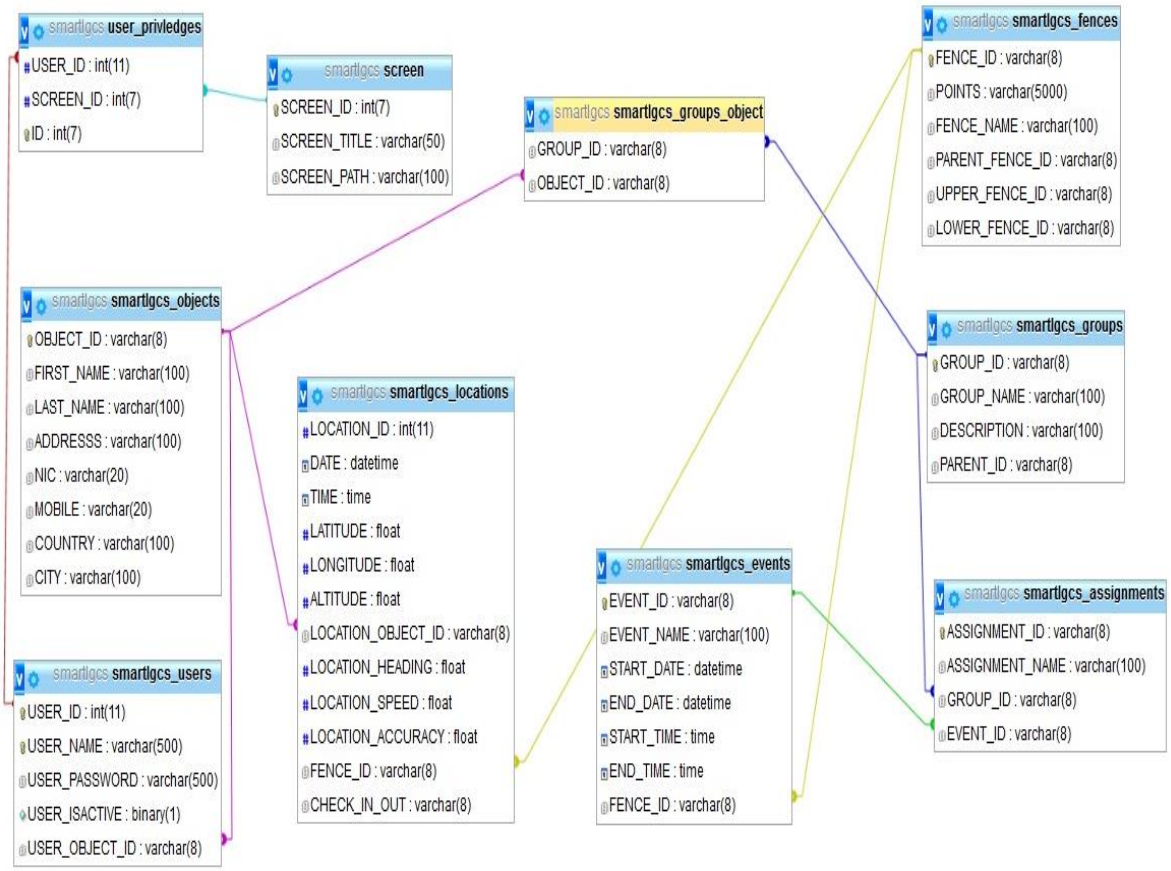


Fig 7: Conceptual data model for the system

## 5. Discussion and Analysis

Our all application is based on Geo Fences. By using the Google map "My Map"[3] we have described the fences in order to make the desired features locations of Saudi Arabia. Polygon based technique is used by us so the interest is defined by a geofence. In **(Fig. 6)** and **(Fig. 7)** the proposed workflow and conceptual database model for the modeled system is illustrated, respectively.

For example, there is particular sets of entities at outside of the polygon that is not expected to stray. Particular collections are applied to Geo fences. There are numbers of properties of each geofence which are ID, Name, Collection IDs, Polygon.

Geofences for Meeqat, Makkah-tul_Mukarramah, Haram, Masjid-al-Haraam, Mataaf, Safaa, Marwah, Mina, Arafaat and Muzdalifah for our application see **(Fig. 8)**. Based on their location and fence user/ Haji will get notifications.

## 6.Conclusion & Future Work

All those aspects which are necessary to tackle during Hajj are presented in this work. The handling of spatio-temporal data is presented in this research for real time applications and it is too useful for Hujjaj. his will also help for further assistance in future for monitoring and tracking of Hujjaj during Hajj. However, Nymi wristband did not function as expected during experiments. Reason is that NFC integrated in band not working. Hence it is dependant with the companion app. This requires application independent band, free to work without any other integrated hardware of software. In the future, the aim of this research is to be more practical, optimized and in a broader situations willing to deploy our prototype.

## Acknowledgement

Part of this work is funded by Dean's Mini Research Project Grant from Federal Urdu University of Arts, Science & Technology, Pakistan.

## 7. References

[1] Saidah Saad, N. S. a. H. Z., "Towards Context-Sensitive Domain of Islamic Knowledge Ontology Extraction", International Journal for Infonomics (IJI), 3(1), pp. 197-206, March 2010.

[2] Erwig M., Güting R. H., Schneider M., and Hagen D., "Spatio-Temporal Data Types : An Approach to Modeling and Querying Moving Objects in Databases" Geoinformatica, vol. 3, no. 3, 1999.

[3] Maps.Google. (n.d.). Retrieved from Maps.Goole.com: https://www.google.com/maps/d/edit?mid=zBb4FNV1ltwE.kuaRXljnR134&usp=sharing

[4] Nymi . (n.d.). Retrieved from https://www.nymi.com

[5] TheGuardian. (2015). Retrieved from TheGuardian: http://www.theguardian.com/

[6] world/2015/sep/24/timeline-of-tragedies-in-mecca-during-hajj

[7] Jin P., Wan S., and Yue L., "Ontology-driven Conceptual Modeling for Spatiotemporal Database Applications," 1st Int. Symp. Data, Privacy, E-Commerce (ISDPE 2007), vol. 4, pp. 110-112, Nov. 2007.

[8] Rizwan K, Mahmood N., and Nadeem A., "Spatio-Temporal Database Modeling and Application for Monitoring, Tracking and Assistance of Hujjaj during Hajj", Proceedings of the 3rd International Conference on Engineering & Emerging Technologies (ICEET), Superior University, Lahore, PK, 7-8 April, 2016.

[9] Rizwan K. (2017). "Spatio-temporal database modeling and applicaions", (Doctoral Dissertation), submitted to Higher Education Commission Pakistan., from Department of Computer Science, University of Karachi, Pakistan.

[10] Mahmood N., Burney A., Shah A., Rizwan K., Abu Bakar A., Bari S.A.K., "Spatio-Temporal Database Design Architecture (STDDA): A Conceptual Framework", Sci.Int.(Lahore),Vol.: 28, No.5, pp.4333-4338, 2016.

[11] Burney, A. & Mahmoud, N. (2006). A Brief History of Mathematical Logic and Applications of Logic in CS/IT, Karachi University Journal of Science, 34(1), 61-75.

[12] GIS Innovation Center, "Tawaf App", http://www.gistic.org/tawafapp/

[13] GIS Innovation Center, "Perform Hajj &Umrah", http://www.gistic.org/perform-hajj-umrah/

[14] GIS Innovation Center, "HajjSense Platform", http://www.gistic.org/hajjsense-platform/

[15] GIS Innovation Center, "Hajj Management System", http://www.gistic.org/hajj-management-system/

[16] Iwaniaka A., Łukowicza J., Strzeleckia M., & Kaczmareka I., Ontology driven analysis of spatio-temporal phenomena, aimed at spatial planning and environmental forecasting, ISPRS-International Archives of the Photogrammetry, Remote Sensing and Spatial Information Sciences, 1(2): 119-124, 2008.

[17] Lyell M., Voyadgis D., Song M., Ketha P., and Dibner P., An ontology-based spatio-temporal data model and query language for use in GIS-type applications, In Proceedings of the 2nd International Conference on Computing for Geospatial Research & Applications - COM.Geo '11, 2011, pages 1–9.

[18] Frank A. U., Ontology for spatio-temporal databases," In: T. Sellis et al. (Eds.): Spatio-temporal Databases, LNCS 2520, 2003, pages 9–77.

[19] Pozzani G. and Combi C., "ST4SQL: a spatio-temporal query language dealing with granularities", Journal of Multimedia Processing Technology, 2(3):140-157, September 2011.

[20] Mahmood N., Burney A. and Ahsan K., "Generic Temporal and Fuzzy Ontological Framework (GTFOF) for Developing Temporal-Fuzzy Database Model for Managing Patient's Data", Journal Universal Computer Science, vol. 18, no. 2, pp. 177-193, 2012.

[21] Ye X., Peng Z., and Guo H., Spatio-temporal data model and spatio-temporal databases, In: Temporal Information Processing Technology and its applications, Springer Berlin Heidelberg, 2010, pages 91-112.

[22] Pelekis N., Theodoulidis B, Kopanakis I, and Theodoridis Y., Literature review of spatio-temporal database models, Knowl. Eng. Rev.,19(3): 235-274, 2004.

[23] Grumbach S. et. al., Spatio-temporal models and languages: An approach based on constraints, In Spatio-Temporal Databases, Springer Berlin Heidelberg 2003, 177–201.

[24] Carvalho A., Ribeiro C., and Sousa A. A., "A STDB System Based on TimeDB and Oracle Spatial," In International Federation for Information Processing, Volume 205, Research and Practical Issues of Enterprise Information Systems, Springer, vol. 205, pp. 11–20, 2006.

[25] Vazirgiannis M. and Wolfson O. A spatiotemporal model and language for moving objects on road networks, In SSTD 2001, LNCS 2121, Springer-Verlag, 2001, pages 20-35.

[26] Innerebner M., Böhlen M., and Timko I., A web-enabled extension of a spatio-temporal DBMS, In: Proceedings of the 15th annual ACM international symposium on Advances in geographic information systems - GIS '07, 2007, pages 1-8.

[27] Boulmakoul A., Moving object trajectories meta-model and spatio-temporal queries, Int. J. Database Manag. Syst., 4(2): 35–54, 2012.

[28] Carvalho A., Ribeiro C., and Sousa A. A., "A STDB System Based on TimeDB and Oracle Spatial," In International Federation for Information Processing, Volume 205, Research and Practical Issues of Enterprise Information Systems, Springer, vol. 205, pp. 11–20, 2006.

[29] Matos L., Moreira J., and Carvalho A., "Representation and management of spatiotemporal data in object-relational databases", Proc. of the 27th Annual ACM Symposium on Applied Computing - SAC '12, p. 13, 2012.

[30] Erwig M., Güting R. H., Schneider M., and Hagen D., "Spatio-Temporal Data Types : An Approach to Modeling and Querying Moving Objects in Databases" Geoinformatica, Vol. 3, No. 3, 1999.

[31] K Rizwan, N Mahmood, SAK Bari, Z Abbas, A Nadeem, A Waqas," Spatio-Temporal Proximity Assistance", published in Future Technology Conference (FTC) 2017, Canada, 2017.

[32] MA Hussain, K Ahsan, S Iqbal, A Nadeem. "Supporting deafblind in congregational prayer using speech recognition and vibro-tactile stimuli ", published in Elsevier International Journal of Human-Computer Studies 123, 70-96, 2019.

# Vehicle Maneuvering-style Recognition in identifying the Culprit for a Road Accident

**Muhammad Shoaib Siddiqui**

Faculty of Computer & Information Systems, Islamic University of Madinah, Kingdom of Saudi Arabia

shoaib@iu.edu.sa

**Abstract:** One of main reasons of road-side accidents (RSA) is the reckless by the driver. Reckless drivers induce danger on the road and their surroundings, which could result in deadly accidents both on road and off the road. High acceleration, frequent lane changes, lane changing in high speed, turning at high speed, and braking late or suddenly are some of the activities by drivers that cause these deadly accidents. In this paper, we have proposed and developed a driving style recognition system, which would alert the driver to drive safely. It would also help in identifying the driver at mistake during a road-side accident. In this paper, we have gathered data from an accelerometer and a gyroscope to recognize the vehicle maneuvering style of the driver. We have applied and compared the results of two well-known classifiers, i.e. Support Vector Machine (SVM) and K-Nearest Neighbor (KNN) to identify the driving activity. We have also explored different features extraction techniques to identify the best solution. After, the driving activity is recognized, it is further classified to detect the driving style, as reckless or adequate. Later on, the system can generate alarm to the driver through an actuator and use a weight-based algorithm to identify the driver at fault, based on the driving style, in case of a RSA.

**Keywords:** maneuvering style; road-side accident, classification; feature extraction; driving style; driving activity.

# التعرف على أسلوب مناورة السيارة في تحديد الجاني لحادث سير

**الملخص**:أحد الأسباب الرئيسية للحوادث المرورية (ر س ا) هو التهور من قبل السائق. السائقون المتهورون يشكلون خطرا على الطريق ومحيطهم، مما قد يؤدي إلى حوادث مميتة سواء على الطريق أو خارجه. تعد بعض التصرفات التي يقوم بها السائقون؛ كالسرعة العالية، والتغييرات المتكررة في المسار، وتغيير المسار في السرعة العالية، والانعطاف بسرعة عالية، والكبح في وقت متأخر أو فجأة، سببا في هذه الحوادث المميتة. في هذه الورقة اقترحنا وطورنا نظام التعرف على نمط القيادة، والذي من شأنه تنبيه السائق إلى القيادة بأمان. كما أنه سيساعد في التعرف على السائق المخطىء أثناء حادث على جانب الطريق. في هذا المقال قمنا باقتراح وتطوير نظام تعرف على طريقة السياقة والذي سينبه السائق للسياقة بحذر. وسيساعد كذلك على تحديد السائق المخطئ خلال حادث مروري. في هذا المقال قمنا بجمع البيانات من مقياس التسارع وجيروسكوب للتعرف على أسلوب السياقة لدى السائق. قمنا بتطبيق ومقارنة نتائج لمصنفين معروفين جدا، لمعرفة دعم ناقلات الجهاز (س ف م) والجار الأقرب-ك (ك ن ن) لتحديد نشاط القيادة. لقد استكشفنا أيضًا عدة تقنيات لاستخلاص ميزات مختلفة من أجل تحديد أفضل الحلول. بعد أن يتم التعرف على نشاط القيادة، يتم تصنيفه أيضًا لاكتشاف نمط القيادة، باعتباره متهورًا أو كاف. في وقت لاحق، يمكن للنظام توليد إنذار للسائق من خلال مشغل، واستخدام خوارزمية ترتكز على الوزن لتحديد السائق المخطىء ، استنادا إلى نمط القيادة ، في حالة وجود ر س ا.

## 1. Introduction

With the increasing rate of vehicles on the road, the frequency of road accidents is increasing. In a country like the Kingdom of Saudi Arabia, the rate is relatively higher. Every year more than five hundred thousand road accident are reported and it is estimated that there are almost 7 million vehicles registered in the Kingdom [1]. According to a trend analytical survey, a warning has been reported that if the safety of the road is not ensured and public is not educated, the amount of accident would pass the value of four million till 2030 [2]. Numerous studies have been performed which identify the various causes of these accidents, such as, distractions, sleep, negative emotions, failure to see or observe, awareness, etc. [3]. According to [4], “The Secretary General of the Shura Council declared that the Kingdom has spent on an average 26 billion riyals annually

on car accidents". According to the data from the Ministry of Interior, General Directorate of Traffic, there were around six hundred thousand accident in the year 2012 [5]. The trend of increase in the number of accident is given in Figure 1. Although the official data are available till 2012; however, the researchers have predicted that the value would increase to four million till 2030 [2].

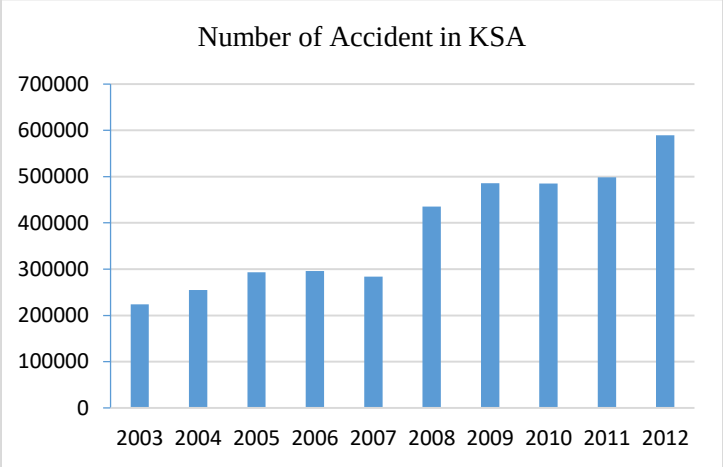


Figure 1: Number of accident in KSA reported (according to the Ministry of Interior - General Directorate of Traffic | Saudi Open Data) [5]

According to the World Health Organization (WHO), about 1.35 million people die every year worldwide, due to road side accidents, while 20.5 million suffer severe trauma. Most of the victims require costly treatments over a long period of time. Along with trauma and suffering, road accidents cause enormous social and economic losses, absorbing 1-3% of the national gross domestic product [29]. Many consequences of a traffic accident can be effectively prevented. However, this requires continuing efforts to develop new methods and programs aimed at improving road traffic safety. The WHO predicted that about 1.9 million people would die each year before 2020 due to road traffic accidents without proper action [30].

Road side accidents (RSA) can be classified as driver-based, infrastructure based, and vehicle based. By providing better road infrastructure, infrastructure traffic accidents can be reduced. Vehicle-based road accidents are caused by defective or outdated vehicles on the road. The governments apply strict rules to vehicle health monitoring and penalties to reduce the number of accidents. Likewise, in the case of driver-based accidents, the authorities imposed heavy fines to prevent reckless and dangerous driving. However, it is a difficult task to check for recklessness and correctly display faulty drivers. Driver based accident are due to over-speeding, reckless

driving, and breaking road rules. In [6], we have proposed a system which can help in identifying the driver at fault in a RSA; however, in this paper, we provide the details of vehicle maneuvering-style recognition system in identifying the culprit for a road accident. The proposed system uses the data gathered from the accelerometer and a gyroscope fitted inside the vehicle and apply pattern recognition mechanism to classify the maneuvering style of the driver. The maneuvering styles are classified as, 'over-cautious', 'normal', 'aggressive', and 'reckless'.

## 2. Related Work

Accelerometer is a device which can recognize the change in velocity of a body. A tri-accelerometer gives value for change in velocity in terms of x-axis, y-axis, and z-axis. However, a gyroscope provides the values in x-axis, y-axis, and z-axis for the angular velocity.

There has been many application of accelerometer and gyroscope sensors, such as, human activity recognition [7], fall detection [8], remote subject monitoring in old houses and clinics [9], step counting [10], vehicle path tracking [11], and vehicle maneuvering detection [12].

Most of the proposed systems for human activity recognition use the tri-accelerometer with either a specialized wearable sensor [13] or sensor available inside the smart-phones [14]. The data is gathered from the sensors and feature extraction and classification algorithms are applied on that data to identify the activity being performed by the subject [15] [14]. Classifiers, such as, decision tree, support vector machines, k-nearest neighbor, naïve Bayes, decision table, random forest, etc. have been applied by the researchers to devise an optimal solution for human activity recognition [16]. Similarly, the use of accelerometer is explored in other applications, such as, fall detection [8], remote subject monitoring in old houses [9], and step counting [10].

Some researchers have applied classification mechanism on data gathered from an accelerometer (or in a smartphone) to identify the transportation mode of the subject [11] [17]. The modes could be classified as, in a car, in a train, in a plane, or motor based and non-motor based [11]. Some vehicle tracking and prediction systems have also used the data from accelerometer and other sensors [17]. Furthermore, driver profiling mechanisms are also proposed which use similar techniques [18] [19].

Vehicle maneuvering detection is relatively a less explored area, in which few solution have been proposed which use the data gathered from an accelerometer. Cervantes-Villanueva et al. [12] have

proposed a solution that detects the maneuvering relative to the kinematic state of the vehicle. They have devised a low-computational solution that can be implemented on a smart-phones, which can be used to gather data through their embedded accelerometer and run classification algorithm to detect the vehicle current maneuver as parked, driving, parking, and stopped.

In [28], the authors have presented a driver behavior detection mechanism using a motion sensor/accelerometer. It uses deep learning technology to learn the sample data collected by the sensor deployed in a vehicle. To solve the problem of small sample size and easy overfitting, they have proposed a joint data augmentation (JDA) scheme and designed a new multi-view convolutional neural network model (MV-CNN). MV-CNN and JDA have better generalization ability, reduce the training variance and deviation, and increase the stability of the model training process.

Our work is quite different to the work done by the other researchers presented above. The target of our research is to identify the driver who caused an accident. To identify if the current driver is at fault, we classify the drivers' driving style based on the vehicle maneuvering. For classifying the maneuvering style of the driver, first we need to identify the driving activity, i.e. right-turn, left-turn, lane-change (left and right), braking, and acceleration, and then classify these activities as 'over-cautious', 'normal', 'aggressive', and 'reckless'. As we performed the experiments, we identify that some of these activities are not recognized with higher accuracy based on accelerometer data. Therefore, we have used the data from the gyroscope also. After including the data from gyroscope the accuracy in detecting the driving activities increases as shown in the results section.

We have used two classification techniques i.e. support vector machine (SVM) [20] and K-nearest neighbor (KNN) [21] and compared the results for optimal solution. Similarly, for features extraction, we have used kernel discriminant analysis (KDA) [22], and linear discriminant analysis (LDA) [25] and autoregressive model [24].

The rest of the paper is articulated as follows. Section 3 provides the details of the proposed system and discusses the model. Section 4 provides the experimentation results. Section 5 concludes the paper.

## 3. Vehicle Maneuvering Detection Methods

The proposed vehicle maneuvering detection system is modelled in Figure 2. A node with an accelerometer and gyroscope is mounted inside the vehicle, through which the data is gathered. There are three main modules in the system. The first module is training module, which is used to collect data for the training of the classifiers and calculating model parameters. The second module is the detection module which perceives the driving activity. The third module is for categorizing the activity as adequate or reckless. The details of the model are discussed in the following subsection.

### 3.1 Data Collection

A MotionNode with a triaxial accelerometer and a gyroscope is used to collect data at 1000 Hz sampling rate. The data from accelerometer shows the change in velocity in x, y, and z directions after every 10 milliseconds, while the data from gyroscope shows the value of angular velocity's x, y, and z components. The data stream is continuously recorded for 1 minutes sample for training scenario created in simulated environment with ideal infrastructure and vehicle conditions. Further specification of data collection is given in the simulatio section 4, "Experiments and Results".

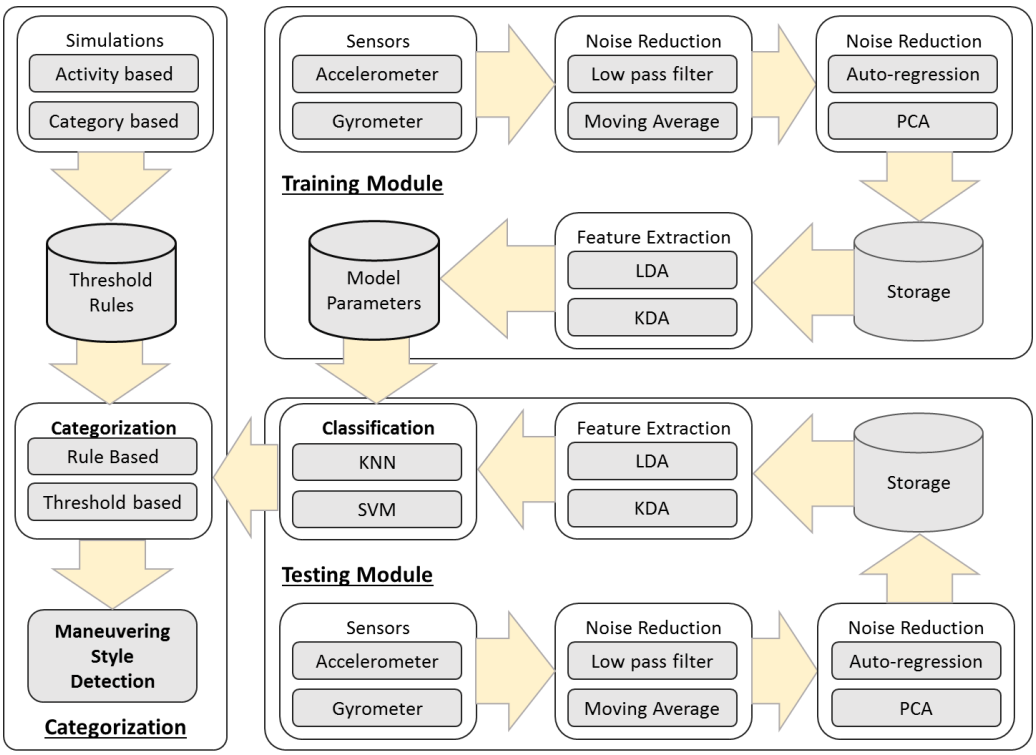


Figure 2. The system model of the proposed driving activity recognition

### 3.2 Noise Reduction

MotionNode [25] accelerometer and gyroscope have noise density of 50 μg/√ Hz (at 2 g range) and 0.1 degrees/second, respectively. There is some noise due to the flexibility of the fiber of which the device in mounted inside the vehicle also. To reduce the noise, we have applied a low pass filter to remove the higher frequencies. As we are using sampling frequency Fs=1000 Hz, we devise out low pass filter with cut-off frequency $f_0$=100 Hz, and used a second order Butterworth filter, with pre-warping. We have used the Butterworth filter as it rolls off more slowly around the cutoff frequency than the Chebyshev filter or the Elliptic filter, but without ripple [27]. We have also applied the moving average algorithm with order three (3) to smooth the signal. A moving average filter smooths data by replacing each data point with the average of the neighboring data points defined within a given span. The Eq. (1) gives the moving average equation that is used with the value of $\alpha = 0.3$.

$$\vartheta_n = \alpha(\vartheta_m) + (1 - \alpha)\vartheta_{n-1} \qquad (1)$$

Where $\vartheta_m$ is the new value and $\vartheta_n$ is the moving average. Figure 3 shows the effect of noise reduction on the collected data after remove high frequencies and applying moving average.

### 3.3 Feature Extraction

#### Segmentation

After the noise is reduced from the data, we apply segmentation to create segments of data called windows for applying feature extraction on each window. As our data is not tagged with events, we have applied sliding window technique for segmentation. Although this puts a lot of load on computation resources; however, for real-time systems, this is the best option as compared to event-based windows and activity-defined windows. We have used a single window length of 90 samples, which we have identified as optimal after using different window sizes.

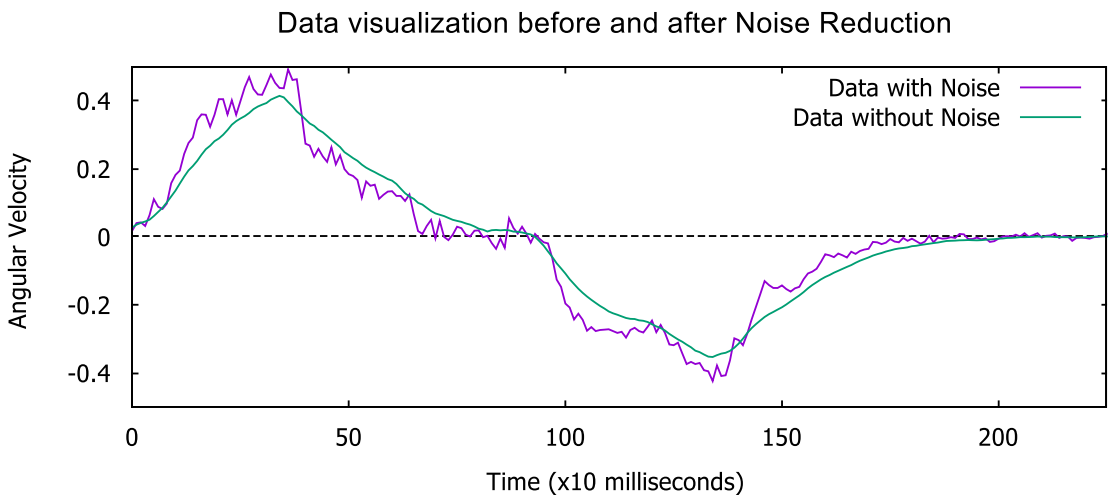


Figure 3. Data from gyroscope for aggressive left-turn, then a right-turn: before noise reduction and after noise reduction applied.

**Autoregressive Coefficients (AR):**

As per related works [7], we have used AR modeling for the gyroscope data. The representation of the AR model is given as Eq. (2)

$$X_n = \sum_{i=1}^{m} \delta X_{n-1} + \varepsilon_n \quad (2)$$

Where, $X_n$ is the current value of the gyroscope data. $\delta_1, \delta_2, \ldots, \delta_m$ are weighting coefficients for gyroscope, $m$ is the model order indication the number of the past values used to predict the current value and $\varepsilon_n$ is the Gaussian white noise.

**Principal Component Analysis**

The data from the accelerometer shows the change is velocity relative to the current position of the body, but it also contains the component of earth gravitational acceleration. To eliminate the gravitational effect, the acceleration of earth coordinate system can be projected in the direction of the vehicle movement. The direction of the vehicle movement would have the largest variance of acceleration. This component can be separated using the PCA algorithm as the first principal in PCA would be the direction of the vehicle [23].

Assume that $\vartheta_x = (\vartheta_x^1, \vartheta_x^2, \ldots \vartheta_x^m)^T$, $\vartheta_y = \left(\vartheta_y^1, \vartheta_y^2, \ldots \vartheta_y^m\right)^T$, and $\vartheta_z = (\vartheta_z^1, \vartheta_z^2, \ldots \vartheta_z^m)^T$ represent the x-axis, y-axis, and z-axis accelerations of earth coordinate system. The combination of the x, y, and z, axis data would result in a matrix, $\mathbf{M} \in \boldsymbol{R^{m \times 3}}$

$$\mathbf{M} = \begin{bmatrix} \vartheta_x^1 & \vartheta_y^1 & \vartheta_z^1 \\ \vartheta_x^2 & \vartheta_y^2 & \vartheta_z^2 \\ \vdots & \vdots & \vdots \\ \vartheta_x^m & \vartheta_y^m & \vartheta_z^m \end{bmatrix} \quad (3)$$

Then the covariance matrix $\mathbf{\Gamma}$can be calculated as,

$$\mathbf{\Gamma} = \frac{1}{m}(\mathbf{M} - \mathrm{E}(\mathbf{M}))\big(\mathrm{M} - \mathrm{E}(\mathbf{M})\big)^{\mathrm{T}} \quad (4)$$

Where E(**M**) is the expectation operation for each column of matrix **M**. $\mathbf{\Gamma}$ can be diagonalized as it is symmetric matrix:

$$\mathbf{\Gamma} = \mathbf{\Omega \Lambda \Omega^T} \quad (5)$$

Where Ω and Λ are eigenvector and eigenvalue matrices of $\mathbf{\Gamma}$, respectively. After ranking the eigenvalue in descending order and reconstructing the eigenvector matrix corresponding to eigenvalues, a new matrix $\widetilde{\mathbf{Q}}$ is obtained. The transformation matrix for PCA can be represented as;

$$\mathbf{P} = \widetilde{\mathbf{Q}}^{\mathbf{T}} \quad (6)$$

The final PCA transformation is:

$$\mathbf{G} = \mathbf{PM^T} \quad (7)$$

Where the first row of the matrix **G** is the first principal component, i.e. our transformed data.

**LDA and KDA**

The goal of LDA [26] is to find a projection which gives the maximum class separation. It tries to find the vector in the underlying space that gives the best discrimination amongst different classes. LDA uses Eq. (8) and Eq. (9) for calculating within $S_W$, and between $S_B$ class comparison, respectively [26].

$$S_B = \sum_{i=1}^{k} J_i\,(\bar{m}_i - \bar{\bar{m}}\,)(\bar{m}_i - \bar{\bar{m}})^{\mathrm{T}} \quad (8)$$

$$S_W = \sum_{i=1}^{k} \sum_{m_s \in C_i} (m_s - \bar{m}_i)\,(m_s - \bar{m}_i)^{\mathrm{T}} \quad (9)$$

Where, $J_i$ is the number of vectors in $i^{th}$ class *C*. *k* is the number of classes, which in this case is the number of driving activities. $\bar{m}_i$is the mean of vectors in class C while, and $\bar{\bar{m}}$ represents the mean of all the vectors.

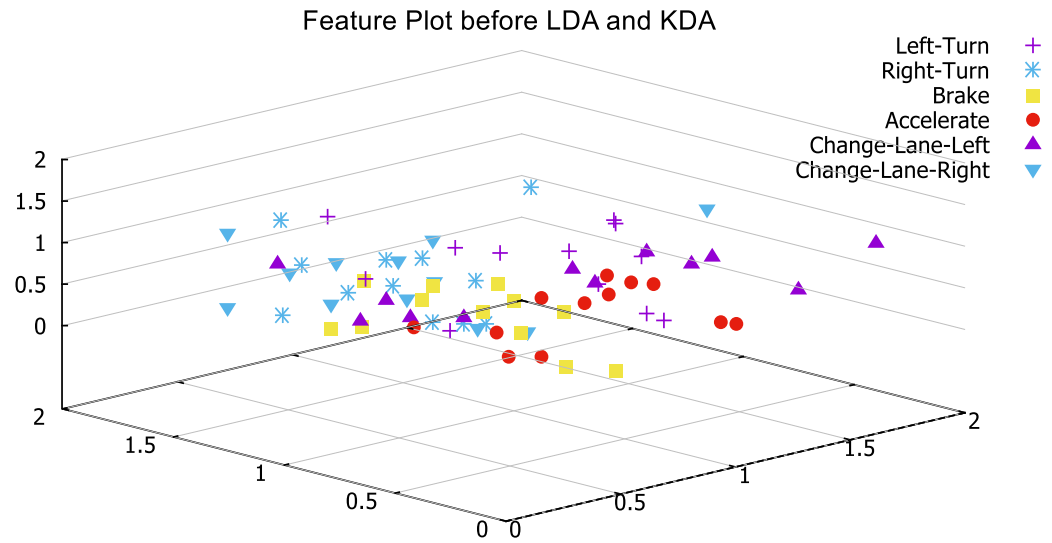


Figure 4. Feature plot for the six activities before discriminant analysis is performed showing high-in and low between class variances.

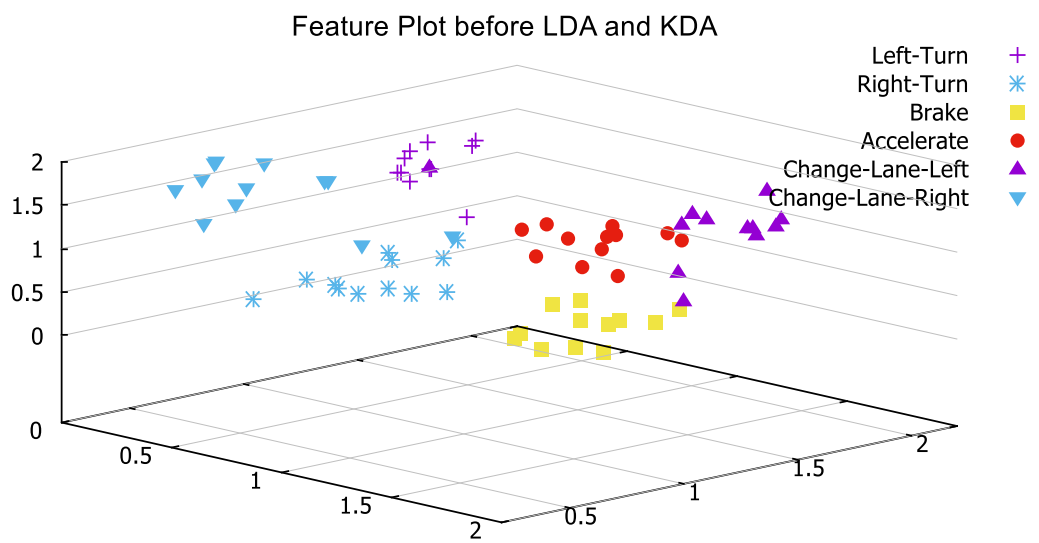


Figure 5. Feature plot for the six activities after KDA showing low-in and low between class variances

To extend LDA to non-linear mappings, the data, given as $l$ points $\vartheta_i$ can be mapped to a new feature space, $F$, via some function $\varphi$. However this mapping is computationally heavy. Therefore, the data can be implicitly embedded by rewriting the algorithm in terms of dot products and using the kernel trick in which the dot product in the new feature space is replaced by a kernel function. As proved by [7], Eq. (8) is equivalent to Eq.(10);

$$J(\vartheta) = \frac{\vartheta^T \mathbf{KWK} \vartheta}{\vartheta^T \mathbf{KK} \vartheta} \qquad (10)$$

Where $\vartheta = [\vartheta_1, \vartheta_2, \dots, \vartheta_m]^{\mathrm{T}}$ are the coefficients, and their optimal values are given by the eigenvectors with respect to the maximum values of:

$$\mathrm{KWK}\vartheta = \lambda \mathrm{KK}\vartheta \qquad (11)$$

Where K is the kernel matrix ($K_{ij} = K(x_i, x_j)$) and W is defined as:

$$W_{ij} = \begin{cases} \frac{1}{m_k}, & if\ x_i\ and\ x_j\ belongs\ to\ k^{th}\ class \\ 0, & otherwise \end{cases} \qquad (12)$$

For a new pattern z, its projection onto KDA basis vector $\omega$ in $F$ is calculated as:

$$\left(\omega, \varphi(z)\right) = \vartheta^{\mathrm{T}} \mathrm{K}(:, z) \qquad (13)$$

Where,

$$\mathrm{K}(:, z) = [K(z_1, z), \dots K(z_m, z)]^{\mathrm{T}} \qquad (14)$$

Figure 4 shows the feature set before applying the discriminant analysis where the features have high-in and low between class variances, while Figure 5 shows the feature plot after the application of KDA has reduced the variance.

The reason for using discriminant analysis is to establish a significant difference in the classes of data which helps in improving the accuracy of the classification algorithm. LDA and KDA are two of the most famous algorithms used for this purpose. LDA is capable of finding only linear mapping, hence the results of feature extraction are not good as our data does not have linear boundaries. KDA applies non-linear mapping; therefore, it provides better feature extraction but creates extra features sets. Therefore, to attain the advantages of both and obtain best results, we have applied LDA on our data first and then applied KDA to further enhance the feature extraction phase. The result can be seen in Figure 5.

### 3.4 Classification

We have considered the driving maneuver activities as, (1) right-turn, (2) left-turn, (3) brake, (4) accelerate, (5) right-lane-change, and (6) left-lane-change. We have experimented with two classifiers, i.e. k-nearest neighbor, and support vector machines.

**K-Nearest Neighbor (KNN)**

K-Nearest Neighbor is a non-parametric classification algorithm in machine learning abundantly used in activity recognition [21]. During the training phase, the features extracted using the LDA and KDA algorithms are provided to the KNN, which are vectors in three dimensional feature space, each with a class label, such as, right-turn, left-turn, brake, accelerate, right-lane-change, and left-lane-change. For training of one class of activity the accelerometer data and the data from the gyroscope are separately forwarded to the classifier and also together. Hence, we have three set of classification based on the input data, called A for accelerometer only, G for gyroscope only, and C for both accelerometer and gyroscope. The feature vectors and class labels are stored as model parameters during the training phase. Euclidian distance is used as the measure of distance metric, while the value of $k=1$ is used in our experimentation.

**Support Vector Machine (SVM)**

SVM is a supervised classification mechanism used in pattern recognition to classify featured data using hyperplanes [20]. We have used one-against-one approach to build and decompose our multiclass classifier as multiple binary classifiers. Training data is created for each class of activity. After noise reduction, auto-regression, the extracted feature-set from the accelerometer and gyroscope is passed to the SVM which builds a model that assigns new examples to one activity or the other, making it a non-probabilistic binary linear classifier. The class of data is pre-defined during the training phase. During the testing/detection phase, as the class is not pre-defined, the supervised learning is not possible. A Gaussian kernel approach is used to devise a non-linear SVM in our experimentation.

### 3.5 Maneuvering Style Detection

After the activity is classified as either a right-turn, a left-turn, a brake, an accelerate, a right-lane-change, or a left-lane-change, the maneuvering style detection is performed to categorize the maneuvering style as ‘over-cautious’, ‘normal’, ‘aggressive’, and ‘reckless’.

Table 1. Threshold variance value for vehicle maneuvering-style detection

| Driving Activity | Maneuvering Style | | | |
|---|---|---|---|---|
| | Over-cautious | Normal | Aggressive | Reckless |
| Left-turn | $0.0 \leq g \leq 0.05$ | $0.05 \leq x \leq 0.20$ | $0.21 \leq x \leq 0.45$ | $x \geq 0.46$ |
| Right-turn | $0.0 \leq g \leq 0.05$ | $0.05 \leq x \leq 0.20$ | $0.21 \leq x \leq 0.45$ | $x \geq 0.46$ |
| Brake | $0.0 \leq a \leq 0.05$ | $0.05 \leq a \leq 0.20$ | $0.21 \leq a \leq 0.5$ | $a \geq 0.5$ |
| Accelerate | $0.0 \leq a \leq 0.05$ | $0.05 \leq a \leq 0.24$ | $0.25 \leq a \leq 0.44$ | $a \geq 0.45$ |
| Lane-change-left | $0.0 \leq g \leq 0.05$ | $0.05 \leq g \leq 0.10$ | $0.11 \leq g \leq 0.4$ | $g \geq 0.4$ |
| Lane-change-right | $0.0 \leq g \leq 0.05$ | $0.05 \leq g \leq 0.10$ | $0.11 \leq g \leq 0.4$ | $g \geq 0.4$ |

We have used a rule-based approach in categorizing the maneuvering style of the driver which is based on the statistical analysis of the data for the concerned activity. For example, if the driving activity is classified as a left turn, then we define the threshold values for the variance of the data (y-axis) as: 0 - 0.05 as over-cautious, 0.05 – 0.2 as normal, 0.2 – 0.45 aggressive, and greater than 0.45 to be reckless. The values for the other driving activities are given in Table 1. In the simulated environment, as discussed before, certain scenarios were artificially created according to the different driving styles for each driving activity. For example, for activity ‘left-turn’, over-cautious (too slow) left turn was performed which gave very small value in G-force (less than 0.05). Similarly, many ‘normal’ left-turns were performed to identify the range of G-force values for non-aggressive left-turn. After that the same simulations are performed to identify the range of G-force for aggressive and reckless classification. These threshold values are calculated after 15 simulations for each category of each driving activity. After visualizing the simulated data, the threshold values were calculated by the author. For activities, right-turn, left-turn, right-lane-change, and left-lane-change, y-axis values from the gyroscope are used, while for activities brake and accelerate, z-axis values from accelerometer are used.

## 4. Experiments and Results

### 4.1 Data Collection

We have used a MotionNode, a miniature 3-DOF inertial measurement unit (IMU), which includes triaxial accelerometer, gyroscope, and magnetometer for use in motion sensing applications [25]. The device is 35 x 35 x 15 mm in size, shown in Figure 6, with orientation output of 3-DOF with full 360 degrees range in all three axes. The tri-accelerometer can measure linear acceleration in the range of 2±g or 6±g with resolution 190 µg ± 5% (at 2 g range). The gyroscope can measure angular velocity with range ± 2000 degrees/second and resolution 0.07 degrees/second. The device is mounted inside the car on the fiber dashboard in a Toyota Camry 2011 for data collection. The data is gathered are the sampling rate of 1000 Hz.

Figure 6. MotionNode device which includes an accelerometer, a gyroscope and a magnetometer.

### 4.2 Experimentation Setup

For the learning/training phase eight simulated scenarios are recorded for each category of each driving activity. Four simulated scenarios are recorded for testing phase for each category in each activity also. Given that there are six activities and four categories, 6 x 4 x (8 + 4) = 288 simulated scenarios are recorded. Four new simulated scenarios and four simulated scenarios from the training phase are used to check the accuracy of the classifiers. Hence, for each driving activity, thirty-two simulated test cases are used for learning and thirty-two cases are used for testing accuracy, out of which sixteen are included in the training.

### 4.3 Results & Discussion

We have performed the experiments with different settings to evaluate the feature extraction and classification algorithms. We have experimented without using LDA and KDA (no-DA), using LDA, and using KDA for features extraction. Similarly, we have evaluated with KNN and SVM separately. Furthermore, we have evaluated the mechanism on accelerometer data only, gyroscope data only, and on data from both the sensors.

Figure 7 shows the results for different classifiers and features extraction techniques on accelerometer data only. Figure 8 shows the results for different classifiers and features extraction techniques on gyroscope data only. Figure 9 shows the results for different classifiers and features extraction techniques on both gyroscope and accelerometer data. As shown by the results, without applying discriminant analysis, the result are very poor. This is because the variance in the features is very high and the classes have no distinct boundaries. After the application of LDA, the accuracy improves but it is less than the accuracy of the KDA. This is due to the fact that LDA is linear, while KDA is a non-linear discriminant analyzer.

For the classifiers, we have observed that SVM performs better that the KNN, although the value for k used is one (1). From the literature review it is also confirmed that for activity recognition, SVM has better classification accuracy than the KNN.

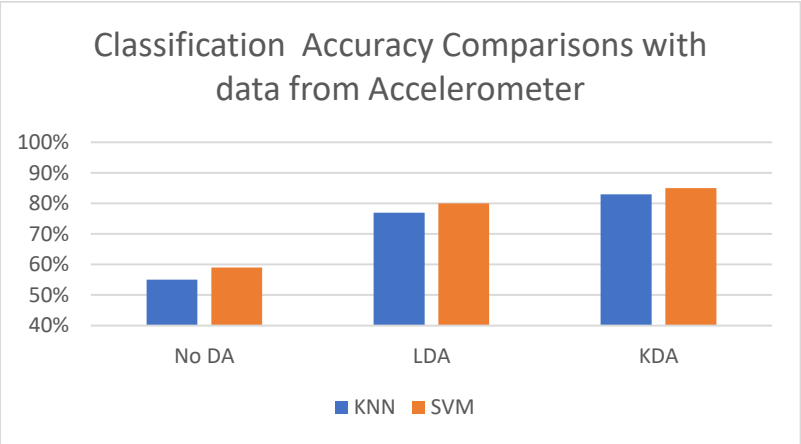


Figure 7. Driving activity classification accuracy for classifiers KNN and SVM for features extraction techniques on accelerometer data only

After the driving activities have been classified and detected, we perform further classification to categorize the activities as ‘over cautious’, “normal’, ‘aggressive’, and reckless. As discussed in section 3, we have applied a rules based approach in categorizing the activities. Table 2 shows the accuracy chart for the driving style classifications. Accuracy shows the driving style is correctly categorized, while the false positive is when a style is detected but that is not the case. The lower values of accuracy for the ‘over-cautious’ is due to the negligible change in the values of accelerometer and gyroscope due to the noise reduction scheme which make the signal smooth and removes the higher frequencies. The normal driving style of the driver becomes similar to the over-cautious style; hence, the high false positive rate.

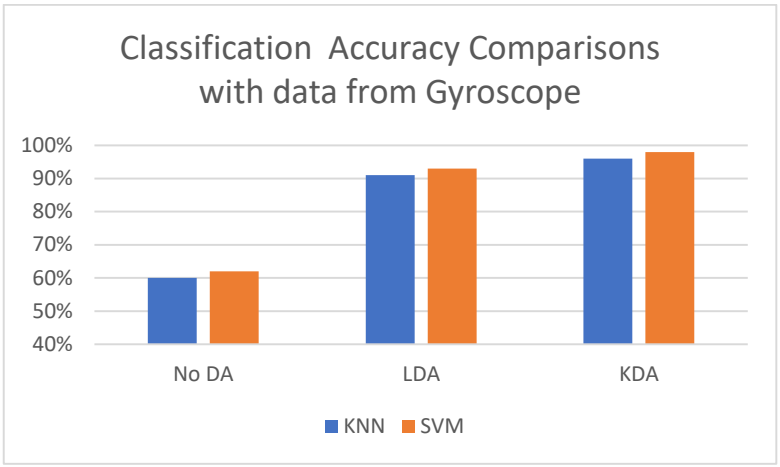


Figure 8. Driving activity classification accuracy for classifiers KNN and SVM for features extraction techniques on gyroscope data only

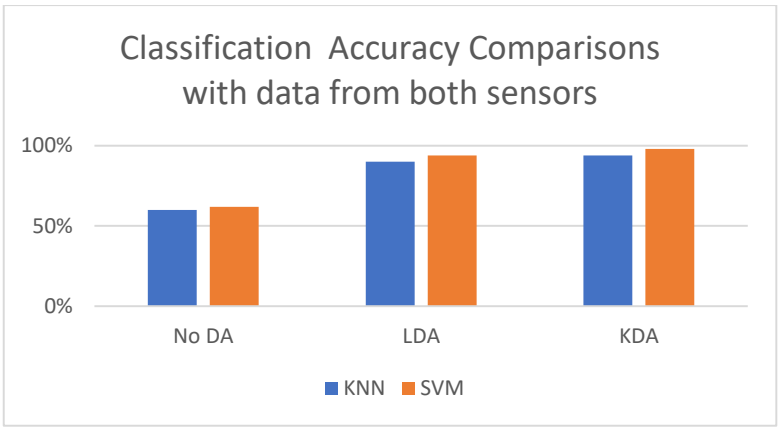


Figure 9. Driving activity classification accuracy for classifiers KNN and SVM for features extraction techniques on gyroscope and accelerometer data

## 5. Conclusion

In this paper, we have presented a model for detecting the maneuvering style of the driver which can help in identifying the culprit driver in case of a road side accident. The driver with the reckless or more aggressive driving style can be accounted for the accident. For our system, we have used an accelerometer and a gyroscope to collect data and apply features extraction and classification algorithm to identify the current driving activity and then based on the variance of values gathered from the gyroscope and accelerometer, categorized the driving style to be either, normal or reckless. We have used and evaluated features extraction algorithms, such as, linear discriminant analysis and kernel discriminant analysis, and classification algorithms, such as, k-nearest neighbor and support vector machine to find the best possible solution for our model. According

to the results, the combination of KDA and SVM provides the best accuracy for driving activity detection. In the future, we aim to explore other classification algorithms, such as, random forest, etc. to improve the efficiency of the system. We aim to implement another classifier for driving style categorization also.

Table 1. Threshold variance value for vehicle maneuvering-style detection

| | Accuracy (Ac) & False Positive (FP) in percentages | | | | | | | |
|---|---|---|---|---|---|---|---|---|
| | Over-cautious | | Normal | | Aggressive | | Reckless | |
| Driving Activity | Ac | FP | Ac | FP | Ac | FP | Ac | FP |
| Left-turn | 70 | 30 | 96 | 4 | 98 | 2 | 99 | 0.5 |
| Right-turn | 70 | 30 | 96 | 4 | 98 | 2 | 99 | 0.5 |
| Brake | 78 | 22 | 99 | 0.5 | 99 | 0.5 | 99 | 0.5 |
| Accelerate | 65 | 35 | 95 | 5 | 97 | 3 | 99 | 1 |
| Lane-change-left | 60 | 40 | 90 | 10 | 95 | 5 | 99 | 1 |
| Lane-change-right | 60 | 40 | 90 | 10 | 95 | 5 | 99 | 1 |

**Acknowledgement**

This work was supported by the Deanship of Research, Islamic University of Madinah, Kingdom of Saudi Arab [Project Title: "Automated Conflict Resolution for Car Accident Insurance Claims using Multi-Model Data Recording Device", 24/39 ~ 1438-1439].

## 6. References

[1] "Report: Saudi Arabia records 526,000 road accidents annually", Saudi Gazette on Dec. 31, 2015, http://english.alarabiya.net/en/News/middle-east/2016/01/01/Report-Saudi-Arabia-records-526-000-road-accidents-annually.html

[2] AM Al-Atwai and W Saleh, "Identification assessment and the enhancement of accident data collection and analysis in KSA" WIT Transactions on the Built Environment, Vol. 138, 2014

[3] T. Nedal et al., "Characterization of crash-prone drivers in Saudi Arabia – A multivariate analysis", Case Studies on Transport Policy, Volume 5, Issue 1, 2017, pp. 134-142

[4] UB Gaffar, SM Ahmed, "A Review of Road traffic accident in Saudi Arabia: the neglected epidemic", Indian Journal of Forensic and Community Medicine, 2015;2(4):242-246

[5] "Traffic Accidents In The Kingdom By Region And Place Of Accident", Ministry of Interior - General Directorate of Traffic, Saudi Open Data, http://www.data.gov.sa/en/dataset/traffic-accidents

[6] "Driver Activity Recognition in identifying the Culprit for a Road Accident" has been published by the International Journal of Research and Analytical Reviews (IJRAR), ISBN-2349-5138 (print); 2348-1269 (online). IJRAR August 2018, Volume 5, Issue 3, page no. 755-761

[7] Khan, A.M.; Tufail, A.; Khattak, A.M.; Laine, T.H. Activity Recognition on Smartphones via Sensor-Fusion and KDA-Based SVMs. Int. J. Distrib. Sens. Netw. 2014, 2014, 1–14.

[8] Thammasat, E.; Chaicharn, J. A simply fall-detection algorithm using accelerometers on a smartphone. Proceedings of the Biomedical Engineering International Conference (BMEiCON), Ubon Ratchathani, Thailand, 5–7 December 2012.

[9] Song, K.-T.; Wang, Y.Q. Remote activity monitoring of the elderly using a two-axis accelerometer. Proceedings of the CACS Automatic Control Conference, Tainan, Taiwan, November 18–19, 2005.

[10] M. Mladenov, M. Mock, "A Step Counter Service for Java-Enabled Devices Using a Built-in Accelerometer", Proc. 1st Int'l Workshop Context-Aware Middleware and Services (CAMS), pp. 1-5, 2009.

[11] Hemminki, S.; Nurmi, P.; Tarkoma, S. Accelerometer-based Transportation Mode Detection on Smartphones. In Proceedings of the 11th ACM Conference on Embedded Networked Sensor Systems (SenSys '13), Roma, Italy, 11–15 November 2013.

[12] Cervantes-Villanueva, J.; Carrillo-Zapata, D.; Terroso-Saenz, F.; Valdes-Vela, M.; Skarmeta, A.F. Vehicle maneuver detection with accelerometer-based classification. Sensors 2016, 16, 1618.

[13] Lara, O.D.; Labrador, M.A. A Survey on Human Activity Recognition using Wearable Sensors. IEEE Commun. Surv. Tutor. 2013, 15, 1192–1209.

[14] Shoaib, M.; Bosch, S.; Incel, O.D.; Scholten, H.; Havinga, P.J. A survey of online activity recognition using mobile phones. Sensors 2015, 15, 2059–2085.

[15] Attal, F.; Mohammed, S.; Dedabrishvili, M. Physical Human Activity Recognition Using Wearable Sensors. Sensors 2015, 15.

[16] Preece, S.J.; Goulermas, J.Y.; Kenney, L.P.; Howard, D.; Meijer, K.; Crompton, R. Activity identification using body-mounted sensors—A review of classification techniques. Physiol. Meas 2009, 30, R1–R33

[17] Wang, S.; Chen, C.; Ma, J. Accelerometer based transportation mode recognition on mobile phones. In Proceedings of the IEEE 2010 Asia-Pacific Conference on Wearable Computing Systems, Shenzhen, China, 17–18 April 2010; pp. 44–46.

[18] Vaitkus, V.; Lengvenis, P.; Žylius, G. Driving style classification using long-term accelerometer information. In Proceedings of the 2014 19th International Conference On Methods and Models in Automation and Robotics (MMAR), Miedzyzdroje, Poland, 2–5 September 2014; pp. 641–644.

[19] Dai, J.; Teng, J.; Bai, X.; Shen, Z.; Xuan, D. Mobile phone based drunk driving detection. In Proceedings of the 2010 4th International Conference on Pervasive Computing Technologies for Healthcare, London, UK, 1–3 April 2010; pp. 1–8.

[20] Anguita, D.; Ghio, A.; Oneto, L.; Parra, X.; Reyes-Ortiz, J.L. Ambient Assisted Living and Home Care. In Human Activity Recognition on Smartphones Using a Multiclass Hardware-Friendly Support Vector Machine, Proceedings of the 4th International Workshop (IWAAL 2012), Vitoria-Gasteiz, Spain, 3–5 December 2012; Springer: Berlin/Heidelberg, Germany, 2012; pp. 216–223.

[21] Thiemjarus, S.; Henpraserttae, A.; Marukatat, S. A study on instance-based learning with reduced training prototypes for device-context-independent activity recognition on a mobile phone. In Proceedings of the 2013 IEEE International Conference on Body Sensor Networks (BSN), Cambridge, MA, USA, 6–9 May 2013; pp. 1–6.

[22] A.M. Khan, Y.-K. Lee, S.Y. Lee, and T.-S. Kim. Human activity recognition via an accelerometer enabled-smartphone using kernel discriminant analysis. In Proceedings of the 5th International Conference on Future Information Technology, pages 1–6, 2010

[23] Abdi H, Williams LJ. Principal component analysis. Wiley interdisciplinary reviews: computational statistics. 2010 Jul;2(4):433-59.

[24] Akaike, Hirotugu. "Fitting autoregressive models for prediction." Annals of the institute of Statistical Mathematics 21, no. 1 (1969): 243-247.

[25] MotionNode Specification. https://www.motionnode.com/MotionNode_Specification.pdf, 2018 (accessed 20 December 2018).

[26] Balakrishnama, Suresh, and Aravind Ganapathiraju. "Linear discriminant analysis-a brief tutorial." Institute for Signal and information Processing 18 (1998): 1-8.

[27] Bianchi, Giovanni, and Roberto Sorrentino. Electronic filter simulation & design. McGraw Hill Professional, 2007.

[28] Zhang, Yong, Junjie Li, Yaohua Guo, Chaonan Xu, Jie Bao, and Yunpeng Song. "Vehicle Driving Behavior Recognition Based on Multi-View Convolutional Neural Network (MV-CNN) with Joint Data Augmentation." IEEE Transactions on Vehicular Technology (2019).

[29] World Health Organization (WHO): Global status report on road safety 2018, https://apps.who.int/iris/bitstream/handle/10665/276462/9789241565684-eng.pdf?ua=1 (accessed on March 10th, 2019)

[30] Aldegheishem, Abdulaziz, Humera Yasmeen, Hafsa Maryam, Munam Shah, Amjad Mehmood, Nabil Alrajeh, and Houbing Song. "Smart road traffic accidents reduction strategy based on intelligent transportation systems (tars)." Sensors 18, no. 7 (2018): 1983.

# An Empirical Study of Community Detection Algorithms on Social and Road Networks

Waqas Nawaz
College of Computer and Information Systems,
Islamic University of Madinah, KSA.
wnawaz@iu.edu.sa

## Abstract

Community detection in social networks is a problem with considerable interest, since, discovering communities reveals hidden information about networks. There exist many algorithms to detect inherent community structures and recently few of them are investigated on social networks. However, it is non-trivial to decide the best approach in the presence of diverse nature of graphs, in terms of density and sparsity, and inadequate analysis of the results. Therefore, in this study, we analyze and compare various algorithms to detect communities in two networks, namely social and road networks, with varying structural properties. The algorithms under consideration are evaluated with unique metrics for internal and external connectivity of communities that includes internal density, average degree, cut ratio, conductance, normalized cut, and average Jaccard Index. The evaluation results revealed key insights about selected algorithms and underlying community structures.

### keywords

Graph Mining, Community Detection, Road Network, Social Network, Algorithms, Community Analysis

# دراسة تطبيقية لخوارزميات اكتشاف المجتمع على الشبكات الاجتماعية والطرق

**الملخص**: تحديد المجتمع في شبكات التواصل الاجتماعي يمثل مشكلة عويصة تتطلب الاهتمام الشديد، لأن اكتشاف المجتمعات يكشف عن معلومات خفية على الشبكات. توجد العديد من الخوارزميات للكشف عن الهياكل المجتمعية المتأصلة، ويتم في الآونة الأخيرة فحص عدد قليل منها على الشبكات الاجتماعية. وليس مضرا تحديد أفضل طريقة في وجود الطبيعة المتنوعة للرسوم البيانية، من حيث الكثافة والكثافة المنخفضة. وعدم ملاءمة تحليل النتائج. لذلك، في هذه الدراسة، نقوم بتحليل ومقارنة الخوارزميات المختلفة لاكتشاف المجتمعات في شبكتين، وهما الشبكات لاجتماعية والطرق، مع خصائص هيكلية متغيرة.

يتم تقييم الخوارزميات قيد الدراسة باستخدام مقاييس فريدة للتوصيل الداخلي والخارجي للمجتمعات التي تتضمن الكثافة الداخلية، ومتوسط الدرجة، ونسبة القطع، والتصريف، والقطع الطبيعي، ومتوسط مؤشر جاكار. وكشفت نتائج التقييم عن معلومات أساسية حول الخوارزميات المختارة والهياكل المجتمعية الكامنة.

# 1 Introduction

Cluster, or community structure, is a grouping of graph vertices together such that intra-group edge density is higher than inter-group edge density [1]. There are plethora of techniques for detecting communities in a network [1, 2, 3, 4, 5, 6, 7, 8] and it is non-trivial to decide the best approach for a certain scenario.

There are few initiatives taken in the literature to simplify this task. One of them investigated graph communities with ground-truth [9], which is not favorable in real life networks. Another made an evaluation on overlapping communities in [10] that is not the focus of this study. Therefore, it is essential to evaluate the community detection algorithms considering the inherent structural properties of graph data and choose respective metric. For instance, the study of LPA [11] shows poor quality results when applied on a dataset with high clustering coefficient, although as per author claim it is the best algorithm for detecting communities. Moreover, other studies [9] and [12] say that it is necessary to use datasets with varying characteristics and corresponding metric for effective evaluation. For example, when the network contains well-separated non-overlapping communities, *conductance* is the best scoring function in such cases.

The existing studies lack behind in diversity of datasets and effective evaluation measures, which we overcome in this work. We study the problem of community detection in diverse networks based on social interactions (email) and physical infrastructure(road), which have varying structural properties. It provides a validation tool to verify the correctness of the claims in literature regarding social network communities. We use unique set of measures to evaluate the resultant communities that includes internal density, 2 average degree, conductance, cut ratio, and normalized cut.

The key findings of this study are summarized as follows.

- The community detection algorithms studied in this paper have shown consistent performance over social graph data in reference to existing benchmark [13].
- We noticed a significant change in proportion of structural properties, neighborhood connectivity and degree distribution, of two social graphs, i.e. email and collaboration network.
- We observed few unexpected behaviors of the selected algorithms in certain cases. For example, LPA approach has shown poor performance for effectiveness (average degree) of communities on collaboration network.

# 2 Existing Work

In this section, we briefly elaborate the existing empirical studies on community detection algorithms and also highlight the differences to our work.

In one of the most relevant study[13], the authors have presented a universal framework for comparison that gives equal conditions to evaluate various community detection approaches. The authors bench-marked a set of algorithms on social networks to better analyze, evaluate, diagnose and further improve them. However, this benchmark is limited when it comes to diversity of networks and evaluation measures. Similarly, G. Misra's work [14] analyzed eight different community detection algorithms for access control decisions in a personalized social network. This study lacks the diversity of the network under-consideration, i.e. social network, and limits the analysis of community detection algorithms to a specific application scenario.

N. Grag et. al. [15] and Z. Zhao et. al. [16] have studied community detection algorithms only in the context of modularity, which is one kind of measure to analyze the quality of resultant communities, with varying size of the graphs rather than the properties . Moreover, they have not considered variety of community detection algorithms. The most recent empirical study on community detection algorithms in [17] highlights only their advantages and disadvantages without actual analysis of community structures of the real networks. This study also overlooked the structural properties of the underlying network for resultant communities.

# 3 Community Detection Algorithms: An Overview

In this section, We briefly outline the community detection approaches under consideration for this study.

Community detection is a well known problem to identify and group strongly connected nodes together in a graph. There are various approaches to detect communities in graphs and often categorized based on their nature of processing such as local (forming communities from local structures to the whole graph), global (separating out communities from the entire graph) and tree-structure (maintaining a tree with branches that represent communities) methods [13]. We chose six methods[1] such that at least one method from each category for representative analysis.

- **Clauset Newman Moore (CNM)** [1] belongs to a hierarchical clustering strategy that maintains hierarchy of the resultant clusters. The hierarchical clustering method follows either agglomerative or divisive approach. CNM uses classical agglomeration approach that is a *bottom up* strategy while divisive method follows *top down* strategy. CNM optimizes the modularity of the final partition by making greedy choices. This algorithm is effectively used for complex networks in research community, and was designed specifically to analyze the community structures of extremely large networks, i.e. millions of nodes.

- **Radicchi** [18] is also a type of hierarchical clustering algorithm but unlike CNM, it takes a

[1]The availability of implementation resources, provided by authors, also affected this selection process.

divisive approach by starting from the whole graph and splitting it into communities gradually.

- **Label Propagation Algorithm (LPA)** [7] is an efficient, near linear time, algorithm to detect community structures in large-scale networks. It is a semi-supervised algorithm that uses unlabeled nodes to find out the labels. It has an advantage in running time and performs well when there is prior information or annotated data.

- **TopLeaders**[4], i.e. Leadership expansion algorithm, extracts clusters from the graph identifying it as sets, consisting of a leader node and its follower nodes that are close to the leader. This algorithm requires to select initial $k$ leaders as the number of desired communities.

- **Sequential Clique Percolation (SCP)** [5] algorithm is based on the clique percolation method and detects $k$-clique subgrpahs for a given value of $k$ from dense graph by sequentially inserting edges and keeping track of the emerging community structure. In comparison to CFinder[19], it finds all the cliques of single size and output the communities for all possible thresholds, while CFinder finds maximal cliques in a graph and produces communities of all possible clique sizes. Therefore, we can consider this algorithm as a alternative to CFinder. Another good thing about SCP algorithm is that it works well with large sparse graphs, however, it may not be a good option when the graph is very dense or it contains large size cliques.

- **Matrix Blocking Dense Subgraph Extraction (MB-DSGE)** [2] algorithm reorders a relatively sparse graph and extracts dense subgraphs as communities. More precisely, for clustering, it constructs a hierarchy tree using matrix blocking technique, which groups similar columns of an adjacency matrix according to the cosine similarity measure.

# 4 Experiments

In this section, we explain the details of experiments including environmental setup, algorithms for comparisons, data sets, and result evaluation criteria. The detailed discussion is provided at the end.

## 4.1 Environment Setup

We analyze six representative algorithms to detect communities. These algorithms are implemented on different platforms. Our evaluation criteria is independent of any platform and considers the output results explicitly. Therefore, it is not essential to execute or implement all the algorithms on a single platform. The implementation detail for each algorithm is as follows. The

default setting for each algorithm is considered for all subsequent experiments unless stated explicitly.

- **CNM** (Clauset Newman Moore) is the agglomeration approach [1]. The authors provide an executable makefile of their implementation written in C [20]. The original version of the provided code works on unweighted and undirected graphs. However, later the authors introduce another version of the code that works on weighted and undirected graphs.
- **Radicchi** is a divisive hierarchical clustering algorithm[18]. The authors provide binaries written in C++ [21] along with the source code files.
- **LPA** (Label Propagation Algorithm) [7]. The implementation is available in R programming language for LPA [22]. However, we also found LPA's implementation in Python language [23] and used for experiments in this study.
- **TopLeaders** algorithm gradually associates nodes to the nearest leaders and locally reelects new leaders during each iteration [4]. The authors provide an executable jar file, written in java [24].
- **SCP** [5]. This algorithm's source code is written in C++ and Python [25], however, we used Python implementation for our analysis.
- **MB-DSGE** [2]. The source code of this algorithm is implemented in C++ with the makefile which is available at [26]. In this implementation, the author used an open source C++ linear algebra library called Eigen [27].

## 4.2 Datasets

We use four widely used real-world network datasets, i.e. communication, collaboration, and road network.

- **Strike** (the communication network of employees in a sawmill): It has 24 vertices (employees), 38 edges (discussed the strike in some minimum frequency), no arcs, no loops, no line values [4].
- **HEP-PH** (High Energy Physics - Phenomenology): This collaboration network is from the e-print arXiv and covers scientific collaborations between authors papers submitted to High Energy Physics - Phenomenology category. If an author i co-authored a paper with another author j, the graph contains a undirected edge from vertex i to vertex j. If the paper is co-authored by k authors, this generates a completely connected (sub)graph of k vertices. It contains 12008 vertices and 118521 edges [28].

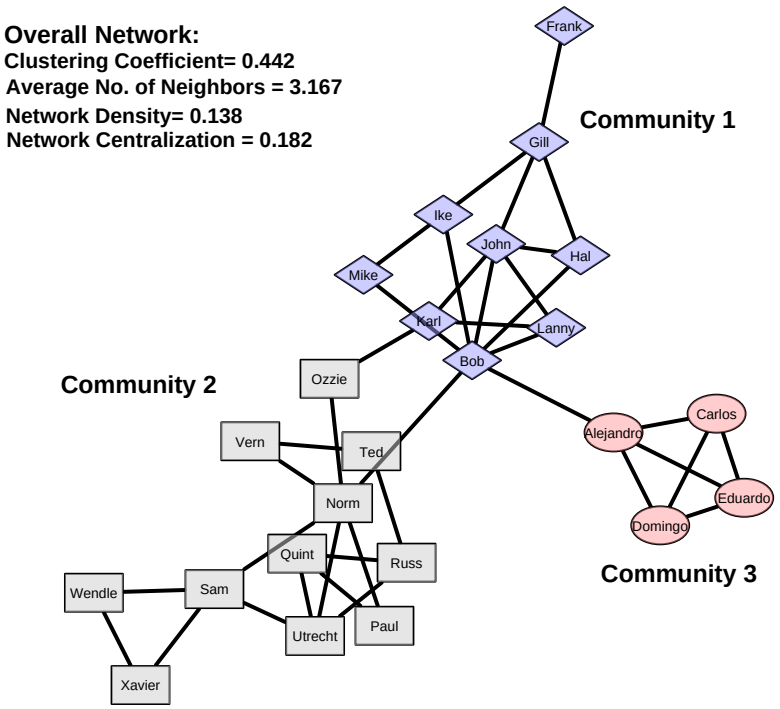


Figure 1: Strike network with communities as a ground truth.

- **Enron** (email network) Enron email communication network [29] covers all the email communication within a dataset of around half million emails. This data was originally made public, and posted to the web, by the Federal Energy Regulatory Commission during its investigation. Nodes of the network are email addresses and if an address i sent at least one email to address j, the graph contains an undirected edge from i to j.

- **roadNet-PA** (road network) This is a road network of Pennsylvania [30]. Intersections and endpoints are represented by nodes, and the roads connecting these intersections or endpoints are represented by undirected edges.

We analyze the aforementioned datasets to highlight the diversity of these networks. It helps us to anticipate the nature of results with given knowledge about original networks. The Strike network is visualized in Figure 1 with communities as a ground truth. We also computed the overall network properties for understanding, e.g. cluster coefficient is 0.44 that shows tendency towards better communities. We have shown the degree distribution of all datasets in Figure 2 to analyze their structural aspects. The road network has limited variations for vertex degree and distribution is somehow different from communication and collaboration networks.

The neighborhood connectivity is critical for graph processing and have more tendency to discover communities. Social networks usually have high neighborhood connectivity that may produce good quality clusters. On the other hand, relatively sparse graphs have lower connectivity among neighbors of vertices, which may produce poor quality clusters due to low edge density.

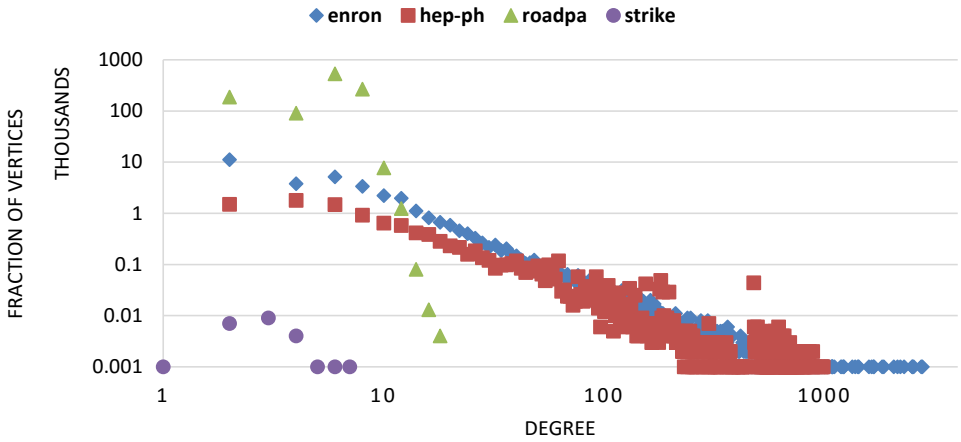


Figure 2: Degree distribution of collaboration, communication, and road networks.

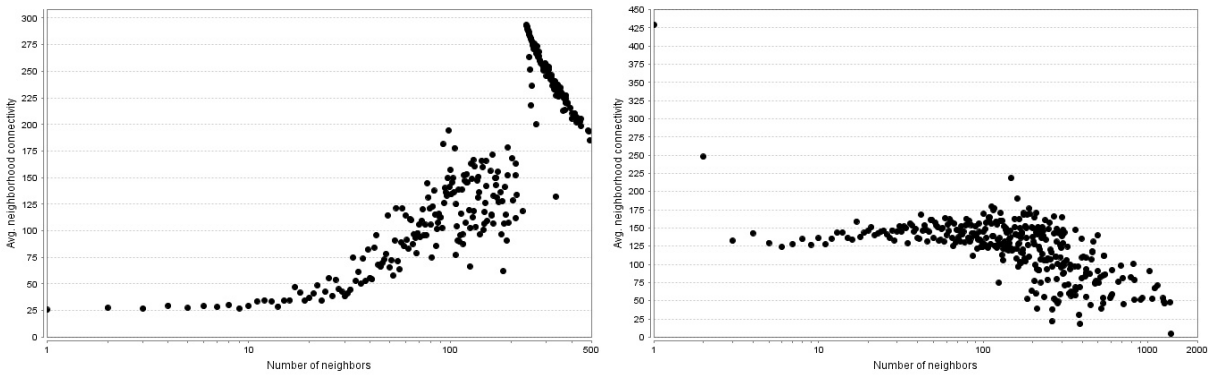


(a) (b)

Figure 3: Graph neighborhood connectivity for (a) collaboration and (b) email networks. The number of neighbors are plotted on x-axis and y-axis shows the average connectivity among neighbors.

We plotted the neighborhood connectivity with respect to number of neighbors for collaboration (hep-ph) and communication (Enron) networks in Figure 3. We observed a considerable difference for neighborhood connectivity between these two networks, e.g. when we consider more than 100 neighbors then the connectivity is higher for collaboration network compared to email network. It is strongly related to the size of resultant communities.

## 4.3 Evaluation criteria

We evaluate algorithms in terms of effectiveness, accuracy and outliers. For effectiveness, we use scoring functions, defined in Section 4.4, based on internal connectivity (internal density, average degree), external connectivity (cut ratio), and metrics that combine internal and external connectivity (conductance, normalized cut). The intuition behind conductance is that a community is a set of nodes strongly connected internally than externally and other metrics following similar intuition

are also popular in research community [12]. For accuracy we chose Jaccard Index that is a widely used similarity measure. It is more sensitive to overcome the small variance of the cross common fraction, i.e. when nodes from several different communities in one result join together as a single community in another result [7].

## 4.4 Community Scoring Functions

The basic intuition for all scoring functions is that communities are sets of nodes with many connections between the members and few connections from the members to the rest of the network. Given a set of nodes S, it is considered a function $f(S)$ that characterizes how community-like is the connectivity of nodes in $S$. Let G(V,E) be an un-directed graph with $n = |V|$ nodes and $m = |E|$ edges. Let S be the set of nodes, where $n_s$ is the number of nodes in S, $n_s = |S|$; $m_s$ the number of edges in S, $m_s = |(u,v) \in E : u \in S, v \in S|$; and $c_s$, the number of edges on the boundary of S, $c_s = |(u,v) \in E : u \in S, v \notin S|$; and $d(u)$ is the degree of node $u$.

- **Conductance**, $f(S) = \frac{c_s}{2m_s+c_s}$. It measures the fraction of total edge volume that points outside the cluster. A good community should have high cohesiveness (high internal conductance) as it should require deleting many edges before the community would be internally split into disconnected components. Conductance captures a notion of "surface area-to-volume" and thus it is widely-used to capture quantitatively the gestalt notion of a good network community as a set of nodes that has better internal- than external-connectivity [31].

- **Internal density**, $f(S) = \frac{m_s}{n_s(n_s-1)/2}$, is the internal edge density of the node set S [18].

- **Average degree**, $f(S) = \frac{2m_s}{n_s}$, is the average internal degree of the members of S [18].

- **Cut ratio**, $f(S) = \frac{c_s}{n_s(n-n_s)}$, is the fraction of existing edges (out of all possible edges) leaving the cluster [32].

- **Normalized cut**, $f(S) = \frac{c_s}{2m_s+c_s} + \frac{c_s}{2(m-m_s)+c_s}$ [31].

- **Jaccard Index** is a widely used similarity measure. It can be defined as $\frac{P_s}{P_s+P_{s1}+P_{s2}}$ where $P_s$ stands for the number of node pairs that are respectively classified into the same community in both results, $P_{s1}$ stands for the number of node pairs appearing in the same community in the algorithm-produced results, but in different communities based on the ground truth, and $P_{s2}$ vice versa [32].

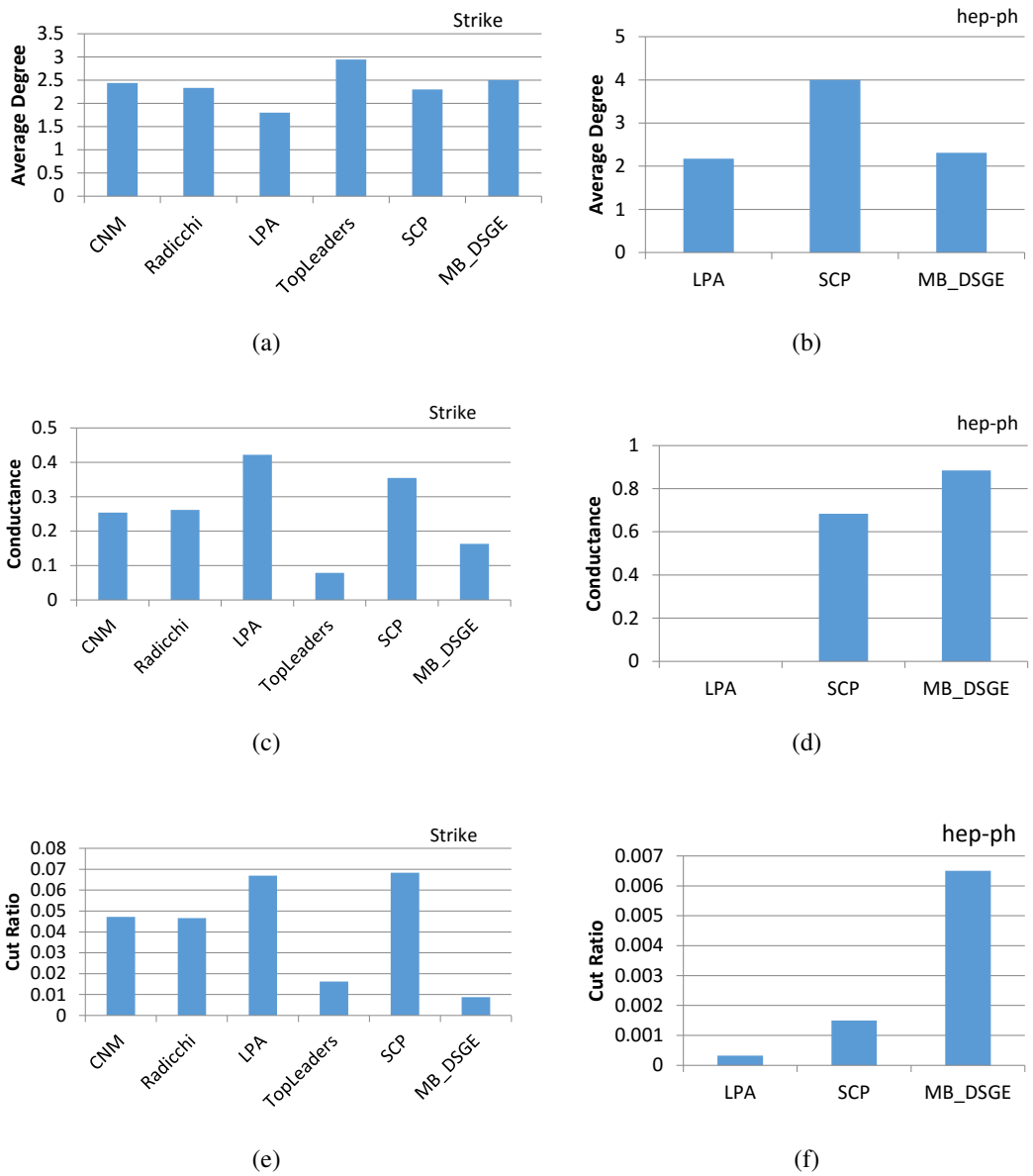


Figure 4: Analyzing the effectiveness of strike and hep-ph network communities respectively (a, b) average degree, (c, d) conductance, and (e, f) cut-ratio.

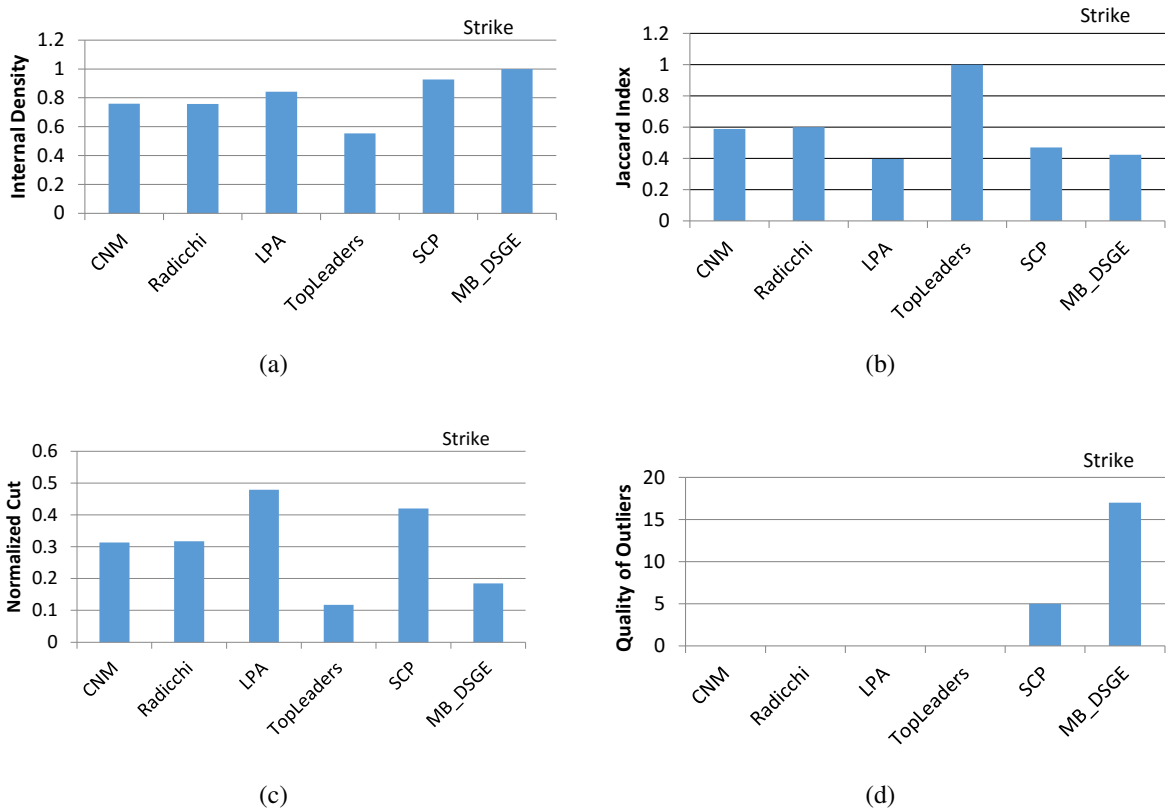


Figure 5: Analyzing the effectiveness, accuracy, and outlier scores for community detection approaches on strike network in terms of (a) internal density, (b) jaccard index, (c) normalized cut, and (d) outliers.

## 4.5 Discussion

The overall discussion in this section is carried out from two aspects: 1) analyzing different evaluation measures using same dataset, and 2) evaluating the clustering quality on datasets with varying properties.

We analyzed the effectiveness of community detection methods on small-scale and medium-scale real life networks, i.e. Strike, Hep-ph, as shown in Figure 4 and Figure 5 respectively. The quality of communities is directly proportional to internal density and average degree values, i.e. good communities have higher values for these internal connectivity measures. In reference to existing study [13], the LPA approach consistently outperforms other approaches through our experiments on Strike dataset, as depicted in Figure 4. Similarly, MB-DSGE approach did not produce good quality clusters as claimed in the reference paper [13]. The only exception we observed for LPA is on Hep-ph dataset for average degree, where it has produced poor quality results compared with other methods, as shown in Figure 4(a) and Figure 4(b).In our understanding, as the connectivity among neighboring nodes is less in Hep-ph dataset compared with strike dataset,

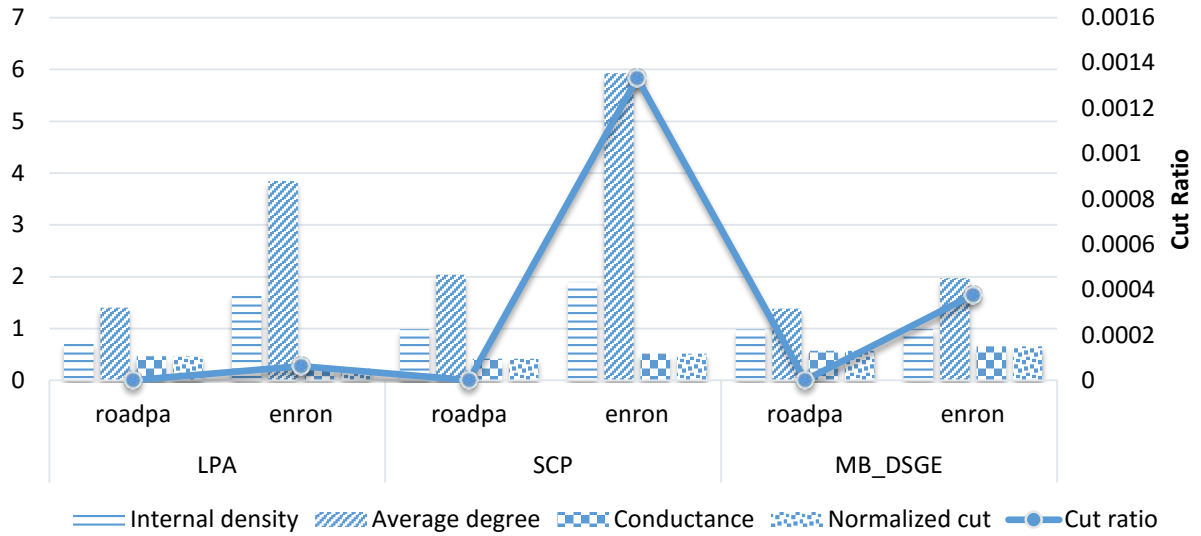


Figure 6: Analyzing the effectiveness of community detection approaches on Email and road-pa network in terms of internal density, average degree, conductance, normalized cut, and cut ratio.

therefore, the same labels are not propagated to majority of the nodes. In other words, very few nodes collected same labels to be grouped together.

It is also important to note, in Figure 4, that very few evaluation measures (community scoring function) may mislead our analysis. For instance, clique percolation approach shows community structures with increased average degree of the nodes but conductance and cut-ratio reveal different story. The reason is that for small size cliques it may result in good quality communities internally but when we analyze how good the community structure is externally then may be it is not. In other words, actual communities may not form clique structures, which is evident in Figure 1 with actual communities as ground truth, and therefore this kind of conclusion can not be drawn from such inadequate analysis. We can conclude that average degree scoring function may not be a good choice in comparison to conductance and cut-ratio.

The strike and hep-ph datasets differ in size as well as in properties but not that different as road-network, however, we observe strange behavior for LPA, SCP and MS-DSGE algorithms. In Figure 4(e), the communities generated through LPA and SCP have high cut-ratio compared with MS-DSGE. But in Figure 4(f), the effect is rather opposite for LPA and SCP. The community structure is already presented for Strike dataset and we can understand that due to better underlying community structures in the data, both LPA and SCP did not performed well. In other words, external links to other communities are too many that is why the resultant communities score is high in terms of cut-ratio. This is not the case with MS-DSGE as it find the dense subgraphs out of sparse graph. Is it the case with hep-ph dataset? In order to understand that we need to carefully look at the Figure 3(a) where we plotted the number of neighbors and neighborhood connectivity. It clearly tells us that number of neighbors and the average neighborhood connectivity

are complementary to each other. Therefore, LPA and SCP could perfom well, i.e. produced communities with low cut-ratio.

The higher conductance, normalized cut (internal and external connectivity), and cut ratio (external connectivity), the worse detected communities are. In other words, these measures are indirectly proportional to the quality of results. LPA shows good results, SCP is medium and MB-DSGE is bad on larger dataset, i.e. Hep-ph. The MB-DSGE algorithm is a method for identifying a set of dense subgraphs of a given sparse graph [2]. Therefore, it has shown different results for these two datasets in Figure 4, i.e. good results for Strike and relatively poor on Hep-ph dataset.

The accuracy of communities is presented in Figure 5(b) where ground-truth is available in advance. In this case, LPA algorithm has lower value for average Jaccard Index that is not same as in the base paper. However, other algorithms have shown the similar performance. Most likely these results deduced from the fact that the Strike dataset is relatively sparse and does not have outliers.

The results quality in terms of outliers is also evaluated and shown in the Figure 5(d). The behavior of each algorithm under consideration is consistent with the claims in literature. MB-DSGE approach has produced the most outliers due to its natural instinct towards identifying the set of dense subgraphs on a given sparse graph. The outlier score for SCP method is relatively lower than MB-DSGE.

We observed the effectiveness of LPA, SCP, and MB-DSGE algorithms on social and road networks, i.e. Enron and roadpa. Our objective is to investigate the variation in results towards diversified properties of these networks. We plotted the internal and external connectivity measures in Figure 6. The internal density and average degree for email (Enron) communities is higher than road (roadpa) communities and it is consistent for all three community detection methods. Since, road network is much sparse then email, therefore, they produced sparse communities with low average degree and density values. For other measures, including conductance, normalized cut, and cut ratio, LPA has outperformed SCP and MB-DSGE methods. The SCP method achieved higher score for internal density and average degree on both datasets compared with LPA, which is non-trivial. However, the accuracy aspect is compromised for SCP. There is a trade-off between effectiveness and accuracy when it comes to SCP method.

It is interesting to see that LPA, SCP and MB-DSGE methods detected better communities in terms of cut-ratio on road network in Figure 6, where the road network is comparatively sparse than Enron email network. It make sense because in road network the detected communities have less number of edges going out of the communities due to sparseness, which is not the case with Enron email network. For other measures like conductance and normalize-cut, we can see the similar behavior of the algorithms on read network where communities have relatively lower values compared with the Enron network. There is an exception for LPA algorithm when it comes to road network where it has produced relatively poor communities in reference to email network. The

reason for such behavior lies in label propagation algorithm where strongly connected nodes end up receiving same labels and resulted in the same community. In other words, it does not include the nodes in the same community having links to nodes of other communities.

# 5 Conclusion and Future Directions

This study provided an experimental evaluation of a set of representative and well-known community detection algorithms on structurally different datasets with varying properties, i.e. density, sparsity, and neighborhood connectivity. We evaluated results of these algorithms for effectiveness, accuracy, and outliers. The extensive evaluation of the resultant communities in terms of unique measures suggested the superiority of LPA method over others in social networks. However, SCP method achieved better internal density and average degree compared to LPA, while with a slight compromise on accuracy. The impact of network properties is proportionally reflected in results, but the behavior of community detection methods persisted.

It is non-trivial to foresee the impact of community detection approaches over weighed and directed graphs. The personal traits of entities in a network, e.g. attributes associated with the vertices, further complicates this process and requires a systematic analysis for better understanding. The analysis problem becomes even more complex when we encounter non-homogeneous networks with varying types of vertices, i.e. heterogeneous networks.

# Acknowledgement

I acknowledge the support of Islamic University of Madinah for disseminating this research work. I also appreciate the help provided by Zilya Yagafarova and support of colleagues at Innopolis University Russia to carryout this work.

# References

[1] A. Clauset, M. E. J. Newman, and C. Moore, "Finding community structure in very large networks," *Phys. Rev. E*, vol. 70, no. 6, p. 066111, 2004.

[2] J. Chen and Y. Saad, "Dense subgraph extraction with application to community detection," *Knowledge and Data Engineering, IEEE Transactions on*, vol. 24, no. 7, pp. 1216–1230, 2012.

[3] J. Huang, H. Sun, Q. Song, H. Deng, and J. Han, "Revealing density-based clustering structure from the core-connected tree of a network," *Knowledge and Data Engineering, IEEE Transactions on*, vol. 25, no. 8, pp. 1876–1889, 2013.

[4] R. R. Khorasgani, J. Chen, and O. R. Zaïane, "Top leaders community detection approach in information networks," in *4th SNA-KDD Workshop on Social Network Mining and Analysis*. Citeseer, 2010.

[5] J. M. Kumpula, M. Kivelä, K. Kaski, and J. Saramäki, "Sequential algorithm for fast clique percolation," *Physical Review E*, vol. 78, no. 2, p. 026109, 2008.

[6] I. X. Leung, P. Hui, P. Lio, and J. Crowcroft, "Towards real-time community detection in large networks," *Physical Review E*, vol. 79, no. 6, p. 066107, 2009.

[7] U. N. Raghavan, R. Albert, and S. Kumara, "Near linear time algorithm to detect community structures in large-scale networks," *Physical Review E*, vol. 76, no. 3, p. 036106, 2007.

[8] F. Zhao and A. K. Tung, "Large scale cohesive subgraphs discovery for social network visual analysis," *Proceedings of the VLDB Endowment*, vol. 6, no. 2, pp. 85–96, 2012.

[9] J. Yang and J. Leskovec, "Defining and evaluating network communities based on ground-truth," *Knowledge and Information Systems*, vol. 42, no. 1, pp. 181–213, 2015.

[10] J. Xie, S. Kelley, and B. K. Szymanski, "Overlapping community detection in networks: The state-of-the-art and comparative study," *Acm computing surveys (csur)*, vol. 45, no. 4, p. 43, 2013.

[11] S. Harenberg, G. Bello, L. Gjeltema, S. Ranshous, J. Harlalka, R. Seay, K. Padmanabhan, and N. Samatova, "Community detection in large-scale networks: a survey and empirical evaluation," *Wiley Interdisciplinary Reviews: Computational Statistics*, vol. 6, no. 6, pp. 426–439, 2014.

[12] J. Leskovec, K. J. Lang, and M. Mahoney, "Empirical comparison of algorithms for network community detection," in *Proceedings of the 19th international conference on World wide web*. ACM, 2010, pp. 631–640.

[13] M. Wang, C. Wang, J. X. Yu, and J. Zhang, "Community detection in social networks: An in-depth benchmarking study with a procedure-oriented framework," *PVLDB*, vol. 8, no. 10, pp. 998–1009, 2015.

[14] G. Misra, J. M. Such, and H. Balogun, "Non-sharing communities? an empirical study of community detection for access control decisions," in *2016 IEEE/ACM International Conference on Advances in Social Networks Analysis and Mining (ASONAM)*. IEEE, 2016, pp. 49–56.

[15] N. Garg and R. Rani, "A comparative study of community detection algorithms using graphs and r," in *2017 International Conference on Computing, Communication and Automation (ICCCA)*. IEEE, 2017, pp. 273–278.

[16] Z. Zhao, S. Zheng, C. Li, J. Sun, L. Chang, and F. Chiclana, "A comparative study on community detection methods in complex networks," *Journal of Intelligent & Fuzzy Systems*, no. Preprint, pp. 1–10, 2018.

[17] K. Chandusha, S. R. Chintalapudi, and M. H. M. Krishna Prasad, "An empirical study on

community detection algorithms," in *Smart Intelligent Computing and Applications*, S. C. Satapathy, V. Bhateja, and S. Das, Eds. Singapore: Springer Singapore, 2019, pp. 35–44.

[18] F. Radicchi, C. Castellano, F. Cecconi, V. Loreto, and D. Parisi, "Defining and identifying communities in networks," *Proceedings of the National Academy of Sciences of the United States of America*, vol. 101, no. 9, pp. 2658–2663, 2004.

[19] B. Adamcsek, G. Palla, I. J. Farkas, I. Derényi, and T. Vicsek, "Cfinder: locating cliques and overlapping modules in biological networks," *Bioinformatics*, vol. 22, no. 8, pp. 1021–1023, 2006.

[20] A. Clauset, "Source code of cnm algorithm," http://www.cs.unm.edu/~aaron/research/fastmodularity.htm (Last accessed on 16 March, 2019).

[21] F. Radicchi, "Source code of radicchi algorithm," http://homes.soic.indiana.edu/filiradi/resources.html (Last accessed on 16 March, 2019).

[22] "R code of lpa algorithm," http://igraph.wikidot.com/community-detection-in-r (Last accessed on 16 March, 2019).

[23] "Python code of lpa algorithm," http://orkohunter-networkx.readthedocs.org/en/latest/_modules/networkx/algorithms/community/asyn_lpa.html (Last accessed on 16 March, 2019).

[24] R. R. Khorasgani, "Source code of topleaders algorithm," https://webdocs.cs.ualberta.ca/~rabbanyk/TopLeader/ (Last accessed on 16 March, 2019).

[25] J. M. Kumpula, "Source codes of scp algorithm," http://complex.cs.aalto.fi/resources/software/ (Last accessed on 16 March, 2019).

[26] "Code of mbdsge algorithm," https://github.com/sranshous/Graph-Community-Detection (Last accessed on 16 March, 2019).

[27] "Eigen: Linear algebra library," http://eigen.tuxfamily.org/index.php?title=Main_Page (Last accessed on 16 March, 2019).

[28] J. Leskovec and A. Krevl, "SNAP Datasets: Stanford large network dataset collection," http://snap.stanford.edu/data (Last accessed on 16 March, 2019), 2014.

[29] J. Leskovec and et. al., "Statistical properties of community structure in large social and information networks," in *Proceedings of the 17th international conference on World Wide Web*. ACM, 2008, pp. 695–704.

[30] J. Leskovec, K. J. Lang, A. Dasgupta, and M. W. Mahoney, "Community structure in large networks: Natural cluster sizes and the absence of large well-defined clusters," *Internet Mathematics*, vol. 6, no. 1, pp. 29–123, 2009.

[31] J. Shi and J. Malik, "Normalized cuts and image segmentation," *Pattern Analysis and Machine Intelligence, IEEE Transactions on*, vol. 22, no. 8, pp. 888–905, 2000.

[32] S. Fortunato, "Community detection in graphs," *Physics Reports*, vol. 486, no. 3, pp. 75–174, 2010.

**بسم الله الرحمن الرحيم و الصلاة و السلام على أشرف المرسلين سيدنا محمد و على آله وأصحابه اجمعين. أما بعد،**

**فإنه يسعدنى و يشرفنى ان أقدم بين أيديكم الاصدار الأول من مجلة الجامعة الإسلامية للعلوم التطبيقية. و لقد أنشأت هذه المجلة بهدف أن تجعل من صفحاتها ميداناً لكلِ ما هو جديدٌ و متميز من الأبحاث العلمية فى مجالات الهندسة و العلوم و الحاسوب من شتى أنحاء البسيطة.**

**ولقد استقبلنا فى العدد الأول الكثير من الأبحاث العلمية فى مختلف المجالات و من دول عديدة و كان ذلك من دواعى السرور و الحبور لهيئة تحرير هذه المجلة الفتية.**

**و تود هيئة التحرير و الهيئة الإستشارية أن تتقدم بخالص الشكر لكلِ من ساهم ببحثٍ أو مقالةٍ فى هذه المجلة. كما تسرها دعوة الباحثين للمساهمة فى الأعداد القادمة بإذن الله.**

**فبكل فخر و إعتزاز اسمحوا لى أن أقدم إليكم العدد الإفتتاحى لهذه المجلة و أتمنى لكم قراءة سعيدة.**

**رئيس هيئة التحرير**

**د. محمد عبد الرؤوف عابدين**

# قواعد النشر في المجلة (*)

- أن يكون البحث جديداً؛ لم يسبق نشره.
- أن يتّسم بالأصالة والجدّة والابتكار والإضافة للمعرفة.
- أن لا يكون مستلًا من بحوثٍ سبق نشرها للباحث/للباحثين.
- أن تراعى فيه قواعد البحث العلميّ الأصيل، ومنهجيّته.
- أن يشتمل البحث على:
  - صفحة عنوان البحث باللغة الإنجليزية
  - مستخلص البحث باللغة الإنجليزية
  - صفحة عنون البحث باللغة العربية
  - مستخلص البحث باللغة العربية
  - مقدمة
  - صلب البحث
  - خاتمة تتضمّن النّتائج والتّوصيات
  - ثبت المصادر والمراجع
  - الملاحق اللازمة (إن وجدت)
- في حال (نشر البحث ورقياً) يمنح الباحث نسخة مجانية واحدة من عدد المجلة الذي نشر بحثه، و (10) مستلات من بحثه.
- في حال اعتماد نشر البحث تؤول حقوق نشره كافة للمجلة، ولها أن تعيد نشره ورقيّاً أو إلكترونياً، ويحقّ لها إدراجه في قواعد البيانات المحلّيّة والعالمية- بمقابل أو بدون مقابل- وذلك دون حاجة لإذن الباحث.
- لا يحق للباحث إعادة نشر بحثه المقبول للنشر في المجلة- في أي وعاء من أوعية النشر- إلا بعد إذن كتابي من رئيس هيئة تحرير المجلة.
- نمط التوثيق المعتمد في المجلة هو نمط (IEEE).

---

(*) يرجع في تفصيل هذه القواعد العامة إلى الموقع الإلكتروني للمجلة:

https://journals.iu.edu.sa/JESC/index.html

## معلومات الإيداع


### النسخة الورقية:

تم الإيداع في مكتبة الملك فهد الوطنية برقم8742 / 1439 وتاريخ 17 / 09 / 1439 هـ

الرقم التسلسلي الدولي للدوريات (ردمد) 1658-7936-

### النسخة الإلكترونية:

تم الإيداع في مكتبة الملك فهد الوطنية برقم 8742 / 1439 وتاريخ 17 / 09 / 1439 هـ

الرقم التسلسلي الدولي للدوريات (ردمد) 1658-7944


### الموقع الإلكتروني للمجلة

https://journals.iu.edu.sa/JESC/index.html


**ترسل البحوث باسم رئيس تحرير المجلة إلى البريد الإلكتروني :**

jesc@iu.edu.sa


بسم الله الرحمن الرحيم

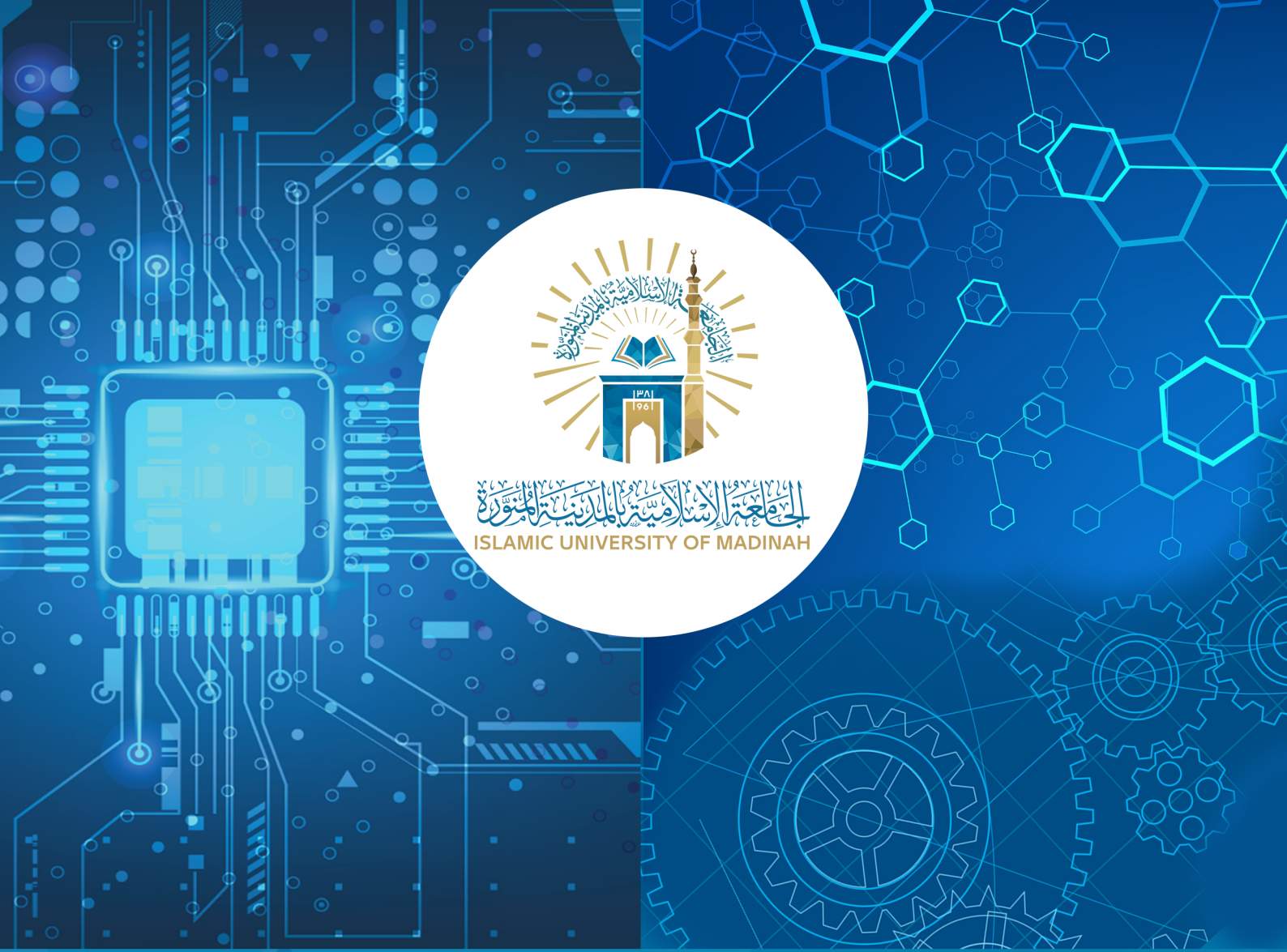


# مجلة الجامعة الإسلامية

## للعلوم التطبيقية

مجلة علمية دورية محكمة

العدد : 1 السنة : الأولى 1440 هـ